Thèse de doctorat

Université de Limoges

Université de Limoges

ED 614 - Chimie , Environnement, Géosciences, Agrosciences (CEGA)

PEIRENE EA 7500

Thèse pour obtenir le grade de

Docteur de l'Université de Limoges

Chimie organique et photophysiques

Présentée et soutenue par

Dáire J. Gibbbons

Le 28 janvier 2022

Triplet state access in multi-component heavy atom free photosensitizers in photomedicine

Thèse dirigée par Stéphanie Leroy-Lhez, Fred Brouwer (Université d'Amsterdam), René M. Williams (Université d'Amsterdam) et Nicolas Villandier

Président du jury
M. Ron Wever, Pr. dr., University of Amsterdam, The Netherlands

JURY:
M. A. M. Brouwer, Pr. Dr., Universiteit van Amsterdam, The Netherlands
Mme. Stéphanie Leroy-Lhez, Dr., Université de Limoges, France
M. René M. Williams Dr., Universiteit van Amsterdam, The Netherlands
M. Nicolas Villandier, Dr., Université de Limoges, France
M. Sander Woutersen, Pr. Dr., Universiteit Van Amsterdam, The Netherlands
M. Maurice C. G. Aalders, Pr. Dr., Universiteit van Amsterdam, The Netherlands
M. Hong Zhang, Pr. Dr., Universiteit van Amsterdam, The Netherlands
Mme. Fabienne Dumoulin, Dr., Acıbadem Mehmet Ali Aydınlar University, Turkey
M. Sylvestre A. Bonnet, Universiteit Leiden, The Netherlands

Triplet state access in multi-component heavy atom free photosensitizers in photomedicine

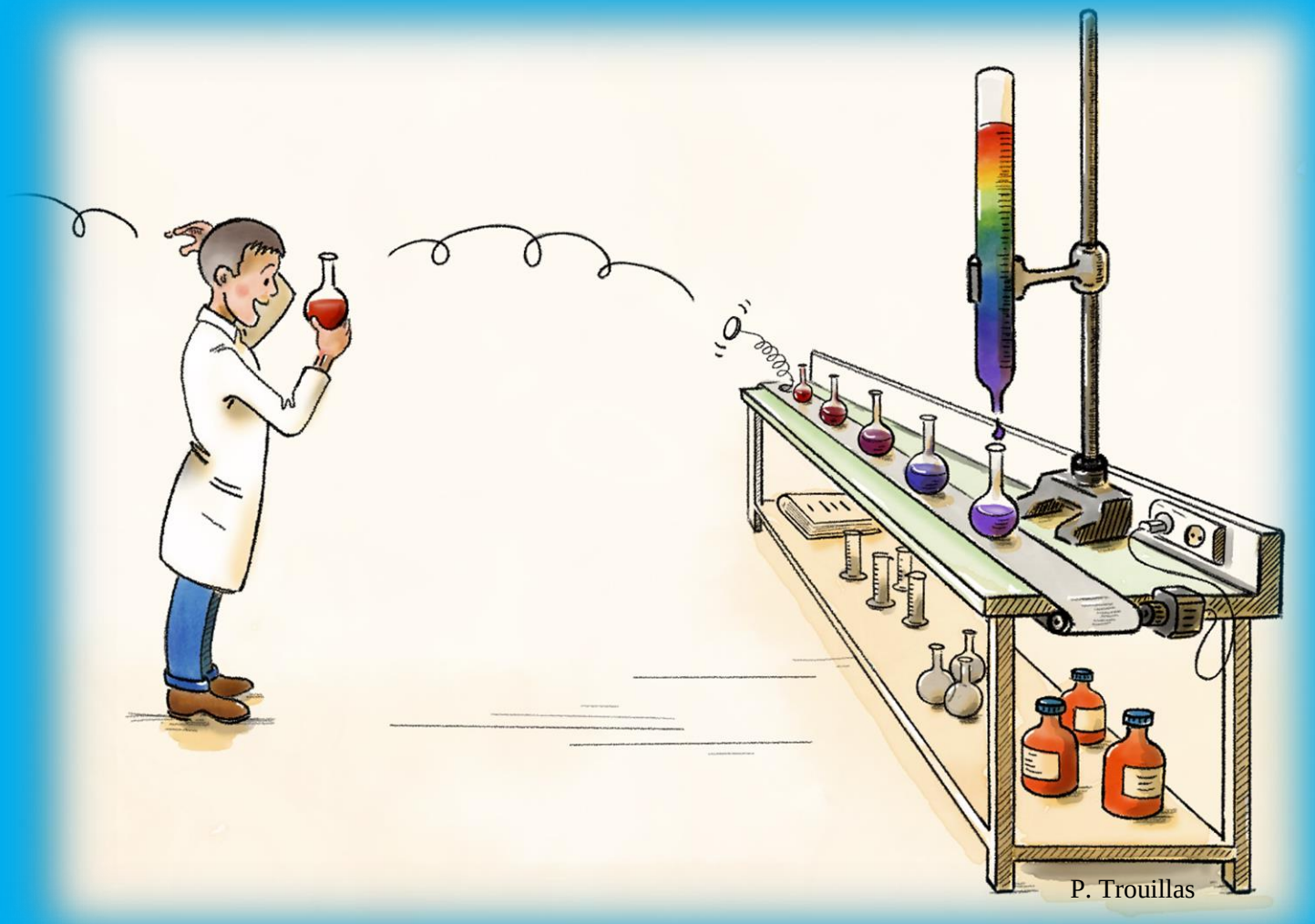

Dáire J. Gibbons

Triplet state access in multi-component heavy atom free photosensitizers in photomedicine

Dáire J. Gibbons

Triplet state access in multi-component heavy atom free photosensitizers in photomedicine

ACADEMISCH PROEFSCHRIFT

ter verkrijging van de graad van doctor

aan de Universiteit van Amsterdam

op gezag van de Rector Magnificus

prof. dr. ir. K.I.J. Maex

ten overstaan van een door het College voor Promoties ingestelde commissie,

in het openbaar te verdedigen in de Aula der Universiteit

op vrijdag 28 januari 2022, te 11.00 uur

door Dáire John Gibbons

geboren te Dublin

Promotiecommissie

Promotores:	prof. dr. A.M. Brouwer	Universiteit van Amsterdam
	dr. S. Leroy-Lhez	Université de Limoges
Copromotores:	dr. R.M. Williams	Universiteit van Amsterdam
	dr. N. Villandier	Université de Limoges
Overige leden:	prof. dr. S. Woutersen	Universiteit van Amsterdam
	prof. dr. M.C.G. Aalders	Universiteit van Amsterdam
	prof. dr. H. Zhang	Universiteit van Amsterdam
	dr. F. Dumoulin	Acıbadem Mehmet Ali Aydınlar University
	prof. dr. S.A. Bonnet	Universiteit Leiden

Faculteit der Natuurwetenschappen, Wiskunde en Informatica

The research covered in this thesis was conducted within a Joint Doctorate in the Molecular Photonics Group at the Van 't Hoff Institute for Molecular Sciences, University of Amsterdam, in the PEREINE laboratoire, Université de Limoges, France and in the company PorphyChem in Dijon, France. The work was financially supported by the European Union's Horizon 2020 research and innovation programme under the Marie Sklodowska-Curie grant agreement no. 764837.

Table of contents

Table of contents i

1. Triplet states in multicomponent photosensitizers for photo-medicine 1

1.1. Introduction to Photodynamic Therapy 2

1.2. Advantages and Disadvantages of Photodynamic Therapy 5

1.2.1. Advantages of Photodynamic Therapy 5

1.2.2. Drawbacks of Photodynamic Therapy 7

1.3. Photochemistry of triplets in photosensitizers 8

1.4. Structural design of Photodynamic Therapy 11

1.4.1. Porphyrin-like molecules – Tetrapyrroles 12

1.4.2. Heptamethine cyanine dye 13

1.4.3. Lignin 14

1.4.4. Ideal photosensitizer for Photodynamic Therapy 17

1.4.4.1. Optical properties 17

1.4.4.2. Physicochemical properties 19

1.4.4.3. Targeting properties 19

1.5. Scope and outline of the thesis 20

2. Making Triplets from Photo-generated Charges: Observations, Mechanisms and Theory 33

2.1. Introduction 34

2.2. Fast Molecular Electron Donor-Acceptor systems (pre-2015) 36

2.3. BODIPY-based dimers and dyads 39

2.4. Polymer-Fullerene blends 51

2.5. Mechanistic aspects 56

2.6. Conclusions and Outlook 68

2.7. References 71

3. Photo-activated thin films of porphyrinoids for reactive oxygen species generation 77

3.1. Introduction 78

3.2. Results and Discussion 80

3.2.1. Synthesis and characterization 80

3.2.2. Photophysical characterization 81

3.2.2.1. Solution properties 81

3.2.2.2. Solid film properties 88

3.3. Conclusion 96

3.4. Experimental 96

3.4.1. Synthesis 96

3.4.2. Photophysical characterization in solution 97

3.4.3. Solid thin films 99

3.5. Supplementary Information 101

3.5.1. Synthesis and characterization 101

3.5.2. Photophysical characterization 105

3.5.2.1. Solution 105

3.5.2.2. Thin film 106

3.6. References 108

4. Lignin conjugates of porphyrins and cyanine dyes for biomedical applications 111

4.1. Introduction 112

4.2. Synthesis 114

4.2.1. Lignin-cyanine 114

4.2.2. Lignin-porphyrin 115

4.2.2.1. Tetra-carboxyphenylporphyrin (TCPP) 115

4.2.2.2. Mono-carboxyphenyl-triphenylporphyrin (m-CPTPP) 117

4.3. Photophysical studies 119

4.3.1. Lignin-cyanine conjugates 119
4.3.2. Lignin-porphyrin conjugates 124
4.3.2.1. TCPP 124
4.3.2.2. *m*-CPTPP 129
4.3.3. Lignin and acetylated lignin 132
4.4. Conclusion 133
4.5. Supplementary information 135
4.5.1. Experimental procedures 135
4.5.2. Supplemental spectra 138
4.5.3. Synthetic characterization 145
4.5.3.1. Lignin-cyanine synthetic characterization 145
4.5.3.2. TCPP-lignin synthetic characterization 148
4.5.3.3. *m*-CPTPP lignin conjugate 151
4.6. References 153
5. Free base porphyrin-cyanine conjugates for photomedicine 157
5.1. Introduction – Porphyrins and heptamethine cyanine dyes 158
5.2. Synthetic reaction schemes 160
5.3. Photophysical studies of the porphyrin-cyanine conjugate - TPPO-IR-783 161
5.3.1. UV-Vis spectroscopy 161
5.3.2. Photoluminescence – Fluorescence emission and singlet oxygen emission spectroscopy 165
5.3.3. Transient Absorption spectroscopy 174
5.4. Conclusion 177
5.5. Experimental procedures 179
5.5.1. Synthetic reaction schemes 179
5.5.2. Photophysical characterization 181

5.6. Supplementary information 182
5.7. References 188
6. Synthesis of photosensitizers for photomedicine 191
6.1. Introduction 192
6.1.1. Porphyrin-cyanine dye conjugates 192
6.1.2. Porphyrins in thin films 196
6.2. Discussion 197
6.2.1. Porphyrin-cyanine dye conjugates 197
6.2.2. Tetra-alkoxy-arylporphyrins 200
6.3. Conclusions 203
6.4. Synthetic experimental procedures 204
6.5. Experimental Spectra 210
6.6. References 222
7. Phenalenone-Triazolium Salt Derivatives for Antimicrobial Photodynamic Therapy 225
7.1. Introduction 226
7.2. Photophysical Results and Discussion 227
7.3. *In vitro* bacterial studies 232
7.4. Experimental section 236
7.5. References 239
Publications 241
Summary 243
Samenvatting 245
Resumé 249
Sommario 251
Acknowledgements 255

Triplet states in multicomponent photosensitizers for photo-medicine

Abstract

Triplet excited states of photosensitizers in photo-medicine are responsible for treating many different diseases using light therapy. In particular, triplets are responsible for curing cancers *via* photodynamic therapy (PDT) and microbial infections using antimicrobial photodynamic therapy (APDT). While there are many advantages and limitations of this therapy, a large amount of research has been conducted towards optimizing the design of the PS to improve the yield of triplet formation. Further importance of the PS design is dictated by the PS' ability to absorb light at a low energy wavelength. These wavelengths, in the near-IR region, are able to penetrate the skin and arrive to the bloodstream, where the PS can be activated. The structure can finally determine the mechanism by which the triplet formation occurs. This introduction entails the background and foundations of PDT as well as a synthetic toolbox. This will enable the future PDT community to create the next big PS that will cure many other kinds of cancer and microbial infections.

1.1. Introduction to Photodynamic Therapy

Cancer and microbial infections can affect everyone in the world. While we are a long way from curing cancer or eradicating microbial infections from the face of the earth, there exists a targeted treatment that can help people with these conditions, a treatment called photodynamic therapy (PDT). This therapy is known for being non-invasive and minimally toxic. It holds great promise in curing cancers and killing harmful microorganisms. It is a treatment that dates back to the ancient Greeks and there is a rather large community that believes it can help the modern world and has the potential to be improved. All that is required are three things: light, a drug (or molecule called a photosensitizer) and oxygen (in its molecular form : $^3O_2$). It is important to distinguish PDT from antimicrobial photodynamic therapy (APDT), or photodynamic antimicrobial chemotherapy (PACT) as it is also called. While PDT describes a cancer treatment, APDT concerns the therapy aimed at microbial infections. PDT and APDT follow the same basic photochemical mechanism (see Figure **1.1**).[1] In this context, we can see what happens, on a chemical level, to the PS when it is excited or "activated" by light.

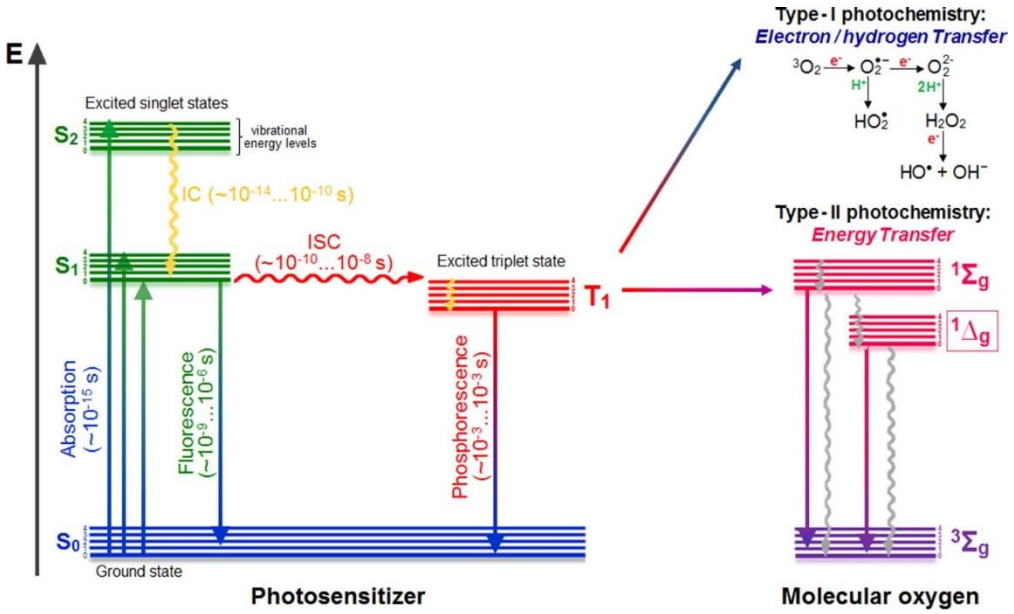

Figure 1.1. *Jablonski diagram showing how the photosensitizer is activated by light, promoting it from its ground state to its excited state (S_1). From here, it can undergo intersystem crossing (ISC) to form a long-lived triplet excited state (T_1). From here, the T_1 can interact with oxygen to form reactive oxygen species (Type I mechanism) and/or singlet oxygen ($^1O_2$; Type II mechanism).*[1]

As previously stated above, PDT involves three components: a photosensitizer (PS), oxygen and light. [1, 2] The PS is a molecule that causes a chemical change in another molecule with the help of light energy. These types of molecules are not only used in the medical fields, but have

been used throughout the photo-sciences. Examples of their applications are photopolymerization, photodegradation, photocatalysis and in photoinactivation of proteins,[3, 4, 5, 6] solving environmental problems,[7, 8, 9, 10] and energy production in the form of hydrogen (H_2).[11] Furthermore, when the photosensitizer absorbs light energy, it can react with other molecules. During scientific discussions about PDT, it is commonly said that the PS is 'activated' by absorbing light energy. Once it has gained this energy, it can interact with oxygen to form singlet oxygen which is toxic for cells and is capable of killing cancer and microbial cells.[12, 13, 14] The advantages and limitations of this therapy are discussed below in section **1.2**.

Historically, light has been employed therapeutically for thousands of years as ancient cultures believed that it was a 'health-bringing deity' that could cure many diseases known to mankind (Figure **1.2**).[15, 19] From antiquity to the end of the 19th century, light, in combination with natural herbs and plant extracts, has been used to treat various skin conditions (non-pigmented skin areas, psoriasis, vitiligo, skin cancer), physical and mental illnesses (such as rickets and psychosis, respectively), in a process known as heliotherapy or phototherapy.[16, 17, 18]

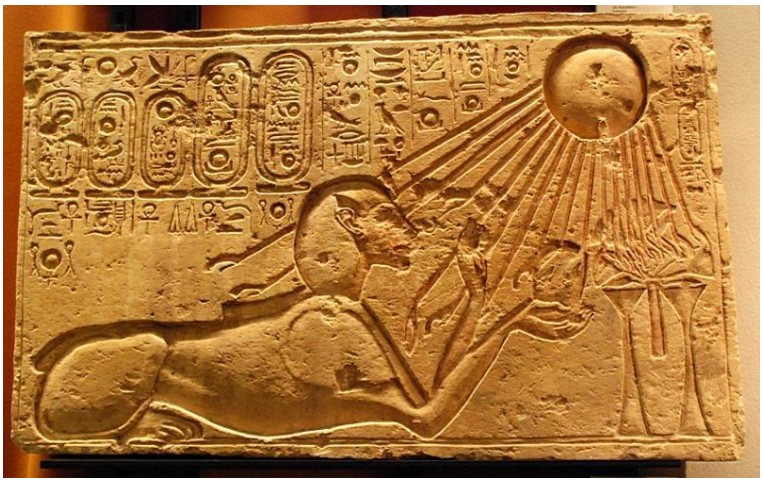

Figure 1.2. *Ancient civilizations worshipping the sun.*[19]

The ancient Greeks believed in the power of sunlight thanks to the 2nd century BC Greek doctor Hippocrates. He was known as the "father" of medical science and educated people about the importance of sun exposure to restore human health. He credited his medical findings to his trips to Egypt, where sunlight treatments were well known.[20] The Greeks had a city known as Heliopolis (city of the sun) that was famous for its healing temples and light rooms equipped with windows covered with special dyed cloths.[19, 21]

The Romans continued the use of this light therapy within their famous baths. It was possible to sunbathe in a solarium and they were the first civilization to treat acne.[16] It was thought that the pores could be cleared and cleansed by mixing sulfur in a mineral bath, which was then able to clear the acne. This would thus conclude the development of phototherapy as when the Roman Empire declined and Christianity began to rise, this type of treatment largely disappeared.

It wasn't until 1877 AD when this type of therapy would crop up once again with Arthur Henry Downes and Thomas Porter Blunt discovering that ultraviolet light exhibited bactericidal effects.[22] This discovery was followed by Niels Finsen publishing a seminal book entitled "Phototherapy." [23, 24] Furthermore, from the period of 1897–1904, Herman Von Tappeiner, alongside his PhD student Oscar Raab, investigated the influence of acridine and it's derivatives on infusoria and other protozoan. They concluded that there was a higher toxicity on protozoan in the presence of light *vs* absence of light.[25, 26] Raab speculated that this toxic effect from the light was mediated by the fluorescence as it was known at the time, that these acridine type dyes could absorb light and emit light as fluorescence. In 1904, Von Tappeiner coined the term "photodynamic reaction" as according to him, it was based on a type of fluorescence effect.

Initially starting in early 1903, without even knowing the real mechanism of action, Von Tappeiner teamed up with Albert Jesionek, to conduct their first human trials of this therapy. Their first research paper on this topic was a study on the photodynamic treatment of cancerous, syphilitic and tuberculous skin conditions.[27] The same year that he described the photodynamic reaction, Von Tappeiner also worked alongside Jodblauer to describe oxygen-consuming reactions in protozoa as a "photodynamic effect."[28] These experiments consisted of aniline dyes giving fluorescence after being applied to the parasitic protozoa. In 1905, Von Tappeiner and Jesionek reformed to report a topically applied PS of 0.1–5 % Eosin dye in their PDT experiments.[29] This PS, with the aid of an artificial light source, successfully treated non-melanoma skin cancers, *condylomata lata* and *lupus vulgaris*. They hypothesized that once this dye got inside the respective harmful cells, a cytotoxic reaction occurred upon light irradiation and it occurred in the presence of oxygen. These early experiments revolutionized the medical world and this concept is still used in the world today where it is more accurately described: when an appropriate PS is applied to the affected region of the skin, it can be absorbed into the target cells within the skin. In the presence of oxygen, and an appropriate light source, a

phototoxic reaction can occur within those skin cells, leading to a photodynamic effect and cell death.

1.2. Advantages and Disadvantages of Photodynamic Therapy

While the major advantage of PDT is the fact that it can cure cancers and fight against microbial infections, it does not come without its disadvantages and limitations. The benefits of this therapy are discussed first, followed by its limitations and drawbacks.

1.2.1. Advantages of Photodynamic Therapy

There exist major benefits of this non-invasive cancer therapy. It can provide reduced long term morbidity compared to other cancer therapies like surgery and chemotherapy.[30] It is more selective and less toxic to healthy human cells, there are no long-term side effects (when used properly), it is less invasive than surgery, less time consuming and targets precisely the area of the body being treated.[31] However, before continuing further, it would also be "advantageous" to know where we are in terms of this therapy. How far has this therapy come since the days of Von Tappeiner and Jesionek in the early 20th century? What cancers does it treat? Is it accessible to the public? To answer simply, yes, it has found its way into the world. It is also possible to get this treatment throughout the Netherlands as well as other countries in the world. A multitude of hospitals in this country offer photodynamic therapy and are detailed in Table **1.1** (along with the type of cancer they treat).[32]

Table 1.1: *Hospitals in the Netherlands and the type of cancer they treat in this hospital via Photodynamic Therapy* [32]

Hospital	Type of cancer treated within this hospital using Photodynamic Therapy
Antoni van Leeuwenhoek- Cancer Institute Amsterdam (Dutch Cancer Institute)	Skin cancer
	Throat cancer
	Oral cavity cancer
	Oral cancer
	Tongue cancer
Universitair Medisch Centrum Groningen	Head and neck cancer
Erasmus MC Rotterdam *	Superficial skin cancer.
Ziekenhuis Nij Smellinghe – Oogheelkunde Drachten	"wet" (exudative) form of Age-related Macular Degeneration (AMD)
Radboud Universitair Medisch Centrum Nijmegen	Basal cell carcinoma, skin cancer, melanoma and various precancerous skin cancer.
St. Antonius Ziekenhuis – Polikliniek Dermatologie Utrecht	Skincancer, Basal cell carcinoma, melanoma.
Universitair Medisch Centrum Utrecht	Various skin conditions, such as actinic keratosis, superficial, basal cell carcinoma and Bowen's disease

*******At the moment, various PDT studies to treat head and neck cancer, and even esophageal cancer, are currently carried out. Also, research on treatment of precancerous uterine cancer and cancer of the vagina is under way.*[32]

As shown above, PDT is commonly used only for skin cancers or cancers that are close to the surface of the skin (throat, head and neck, and oral cancers). Clinical trials using PDT in other types of cancers are currently undergoing (or have been completeled) that include: bladder, lung, breast, pancreatic and cervical cancers[33]. In PDT, an added advantage over surgery is that there is no risk of infections occurring or recurrence of the cancer[34] post-surgery. Furthermore, to the best of our knowledge, no studies have indicated the risk of harmful side effects that occur in chemotherapy.

While there have been great strides to treat other forms of cancer: pancreatic and prostate cancer[35, 36] to name a few, PDT has been clinically approved for treating skin cancers and early-stage cancers. In January 2020, there was some bad news for the PDT community, as the FDA refused the approval of Tookad Soluble into the North American market.[36] This drug has previously been approved by the European Medicines Agency in November 2017 for

prostate cancer and shows good results. The American critique was that the studies were conducted poorly and lacked follow up data. Therefore, there is still hope that Tookad Soluble can break into the North American market.

1.2.2. Drawbacks of Photodynamic Therapy

The main disadvantages of PDT are the time it takes to administer the PS, accumulate at the target and treat the cancer, photosensitivity caused by the PS and the pain associated with the light treatment.[37, 38] Upon admission of the drug, it takes time for the PS to accumulate to the target (from three to 6 hours) and depends obviously on the PS and location of the tumor. In terms of pain arising due to the PS and light irradiation, it has been reported that Foscan (or Temoporfin) caused photosensitivity in patients and the light source burnt the patients' skin (see Figure **1.3** for structure).[38]

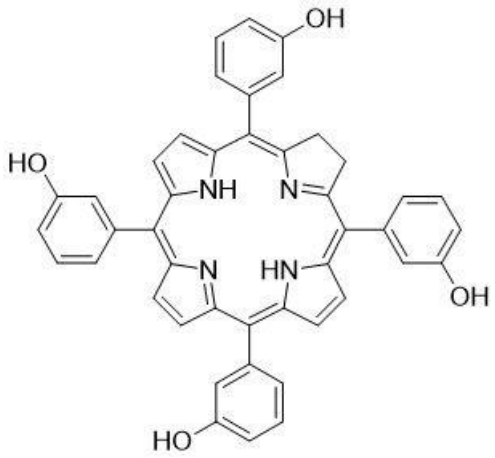

Figure 1.3. *Chemical structure of Foscan (Temoporfin).*

Foscan is used in the treatment of malignant pleural mesothelioma (a type of lung cancer). The photosensitivity issue signified that it is too stable and patients were obliged to quarantine indoors away from the sunlight for weeks. Then once Foscan degraded and the patients were no longer photosensitive, they could resume their lives. In an ideal case, the PS should treat the cancer, breakdown and be excreted from the body without being toxic to the patient.

It is clear that the burning effect experienced by patients during treatment needs to be eliminated or severely reduced. Therefore, the optimization of current light sources used in PDT is needed. Lasers, light emitting diodes and lamps are the main light sources used in the clinic.[39] The light source needed for the specific PDT treatment can vary greatly and depends

on the depth of the target in the body as well as the wavelength the PS absorbs. It is optimal to have a photosensitizer that absorbs strongly in the therapeutic region (approximately 650-850 nm). This can allow for deeper tissue penetration that activates the PS to kill cancer cells.[39, 40] Therefore, creating photosensitizers that can absorb strongly in the therapeutic region (and are stable enough) is of utmost clinical importance as lower energy light can penetrate deeper within the body, be less harmful for the patient and potentially reduce the irritation arising from the treatment.

Overall, PDT is a clinically approved therapy that is in need of new approaches to optimize the current treatments in place. Furthermore, advancement of the current PSs and effecting actual change in the treatment standards are required.[40, 41, 42]

1.3. Photochemistry of triplets in photosensitizers

The main aim of this thesis is to investigate the novel ways to access the triplet excited state (T_1; see Figure **1.1.** and **1.5**). The formation of this state is fundamental in electroluminescence,[43, 44] photocatalysis,[45] photodynamic therapy,[7, 30, 31, 33, 35] photovoltaics[46] photo-oxidation and triplet–triplet annihilation up-conversion.[47, 48, 49] In photovoltaics, there is a known triplet forming mechanism called singlet fission. This encompasses the potential of passing the Shockley-Queisser limit, by creating two T_1 states from one singlet excited state (S_1).[50. 51, 52] This mechanism has been reported in some BODIPY-based PSs and it is outside of the scope of this thesis.

On a chemical level, when the photosensitizer is in its ground state (lowest in energy), it has two electrons that have opposite spins in its highest occupied molecular orbital (HOMO; See Figure **1.4**).[53]

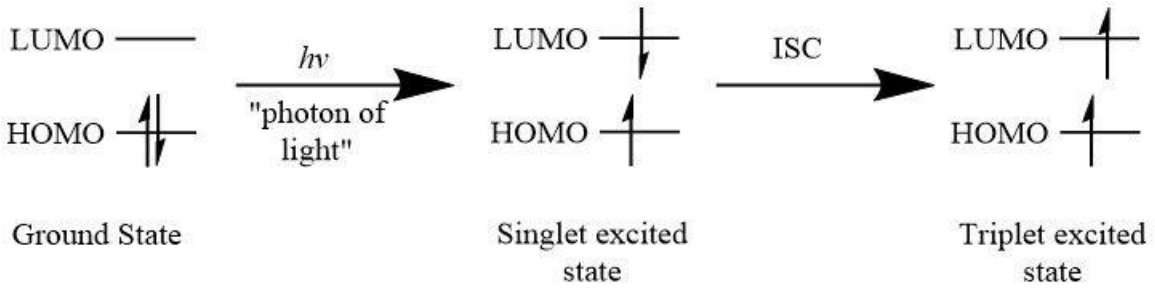

Figure 1.4. *Frontier molecular orbital diagram of the three main states of a photosensitizer.*

It must be noted that while there are many electrons and orbitals in molecules like PSs, the HOMO and LUMO are the most important orbitals in terms of reactivity. PSs are light harvesting complexes[54] and thus have the ability to absorb a lot of light efficiently. When the PS absorbs a photon, this energy is used to promote an electron from a lower energy level to a higher energy level (HOMO to LUMO electron transition). Thus, the PS absorbs this energy and is now in a singlet excited state. The PS in this state has a short lifetime and is unstable, thus, it can undergo two essential mechanisms from here: the first mechanism involves the singlet excited state returning to the ground state and giving off energy in the form of light in a process called fluorescence.[55] The second mechanism that can occur is intersystem crossing (ISC). This involves the photosensitizer passing to a more stable state *via* a spin-flip of the electron in the LUMO. Here, the photosensitizer is in a much more stable excited state called the triplet excited state (T_1) where the lifetime is a lot longer (100s of microseconds) than that of the singlet excited state (~ 1 ns). The singlet excited state can also lose its energy by vibrations and collisions, resulting in heat.

As mentioned, intersystem crossing occurs from the S_1 to the T_1. This pathway is highly favorable when the molecule has a heavy atom included – called the heavy-atom effect.[56, 57] The introduction of a heavy atom can enhance the spin-orbit coupling, rendering the ISC pathway more favorable and increase the formation of T_1 states. After the triplet has formed *via* ISC, the diagram in Figure **1.5** illustrates the likely reactions and pathways that can occur.[1]

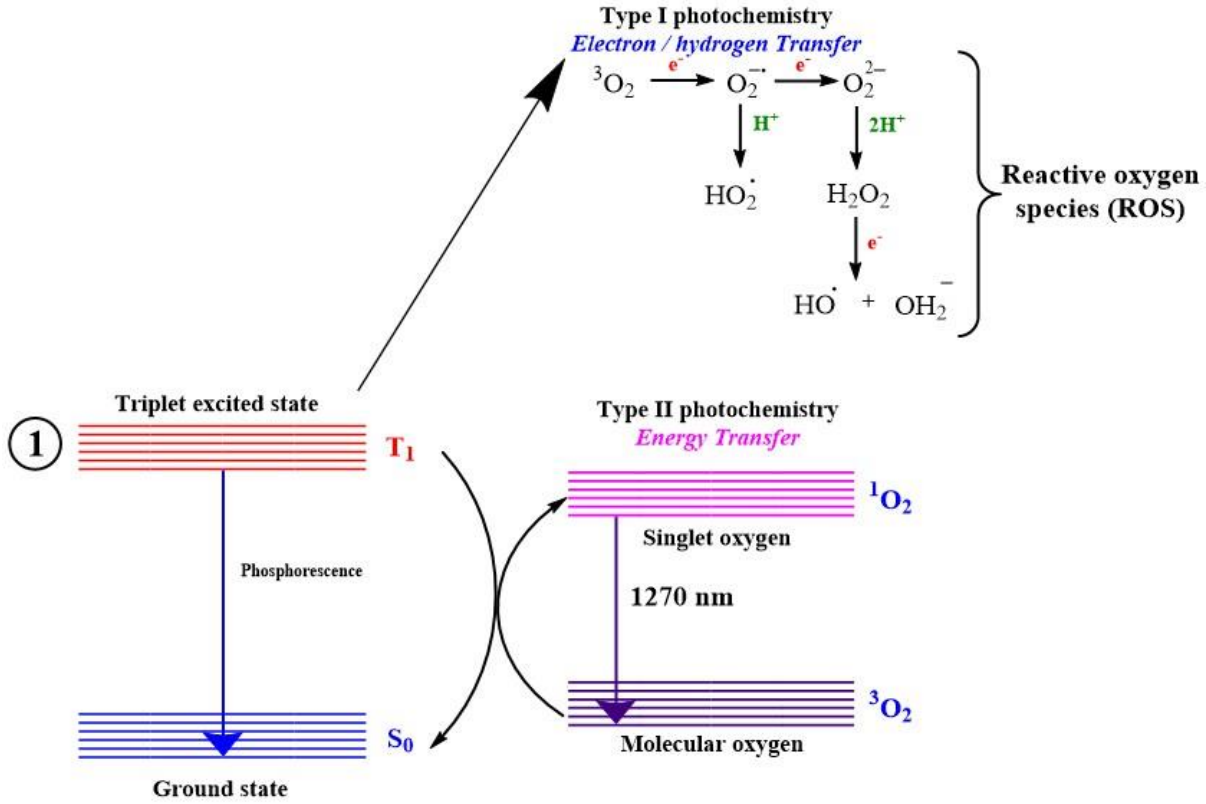

Figure 1.5. *Modified Jablonski diagram illustrating common pathways once the PS is in the triplet excited state (T_1). Once in this state, the molecule can 1) return to its ground state via phosphorescence; 2) undergo type I photochemistry reactions in the form of electron (e^-) and proton (H^+) transfers to create reactive oxygen species (ROS) or 3) transfer its energy to molecular oxygen, thus creating cytotoxic singlet oxygen.*[1]

Once in the T_1 state, the molecule can go back to its ground state *via* phosphorescence. This is a spin-forbidden process that is attributed to the long-term (from minutes to hours) luminescence observed, even after light irradiation has ceased.[58, 59] As well as returning to the ground state, the triplet excited state can undergo reverse intersystem crossing back to the S_1 state,[60] and two photochemical reactions: commonly known as Type 1 and Type 2 photochemical mechanisms.

The type 1 pathway involves electron and proton (H^+) transfer reactions from the PS, in its triplet excited state, to surrounding substrate molecules (that can then react with molecular oxygen), to form toxic oxygen anion and cation species, or radicals, such as $O_2^{-\bullet}$.[2, 61, 62] These species can undergo similar reactions that eventually lead to the formation of reactive oxygen species (ROS) – like H_2O_2.[63] In biological media, it is then possible for this H_2O_2 to reform $O_2^{-\bullet}$ as well as another cytotoxic oxygen species, $^\bullet OH$ by a chain of reactions, involving a divalent Fe^{2+} ion, called the Fenton reaction cascade.

The type 2 mechanism involves the transfer of the PS' triplet energy to molecular oxygen ($^3O_2$) to singlet oxygen ($^1O_2$).[64, 65] This energy transfer is a type of triplet-triplet annihilation process, whereby the T_1 of the PS interacts with the triplet oxygen to form the ground state of the PS and the cytotoxic singlet state of oxygen. Singlet oxygen is capable of causing oxidative stress to living cells and is the most well-known cytotoxic agent in PDT.[66] The dosing (measuring the production) of this reactive oxygen species is a common photophysical indicator of PDT's treatment efficacy for treating a certain cancer or microbial infection. Lastly, while the Jablonski diagram highlights the most common PDT mechanism, there is another mechanism that has recently received attention called triplet formation by charge recombination (TCR). In order to form singlet oxygen *via* this pathway, there must be two molecules joined together (donor-acceptor dyad = two molecules joined together by a specific linker), light and molecular oxygen (see Figure **1. 6**).[67]

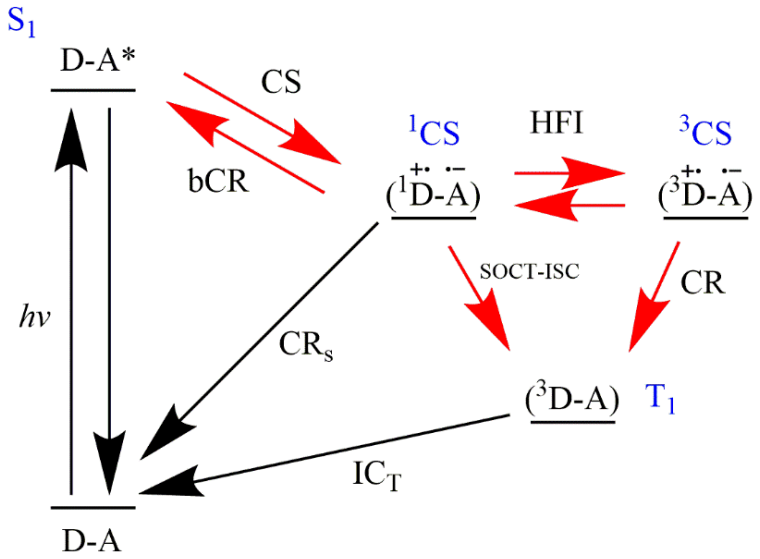

Figure 1.6. *Diagram showing the process of triplet formation via charge recombination (TCR).*[2]

The formation of the T_1, *via* this exotic TCR mechanism, is highly dependent on a number of factors that are discussed in the TCR chapter (see chapter **2** for details and full discussion: Making Triplets from Photo-generated Charges: Observations, Mechanisms and Theory).

1.4. Structural design of Photodynamic Therapy

In order to improve or enhance PDT, it is necessary to focus on one of the three factors: increase oxygen levels, use different sources of light (or different wavelengths), or the design of PS. While the oxygen content *in vivo* is rather difficult to increase without harming the human patient, the other two elements of PDT can be altered to have largely different effects. It must

also be noted that while these latter two elements are of paramount importance, they would both be rendered useless and even toxic, if the PS did not accumulate at the target site. In these cases, an appropriate delivery system is needed.[68] When a PS is administered to the body, time needs to be allowed to reach its target. This thesis will discuss three main PS-type molecules: porphyrins, cyanines and lignins (see Figures **1.7, 1.9, 1.10**).

1.4.1. Porphyrin-like molecules - Tetrapyrroles

Porphyrin, meaning "purple" in Greek, is the most common and studied PS.[69] They are intensely coloured compounds and serve nature in several ways.[70] Some of the services provided by the porphyrin is the backbone of heme, a porphyrin with an iron metal in the centre and is responsible for carrying oxygen around in our bodies. Another famous example is chlorophyll (actually a chlorin). Their chemical structure consists of 4 pyrrole moieties bound together by methine bridges (Figure **1.7**).

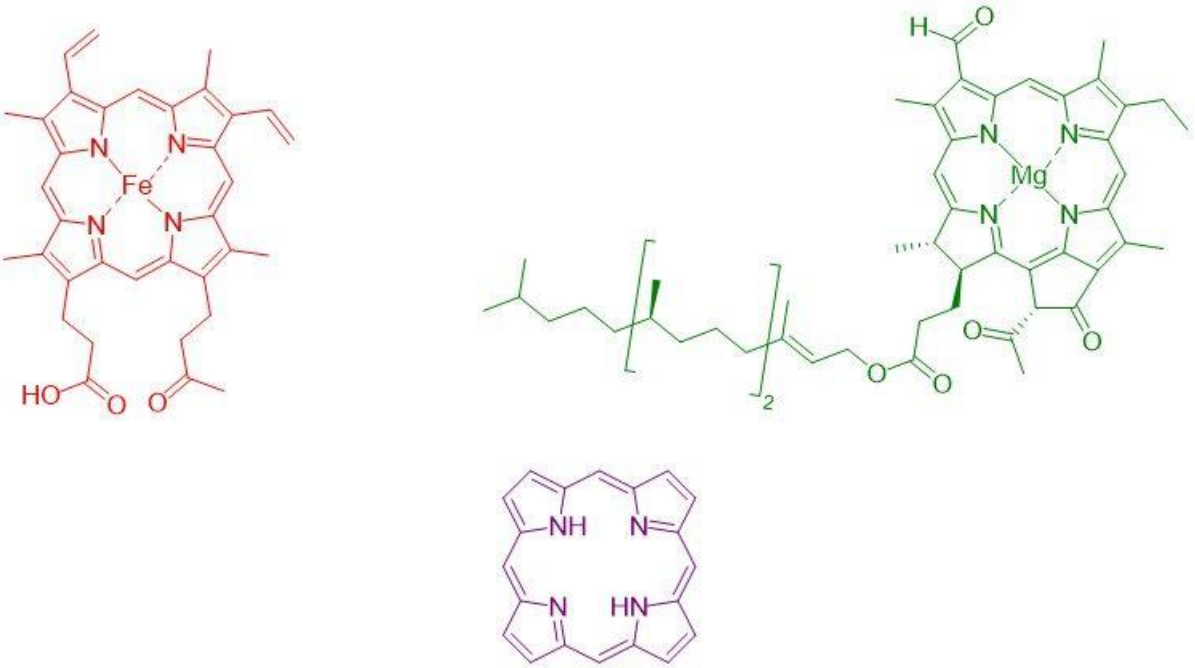

Figure 1.7. *Chemical structures of (Top left): Heme; (Top right): chlorophyll and (Bottom): unsubstituted porphyrin.* ***Note:*** *Heme is an iron-metalated porphyrin whereas chlorophyll is a phytochlorin derivative. The most basic form of a phytochlorin, is a chlorin with a five membered ring.*

These macrocycles are capable of binding metals *via* the nitrogen atoms in the centre. Once metallated, the photophysical, photochemical and photobiological properties change. Porphyrins are characterized by a specific UV-Vis spectrum (from 400 nm to 800 nm). All porphyrins show a spectrum where a large intense band, the Soret band, is detected. In the free-base porphyrin, the Soret band is accompanied by four smaller bands called Q-bands whereas the metallated derivatives only have two Q bands (Figure **1.8**).[71]

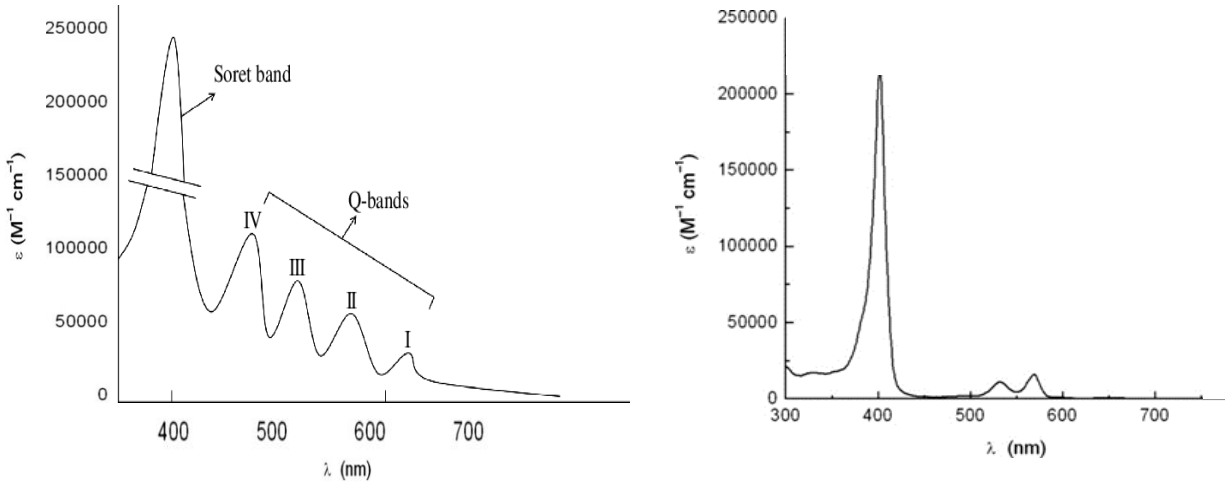

Figure 1.8. *Porphyrin absorption spectrum of the,* ***(Left):*** *free-base porphyrin; and of the* ***(right)****: metallated porphyrin.*[71]

1.4.2. Heptamethine cyanine dye

Near Infrared (NIR) cyanine dyes (Figure **1.9**) have attracted attention in many fields in photomedicine for their intraoperative imaging,[72] and cancer targeting properties.[73]

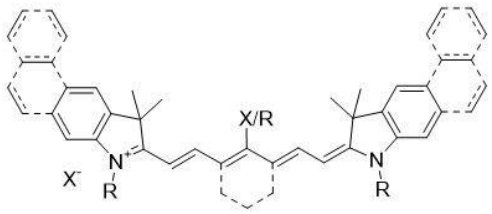

Figure 1.9. *Chemical structure of the cyanine dye.*

In 2017, their potential as triplet photosensitizer in photodynamic therapy was reported.[74] Their structure consists of two heterocyclic components that are connected by a

polymethine bridge, bearing an odd number of carbons. These dyes have large molar absorption coefficients between 700 and 1000 nm and show bright fluorescence in aqueous solutions. Modification of the dye's base structure, like extension of the bridge, results in the red-shift (moving from shorter wavelength to longer wavelength) of absorption and fluorescence maxima. It is also common for sulfonate groups to be attached to the structure to increase its water solubility for use in biological applications.[75]

1.4.3. Lignin

Lignin is one of the principal constituents of the lignocellulosic biomass, alongside cellulose and hemicellulose (see structure in Figure **1.10**).[76] Moreover, it is a polymer that is made in large quantities every year by the pulp and paper industry and has been identified as an ideal starting material for value-added products.[77, 78] Recently, it has been identified can be utilized as a starting material for the fabrication of novel PSs.[79] It is a highly branched 3D polymer that appears as one of the most attractive alternative to fossil fuels in the production of energy and chemicals.[80] The lignin component makes up approximately 15–30 % by weight, while cellulose and hemicellulose make up 30-50 % and 20-35 %, respectively. Located naturally in plant cell walls,[80] lignin is relatively abundant to be considered a renewable resource in the production of aromatic chemical compounds.[81] Lignin is mainly composed of three 4-hydroxyphenylpropanoid moieties: H (p-hydroxyphenyl), G (guaiacyl) and S (syringyl) units, respectively (see Figure **1.10**).[82] These moieties are more commonly known as monolignols, which subsequently form the lignin polymer in a process called lignification.

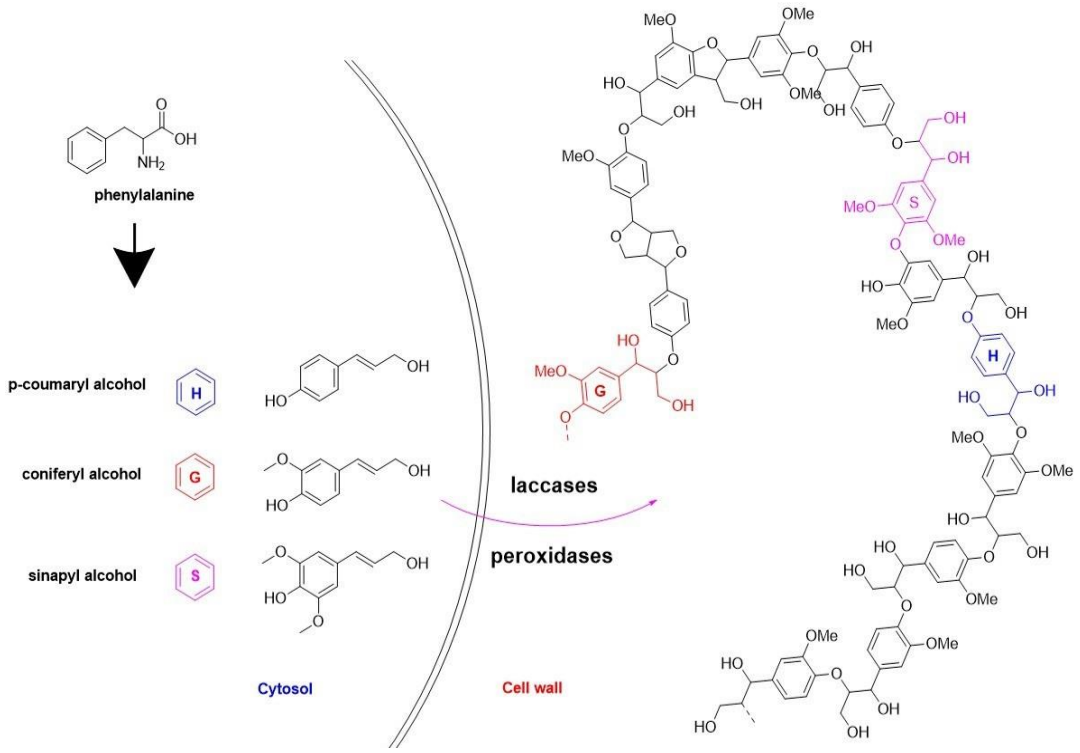

Figure 1.10. *The lignification process in plant cells. Monolignols are biosynthesized from phenylalanine in the cytosol. After being exported to the cell wall, monolignols are oxidized to radicals by peroxidases or laccases after which they undergo purely chemical radical coupling reactions to polymerize to lignin polymers, a process termed lignification.*[83]

While the lignification process is known, the mechanisms that regulate it are still unknown and further studies and investigations are needed for further understanding. The structure of lignin itself can depend on the plant that it was extracted from, the plant tissue within this plant, temperature, lack of nutrients, water and plant pathogens that affect the plant.[83] Therefore it begs the question: How do we extract this lignin from nature so that it is useful in the area of photodynamic therapy?

There are various extraction techniques as shown in **Table 1.2**.[84] In the pulping and biorefinery industry, over 50 million tons of lignin are generated every year as a side product.[85] Therefore in the last number of years, there has been a shift from lignin being used as a side product, to being viewed as an attractive alternative raw material for value-added products.[86]

*Table **1.2.** Extraction processes of lignin including the temperature, pH and chemicals used to create the products indicated in the far right column.*[85]

Extraction process	pH	Temperature (ºC)	Chemicals used/solvents	Product
Sulfite	1–2	125–175	HSO_3^-/ SO_3^-	Lignosulfonates
Kraft	13	150–170	NaOH / NaS_2	Kraft lignin
Organosolv	-	150–200	Organic solvents	Organosolv lignin
Soda	11–13	150–170	NaOH	Soda lignin

In 2018, the rate of adding value (also known as valorisation rate) of lignin was less than 2 %.[87] Thus, only 2 % of this 50 million tons are used in the world annually and thus there is a need for technological advancement to capitalize lignin as a versatile feedstock. The majority of this lignin used is lignosulfonate, which is mainly used as an additive in building materials.[88] There have been reports of value-added chemicals produced from lignin by means of tailored thermochemical technologies. These chemicals include: ethyl benzene (common intermediate in organic synthesis),[89] *p*-hydroxyl acetophenone (perfume industry),[87] vanillin (perfume and pharmaceutical industry)[90] and carbon materials for supercapacitors and catalysts.[91]

Lignin possesses a high thermal stability, has oxidative properties and antioxidant activity.[92] Moreover, while it is insoluble in water,[93] it is capable of forming nanoparticles. It was shown that the acetylation of alkali lignin allowed the possibility of colloidal sphere nanoparticles in certain solvents.[94] This thus created the possibility of nanoparticle formation from lignin. These nanoparticles have served as "vehicle" type structures for therapeutic drugs in pharmaceutical applications that include anticancer treatment.[95] In the past few years, there have been reports of these nanoparticles encapsulating porphyrin-type PSs for their application in antimicrobial photodynamic therapy (APDT). This is a branch of PDT that is used to fight against bacteria, mainly gram-positive bacteria.[96]

As previously mentioned, lignin acetylation facilitates nanoparticle formation,[94] it has also been suggested that acetylated lignin can be a potential photosensitizer.[76] This work was conducted by the PEREINE group in Limoges, in collaboration with the molecular photonics group in Amsterdam. These groups showed that by blocking the anti-oxidant behaviour of the phenol groups in lignin, by acetylating the hydroxy groups, the photoinduced generation of reactive oxygen species was increased. They provide ample evidence that, in terms of the superoxide anion formation, there was no difference in the origin of the lignin (kraft or

organosolv extraction processes). The singlet oxygen generation was however slightly lower in one of the acetylated kraft lignin samples tested. The authors conclude saying that the acetylated lignin could be used to kill harmful micro-organisms.[76]

1.4.4. Ideal photosensitizer for Photodynamic Therapy

It is important to note, and hopefully rather obvious, that there is no "one" ideal photosensitizer in PDT. As many scientists from the drug discovery domain know, there are so many different types of cancers that need one drug to be able to treat them separately. This same basic principle applies to PDT: one photosensitizer is needed to treat each cancer using light. Therefore, in order to construct a general strategy for the PDT community, to create an ideal photosensitizer that treats the cancer of interest, there are various aspects (or properties) that need to be taken into account: the optical properties, physicochemical properties and targeting properties. Within this section of the introduction, the aim is to discuss the various aspects that an ideal photosensitizer should contain in order to be able to provide a "synthetic toolbox" for the PDT community. This toolbox can then give scientists the necessary guidelines to design a plethora of new PSs that can fight against cancer.

1.4.4.1. Optical properties

With regard to the properties of the ideal photosensitizer that are correlated with the interaction of light, the following design aspect should be taken into account:

• The optimal wavelength for treatment lies within the biological window, between 650 and 900 nm. Considering all aspects in the area of PDT, the optimal wavelength is 808 nm.[97, 98, 99] This also correlates to affordable diode lasers with 808 nm (also used in Diode Laser Hair Removal).[100] This means that ideally the wavelength of absorption is 808 nm, or is rather close to that. The closer the better: 690 nm is better than 650 nm.[101] The molar absorption coefficient at around that wavelength (~800 nm) should be as high as possible. Between 200 000 and 300 000 $M^{-1}cm^{-1}$ seems feasible;[102]

• A small yield of fluorescence emission (between 1 and 5%) is needed for localization. If the photosensitizer can accumulate at the tumor site, medical doctors use the emission of photosensitizers for (tumor) localization using microscopy; [103]

• The system should pertain molecular properties that are not influenced by intermolecular interactions between PS molecules. The systems should not aggregate, form dimers or trimers or interact with the medium (serum) leading to a reduction of singlet or triplet excited state lifetime;

• A very high yield of intersystem crossing is needed in order to populate the triplet excited state.[104] Spin Orbit Coupling should be efficient in these systems, giving triplet yields between 99 to 70%. Spin Orbit Coupling can be influenced by heavy metal ions (e.g. Pt or Pd), heavy atoms in the form of bromo- or iodo-substituents, or by a special charge recombination interaction (SOCT-ISC); [105]

• The triplet state should interact with oxygen and give a high yield of singlet oxygen production (operating by the Type II mechanism).[106] If the Type I mechanism is important, then the triplet state should have a high oxidizing power, to abstract electrons from biological molecules leading to superoxide radical anion formation. This value (singlet oxygen quantum yield or $\boldsymbol{\Phi_{\Delta}}$) should be between 99 and 60%;

• In the absence of oxygen, the (intrinsic) triplet excited state lifetime should be as long as possible. An intrinsic triplet excited state lifetime at room temperature of 1 ms should be an attainable goal. This is important for biological materials with low oxygen concentration and the oxygen consumption that will occur in the process;

• The above molecular properties should be available in biological media, implying *in vitro* conditions with cells or *in vivo* conditions in patients. Using the PBS buffer can give a first approximation to these conditions (Phosphate Buffered Saline, pH 7.4);

• Under these conditions, at relatively high laser power irradiation, the photosensitizer molecules should be chemically photo-stable.[107, 108] They should not chemically react with oxygen, singlet oxygen, water, NaCl or other regular components of serum. Their optical properties described above should not be lost during the treatment with light;

• All together, these properties should lead to the efficient production of ROS (reactive oxygen species): singlet oxygen [Type II] and/or superoxide radical anion [Type I].[109] These primary ROS then react further to create hydroxy- and peroxy-radicals.[110] Additions to biological molecules should then lead to peroxy-lipids, peroxy-nucleotides, peroxy-acids. Next to ROS production, a highly interesting approach is to target NO releasing photosensitizers: NO radicals are signaling molecules that play an important role in apoptosis, necrosis, phagocytosis

and paraptosis.[111] They are secondary products of photodynamic therapy, produced by the cells as a result of the ROS generation by light.

The optical properties formulated above are in agreement with photophysical properties that are compatible with biological media and maximize ROS production. Therefore, photosensitizers should not aggregate in solution (nor undergo excited state quenching). They should be resistant to photobleaching and induce maximum light toxicity when irradiated.

1.4.4.2. Physicochemical properties

The next set of properties that need to be discussed, and relate to the intrinsic chemical properties, has been published in the Callaghan and Senge review, and are well known in the PDT community.[23] These properties are the physicochemical properties and are described below. An ideal PS for PDT should have:

• A facile and reproducible synthesis;

• Chemical purity;

• Water-solubility;

• Straightforward administration (intravenous, however oral administration is highly sought after);

• Minimum dark toxicity;

• Minimal side effects;

• Swift activation in the body;

• Swift excretion from the body.

1.4.4.3. Targeting properties

One of the most important and difficult aspects of photosensitizers to control, is related to the magic bullet effect:[112] the drug should go to a specific place in the body only, and not to the other parts. This ratio, of regular distribution through the body compared to specific accumulation at the tumor tissue, is very important and should be as high as possible. A factor of 20 to 100 is a desirable goal. Although PDT relies on three local factors: photosensitizer,

light and oxygen, targeting is still of crucial benefit. The main targeting strategies that exist are:

• the use of antibodies (like Epidermal growth factor receptor or **EGFR**). The PS can be coupled to a known antibody that has strong affinity for tumor tissue;[113]

• the use of nanobodies.[114] The PS can also be coupled to a smaller active part of an antibody (= nanobody) that implies easier access and purity, and can have a better mode of operation than antibodies;

• the use of folate receptors on tumor cells.[115] Folic acid substituted PS can have a higher affinity for cancer cells;

• the use of transferrin.[116] Transferrin substituted PS can have a higher affinity for cancer cells;

• the use of ligands that have strong affinity for tumor tissue. The use of ligands is the broadest section of targeting molecules. As of today, there is a lot of research in the PDT community into novel targeting properties. In a review by Gierlich *et al.*, the authors detailed the recent advances in the active targeting of PSs *via* ligand-derived bioconjugates and ligand-targeting nanocarriers.[117]

Therefore it is hopeful that this section (section **1.4.4**), as well as the literature cited, can act as a synthetic toolbox in the PDT community. This can enable the future chemists and PDT community to create their own ideal photosensitizer for the many different types of cancers that exist.

1.5. Scope and outline of the thesis

This thesis describes the exploration of triplet excited state formation for use in the photo-sciences. It entails the detailed description of the mechanisms that are used to create the sought after triplet state, with a specific focus on applications in photomedicine. Then, it entails an investigation into the application of these mechanisms in novel combinations of photosensitizers and fluorophores.

While this introductory chapter explained the basics, the second chapter describes in detail the main factors that affect the mechanisms of triplet formation *via* charge recombination. Examples in which this rare triplet forming mechanism occurs are shown. Large aromatic dyad and triad systems reported in the years preceding 2015 are described.

Then a comprehensive summary of the findings in BODIPY-based dyads is discussed, followed by the mechanistic details.

Chapter **3** entails the synthesis and photophysical studies of a tetra-hexyloxyphenylporphyrin (see structure in Figure **1.11**) in solution and in a thin film. This porphyrin was synthesized with the idea that the alkyl tails on the *para* position of the phenyl moiety will optimize the properties. Thus, this would aid in the assembly in the thin film by minimizing aggregation, a commonly encountered problem in porphyrin PSs. Thin films of the porphyrin were made using spin coating and vapour phase deposition (see thin films in Figure **1.11**). The photophysical properties were measured using standard fluorescence emission and direct singlet oxygen measurement. Furthermore, time-resolved spectroscopy was conducted namely, nanosecond transient absorption spectroscopy and single photon counting. For the singlet oxygen determination of the porphyrin in the thin film, a singlet oxygen probe was used. This chapter concludes by highlighting the possible applications this porphyrin in a thin film could have.

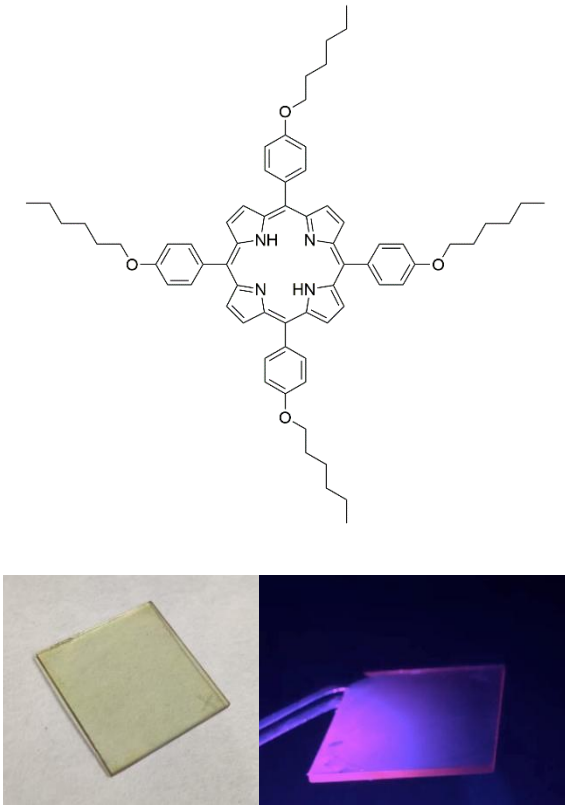

Figure 1.11. *(Top): Chemical structure of the tetra-hexyloxyphenylporphyrin; (Bottom Left): Tetra-alkoxyphenylporphyrin in a thin film and (right): the thin film under UV-light.*

Chapter **4** entails the organic synthesis and photophysical studies conducted on molecules that were covalently attached to lignin (lignin conjugates). This chapter reveals the synthetic methods used to create novel lignin-containing compounds with the aim of improving their photophysical properties for photodynamic therapy.

In Chapter **5**, the synthesis of a novel porphyrin-cyanine conjugate is described. Porphyrin-cyanine conjugates have been synthesized before, however their photophysical properties have never been fully described, to the best of our knowledge. The synthetic details are described followed by the synthetic characterization. This conjugate's photophysical properties were studied for its application in photomedicine. This included steady state and time-resolved emission spectroscopy, followed by nanosecond transient absorption spectroscopy.

Chapter **6** synthesis of cyanine dye starting materials and *meso*-A_4-porphyrins, and starting materials for other A_4 porphyrins like **THOPP** in chapter **3**. Whereas, chapter **7** focuses on the experiments conducted on derivatives of a natural photosensitizer called phenalenone (see structure in Figure **1.12**).[118] Phenalenone is known as a natural photosensitizer that has a singlet oxygen quantum yield of approximately 1.

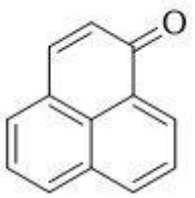

Figure 1.12. *Chemical structure of the natural photosensitizer, phenalenone.*

[1] J. M. Dąbrowski, B. Pucelik, A. Regiel-Futyra, M. Brindell, O. Mazuryk, A. Kyzioł, G. Stochel, W. Macyk and L. G. Arnaut, Engineering of relevant photodynamic processes through structural modifications of metallotetrapyrrolic photosensitizers, *Coord. Chem. Rev.*, 2016, **325**, 67–101. doi: 10.1016/j.ccr.2016.06.007

[2] P. Agostinis, K. Berg, K. A. Cengel, T. H. Foster, A. W. Girotti, S. O. Gollnick, S. M. Hahn, M. R. Hamblin, A. Juzeniene, D. Kessel, M. Korbelik, J. Moan, P. Mroz, D. Nowis, J. Piette, B. C. Wilson and J. Golab, Photodynamic Therapy of Cancer: An Update, *CA: Cancer J. Clin.*, 2011, **61**, 250–281. doi: 10.3322/caac.20114.

[3] S. Das, M. Tiwari, D. Mondal, B. R. Sahoo and D. K. Tiwari, Growing Tool-Kit of Photosensitizers for Clinical and Non-Clinical Applications, *J. Mater. Chem. B.*, 2020, **8**, 10897–10940. doi: 10.1039/D0TB02085K.

[4] T. -Y. Yang, G. Gregori, N. Pellet, M. Grätzel and J. Maier, The Significance of Ion Conduction in a Hybrid Organic–Inorganic Lead-Iodide-Based Perovskite Photosensitizer, *Angew. Chem. Int. Ed.*, 2015, **54**, 7905–7910. doi: 10.1002/anie.201500014.

[5] J. C. Liao, J. Roider and D G Jay, Chromophore-Assisted Laser Inactivation of Proteins Is Mediated by the Photogeneration of Free Radicals, *PNAS*, 1994, **91**, 2659–2663. doi: 10.1073/pnas.91.7.2659

[6] Y. Sano, W. Watanabe and S. Matsunaga, Chromophore-Assisted Laser Inactivation--towards a Spatiotemporal-Functional Analysis of Proteins, and the Ablation of Chromatin, Organelle and Cell Function, *J. Cell Sci.*, 2014, **127**, 1621–1629. doi: 10.1242/jcs.144527.

[7] A. Almeida, Â. Cunha, N. C. M. Gomes, E. Alves, L. Costa and M. A. F. Faustino, Phage Therapy and Photodynamic Therapy: Low Environmental Impact Approaches to Inactivate Microorganisms in Fish Farming Plants, *Mar. Drugs*, 2009, **7**, 268–313. doi: 10.3390/md7030268.

[8] M. Wainwright, D. A. Phoenix, S. L. Laycock, D. R. A. Wareing and P. A. Wright, Photobactericidal Activity of Phenothiazinium Dyes against Methicillin-Resistant Strains of Staphylococcus Aureus, *FEMS Microbiol. Lett.*, 1998, **160**, 177–181. doi: 10.1111/j.1574-6968.1998.tb12908.x.

[9] V. Ambrosini, M. Issawi, V. Sol, and C. Riou, Photodynamic Inactivation of Botrytis Cinerea by an Anionic Porphyrin: An Alternative Pest Management of Grapevine, *Sci. Rep.*, 2020, **10**, 17438–17449. doi: 10.1038/s41598-020-74427-9.

[10] M. I. Rodríguez-López, V. M. Gómez-López, V. Lukseviciute and Z. Luksiene, Modelling the Inactivation and Possible Regrowth of Salmonella Enterica Treated with Chlorophyllin-Chitosan Complex and Visible Light, *Food Technol. Biotechnol.*, 2020, **58**, 64–70. doi: 10.17113/ftb.58.01.20.6374.

[11] E. Ture, Hydrogen Production from Solar Energy, In *Assessment of Hydrogen Energy for Sustainable Development*, edited by John W. Sheffield and Çiğdem Sheffield, 135–146. NATO Science for Peace and Security Series C: Environmental Security. Dordrecht: Springer Netherlands, 2007. doi: 10.1007/978-1-4020-6442-5_12.

[12] H. Guo, H. Qian, N. M. Idris and Y. Zhang, Singlet Oxygen-Induced Apoptosis of Cancer Cells Using Upconversion Fluorescent Nanoparticles as a Carrier of Photosensitizer, *Nanomedicine Nanomed-Nanotechnol.*, 2010, **6**, 486–495. doi: 10.1016/j.nano.2009.11.004.

[13] S. Rajesh, E. Koshi, K. Philip and A. Mohan, Antimicrobial Photodynamic Therapy: An Overview, *J. Indian Soc. Periodontol.*, 2011, **15**, 323–327. doi: 10.4103/0972-124X.92563.

[14] M. Wainwright, Photodynamic Antimicrobial Chemotherapy (PACT), *J. Antimicrob. Chemother.*, 1998, **42**, 13–28. doi: 10.1093/jac/42.1.13.

[15] M. H. Abdel-kader, CHAPTER 1 The Journey of PDT Throughout History: PDT from Pharos to Present, 2016, 1–21. doi: 10.1039/9781782626824-00001.

[16] R. Ackroyd, C. Kelty, N. Brown and M. Reed, The History of Photodetection and Photodynamic Therapy, *Photochem. Photobiol.*, 2001, **74**, 656–669. doi: 10.1562/0031-8655(2001)074<0656:thopap>2.0.co;2.

[17] A. F. McDonagh, Phototherapy: From Ancient Egypt to the New Millennium, *Am. J. Perinatol.*, 2001, **21**, S7–S12. doi: 10.1038/sj.jp.7210625.

[18] J. -C. Diels and L. Arissian, Lasers: The Power and Precision of Light, *Wiley*, 2011, **1**, 93. IBSN: 978-3-527-64003-4.

[19] I. Petricevic, The Ancient Worship of the Sun, and 5 Ancient Civilizations That Venerated It." Curiosmos, September 15, 2020. https://curiosmos.com/the-ancient-worship-of-the-sun-and-5-ancient-civilizations-that-worshipped-it/.

[20] R. Hobday, The healing sun: sunlight and health in the 21st century, Findhorn press, Scotland, 1999, p. 90.
[21] M. D. Daniell and J. S. Hill, A history of photodynamic therapy, *Aust. N. Z. J. Surg.*, 1991, **61**, 340. doi: 10.1111/j.1445-2197.1991.tb00230.x
[22] R. -M. Szeimies, J. Dräger, C. Abels and M. Landthaler, Chapter 1 History of Photodynamic Therapy in Dermatology. In *Comprehensive Series in Photosciences*, edited by Piergiacomo Calzavara-Pinton, Rolf-Markus Szeimies, and Bernhard Ortel, **2**, 3–15. Photodynamic Therapy and Fluorescence Diagnosis in Dermatology. Elsevier, 2001. doi: 10.1016/S1568-461X(01)80105-8.

[23] S. Callaghan and M. O. Senge, The Good, the Bad, and the Ugly – Controlling Singlet Oxygen through Design of Photosensitizers and Delivery Systems for Photodynamic Therapy, *Photochem. Photobiol. Sci.*, 2018, **17**, 1490–1514. doi: 10.1039/C8PP00008E.

[24] N. R. Finsen, *La Photothérapie*, *Georges Carre et C. Naud*, 1899.
[25] O. Raab, Ober die Wirkung fluorescierender Stoffe auf Infusoria, *Z. Biol*., 1900, **39**, 524.
[26] H. Von Tappeiner and A. Jodlbauer, Uber die Wirkung der photodynamischen (fluoreszierenden) Stoffe auf Infusorien, *Dtsch. Arch. Klin. Med*., 1904, **80**, 427–487.
[27] H. Von Tappeiner and A. Jesionek, Therapeutische Versuche mit fluoreszierenden Stoffen, *Miinch. Med. Wochenschr*., 1903, **50**, 2042–2044.
[28] M. H. Gold, A Historical Look at Photodynamic Therapy, *Cosmetic Photodynamic Therapy*, 2016, **3**, 1–7. doi: 10.1159/000439327.

[29] A. Jesionek and H. Von Tappeiner, Zur Behandlung der Hautcarcinome mit fluoreszierenden Stoffen, *Dtsch. Arch. Klin. Med.*, 1905, **85**, 223–227.
[30] A. F. dos Santos, D. R. Q. de Almeida, L. F. Terra, M. S. Baptista and L. Labriola, Photodynamic Therapy in Cancer Treatment - an Update Review, *J. cancer metastatis treat.*, 2019, **5**, 25–45. doi: 10.20517/2394-4722.2018.83.

[31] "Getting Photodynamic Therapy." Accessed April 14, 2021. https://www.cancer.org/treatment/treatments-and-side-effects/treatment-types/radiation/photodynamic-therapy.html.

[32] Photoimmune Discoveries. "PDT Hospitals & Clinics Netherlands." Accessed April 7, 2021. http://photoimmune.org/6227-2/.

[33] H. O. Alsaab, M. S. Alghamdi, A. S. Alotaibi, R. Alzhrani, F. Alwuthaynani, Y. S. Althobaiti, A. H. Almalki, S. Sau and A. K. Iyer, Progress in Clinical Trials of Photodynamic Therapy for Solid Tumors and the Role of Nanomedicine, *Cancers*, 2020, **12**, 2793–2818. doi: 10.3390/cancers12102793.

[34] G. Chen, Z. Wang, X. -Y. Liu and L Fy, Recurrence Patterns of Esophageal Cancer after Ivor-Lewis Esophagectomy--a Report of 196 Cases, *Chin. J. Cancer*, 2006, **25**, 96–99. PMID: 16405760.

[35] Y. Wang, H. Wang, L. Zhou, J. Lu, B. Jiang, C. Liu and J. Guo, Photodynamic Therapy of Pancreatic Cancer: Where Have We Come from and Where Are We Going, *Photodiagnosis Photodyn. Ther.*, 2020, **31**, 101876. doi: 10.1016/j.pdpdt.2020.101876.

[36] https://www.bioworld.com/articles/433332-too-bad-for-tookad-fda-adcom-votes-against-stebas-prostate-cancer-treatment?v=preview. Accessed on the 9th of June 2021.
[37] L. Pérez-Pérez, J. García-Gavín and Y. Gilaberte, Daylight-Mediated Photodynamic Therapy in Spain: Advantages and Disadvantages, *Actas Dermosifiliogr.*, 2014, **105**, 663–674. doi: 10.1016/j.adengl.2014.06.002.

[38] J. S. Friedberg, R. Mick, J. Stevenson, J. Metz, T. Zhu, J. Buyske, D. H. Sterman, H. I. Pass, E. Glatstein and S. M. Hahn, A Phase I Study of Foscan-Mediated Photodynamic Therapy and Surgery in Patients with Mesothelioma, *Ann. Thorac. Surg.*, 2003, **75**, 952–959. doi: 10.1016/s0003-4975(02)04474-0.

[39] D. Van Straten, V. Mashayekhi, H. S. de Bruijn, S. Oliveira and D. J. Robinson, Oncologic Photodynamic Therapy: Basic Principles, Current Clinical Status and Future Directions, *Cancers*, 2017, **9**, 19–72. doi: 10.3390/cancers9020019.

[40] M. O. Senge, mTHPC – A drug on its way from second to third generation photosensitizer?, *Photodiagn. Photodyn. Ther*., 2012, **9**, 170–179. doi: 10.1016/j.pdpdt.2011.10.001

[41] M. O. Senge and J. C. Brandt, Temoporfin (Foscan©, 5,10,15,20-Tetra(mhydroxyphenylchlorin) – a second generation photosensitizer, *Photochem. Photobiol*., 2011, **87**, 1240–1296. doi: 10.1111/j.1751-1097.2011.00986.x

[42] H. Abrahamse and M. R. Hamblin, New photosensitizers for photodynamic therapy, *Biochem. J*., 2016, **473**, 347–364. doi: 10.1042/BJ20150942

[43] S. Hoshino and H. Suzuki, Electroluminescence from Triplet Excited States of Benzophenone, *Appl. Phys. Lett.*, 1996, **69**, 224–226. doi: 10.1063/1.117379.

[44] T. Peng, Y. Yang, Y. Liu, D. Ma, Z. Hou and Y. Wang, A Phosphorescent Material with High and Balanced Carrier Mobility for Efficient OLEDs, *Chem. Commun.*, 2011, **47**, 3150–3152. doi: 10.1039/C0CC04684A.

[45] X. Yang and D. Wang, Photocatalysis: From Fundamental Principles to Materials and Applications, *ACS Appl. Energy Mater.*, 2018, **1**, 6657–6693. doi: 10.1021/acsaem.8b01345.

[46] Z. Xu and B. Hu, Photovoltaic Processes of Singlet and Triplet Excited States in Organic Solar Cells, *Adv. Funct. Mater.*, 2008, **18**, 2611–2617. doi: 10.1002/adfm.200800331.

[47] D. Sasikumar, A. T. John, J. Sunny and M. Hariharan, Access to the Triplet Excited States of Organic Chromophores, *Chem. Soc. Rev.*, 2020, **49**, 6122–6140. doi: 10.1039/D0CS00484G.

[48] S. Guo, W. Wu, H. Guo and J. Zhao, Room-Temperature Long-Lived Triplet Excited States of Naphthalenediimides and Their Applications as Organic Triplet Photosensitizers for Photooxidation and Triplet–Triplet Annihilation Upconversions, *J. Org. Chem.*, 2012, **77**, 3933–3943. doi: 10.1021/jo3003002.

[49] J. Zhao, K. Xu, W. Yang, Z. Wang and F. Zhong, The Triplet Excited State of BODIPY: Formation, Modulation and Application, *Chem. Soc. Rev.*, 2015, **44**, 8904–8039. doi: 10.1039/C5CS00364D.

[50] D. N. Congreve, J. Lee, N. J. Thompson, E. Hontz, S. R. Yost, P. D. Reusswig, M. E. Bahlke, S. Reineke, T. Van Voorhis and M. A. Baldo, External Quantum efficiency above 100% in a Singlet-Exciton-Fission—Based Organic Photovoltaic Cell, *Science*, 2013, **340**, 334–337. doi: 10.1126/science.1232994

[51] W. Shockley and H. J. Queisser, Detailed Balance Limit of Efficiency of p-n Junction Solar Cells, *J. Appl. Phys*., 1961, **32**, 510–519. doi: 10.1063/1.1736034.

[52] R. Prieto-Montero, A. Prieto-Castañeda, R. Sola-Llano, A. R. Agarrabeitia, D. García-Fresnadillo, I. López-Arbeloa, A. Villanueva, M. J. Ortiz, S. de la Moya and V. Martínez-Martínez, Exploring BODIPY Derivatives as Singlet Oxygen Photosensitizers for PDT, *Photochem. Photobiol.*, 2020, **96**, 458–477. doi: 10.1111/php.13232.

[53] F. Vatansever, W. Melo, P. Avci, D. Vecchio, M. Sadasivam, A. Gupta, R. Chandran, M. Karimi, N. A. Parizotto, R. Yin, G. P. Tegos and M. R. Hamblin, Antimicrobial Strategies Centered around Reactive Oxygen Species - Bactericidal Antibiotics, Photodynamic Therapy, and Beyond, *FEMS Microbiol. Rev.*, 2013, **37**, 955–989. doi: 10.1111/1574-6976.12026.

[54] F. F. Özgen, M. E. Runda, B. O. Burek, P. Wied, J. Z. Bloh, R. Kourist and S. Schmidt, Artificial Light-Harvesting Complexes Enable Rieske Oxygenase Catalyzed Hydroxylations in Non-Photosynthetic Cells, *Angew. Chem. Int. Ed.*, 2020, **59**, 3982–3987. doi: 10.1002/anie.201914519.

[55] B. Valeur, Molecular Fluorescence, In *Digital Encyclopedia of Applied Physics*, 477–531. American Cancer Society, 2009. doi: 10.1002/3527600434.eap684.

[56] D. S. McClure, Triplet-Singlet Transitions in Organic Molecules. Lifetime Measurements of the Triplet State, *J. Chem. Phys*., 1949, **17**, 905–913. doi: 10.1063/1.1747085

[57] J. C. Koziar and D. O. Cowan, Photochemical Heavy-Atom Effects, *Acc. Chem. Res.*, 1978, **11**, 334–341. doi: 10.1021/ar50129a003.

[58] G. Baryshnikov, B. Minaev and H. Ågren, Theory and Calculation of the Phosphorescence Phenomenon, *Chem. Rev.*, **117**, 6500–6537. doi: 10.1021/acs.chemrev.7b00060.

[59] G. N. Lewis and M. Kasha, Phosphorescence and the Triplet State, *J. Am. Chem. Soc.*, 1944, **66**, 2100–2116. doi: 10.1021/ja01240a030.

[60] U. Shakeel and J. Singh, Study of Processes of Reverse Intersystem Crossing (RISC) and Thermally Activated Delayed Fluorescence (TADF) in Organic Light Emitting Diodes (OLEDs), *Org. Electron.*, 2018, **59**, 121–124. doi: 10.1016/j.orgel.2018.04.035.

[61] H. Abrahamse and I. M. Tynga, Photodynamic Therapy, a Potential Therapy for Improve Cancer Management, 2018. https://doi.org/10.5772/intechopen.74697.

[62] J. Ferlay, C. Héry, P. Autier and R. Sankaranarayanan, Global burden of breast cancer, In: Li C, editor. Breast Cancer Epidemiology. New York, NY: Springer; 2010. doi: 10.1007/978-1-4419-0685-41.

[63] J. Glaeser, A. M. Nuss, B. A. Berghoff and G. Klug, Singlet Oxygen Stress in Microorganisms, *Adv. Microb. Physiol.*, 2011, **58**, 141–173. doi: 10.1016/B978-0-12-381043-4.00004-0.

[64] C. F. Borland, D. J. McGarvey, A. R. Morgan and T. G. Truscott, Laser Flash Photolysis of Purpurins: Novel Potential Photosensitizers of Interest in Photodynamic Therapy, *J. Photochem. Photobiol. B.*, 1988, **2,** 427–434. doi: 10.1016/1011-1344(88)85071-1.

[65] A. Telfer, Too Much Light? How β-Carotene Protects the Photosystem II Reaction Centre, *Photochem. Photobiol. Sci.*, 2005, **4**, 950–956. doi: 10.1039/B507888C.

[66] X. Liang, K. K. -H. Wang and T. C. Zhu, Singlet Oxygen Dosimetry Modeling for Photodynamic Therapy, *Proc. SPIE*, 2012, 8210. doi: 10.1117/12.908317.

[67] D. J. Gibbons, A. Farawar, P. Mazzella, S. Leroy-Lhez and R. M. Williams, Making Triplets from Photo-Generated Charges: Observations, Mechanisms and Theory, *Photochem. Photobiol. Sci.*, 2020, **19**, 136–158. doi: 10.1039/C9PP00399A.

[68] M. M. Kim and A. Darafsheh, Light Sources and Dosimetry Techniques for Photodynamic Therapy, *Photochem. Photobiol.*, 2020, **96**, 280–294. doi: 10.1111/php.13219.,

[69] L. R. Milgrom, The Colours of Life: An Introduction to the Chemistry of Porphyrins and Related Compounds; Oxford University Press Inc.: New York, 1997.

[70] R. Lemberg, Porphyrins in Nature, In *Fortschritte Der Chemie Organischer Naturstoffe / Progress in the Chemistry of Organic Natural Products / Progrés Dans La Chimie Des Substances Organiques Naturelles*, edited by A. Albert, K. Brückner, R. B. Corey, K. Freudenberg, H. H. Inhoffen, R. Lemberg, L. Pauling, et al., 299–349. Fortschritte Der Chemie Organischer Naturstoffe / Progress in the Chemistry of Organic Natural Products / Progrés Dans La Chimie Des Substances Organiques Naturelles. Vienna: Springer, 1954. doi: 10.1007/978-3-7091-8014-3_7.

[71] Z. Valicsek and O. Horváth, Application of the electronic spectra of porphyrins for analytical purposes: The effects of metal ions and structural distortions, *Microchem. J.*, 2013, **107**, 47–62. doi: 10.1094/MPMI-22-8-0987.

[72] R. Tian, Q. Zeng, S. Zhu, J. Lau, S. Chandra, R. Ertsey, K. S. Hettie, T. Teraphongphom, Z. Hu, G. Niu, D. O. Kiesewetter, H. Sun, X. Zhang, A. L. Antaris, B. R. Brooks and X. Chen, Albumin-Chaperoned Cyanine Dye Yields Superbright NIR-II Fluorophore with Enhanced Pharmacokinetics, *Sci. Adv.*, 2019, **5**, eaaw0672. doi: 10.1126/sciadv.aaw0672.

[73] S. Luo, E. Zhang, Y. Su, T. Cheng and C. Shi, A Review of NIR Dyes in Cancer Targeting and Imaging, *Biomaterials*, 2011, **32**, 7127–7138. doi: 10.1016/j.biomaterials.2011.06.024.

[74] J. Atchison, S. Kamila, H. Nesbitt, K. A. Logan, D. M. Nicholas, C. Fowley, J. Davis, B. Callan, A. P. McHale and J. F. Callan, Iodinated cyanine dyes: a new class of sensitisers for use in NIR activated photodynamic therapy (PDT), *Chem. Commun.*, 2017, **53**, 2009–2012. doi: 10.1039/C6CC09624G.
[75] W. Pham, Z. Medarova and A. Moore, Synthesis and Application of a Water-Soluble near-Infrared Dye for Cancer Detection Using Optical Imaging, *Bioconj. Chem.*, 2005, **16**, 735–740. doi: 10.1021/bc049700+.

[76] **(a)** Y. Lu, Y. -C. Lu, H. -Q. Hu, F. -J. Xie, X. -Y. Wei and X. Fan, Structural Characterization of Lignin and Its Degradation Products with Spectroscopic Methods, *J. Spectrosc.*, 2017, e8951658. doi: 10.1155/2017/8951658; **(b)** G. Marchand, C. A. Calliste, R. M. Williams, C. McLure, S. Leroy-Lhez and N. Villandier, Acetylated Lignins: A Potential Bio-Sourced Photosensitizer, *ChemistrySelect*, 2018, **3**, 5512–5516. doi: 10.1002/slct.201801039.

[77] I. Haq, P. Mazumder and A. S. Kalamdhad, Recent Advances in Removal of Lignin from Paper Industry Wastewater and Its Industrial Applications – A Review, *Bioresour. Technol.*, 2020, *312*, 123636. doi: 10.1016/j.biortech.2020.123636.

[78] M. Alekhina, O. Ershova, A. Ebert, S. Heikkinen and H. Sixta, Softwood Kraft Lignin for Value-Added Applications: Fractionation and Structural Characterization, *Ind Crops Prod.*, 2015, **66**, 220–228. doi: 10.1016/j.indcrop.2014.12.021.

[79] S. Chandna, N. S. Thakur, R. Kaur and J. Bhaumik, Lignin–Bimetallic Nanoconjugate Doped PH-Responsive Hydrogels for Laser-Assisted Antimicrobial Photodynamic Therapy, *Biomacromolecules*, 2020, **21**, 3216–3230. doi: 10.1021/acs.biomac.0c00695.

[80] C. Espro, B. Gumina, E. Paone and F. Mauriello, Upgrading lignocellulosic biomasses: Hydrogenolysis of platform derived molecules promoted by heterogeneous Pd-Fe catalysts, *Catalysts*, 2017, **7**, 78–113. doi: 10.3390/catal7030078
[81] J. S. Luterbacher, D. Martin Alonso and J. A. Dumesic, Targeted Chemical Upgrading of Lignocellulosic Biomass to Platform Molecules, *Green Chemistry*, 2014, **16**, 4816–4838. doi: 10.1039/C4GC01160K.

[82] C. Simon, C. Spriet, S. Hawkins and C. Lion, Visualizing lignification dynamics in plants with click chemistry: Dual labeling is BLISS!, *J. Vis. Exp.*, 2018, **131**, 56947. doi: 10.3791/56947.
[83] J. C. M. S. Moura, C. A. V. Bonnine, J. O. F. Viana, M. C. Dornelas and P. Mazzafera, Abiotic and biotic stresses and changes in the lignin content and composition in plants, *J. Integr. Plant Biol.*, 2010, **52**, 360–376. doi: 10.1111/j.1744-7909.2010.00892.x

[84] S. Laurichesse and L. Avérous, Chemical modification of lignins: Towards biobased polymers, *Prog. Polym. Sci*., 2014; **39**, 1266–1290. doi: 10.1016/j.progpolymsci.2013.11.004
[85] B. Wang, D. Sun, H. -M. Wang, T. -Q. Yuan and R. -C. Sun, Green and Facile Preparation of Regular Lignin Nanoparticles with High Yield and Their Natural Broad-Spectrum Sunscreens, *ACS Sustain. Chem. Eng.*, 2019, **7**, 2658–2666. doi: 10.1021/acssuschemeng.8b05735.

[86] O. Yu and K. H. Kim, Lignin to Materials: A Focused Review on Recent Novel Lignin Applications, *Appli. Sci.*, 2020, **10**, 4626–4241. doi: 10.3390/app10134626.

[87] L. Cao, I. K. M. Yu, Y. Liu, X. Ruan, D. C. W. Tsang, A. J. Hunt, Y. S. Ok, H. Song and S. Zhang, Lignin Valorization for the Production of Renewable Chemicals: State-of-the-Art Review and Future Prospects, *Bioresour. Technol.*, 2018, **269**, 465–475. doi: 10.1016/j.biortech.2018.08.065.

[88] R. V. Gadhave, P. A. Mahanwar and P. T. Gadekar, Lignin-Polyurethane Based Biodegradable Foam, *Open J. Polym. Chem.*, 2018, **8**, 1–10. doi: 10.4236/ojpchem.2018.81001.

[89] Y. N. Regmi, J. K. Mann, J. R. McBride, J. Tao, C. E. Barnes, N. Labbé and S. C. Chmely, Catalytic Transfer Hydrogenolysis of Organosolv Lignin Using B-Containing FeNi Alloyed Catalysts, *Catalysis Today*, Selected Contributions to the Symposium on Catalysts & Catalytic Technologies for Conversion of Biomass & Its Derivatives (252nd ACS Meeting and Exposition, Philadelphia, PA), 2018, **302**, 190–195. doi: 10.1016/j.cattod.2017.05.051.

[90] R. Rinaldi, R. Jastrzebski, M. T. Clough, J. Ralph, M. Kennema, P. C. A. Bruijnincx and B. M. Weckhuysen, Paving the way for lignin valorisation: Recent advances in bioengineering, biorefining and catalysis, *Angew. Chem. Int. Ed.*, 2016, **55**, 8164–8215. doi: 10.1002/anie.201510351.

[91] H. Zhang, D. Jia, Z. Yang, F. Yu, Y. Su, D. Wang and Q. Shen, Alkaline lignin derived porous carbon as an efficient scaffold for lithium-selenium battery cathode, *Carbon*, 2017, **122**, 547–555. doi: 10.1016/j.carbon.2017.07.004.

[92] D. Kai, M. J. Tan, P. L. Chee, Y. K. Chu, Y. L. Yap and X. J. Loh, Towards lignin-based functional materials in a sustainable world, *Green Chem.*, 2016, **18**, 1175–1200. doi: 10.1039/C5GC02616D.

[93] M. Lievonen, J. J. Valle-Delgado, M. -L. Mattinen, E. -L. Hult, K. Lintinen, M. A. Kostiainen, A. Paananen, G. R. Szilvay, H. Setälä and M. Österberg, A Simple Process for Lignin Nanoparticle Preparation, *Green Chem.*, 2016, **18**, 1416–1422. doi: 10.1039/C5GC01436K.

[94] Y. Qian, Y. Deng, X. Qiu, H. Li and D. Yang, Formation of Uniform Colloidal Spheres from Lignin, a Renewable Resource Recovered from Pulping Spent Liquor, *Green Chem.*, 2014, **16**, 2156–2163. doi: 10.1039/C3GC42131G.

[95] R. Kumar, A. Butreddy, N. Kommineni, P. G. Reddy, N. Bunekar, C. Sarkar, S. Dutt, V. K. Mishra, K. R. Aadil, Y. K. Mishra, D. Oupicky and A. Kaushlik, Lignin: Drug/Gene Delivery and Tissue Engineering Applications, *Int. J. Nanomedicine*, 2021, **16**, 2419–2441. doi: 10.2147/IJN.S303462.

[96] N. Maldonado-Carmona, T. -S. Ouk, N. Villandier, C. A. Calliste, M. J. F. Calvete, M. M. Pereira and S. Leroy-Lhez, Photophysical and Antibacterial Properties of Porphyrins Encapsulated inside Acetylated Lignin Nanoparticles, *Antibiotics*, 2021, **10**, 513–538. doi: 10.3390/antibiotics10050513.

[97] D. E. Hudson, D. O. Hudson, J. M. Wininger and B. D. Richardson, Penetration of Laser Light at 808 and 980 Nm in Bovine Tissue Samples, *Photomed. Laser Surg.*, 2013, **31**, 163–168. doi: 10.1089/pho.2012.3284.

[98] S. Kolemen, T. Ozdemir, D. Lee, G. M. Kim, T. Karatas, J. Yoon and E. U. Akkaya, Remote-Controlled Release of Singlet Oxygen by the Plasmonic Heating of Endoperoxide-Modified Gold Nanorods: Towards a Paradigm Change in Photodynamic Therapy, *Angew. Chem. Int. Ed.*, 2016, **128**, 3670–3674. doi: 10.1002/ange.201510064.

[99] D. Wang, B. Xue, X. Kong, L. Tu, X. Liu, Y. Zhang, Y. Chang, Y. Luo, H. Zhao and H. Zhang, 808 Nm Driven Nd 3+ -Sensitized Upconversion Nanostructures for Photodynamic Therapy and Simultaneous Fluorescence Imaging, *Nanoscale*, 2015, **7**, 190–197. doi: 10.1039/C4NR04953E.

[100] M. Lapidoth, M. Adatto, S. Cohen, D. Ben-Amitai and S. Halachmi, Hypertrichosis in Becker's Nevus: Effective Low-Fluence Laser Hair Removal, *J. Lasers Med. Sci.*, 2014, **29**, 191–193. doi: 10.1007/s10103-013-1314-5.

[101] S. Y. Lee, R. Lee, E. Kim, S. Lee and Y. Il Park, Near-Infrared Light-Triggered Photodynamic Therapy and Apoptosis Using Upconversion Nanoparticles With Dual Photosensitizers, *Front. Bioeng. Biotechnol.*, 2020, **8**, 1–9. doi: 10.3389/fbioe.2020.00275.

[102] A. Escudero, C. Carrillo-Carrión, M. Carmen Castillejos, E. Romero-Ben, C. Rosales-Barrios and N. Khiar, Photodynamic Therapy: Photosensitizers and Nanostructures, *Mater. Chem. Front.*, 2021, **5**, 3788–3812. doi: 10.1039/D0QM00922A.

[103] J. P. Celli, B. Q. Spring, I. Rizvi, C. L. Evans, K. S. Samkoe, S. Verma, B. W. Pogue and T. Hasan, Imaging and Photodynamic Therapy: Mechanisms, Monitoring and Optimization, *Chem. Rev.*, 2010, **110**, 2795–2838. doi: 10.1021/cr900300p.

[104] Y. Dong, B. Dick and J. Zhao, Twisted Bodipy Derivative as a Heavy-Atom-Free Triplet Photosensitizer Showing Strong Absorption of Yellow Light, Intersystem Crossing, and a High-Energy Long-Lived Triplet State, *Org Lett.*, 2020, **22**, 5535–5539. doi: 10.1021/acs.orglett.0c01903.

[105] M. A. Filatov, Heavy-Atom-Free BODIPY Photosensitizers with Intersystem Crossing Mediated by Intramolecular Photoinduced Electron Transfer, *Org. Biomol. Chem.*, 2019, **18**, 10–27. doi: 10.1039/C9OB02170A.

[106] M. S. Baptista, J. Cadet, P. Di Mascio, A. A. Ghogare, A. Greer, M. R. Hamblin, C. Lorente, S. C. Nunez, M. S. Ribeiro, A. H Thomas, M. Vignoni and T. M. Yoshimura, Type I and Type II Photosensitized Oxidation Reactions: Guidelines and Mechanistic Pathways, *Photochem. Photobiol.*, 2017, **93**, 912–919. doi: 10.1111/php.12716.

[107] T. Yogo, Y. Urano, Y. Ishitsuka, F. Maniwa and T. Nagano, Highly Efficient and Photostable Photosensitizer Based on BODIPY Chromophore, *J. Am. Chem. Soc.*, 2005, **127**, 12162–12163. doi: 10.1021/ja0528533.

[108] J. Ferreira, P. F. C. Menezes, C. Kurachi, C. Sibata, R. R. Allison and V. S. Bagnato, Photostability of Different Chlorine Photosensitizers, *Laser Phys. Lett.*, 2007, **5**, 156–161. https://doi.org/10.1002/lapl.200710099.

[109] R. L. Auten and J. M. Davis, Oxygen Toxicity and Reactive Oxygen Species: The Devil Is in the Details, *Pediatr. Res.*, 2009, **66**, 121–127. doi: 10.1203/PDR.0b013e3181a9eafb.

[110] G. Barrera, Oxidative Stress and Lipid Peroxidation Products in Cancer Progression and Therapy, *ISRN Oncology*, 2012, **2012**, 137289. doi: 10.5402/2012/137289.

[111] A. Fraix and S. Sortino, Combination of PDT Photosensitizers with NO Photodononors, *Photochem. Photobiol. Sci.*, 2018, **17**, 1709–1727. doi: 10.1039/C8PP00272J.

[112] P. Majumdar, R. Nomula and J. Zhao, Activatable Triplet Photosensitizers: Magic Bullets for Targeted Photodynamic Therapy, *J. Mater. Chem. C.*, 2014, **2**, 5982–5997. doi: 10.1039/C4TC00659C.

[113] E. O. Serebrovskaya, E. F. Edelweiss, O. A. Stremovskiy, K. A. Lukyanov, D. M. Chudakov and S. M. Deyev, Targeting Cancer Cells by Using an Antireceptor Antibody-Photosensitizer Fusion Protein, *PNAS.*, 2009, **106**, 9221–9225. doi: 10.1073/pnas.0904140106.

[114] R. Heukers, P. M. P. van Bergen en Henegouwen and S. Oliveira, Nanobody-Photosensitizer Conjugates for Targeted Photodynamic Therapy, *Nanomedicine Nanomed-Nanotechnol.*, 2014, **10**, 1441–1451. doi: 10.1016/j.nano.2013.12.007.

[115] M. García-Díaz, S. Nonell, A. Villanueva, J. C. Stockert, M. Cañete, A. Casadó, M. Mora and M. Lluïsa Sagristá, Do Folate-Receptor Targeted Liposomal Photosensitizers Enhance Photodynamic Therapy Selectivity?, *Biochim. Biophys. Acta*, 2011, **1808**, 1063–1071. https://doi.org/10.1016/j.bbamem.2010.12.014.

[116] S. Dixit, T. Novak, K. Miller, Y. Zhu, M. E. Kenney and A. -M. Broome, Transferrin Receptor-Targeted Theranostic Gold Nanoparticles for Photosensitizer Delivery in Brain Tumors., *Nanoscale*, 2015, **7**, 1782–1790. doi: 10.1039/c4nr04853a.

[117] P. Gierlich, A. I. Mata, C. Donohoe, R. M. M. Brito, M. O. Senge and L. C. Gomes-da-Silva, Ligand-Targeted Delivery of Photosensitizers for Cancer Treatment, *Molecules*, 2020, **25**, 5317–5370. https://doi.org/10.3390/molecules25225317.

[118] J. Godard, D. Gibbons, S. Leroy-Lhez, R. M. Williams, N. Villandier, T. -S. Ouk, F. Brégier and V. Sol, Development of Phenalenone-Triazolium Salt Derivatives for APDT: Synthesis and Antibacterial Screening, *Antibiotics*, 2021, **10**, 626–638. https://doi.org/10.3390/antibiotics10060626.

Making Triplets from Photo-generated Charges: Observations, Mechanisms and Theory[‡]

Abstract

Triplet formation by charge recombination is a phenomenon that is encountered in many fields of the photo-sciences and can be a detrimental unwanted side effect, but can also be exploited as a useful triplet generation method, for instance in photodynamic therapy. In this chapter, we describe the various aspects that play a role in the decay of charge separated states into local triplet states. The observations and structures of a selection of (pre-2015) molecular electron donor-acceptor systems in which triplet formation by charge recombination occurs are reported. An overview is given of some more recent systems consisting of BODIPY dimers, and BODIPYs attached to various electron-donor units displaying this same triplet formation process. A selection of polymer-fullerene blends in which triplet formation by (non-geminate) charge recombination has been observed, is presented.

Furthermore, in-depth information regarding the mechanistic aspects of triplet formation by charge recombination is given on spin dephasing, through hyperfine interactions, as well as on spin-orbit coupling occurring simultaneously with charge recombination. The limits and constraints of these factors and their role in intersystem crossing are discussed. A pictorial view of the two mechanisms is given and this is correlated to aspects of the selection rules for triplet formation, the so-called El-Sayed rules. It is shown that the timescale of triplet formation by charge recombination is indicative for the mechanism that is responsible for the process. The relatively slow rates (${}^{CR}k_T \sim 1 \times 10^8$ s^{-1} or slower) can be correlated to proton hyperfine interactions (also called the radical pair mechanism), but substantially faster rates (${}^{CR}k_T \sim 1 \times 10^9$ up to 2.5×10^{10} s^{-1} or faster) have to be correlated to spin-orbit coupling effects. Several examples of molecular systems showing such fast rates are available and their electron donor and acceptor orbitals display an orthogonal relationship with respect to each other. This orientation of (the nodal planes of) the π-orbitals of the donor and acceptor units is correlated to the mechanisms in photodynamic agents and photovoltaic blends.

[‡]The content of this chapter has been adapted from the publication: Dáire J. Gibbons, Aram Farawar, Paul Mazzella, Stéphanie Leroy-Lhez and René M. Williams, *Making triplets from photo-generated charges: observations, mechanisms and theory*, Photochem. Photobiol. Sci., 2020, 19, 136–158, DOI: 10.1039/c9pp00399a.

2.1. Introduction

Triplet excited state formation is of great importance for many applications such as photo-initiators for photopolymerization,[1] photodynamic (anticancer) therapy,[2] photodynamic antimicrobial chemotherapy[3] as well as light emitting diodes containing triplet emitters.[4] In photovoltaics, making triplets by using singlet fission[5] entails the promise of passing the Shockley-Queisser limit[6] by creating two free charged pairs from one photon. However, next to creating charges by using triplet excited states, also the reverse process, the formation of triplet states from charges has gained a lot of interest, especially in recent investigations of organic thin film blends that relate to photovoltaic materials.[7, 8, 9] Various reports on these matters state that there is no clarity regarding the mechanistic aspects of this loss channel in organic photovoltaic materials,[10, 11, 12] especially when occurring on a sub-nanosecond timescale.

Upon local photo-excitation of an electron donor-acceptor system, the excited singlet state is formed, from which charge separation can occur. The process of photoinduced charge separation has been described extensively,[13] and will not be dwelled upon here. Most charges that are photogenerated recombine back to a ground state singlet. Sometimes, high lying charge-transfer states can even repopulate the singlet excited state, leading to so-called delayed luminescence.[14] However, instead of recombining to the singlet, the charges can also recombine to form a triplet state. This pathway is more exotic, but there are many examples where this triplet formation by charge recombination process, sometimes also called triplet charge recombination, plays a role in the photophysical processes occurring after photoexcitation.

The triplet excited state contains two unpaired electrons with the same spin in separate orbitals. In the absence of a magnetic field, the three triplet levels are degenerate only for a totally symmetric system. However, for an asymmetric environment the so-called zero field splitting (characterized by D and E) orients the spin-vectors along the molecular x-y-z axis giving the T_x, T_y and T_z triplet levels. Applying a magnetic field results in the Zeeman effect and the thus introduced magnetic operator (Hamiltonian) converts the levels into the more often encountered T_+, T_0 and T_- levels represented by their spin orientations relative to the magnetic field[15, 16].

In this work, examples are given of the experimental observations regarding triplet formation by charge recombination in molecular electron donor-acceptor systems studied in solution as well as in various polymer-fullerene thin film blends. Special attention is given to

recent work on BODIPY dyes that are attached to electron donors, as well as BODIPY dimers. Next, the currently known mechanistic aspects for these processes are presented. Both (H-HFI) proton hyperfine interactions (= radical pair mechanism, RPM) as well as spin-orbit coupling are discussed in detail with relation to charge recombination. Focus is on the mechanistic aspects regarding the "electron spin-flip", implying that this is the rate determining step in these systems (not the energetics). A correlation (as well as a visualization) is made between the spin-orbit charge transfer intersystem crossing (SOCT-ISC) mechanism and the El-Sayed rules, the spin selection rules for triplet state formation (see section 5).

It has to be noted that a third, more exotic (singlet fission) mechanism has also been proven. In a thin film of a TDI (terrylene-3,4:11,12-bis(dicarboximide)) derivative, an excited state dimer with charge-transfer character can split into two triplet states by singlet fission.[17] This third mechanism is beyond the scope of this chapter.

Magnetic field effects in time resolved electron spin /paramagnetic resonance (TR-ESR/TR-EPR) also fall beyond the scope of this chapter. Interestingly these aspects regarding triplet formation by charge recombination have been reviewed very recently.[18]

This chapter is partly meant to be set up as a tutorial review. It assumes general knowledge of photoinduced charge separation as well as basic knowledge on triplet states. Indeed, the recombination of charges forming a triplet state as the "product" is our topic. This is an illustrative review, it is not a comprehensive survey, and reports on research published between 1968 and June 2019.

Within the theory of electron transfer, creating charges with light is often well described and understood within the frame-work of the Classical Marcus equation. The recombination of the charges is always more complex, often requiring the Semi-classical Marcus theory. Creating long-lived charges (by controlling the charge recombination) in order to use the energy of the photons to create an (electro)chemical potential or electricity still is an important scientific challenge. We believe that charge recombination to a triplet state is one of the most complex aspects of the electron transfer theory, as the role of spin comes into play and becomes one of the determining factors, next to all the other factors in the electron transfer theory.

Triplet formation by charge recombination is an alternative method to generate triplet states. Other methods are using the heavy atom effect or using triplet sensitization. The heavy atom effect is potentially expensive (for instance with Pd or Pt) and also enhances spin orbit coupling back to the ground state. For triplet sensitization we need other triplet forming systems that can transfer their triplet excited state energy. By simply incorporating an electron donor or

acceptor we can change the properties of molecules converting them into systems with high triplet yields by applying the triplet formation by charge recombination mechanism.

2.2. Fast Molecular Electron Donor-Acceptor systems (pre-2015):

We start with a selection of four molecular electron donor acceptor systems to show that structural factors play an important role in fast charge recombination to the triplet state. It is instructive to look at the some of the old work of Noburu Mataga, one of the most excellent Japanese photochemists of the 20th century. The amount of detail and insight that this work displays is flabbergasting and a more in-depth explanation of some of these insights is part of our current mission.

Mataga and co-workers[19] observed the formation of locally excited triplet states (with $\tau_{CR}(T)$ = 40 ps, $\tau_{CR}(T)$ = decay time of charge-transfer (CT) state correlating to the time of formation of the local triplet state T) from charge-transfer intermediates in 1981. The fastest rate of triplet formation by charge recombination ($^{CR}k_T = 2.5 \times 10^{10}$ s^{-1}) was observed for N-methyl-N-phenyl-1-pyrenemethanamine (see figure **2.1**) in hexane.

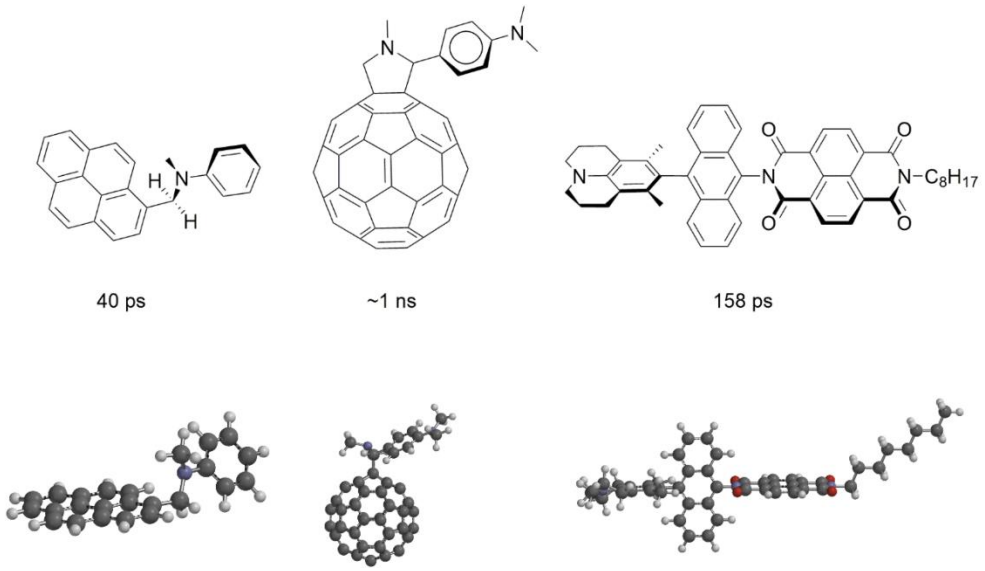

***Figure 2.1. (Top)**: Structures of molecular electron donor-acceptor systems that display triplet formation by charge recombination on a ~ns timescale. The characteristic times of triplet formation by charge recombination are indicated for each molecule. Orientation of separate units is accentuated in the Lewis structure; **(Bottom)**: 3D structures calculated here with DFT (using Spartan).*

These studies uncovered "the very fast generation of the triplet state localized on the pyrene (acceptor) moiety *via* the intramolecular charge-transfer state (referred to as hetero-excimer). The intersystem crossing rate depends rather strongly upon the mutual configuration of donor and acceptor groups as well as the solvent polarity.[19] The compounds with one CH_2 group where the two moieties are close but not parallel have much larger ${}^{CR}k_T$ values compared to compounds with two or three CH_2 groups where the formation of a sandwich-type charge-transfer complex is possible." As reported by Mataga et al. [19] "the matrix element of the spin-orbit coupling interaction between the heteroexcimer state and the so-called ${}^3L_a$ state of pyrene, will become enhanced in the perpendicular configuration" (the L_a transitions of pyrene are directed in the long axis of the molecule). This reasoning is the same as in the case of the relatively large spin-orbit coupling matrix element between π-π^* and n-π^* transitions.[19] Mataga and co-workers point to the perpendicular nodal planes of the molecular orbitals of the (aniline)donor and (pyrene)acceptor playing a role in the process (see also section 5).

In 1995 Williams and Verhoeven reported[20] that "the relatively high triplet yield (Φ_T = 0.8) and the absence of fluorescence (97% quenched) of the bridged C_{60} (acceptor) - aniline (donor) system (see figure **2.1**) indicates that charge recombination to the local fullerene triplet is a major decay pathway of the charge-transfer state in dichloromethane (a solvent with medium polarity)." Since nanosecond transient absorption spectroscopy was applied, it can be inferred that this charge recombination is occurring on a ~ns time-scale. The 3D structure (Figure **2.1**) shows that the aniline donor is virtually orthogonal to the curvature of the fullerene π-system. Just like the molecule studied by Mataga, a ~90˚ angle between donor and acceptor is present.

Indeed, Williams et al. encountered triplet formation by charge recombination in 1995 as an exotic event without putting much emphasis on it. This work however has triggered computational studies that give useful insight: computational chemistry has advanced to such a level that excited state charge transfer processes are within reach. It is important to note that for such systems TD-DFT calculations on excited state electron transfer processes are possible. TD-DFT calculations of the electron transfer time (τ_{CS} = 27 ps) of this system[21] in the strongly polar benzonitrile solvent as well as more exact determination of experimental times[22] of charge separation (τ_{CS} = 5 ps) and recombination to the ground state (τ_{CR} = 32 ps) have been reported. These latter results imply that accurate TD-DFT computations can be obtained for such excited state charge transfer processes and it would be highly interesting and computationally challenging to use TD-DFT to determine the charge-transfer integrals for triplet formation by charge recombination (see section 5).

Wasielewski et al. investigated "intersystem crossing in a series of donor-bridge-acceptor molecules involving photo-generated strongly spin exchange-coupled radical ion pairs" in 2012.[23] Their fastest system has a 3,5-dimethyl-4-julolidine (DMJ) donor, which is connected *via* an anthracene bridge to a naphthalene-1,8:4,5-bis(dicarboximide) (NI) acceptor. "Femtosecond transient absorption spectroscopy shows that photo-driven charge separation produces $DMJ^{+\bullet}$-An-$NI^{-\bullet}$ quantitatively ($\tau_{CS} \leq 10$ ps), and that charge recombination (with $\tau_{CR}(T)$ = 158 ps) to the triplet state on An occurs ($^{CR}k_T = 6.3 \times 10^9$ s^{-1})." The NI π system is perpendicular to that of An and parallel to that of DMJ. "Clearly, charge recombination in $DMJ^{+\bullet}$-An-$NI^{-\bullet}$ will formally require two electron and/or hole transfers between mutually perpendicular π systems to produce ^{3*}An and necessitates consideration of the orbital changes of both charge transfers."

"The triplet sublevels populated by spin-orbit coupling in these molecules depend on the donor-acceptor geometry of the charge-separated state. This is consistent with the fact that the intersystem crossing mechanism requires suitable donor and acceptor orbitals which are nearly perpendicular. Electron transfer results in a large orbital angular momentum change that must be compensated by a fast spin flip to keep the overall angular momentum of the system constant".[23] Spin-orbit charge-transfer intersystem crossing (SOCT-ISC) is the nomenclature for the mechanism of these molecular systems. It relates directly to the mechanistic aspects for the orthogonal systems reported by Mataga and co-workers, as described earlier. In some of the slower molecules reported by Wasielewski, the radical pair mechanism (HFI) and SOCT-ISC operate simultaneously, with similar rates ($\tau_{CR}(T)$ = 10 ns).

Van Willigen and co-workers observed fast direct conversion of the singlet charge-transfer state into a local triplet state for naphthyl-acridinium compounds with EPR. Their experimental data is consistent with a (charged-shifted singlet state) ^{1}CSH $\rightarrow$ ^{3}LE (locally excited triplet state) mechanism of triplet-state formation.[24] In particular, the 10-methyl-9-(1-naphthalenyl)acridinium hexafluorophosphate dyad (**1**) (see figure **2.2**) was held orthogonal due to steric rotational hindrance of the C-H groups of both electron donor (naphthyl) and acceptor (acridinium) subunits.

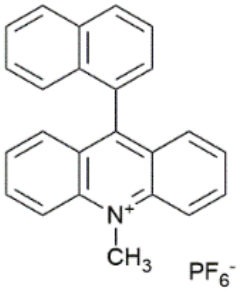

1

Figure 2.2. *10-methyl-9-(1-naphthalenyl)acridinium hexafluorophosphate dyad that undergoes triplet formation by charge recombination from a charge-transfer state.*[24]

These examples of molecular electron donor-acceptor systems indicate that the specific orientation of the π-systems of the donor and acceptor are of great importance for the occurrence of fast triplet formation by charge recombination, and that this process is facilitated by spin-orbit coupling.

Many more examples of molecular systems are available in which the more general, slower triplet formation by charge recombination occurs. Verhoeven *et al*. reported rates of ${}^{CR}k_T \sim 1 \times 10^8$ s^{-1} for (HFI-limited) co-planar dimethoxynaphthanlene(donor)-dicyanovinyl(acceptor) systems studied with EPR[25] and with transient absorption spectroscopy.[26] Furthermore, for an artificial photosynthetic reaction center[27] a rate of ${}^{CR}k_T = 2.2 \times 10^7$ s^{-1} was obtained. Based on these examples it is concluded that relatively slow rates (${}^{CR}k_T \sim 1 \times 10^8$ s^{-1} or slower) can be correlated to and can be dominated by proton hyperfine interactions (if spin inversion is the rate determining step and not the electron transfer energetics). Substantially faster rates however (${}^{CR}k_T \sim 1 \times 10^9$ up to 2.5×10^{10} s^{-1} or faster), have to be correlated to spin-orbit coupling effects in orthogonal systems, as also inferred by Mataga et al.[19] and Wasielewski et al.[23]

2.3. BODIPY-based dimers and dyads

We proceed with an overview of recent work on BODIPY systems. The renewed strong interest in making triplets from charged states has resulted in a great variety of molecular structures, and attempts are made to obtain the ultimate system for this purpose. If we combine these works with the results presented in the previous section we can unify these two parts (see section 5).

Over the past two years, there have been a score of investigations into the use of BODIPY-related dyads as a heavy atom-free photosensitizer (PS). The following discussion entails these investigations as well as their outcomes, impact and applications. In general, BODIPY dyes by themselves are strongly fluorescent and are generally characterized by a fluorescence quantum yield close to unity.[28] Early 2017, Filatov *et al.*[29] demonstrated that BODIPY(acceptor)-anthracene(donor) dyads (BADs) form triplet states *via* photoinduced electron transfer (PeT). When excited with light these BADs yield charge separated states (CS or CT state) which, under the right conditions (solvent, donor-acceptor strength, distance) undergo charge recombination (CR) to form the desired triplet state. Using single crystal X-ray crystallography, the authors demonstrated that when irradiated under aerobic conditions, these BADs react with singlet oxygen ($^1O_2$) resulting in oxygen addition onto the anthracene moiety. Upon reaction with $^1O_2$, these dyads formed adducts where the $^1O_2$ was covalently bound to the anthracene by breaking the aromaticity. These showed strongly increased fluorescence (because PeT is now impossible) and the authors noted that this property could be used in *in vivo* imaging in the future.

Zhao has made several contributions in the area of "BODIPY-based dyads that undergo triplet generation by CR." In 2017, with Wang[30] they studied BADs similar to ones of Filatov *et al.*[29] (Figure **2.3**). Additionally, other BADs were also prepared in order to enhance spin-orbit charge-transfer intersystem crossing (SOCT-ISC), which is related to an orthogonal geometry.

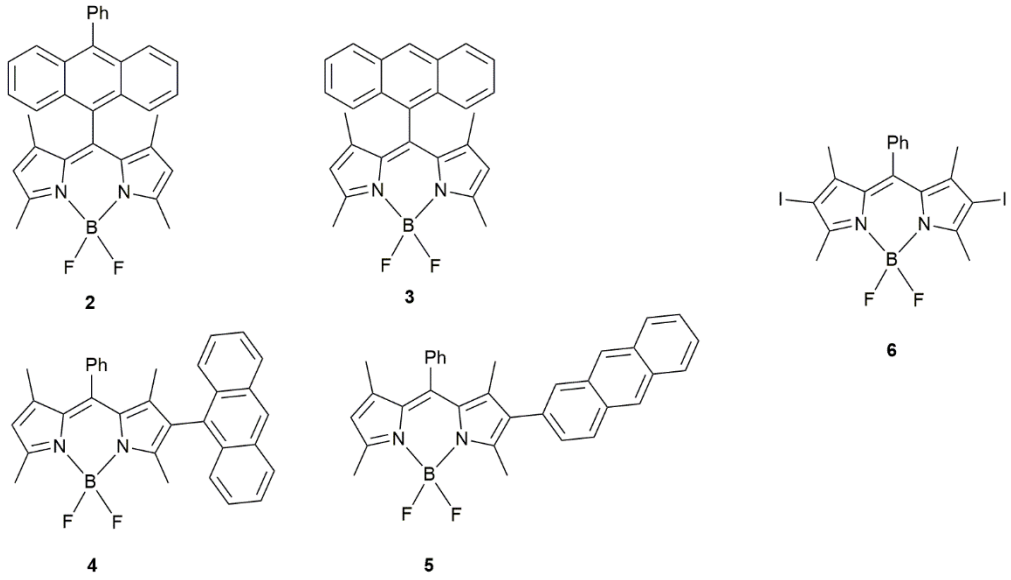

Figure 2.3. *BODIPY-anthracene dyads studied by Wang and Zhao to determine how chromophore orientation influences their application as triplet PSs.*[30]

Dyads, **4** and **5**, were compared with **2** and **3** (also studied by Filatov *et al.* in 2018, *vide infra*).[31] Using DFT calculations, they showed that **4** had the most restricted orthogonal geometry followed by **2**, **3** and **5**. The triplet yields however, did not follow that trend in polar solvents. In fact, the electron donor-acceptor structures that were connected *via* the *meso* (5 position) of the BODIPY unit had the highest triplet yields (**3** = 96% triplet yield in acetonitrile). BADs **4** and **5**, whose donor-acceptor moieties were connected *via* the position 2 of the BODIPY, only had triplet yields of ≤ 31% measured in dichloromethane, acetonitrile and toluene.

The authors state that orthogonality isn't the only necessity for quantitative triplet yields. They tentatively propose that the parallel/antiparallel (ground state) dipole moment orientation of the donor and acceptor results in more efficient intersystem crossing (ISC), thus creating higher triplet state yields. To our knowledge however, there is no theory that links these two aspects.

As reported[19] by Mataga et al., it is the matrix element of the spin-orbit coupling interaction between the charge-transfer state and the triplet state that will become enhanced in the perpendicular configuration and is responsible for the rate of triplet formation by charge recombination. (See also section 5: Mechanistic Aspects).

Zhao and Wang tested the capability of **2** in triplet-triplet annihilation up-conversion (TTA UC). Using perylene as a triplet acceptor, the quantum yield for up-conversion was 15.8%, which is slightly higher than conventional TTA UC candidates (like the heavy atom containing BODIPY **6**, that was also studied).

Zhang *et al.* synthesized four covalent BODIPY heterodimers in which dihedral angles tune the photosensitizing ability.[32] They aimed to understand the mechanism of triplet formation in BODIPY dimers as well as to elucidate "how dihedral angles in a BODIPY dimer affect the triplet state formation and whether it is possible to tune the T_1 formation efficiency." With the use of laser-flash photolysis and Near-Infrared (NIR) luminescence, the authors reported that the dimers in which the two units are perpendicular to each other are better triplet PSs than ones where the BODIPY units are coplanar. Comparing the UV-Vis absorption spectra of the dimers, the authors indicated that the lower dihedral angles between the BODIPY units result in the larger exciton coupling. The BODIPY dimer with a dihedral angle of 62º (**d2**; Figure **2.4**) showed the largest triplet yield (94% in Toluene), which was corroborated by other models.[33]

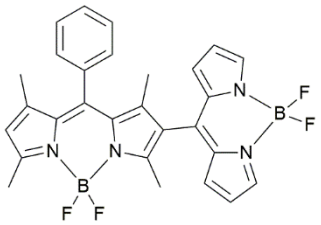

Figure 2.4. *BODIPY dimer* ***d2****, studied by Zhang et al.*[32]

Polar solvents stabilize the CS state and therefore solvent polarity has a substantial effect on the triplet formation and $^1O_2$ production. The steric hindrance induced by the methyl groups in the BODIPY dimers make the two chromophores orthogonal to each other and thus, allow them to be excellent triplet PSs.[31] The triplet formation is due to CR from CSS that results from PeT (Figure **2.5**). The photosensitizing ability of these PSs can be tuned not only by dihedral angles, but also by manipulation of solvent polarity.

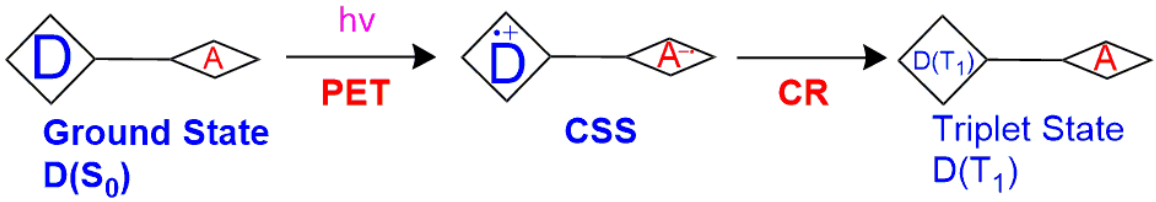

Figure 2.5. *Illustration of triplet formation shown by Zhang et al.*[32] *D is electron donor, A is electron acceptor.*

Liu *et al.* prepared BODIPY dimers to determine the mechanism of triplet formation in these compounds (Figure **2.6**).[34] The rates of triplet formation are given in table **2.1**. The photophysical properties were studied using time-resolved and steady-state fluorescence spectroscopy. The fluorescence properties were solvent polarity dependent whereas this was not the case for the UV-absorption.

A red shifted BODIPY dimer, (**8**; with a carbazole moiety) as well as BODIPY dimers with donating or withdrawing groups attached to these BODIPY dimers (**9** and **10**) showed a decrease in the triplet yield. This was determined by comparing the intensity of the ground state bleaching signals and singlet oxygen quantum yields.

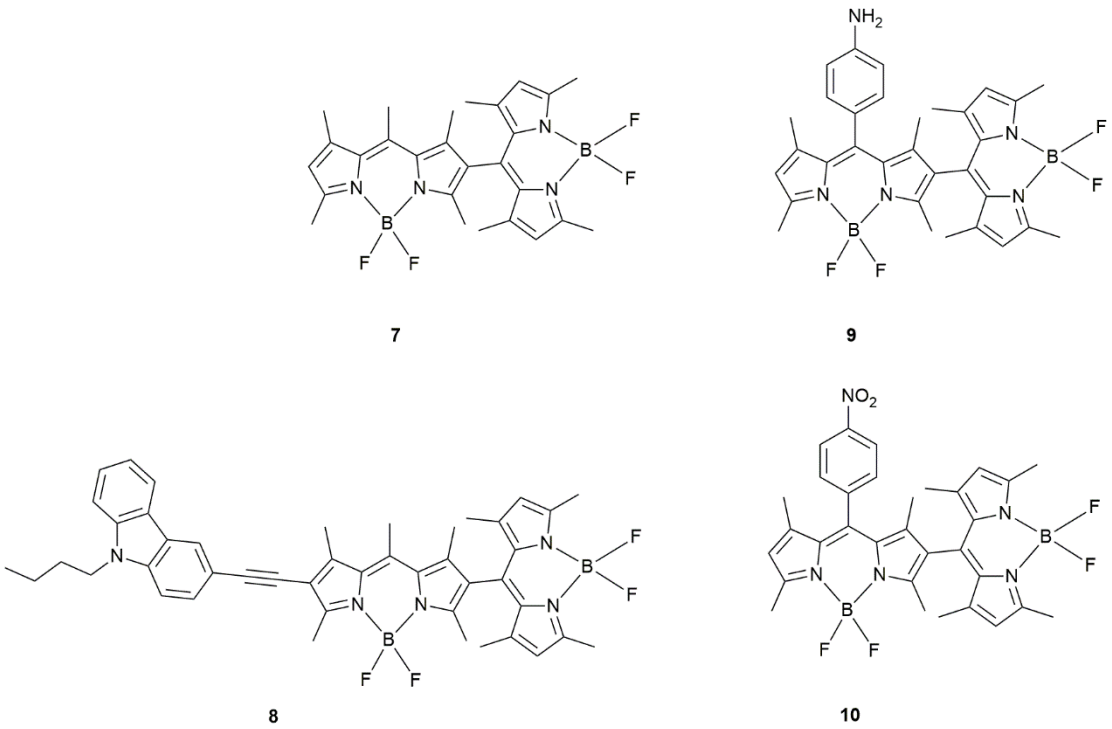

Figure 2.6. *BODIPY dimers prepared by Liu et al.*[34]

A calculation of the Gibbs free energy for PeT in these BODIPY dimers determined that charge separation in **10** is thermodynamically allowed. The authors stated that the triplet state yield is highest in solvents with moderate polarity. They claim that the ISC involved in this CR process is now most efficient (Table **2.1**) as the triplet state is accessible in these moderate polarity solvents.

Table 2.1. *Photophysical data for compounds **2** to **12**. Rates of triplet charge recombination ($^{CR}k_T$) are given where available. Fluorescence quantum yields (Φ_F), $^1O_2$ quantum yields (= Φ_Δ) are indicated.*

cmpds	Solvent	$^{CR}k_T$ (s^{-1})	(ϕ_F)	Φ_Δ	$\Phi\Delta/\Phi\Delta_R$[a]	Ref.
2	TOL		0.81; 0.79	0.10		30, 31
2	DCM		0.01; 0.024	0.95		30, 31
2	ACN	3.5×10^8	0.002; 0.007	0.84		30, 31, 39
2	DMF	1.75×10^5	0.01	0.59[b]		31
3	TOL		0.84; 0.92	0.04		30, 31
3	DCM		0.14; 0.072	0.82		30, 31
3	ACN		0.01; 0.006	0.86		30, 31
3	DMF	1.25×10^5	0.011	0.53 [b]		31
4	TOL		0.39	0.20		30
4	DCM		0.10	0.24		30
4	ACN		0.01/0.02	0.11		30
5	TOL		0.42	0.11		30
5	DCM		0.20	0.13		30
5	ACN		0.04	0.05		30
7	TOL	[c]	0.80		0.16	34
7	THF	4.0×10^8	0.063		0.85	34
7	DCM	7.7×10^8	[d]		1.41	34
7	ACN	2.1×10^9	0.001		0.41	34
9	TOL		0.628		0.18	34
9	THF		0.001		[e]	34
9	DCM		[d]		0.85	34
9	ACN		0.001		0.14	34
10	TOL		0.033		0.55	34
10	THF		0.001		[e]	34
10	DCM		[d]		0.25	34
10	ACN		0.001		[e]	34
11	DCM	1×10^9	0.04		0.81	36
12	DCM	1×10^9	0.07		0.65	36

*[a] Ratio relative to Rose Bengal in MeOH (= $\Phi\Delta_R$); [b] $^1O_2$ quantum yields (= Φ_Δ) determined in EtOH; [c] Not given in paper; [d] Not determined; [e] Too low to be determined;[29, 30, 31, 34, 36] The relatively slow rates in DMF of compounds **2** and **3** are remarkable. The fast rate in ACN is from ref. 39.*

Even though no long-lived triplet state was observed in **8**, it has a cathodic shift of oxidation potential as well as an anodic shift of its reduction potential. Therefore, the authors conclude that the carbazole (donor) moiety facilitates charge separation leading to a unique CSS between one of the BODIPYs and this functional group. These results were not seen in the BODIPY dimers **9** and **10**. Using femtosecond TA spectroscopy, the authors found ISC was most efficient in solvents with moderate polarity, especially for the unsubstituted dimer **7**. These studies were also supported by TD-DFT calculations showing that the energy of the CSS was high in non-polar solvents and low in polar solvents. This implied CR was a driving force of ISC in solvents with moderate polarity and thus clarified the mechanism of SOCT-ISC in orthogonal BODIPY dimers. The carbazole containing BODIPY dimer (**8**) exhibits inefficient ISC.

BODIPY dimer **7** has the highest singlet oxygen yield and the nitro-containing BODIPY dimer **10** shows a decrease in the triplet yield in solvents like dichloromethane and THF. In the amino-containing BODIPY dimer **9**, however, there appears to be inefficient ISC in THF.

In 2018 Filatov et. *al* also reported that the solvent dependent fluorescence of BADs and their ISC relied on donor-acceptor couplings.[31] The authors compared the triplet state yields (formed either by RP-ISC or SOCT-ISC from the CT state) of their BADs to the values published in their previous paper.[29] This comparison showed that especially the unsubstituted BAD displayed high populations of the CT state that was independent of the solvent polarity. Studying the steady state absorption and emission properties of these BADs, it was found that the emission of the BADs was greatly affected by solvent polarity. Changing the substitution pattern in the BODIPY or anthracene subunits has a strong effect on the spectroscopic properties of these dyads. For example, BADs containing methyl groups on the 1, 3, 5 and 7 positions of the BODIPY indicated very efficient PeT in these dyads. The PeT efficiency of the BADs mainly depends on the electronic coupling between the donor-acceptor subunits and their redox potentials.

$^1O_2$ sensitization experiments were conducted with a variety of different BADs in both ethanol and hexane. They differed in extended conjugation, phenylene spacers and alkyl substitutions on the anthracene and BODIPY moieties. The emission quantum yields varied depending on solvent polarity and subunit structure. In hexane, there were higher $^1O_2$ quantum yields obtained for 3,5-dimethyl-substituted BADs. The BADs with unsubstituted BODIPY (see figure **2.7**) showed the lowest $^1O_2$ quantum emission yields in ethanol (0.05–0.12) and higher values of 0.43 in hexane. The introduction of a phenylene spacer, thus increasing the

distance between the electron donor and acceptor, reduces the PeT efficiency as the electronic coupling is decreased. The authors claimed that the different $^1O_2$ emission quantum yields can be partly due to the larger energy gap between the local excited singlet state of the BODIPY (S^{BDP}) and the CT singlet state (S^{CT}), which is altered by the introduction of alkyl substituents. The authors found that the PeT is largely dependent on the S^{CT}/S^{BDP} energy gap and that increasing the distance between the donor and acceptor (by a phenylene spacer) minimizes ISC and results in poor triplet yields.

Femtosecond and nanosecond TA spectroscopy was carried out on these dyads and they were split into two different sets. The first set was composed of molecules with the same anthracene unit and chemically varied BODIPY components while the second set kept the BODIPY constant and varied the anthracene. TA spectroscopy proved fast energy transfer (EnT) between Anthracene and BODIPY in orthogonal BADs. In lower polarity solvents, like toluene, the generated singlet states of these BADs decayed to the ground state without forming the CT states, indicating poor PeT. The authors were able to prove that in their orthogonal BAD (9-methylanthrancene and 1,3,5,7-tetramethyl BODIPY), the mechanism of triplet state formation was CT state recombination as opposed to direct ISC. With TA spectroscopy the authors show that in their BADs, triplet generation *via* CR was much less efficient in non-polar solvents even though a small amount of triplet formation occurred.

DFT calculations and X-ray crystallography proved that directly linked BADs had almost orthogonal angles (68–88 ^oC) clearly showing that all BADs studied were orthogonal with respect to the orientation of the BODIPY and anthracene subunits. This orthogonality would increase ISC. The electronic coupling between the local excited singlet state of the BODIPY (S^{BDP}) and the CT singlet state (S^{CT}) is responsible for PeT efficiency. This orthogonal geometry allows efficient electron transfer, providing high yields of CT resulting in efficient ISC and high triplet yields. Increasing the steric bulk onto already orthogonal BADs, by adding ethyl groups onto the 2 and 6 position of the BODIPY, results in a decreased PeT efficiency which decreases CT yields, ISC efficiency and overall triplet yields. Deviations from orthogonality in their BADs also reduced triplet state yields highlighting the importance of orthogonality in their dyads to produce the desired triplet state.

In summary of the study of Filatov et. *al.*,[31] structural factors and media polarity determine the dominant decay pathway. The correct amount of steric bulk, in terms of alkyl substituents, is needed to make PeT feasible for the BADs in polar solvents. Orthogonality reduces the gap between singlet CT state and triplet CT state. The authors also noticed triplet excited state generation in non-polar solvents in hexa-alkylated BADs.

In 2018, Filatov *et al.* reported on other dyads that can be used as heavy atom-free oxygen photosensitizers.[35] In BODIPY-pyrene (BpyrD) and BODIPY-perylene dyads (BperD), BODIPY triplet states were formed following CSS formation.

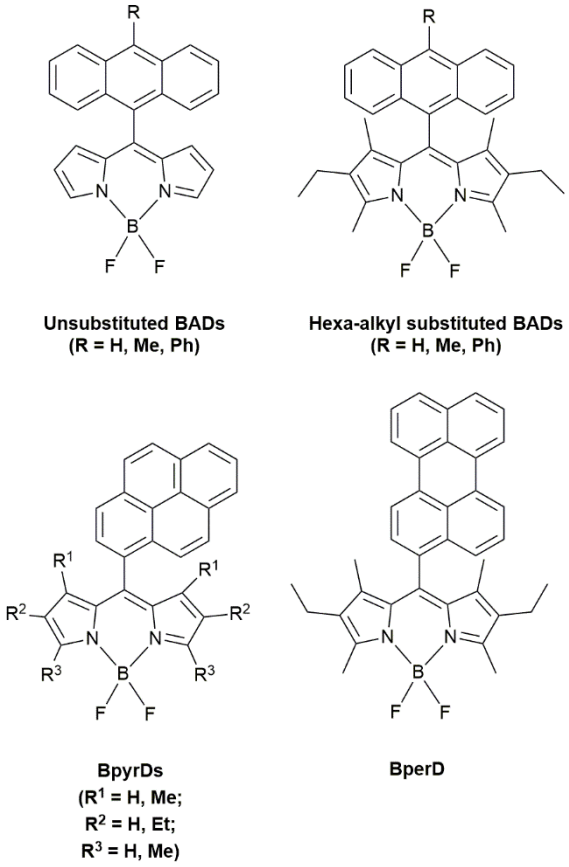

Figure 2.7. *BODIPY dyads studied by Filatov et. al.*[31, 35]

They found that the BpyrD dyads produced higher triplet yields compared to previously reported BADs by the same group.[29, 31] The singlet excited states of pyrene(donor) undergo EnT to the BODIPY(acceptor) core in these dyads, following excitation at 355 nm. This is followed by PeT, generating a CSS equivalent to a radical cation of pyrene ($Pyr^{\cdot+}$) and a radical anion of BODIPY ($BDP^{\cdot-}$). From this point, the CSS state can undergo ISC *via* two mechanisms: the radical pair ISC (RP-ISC) or spin-orbit charge-transfer ISC (SOCT-ISC). With the use of transient absorption (TA) spectroscopy, the authors confirmed triplet formation *via* PeT.

$^1O_2$ sensitization, of the triplet states formed from the CT states in these dyads, was evaluated by studying the trapping of 1,3-diphenylisobenzofuran (DPBF) in a polar and non-polar solvent (ethanol and hexane, respectively). They found the most efficient sensitization

occurred in the unsubstituted BpyrD dyad in ethanol. The authors concluded that in order for PeT to occur, the energy level of the charge-transfer state (S^{CT}) must be energetically close to that of the electron donor-acceptor's excited energy level (D-A*). Using DFT calculations, they explained that the alkyl groups increased the S^{CT} and reduced the electron accepting ability of the BODIPY moiety.

Hou *et al.* [36] synthesized phenothiazine(PTZ)-anthracene(An) dyads (Figure **2.8**) with the aim of achieving orthogonal geometry thus enhancing SOCT-ISC. The bond between the electron donor and acceptor was 'varied to systematically tune the geometry constraint', therefore resulting in different coupling strengths (V_{DA}) and hopefully, increasing triplet yields. V_{DA} values were determined by using the charge-transfer absorption bands as well as the charge-transfer emission properties.

They introduced their paper by stating that it had been recently shown that weakly coupled orthogonal multi-chromophore systems exhibit CR induced ISC.[37] Hou et al. assume that the more coplanar the donor and acceptor units within the dyad are to each other, the stronger the electronic coupling (higher V_{DA}). The emissive properties of their compounds indicated that the emission was governed by the strength of V_{DA} between the electron donor and acceptor parts of the dyad. The emission of the acceptor appears to be controlled by modulating the conformational restriction.

The authors use time-resolved electron paramagnetic resonance spectroscopy (TR-EPR) to confirm that the overall ISC is not due to the intrinsic ISC of anthracene, but SOCT-ISC must also play a role. The Gibbs free energy values indicated that PeT shows a thermodynamically favoured preference for polar solvents compared to non-polar solvents in their dyads. This corresponds to the fluorescent properties.

Using nanosecond TA spectroscopy, they confirmed that anthracene is a good electron acceptor and show that SOCT-ISC is the main mechanism in their PTZ-An dyads. Using femtosecond TA spectroscopy, they analysed the kinetics of charge transfer and triplet-state formation for their compounds (see also Table **2.1**). TR-EPR can be used to discriminate between different ISC mechanisms (RP-ISC, SOCT-ISC or normal spin-orbit coupling ISC (SO-ISC)).[38, 18] Each mechanism yields different ESP (electron spin polarization) patterns. The ESP pattern of anthracene was drastically different from that of the PTZ-An dyads. Therefore, the ISC mechanism was largely affected by the attachment of PTZ(donor) to the anthracene.
They reported a novel finding for SOCT-ISC. Not only does the ESP pattern depend on the molecular conformation (orthogonal vs coplanar), but it is also dependent on the electron donor structure. Using DFT calculations, they verified their approach to be efficient for

conformational restriction and thus SOCT-ISC purposes (see also section 5). By introducing a methyl group on a julodine-An dyad that was previously studied by Dance *et al.*,[37] they determined that the conformation was restricted to 69-102º between the electron donor and acceptor.

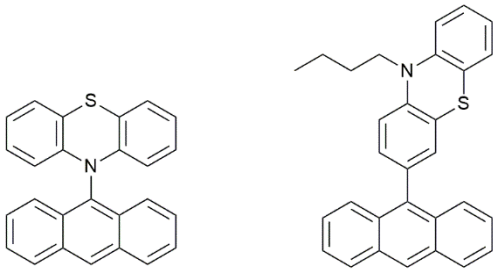

Figure 2.8. *Examples of PTZ-anthracene dyads (**11**) and (**12**).*[36]

The authors use electron density difference maps to show that, for compound **11** (chemical structure in figure **2.8**), singlet (S_1 = ^{1}CT) and triplet (T_2 = ^{3}CT) states are characterized by an intramolecular charge-transfer. According to the El-Sayed rules, the rate of ISC is greater if a radiationless transition involves a change of molecular orbital type. Leading on from this, the increasing spin-orbit coupling between the ^{1}CT and T_1 states can lead to a higher ISC rate. Computational results of this work are discussed further in section 5.

In 2019, Buck *et al.* reported that triplet formation in BODIPY-based dyads is controlled by spin-allowed transitions.[39] SOCT-ISC has to be faster than competing processes in order to form triplets in 'non-triplet-forming compounds' like BODIPY or perylene. The authors show a generic scheme for triplet formation in donor-acceptor dyads (Figure **2.9**) that complies to the work of El-Sayed in 1974,[40] the work of Van Willigen,[24] Wasielewski,[23, 37, 41] and Filatov, Senge[29, 31, 35] and Buck *et al.*[39]

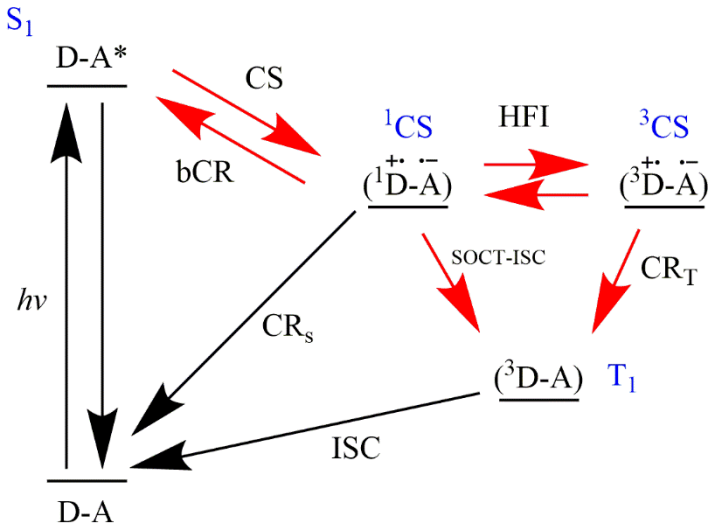

Figure 2.9. *Jablonski-type energy diagram of process involving the photon absorption of a donor-acceptor dyad (D-A) to form a singlet localized on A ($^{S1}A^*$). This singlet can then undergo charge separation to a charge-separated state (^1CS). In certain conditions, a triplet (T_1) can be formed by recombination of the charges.*[39]

According to the authors, the recent studies conducted by Filatov *et al.*,[29, 31, 35] Zhao *et al.*,[30, 34, 36] lack magnetic field effects (MFE) measurements clearly indicating that SOCT-ISC is the main transition to populate triplet excited states. Buck *et al.* proceeded to carry out studies to answer one question: in relation to Figure **2.9**, "how do the processes: CS, CR_S and CR_T; relate to each other in terms of producing triplets?"

The authors used general orthogonal BODIPY-based D-A dyads to systematically tune the oxidation and reduction potentials therefore investigating the Gibbs energy changes associated with the three processes and how they affect triplet quantum yields. Their study revealed that the spin-allowed processes (CS and CR_S) largely control the triplet yield formation, rather than CR_T (or SOCT-ISC). They also provided two general guidelines for improving triplet quantum yields in orthogonal D-A motifs, namely the close distance between donor and acceptor (< 5 Å) and the adjustment of the CS state energy to suppress CR_S pathway. The latter can most likely be done by making the CS energetically close to S_1.

In this section, we see that BODIPY moieties in donor-acceptor dyads that form triplet states *via* charge recombination can act as the electron acceptor or as both donor and acceptor (in the case of BODIPY dimers). BODIPY-based dyads have applications in *in vivo* imaging as well as in the many other photochemical processes. When these dyads are orthogonal they can undergo SOCT-ISC to form triplet states. In sterically strained BODIPY-anthracene Dyads (BADs), the highest triplet yields are observed in non-polar solvents. An optimal dihedral angle

of approximately 62° is repeatedly found between the donor and acceptor moieties of these BADs. The ISC of these PSs can be tuned, not only by the angles between the two electron transfer moieties, but also by manipulation of the solvent polarity. Attaching electron donating and withdrawing groups to BODIPY dimers has reportedly resulted in a decrease in triplet yield. However, it is yet to be investigated whether this statement is true for all BODIPY dimers. The driving force for charge recombination and SOCT-ISC in orthogonal BODIPY dimers is optimal in solvents with moderate polarity. Singlet oxygen quantum yields vary depending on solvent polarity and subunit structure.

In summary, the key is to find the ideal balance between initial charge separation and recombination pathways. It has been shown that promoting SOCT-ISC, by suppressing the spin-allowed transitions using a unique feature of electron-transfer reactions known as the Marcus inverted region, allows triplet formation by charge recombination to occur under favourable conditions but it is not always the preferred route. It is clear that ISC is dependent on solvent polarity and that SOCT-ISC can be the main ISC mechanism in orthogonal dyads. Some of the dyads discussed have shown promising results *in vitro*. Specifically, derivatives of the BODIPY-Anthracene Dyads and BODIPY-pyrene dyads, that were discussed by Filatov *et al.*, have shown to have *in vitro* cytotoxicity against human breast cancer cells.[42] For more information on recent work on BODIPY molecules and their triplet states we refer to some excellent review papers.[43, 44, 45]

From the great variety of compounds presented above we tentatively select two molecules to discuss a unifying theme in section 5: the BAD compound **2** (see figure **2.3**) and the BODIPY dimer **d2** (see figure **2.4**). Both compounds give singlet oxygen / triplet yields above 90 % in the optimal solvent.

2.4. Polymer-Fullerene blends

Within organic photovoltaic research, there are many examples where triplet formation by charge recombination is reported to occur in thin solid films.[7] These films consist of electron donating polymers with the (fullerene) electron acceptor incorporated into it. However, in contrast to the molecular electron donor-acceptor and BODIPY systems discussed before, these observations cannot be correlated to structural information regarding donor-acceptor orientation. The most studied combination with respect to this particular triplet formation pathway is PCPDTBT : $PC_{60}BM$.

In 2013, Friend and co-workers[7] observed formation of the polymer T_1 state due to bimolecular charge recombination (= triplet formation by charge recombination) in a series of polymer-fullerene systems in which the lowest-energy molecular triplet exciton (T_1) of the polymer is lower in energy than the charge-transfer (CT) state. They stated that the formation of triplet excitons can be the main loss mechanism in organic photovoltaic cells. Four fullerene derivatives ($PC_{60}BM$, $PC_{70}BM$, $IC_{60}MA$, $IC_{60}BA$) and two polymers were used (PIDT-PhanQ = (poly(indacenodithiophene-co-phenanthro[9,10-b]quinoxaline) as well as PCPDTBT = (poly([2,6-(4,4-bis-(2-ethylhexyl)-4H-cyclopenta[2,1-b;3,4-b']-dithiophene)-alt-4,7-(2,1,3-benzothiadiazole)]). Charges are formed within the instrument response time (2 ns) in all blends (see figure **2.10** for the molecular structures).

In the polymer-fullerene blends of PIDT-PhanQ : $IC_{60}MA$ and PIDT-PhanQ : $IC_{60}BA$, triplet excitons are formed through bimolecular recombination on nanosecond timescales. They report that the values of β (rate constant for triplet-charge annihilation) vary by a factor of two with laser fluence. Triplet-charge annihilation occurs when a triplet state (in the film) interacts with a charge (in the film) and they annihilate each other. At fluence of 2 $\mu J/cm^2$ for the PIDT-PhanQ : ICBA blend they obtained a value of 0.58 for α (final triplet fraction) and a value of 2.2×10^{-10} cm^3/s for β. This demonstrates that a large fraction of charges underwent bimolecular recombination mediated by ^3CT, to form triplet excitons. A characteristic timescale for their observations is 10 ns. By using PCPDTBT as the second polymer the authors generalized the results.

"According to spin statistics, the encounters of spin-uncorrelated electrons and holes generate charge-transfer states with both singlet (^1CT) and triplet (^3CT) spin character in a 1:3 ratio. Relaxation of ^3CT states to T_1 states (energetically favoured), can be strongly suppressed by wave-function delocalization, allowing for the dissociation of ^3CT states back to free charges and enhancing the device performance. Decreasing charge recombination is possible due to the interplay between electron spin, energetics and delocalization of charges in these organic semiconductors."[7] This work focuses on proton hyperfine interactions being the mechanism for the interconversion of singlet CT into triplet CT states. Spin-orbit coupling is not considered. At their earliest observation time of t = 2 ns, 50 % of the triplet states in PIDT-PhanQ : ICBA are already formed. Interestingly, this could imply that spin-orbit coupling plays a role here.

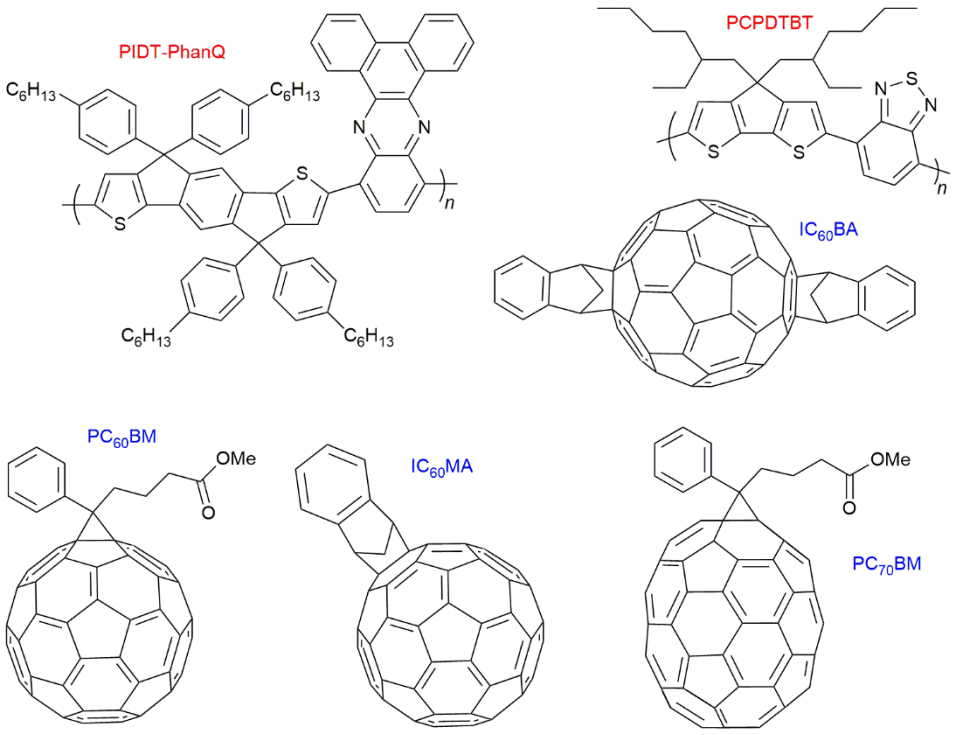

***Figure 2.10**. Molecular structures of the polymers and fullerene acceptors used by Friend and co-workers.* [7]

The same PCPDTBT polymer was studied in 2015 by Laquai et al.[9] who demonstrated that after exciton dissociation and free charge formation, fast sub-nanosecond non-geminate recombination (recombination of charges that were not created together by one photoexcitation) leads to a substantial population of the polymer's triplets state in a PCPDTBT : $PC_{60}BM$ blend. This complements the earlier work of Friend. It seems that in this blend of materials, two rates of triplet formation by charge recombination can occur, a fast sub-ns rate and a slow process on the 10 ns timescale. Laquai et al.[9] also reported that PSBTBT : $PC_{60}BM$ blends (with a silicon atom bridgehead) show a higher charge generation efficiency, but less triplet state formation at similar free charge carrier concentrations. The film morphology of the two blends are similar in terms of crystallinity, phase segregation, and interfacial contacts. But silicon substitution has a significant impact on the morphology of the blend (as well as hole mobility) and solid-state morphology. The interfacial structures of PSBTBT : $PC_{60}BM$ blends reduce non-geminate recombination, leading to superior device performance compared to optimized PCPDTBT : $PC_{60}BM$ blends. It is characterized by a decreased π-π stacking distance in conjunction with an increased lamellar stacking distance. For the PSBTBT : $PC_{60}BM$ blend, there is a significant change in the solid-state morphology that is not only related to the 2-ethylhexyl side chain organization, but also to an increase in molecular order and

packing/aggregation of the PSBTBT polymer chains. Solid-state NMR studies also indicate a possible folding of the butyric methyl ester functionalities of the fullerene of PCBM to the PCPDTBT.

In 2014, Friend and co-workers revealed that upon addition of ODT (octane-dithiol), triplet generation in PCPDTBT : $PC_{70}BM$ was strongly promoted due to an increased generation of free charges.[46] Recent measurements[47, 48] on PCPDTBT : $PC_{60}BM$ blends revealed a lifetime of these CT states of a few hundred picoseconds, which according to the authors is too short to create a substantial yield of triplets by intersystem crossing (but as we discussed earlier, such observations have been made for molecular systems in solution, see section 2). The population of polymer triplet states occurs if the triplet state is lower in energy than the interfacial triplet CT state. This causes a downhill energy transfer process, which competes with re-dissociation of the CT state. This process adds another loss channel to the efficiency-limiting processes in organic solar cells, and hence likely decreases its efficiency.

Durrant and co-workers observed the generation of polymer triplet excitons in SiIDT–2FBT : $PC_{70}BM$ (but not for SiIDT–DTBT : $PC_{70}BM$), (Figure **2.11**). This occurs on a timescale of 1 ns (independent of laser-fluence, but charge generation is influenced by applied electrical bias). Population of singlet CT states is assumed to be followed by intersystem crossing (by HFI) to degenerate triplet CT states. There is no comment on the short time scale of this process. Charge recombination from ^3CT then populates the lowest lying polymer triplet state (T_1), thus limiting free charge generation in this system. Instead of CT state, the authors used the terminology of bound polaron pair (BPP). In contrast to the work of Friend and co-workers, the authors have inferred geminate charge recombination, implying that the charges that recombined into triplets have not escaped each other's coulomb field. The dynamics of free charge separation competing with recombination to polymer triplet states is studied in two closely related polymer-fullerene blends with differing polymer fluorination, differing linking thiophene groups and different photovoltaic performance by Durrant and co-workers. No quantification of the theoretical timescales relating to HFI or SOCT-ISC were reported.

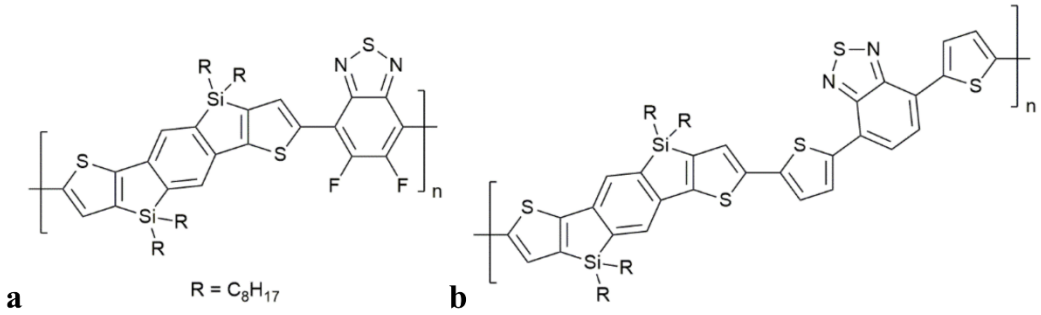

Figure 2.11. *Structures of polymers in which triplet formation by charge recombination has been observed, in combination with fullerene adducts: SiIDT–2FBT (**a**), SiIDT–DTBT (**b**), studied by Durrant et al.*[8]

"For the SiIDT–2FBT:$PC_{70}BM$ blend, electron transfer across the interface creates coulomb-bound BPP states with a spin singlet character, in which the hole resides on the polymer chain, while the electron resides on the fullerene molecule. Motion of the polarons within their coulomb attraction field is likely to reduce their charge-exchange integral thus creating energetically degenerate triplet and singlet bound states that can efficiently interconvert, enabled by hyperfine interactions.[49] Once generated, the triplet BPP states serve as precursors for subsequent efficient back electron transfer to the lower lying polymer triplet excitons."[8]

Other studies on charge recombination in low band gap polymer : fullerene donor-acceptor blends also show sub-ns triplet state formation from charges for both PDBTTT : $PC_{60}BM$[50,] and diketopyrrolopyrrole (DPP) type polymer blends with fullerene adducts. [51, 52] The formation of triplet states in thin film blends of low band gap polymers and fullerene adducts has been the focus of many studies. The great variety of polymer molecular structures, the different types of morphologies and crystalline regions, different energetics as well as the large influence of laser power applied in optical studies makes triplet formation by charge recombination difficult to pinpoint within this field. Furthermore, interface layers and a potential difference (of 0.5 to 1 V) in real operating devices will induce band bending and change energetics. However, recombination to triplets can proceed faster than charge extraction and can be observed in working devices even under short-circuit conditions. The studies reported here are performed on spin-coated films on quartz.

Considering the previous sections on molecular donor-acceptor systems and BODIPY's, there are hints to the following suggestion: the orientation of the π systems of

electron donor and acceptor units in the solid state will influence the charge recombination process to the same extent as in well-defined molecular systems in solution. This implies that the specific orientation of the π systems of the polymer, relative to the π system of the fullerene adduct will be an important factor to control (Figure **2.12**).

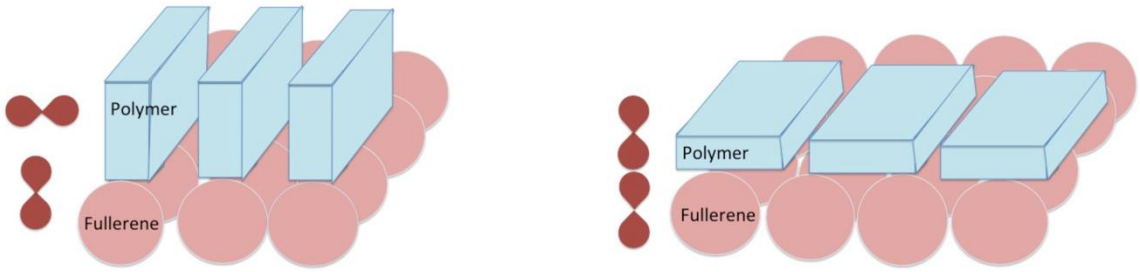

Figure 2.12. *Representation of the different orientations of polymer donor and fullerene acceptor units in a thin solid film, in which the aromatic core of the polymer units is considered as a relatively flat building block for simplicity. Schematic orientation of the π-orbitals is indicated (brown p orbitals). In the left structure triplet formation by charge recombination will be enhanced due to orthogonal π-orbitals.*

The suggestion that we postulate and model in figure **2.12** indicates that for the thin films containing two dyes (perylene red and pyrene), two different conformations/complexes (similar to those in figure **2.12**) must be present too. These two conformations are in agreement with the two reported rates of $\sim 1.04 \times 10^{10}$ and 7.21×10^{7} s^{-1} for triplet state formation by charge recombination in a mixture of pyrene and perylene red (N,N′-bis(2,6-di-isopropylphenyl)-1,6,7,12-tetraphenoxy-perylene- 3,4:9,10-tetracarboxylic acid bis-imide).[53]

2.5. Mechanistic Aspects

In the previous sections we have reported various examples of molecules and materials in which triplet formation by charge recombination has been observed, and important factors such as the orientation of donor and acceptor, the nodal planes of orbitals involved, hyperfine interactions and spin-orbit coupling have been indicated. Here we describe some of these mechanisms in more detail and correlate them to representative rates.

Proton Hyperfine Interactions

Next to spin-lattice relaxation (T_1) and spin-spin (longitudinal) relaxation (T_2), spin de-phasing can also occur due to hyperfine coupling (coupling between nuclear spin and electron spin) and cause intersystem crossing. This process can be approximated by using T_2^*, the transverse relaxation time ($T_1 > T_2 > T_2^*$) also known as the spin de-coherence or the spin de-phasing (interconversion) timescale, which is given by:

$$T_2^* \approx \frac{\hbar}{g\mu_B a_H}$$

It depends on the g-value (mainly ranging between 1.80 up to 2.20), μ_B, the electronic Bohr magneton (5.78838×10^{-5} (eV T^{-1})), the hyperfine coupling constant (a_H) as well as Planck's constant (6.58212×10^{-16} (eV s)). The magnitude of the hyperfine constant (in Tesla) has a large influence on the spin de-phasing time. If we simplify this and assume g = 2 we get $T_2^* = (5.686 \times 10^{-9} / a_H)$, with the a_H values expressed here in mT. Through the hyperfine interaction, the spin of the nuclei can interact with the electron spin causing it to change and thereby spin-flip. Hyperfine interactions are named after the hyperfine splitting of the peaks observed in EPR (or ESR) spectra.

For the molecular donor-acceptor system of Mataga and co-workers,[19] we can take values for the radical anion of pyrene and the radical cation of dimethylaniline. The three hyperfine coupling constants for the unsubstituted pyrene radical anion have been reported[54] to be 0.489, 0.226 and 0.10 mT with the *g*-value[55] being 2.002724. We can then estimate the value of T_2^* to be between 1.16×10^{-8} s and 5.68×10^{-8} s. The fastest rate would be $^{CR}k_T = 8.61 \times 10^7$ s^{-1}, which is remarkably close to that measured[53] in thin films containing pyrene $^{CR}k_T = 7.21 \times 10^7$ s^{-1}. However, clearly the rate in the orthogonal molecular system studied by Mataga *et al.* in solution is much higher,[19] and cannot be explained with the T_2^*.
For N,N-dimethylaniline, the hyperfine coupling constants for the ortho and meta hydrogen atoms[56] are between 0.6 and 0.079 mT from which we can estimate T_2^* between 7.18×10^{-8} s and 9.48×10^{-9} s (fastest rate of $^{CR}k_T = 1.05 \times 10^8$ s^{-1}) in reasonable agreement with those obtained for pyrene.

In order to estimate the timescale of intersystem crossing, we need to look into EPR data of polymer-fullerene blends. In purely organic photovoltaic materials, the main nuclear spin that is present is related to the protons (H-HFI). The presence of other atoms in the polymer (besides hydrogen, carbon and nitrogen) that have a high relative abundance of isotopes with nuclear spin like fluorine, sulphur or phosphorus can be of importance.

There are various reports[57], [58] of *g*-values for polymer-fullerene blends and they all are very close to 2, ranging from ~1.998 to 2.005. For P3HT/PC_{61}BM and P3HT/PC_{71}BM composites effective, isotropic g-factors of the methanofullerene anion radicals were 1.99983 and 2.00360, respectively.

The hyperfine constants, however, are not so easily obtained, but also indicate a slow process (~5 to 22 ns timescale relating to a_H values of 32.2 and 7.3 MHz [~(32.2/28) = 1.15 and ~0.26 mT] reported for thin films with fluorine containing oligomers [e.g. dithienosilole-fluorobenzothiadiazole] and PBCM).[59] The hyperfine coupling constant is directly related to the distance between peaks in a spectrum and its magnitude indicates the extent of delocalization of the unpaired electron over the molecule. However, we can also use the Δg values.

A second approach to estimate the rate of triplet formation by charge recombination is related to magnetic field effects. [60, 61] Using the magnitude of the magnetic field (*B*) of the Earth, together with the g-values of the radical cationic and radical anionic species, it is possible to estimate a timescale for the process.

$$\Delta\nu = \frac{\Delta g \mu_B B}{\hbar} = \frac{\Delta g B}{0.71446}$$

with ν in GHz and *B* in kG. The Earth's magnetic field is ~50 μT (0.5 G). Δg for typical radical pairs can be up to 0.004, leading to a rate of ~2.8 x 10^{-6} GHz. At low magnetic fields, the rate for magnetic field induced triplet CT state formation is very low (2.8×10^3 s^{-1}).

Based on the information on H-HFI, we have to conclude that rates of triplet formation by charge recombination (10^9 s^{-1} up to 10^{10} s^{-1}), that are one or two orders of magnitude higher than the rates related to HFI (10^8 s^{-1}), have to be related to other physical effects and can be not be explained by spin dephasing.

By looking into the quantum chemical background of the H-HFI interactions more insight can be gained into this mechanism. The Hamiltonian given[62] by Frankevich *et al*. describes the hyperfine interactions:

$$\hat{H}_{HFI} = 2g\hat{S}H + \hbar a_1 I\hat{S}_1 + \hbar a_2 I\hat{S}_2 - \hbar J(r)\left[\frac{1}{2} - 2\hat{S}_1\hat{S}_2\right]$$

The first term represents the Zeeman interaction which depends on the g factor, with $\hat{S}$ the total spin vector, *H* the magnetic field. The second and third terms represent the interaction between the electron ($\hat{S}_{1,2}$) and nuclear (*I*) spins while the fourth term represents the exchange interaction *J(r)* or the quantum mechanical correction to the classical electron-electron repulsion. *J(r)* is based on the Pauli exclusion principle, which says that no two electrons can have the same four quantum numbers (In other words if two electrons occupy the same orbital, they must have antiparallel spins). This leads to a quantum mechanical correction to the classical electron-electron repulsion. This will usually increase the energy for paired spins or singlets and decrease the energy of unpaired spin states or triplet states because the electrons cannot occupy the same orbital.

These H-HFI effects in a system can be visualized by looking at the interactions between the hydrogen atoms nuclear spin (*I)* and the spin of the electron (S_1) (Figure **2.13**). The relatively slow process can be viewed as small separate pushes of the nuclear spin momenta resulting in a relatively slow dephasing of the electron spin of the radical cation or radical anion. A vector description of these spin-spin interactions is given in figure **2.13**.

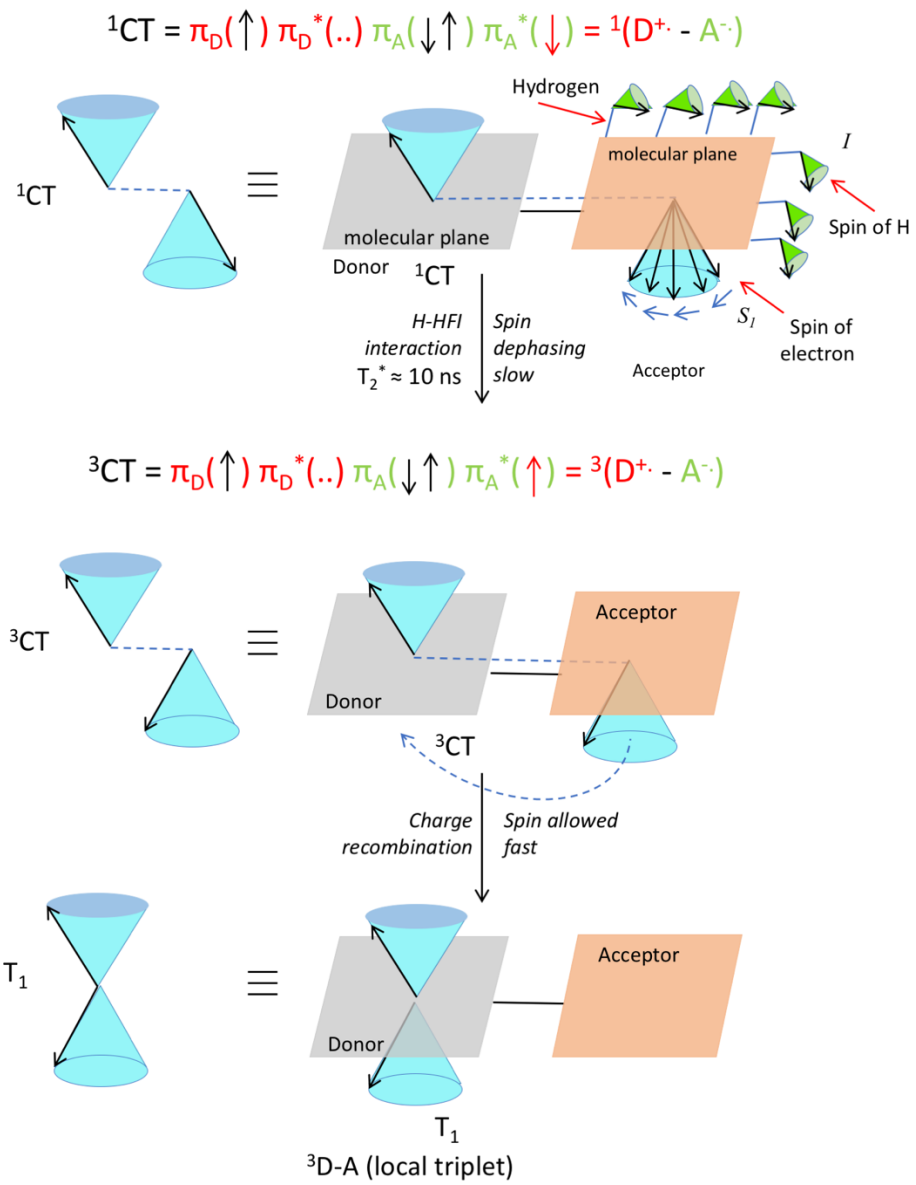

Figure 2.13*.Visualization of proton hyperfine interactions (H-HFI) within a co-planar electron donor-acceptor compound. Within the singlet charge-transfer excited state (top), the interaction between the electron spin (S_1) and the nuclear spin of the H atoms (I), leads to slow spin dephasing (T_2^*). This interconverts the singlet charge-transfer excited state into the triplet charge-transfer excited state (middle). When this is formed, fast spin allowed charge recombination to a local triplet state can occur (bottom). The T_0 level is populated specifically (and not the T_+ or T_-, see also figure* ***2.15****). The red arrow in the three electron configurations depicts the dephasing and transferring electron. A magnetic field is present in the z direction, for the purpose of simple spin representation*

Spin-Orbit Coupling

Due to the conservation of momentum, a change in (electron) spin magnetic momentum has to be compensated by a change in orbital magnetic momentum. The change of molecular orbitals related to a transition is coupled to the change in electron spin. “In molecules such as acetone and, for example, aromatic ketones, that are known for their high triplet yields, the n−π* transition of the carbonyl group can be viewed as the transfer of charge from the lone pair of the oxygen atom to the π* orbital mainly located on the carbon atom.[63] This exemplifies the importance of charge transfer in triplet state formation. The orbital magnetic momentum is changed when the interacting orbitals are located in different areas of the space on the molecule, compensating the change of spin magnetic momentum of the electron (spin−orbit coupling).” In fullerene C_{60}, the orbitals related to the (very efficient) transition to the triplet state change from “pole” based to “equator” based.[64] Thereby, the change in orbital magnetic momentum can be anticipated.

Orthogonal donor and acceptor units can easily fulfil the change in orbital magnetic momentum, upon back electron transfer interaction. As discussed earlier, this mechanism has been implied by Mataga and co-workers[19] in 1981. It was also inferred in 1996 on the basis of TR-EPR of acridinium systems by van Willigen et al.[24]

By looking into the quantum chemical background of spin-orbit coupling interactions, we can gain more insight into this mechanism. Spin-orbit coupling is the result of the spin-operator expressed by its Hamiltonian.

We can use the approach given[65] by Beljonne and Bredas:
“The spin-orbital Hamiltonian is the interaction between the spin and orbital motions of an electron (spin-orbit coupling) and induces a mixing between singlet and triplet excitations.

$$\hat{H}^{SO} = \alpha_{fs}^{2} \sum_{\mu}^{N} \sum_{i}^{n} \frac{Z_{\mu}}{r_{i\mu}^{3}} \overrightarrow{L_i} \overrightarrow{S_i}$$

in which α_{fS} is the fine structure constant, Z_{μ} is the effective nuclear charge for nucleus μ, L

and *S* are the orbital and spin momenta, respectively, r = distance between the nucleus and the electrons.

This Hamiltonian represents the coupling between the spin and orbital momenta of the nucleus (μ) and the electron (i).

$$\hat{H}^{SO} = {\alpha_{fs}}^2 \sum_{\mu}^{N} \sum_{i}^{n} \frac{Z_\mu}{{r_{i\mu}}^3} \overrightarrow{L_i} \overrightarrow{S_i}$$

The Golden-rule expression for radiation-less transitions can be used to compute the intersystem crossing rates, k^{IF}_{ISC}, between an initial singlet state I and a final triplet state F:

$$k_{ISC}^{IF} = (2\pi/\hbar) <{}^1\Psi_1^0 | H_{SO} | {}^3\Psi_F^0>^2 \text{ [FCWD]}$$

where the Franck-Condon weighted density of states, FCWD, is the density of vibrational states in the triplet times the Franck-Condon vibrational overlap.

The FCWD term (in high-temperature limit) is given by:

$$\text{[FCWD]} = \frac{1}{\sqrt{(4\pi\lambda RT)}} e^{\left(\frac{-(\Delta E+\lambda)^2}{4\lambda RT}\right)}$$

Here, ΔE is the energy difference between the initial and final states, (here the singlet-triplet energy splitting), and λ denotes the Marcus reorganization energy."

So basically, the expressions are very similar to the regular equations for electron transfer, but the main difference is the Hamiltonian. In regular electron transfer processes, this is related to the electronic coupling between the electronic orbitals of two states. Now it relates to the coupling of the spin magnetic momenta and the orbital magnetic momenta of the two states. It is not the electronic coupling (normally called *V, or* H_{DA}) but the spin-orbit coupling between the initial and final states.

The wavefunctions on which the spin-orbit Hamiltonian operates can be specified in more detail: the orbitals of the radical anion and the orbitals of the radical cation (the charge-transfer state) and the orbitals belonging to the final triplet state should be the ones to consider.

This gives us the so called "spin-orbit coupling matrix element"(= SOCME). Orthogonality of

the nodal planes of the interacting orbitals may be an important factor.

$$<{}^1\Psi_1^0 | H_{SO} | {}^3\Psi_F^0> = <{}^1D^{+\cdot}\text{-}A^{-\cdot}{}_1^0 | H_{SO} | {}^3\text{D-A}_F^0>$$

The selection rules for triplet state formation are known from the work of Mostafa El-Sayed (El-Sayed rules).[40, 66] These rules have been visually correlated to orbitals and electron spin by Turro.[67] Turro demonstrated *via* the use of orbitals in the carbonyl group of acetone how intersystem crossing is the movement of an electron from a P_y orbital to a P_x orbital (Figure **2.14**). First, such an example is presented here using a rotating vector description of electron spin, which is then correlated to the spin-vector description and to molecular orbital changes occurring in orthogonal electron donor-acceptor systems (Figure **2.15**).

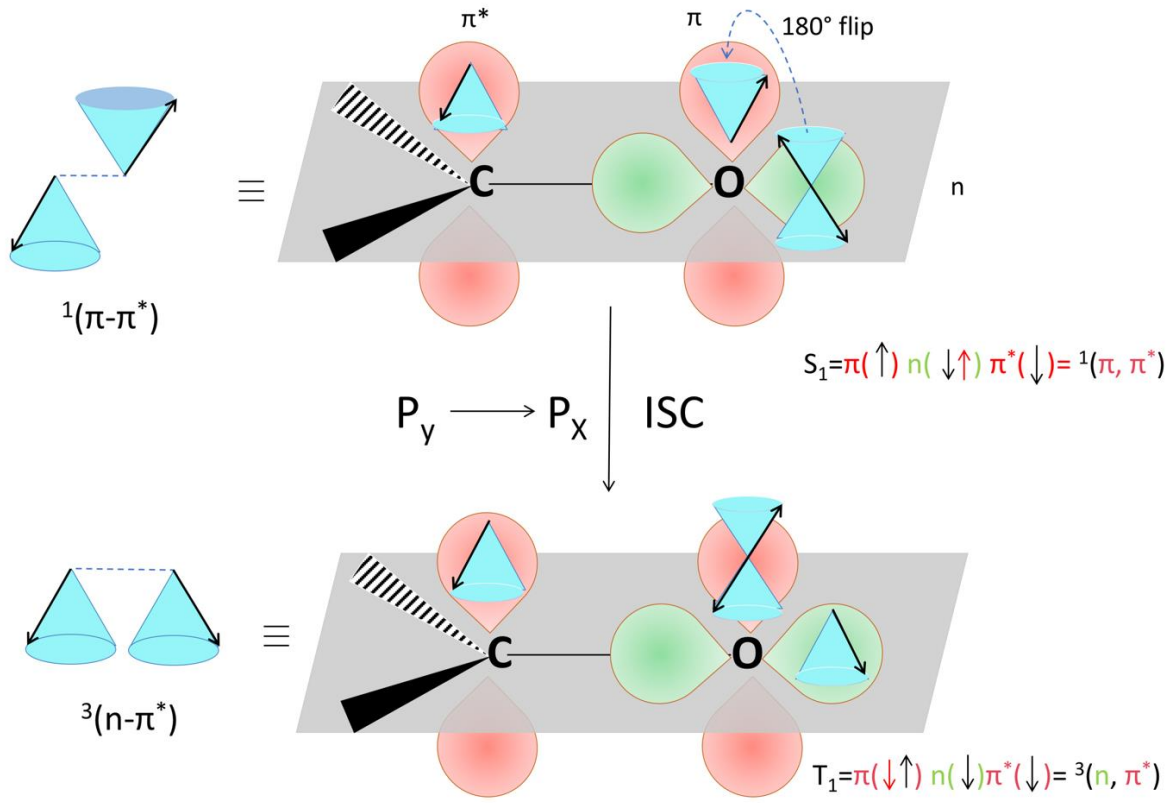

Figure 2.14. *Visualization of the selection rules for spin-orbit coupling for a carbonyl compound. For a* $^1(\pi\text{-}\pi^*)$ *singlet excited state (top), the transition between the orthogonal doubly occupied n orbital (green) and* π *orbital (red, single occupation) provides the spin-orbit coupling to enable the electron spin flip and produce the* $^3(n\text{-}\pi^*)$ *triplet excited state (bottom). We use the rotating frame vector representation and the selection rules for triplet state formation of a* $^1(\pi\text{-}\pi^*)$ *singlet into a* $^3(n\text{-}\pi^*)$ *triplet (adapted from reference* [67]*). It is a qualitative orbital description of the basis for allowed intersystem crossing. The red arrow in the two electron configurations depicts the flipping electron. A magnetic field is present in the z direction, for the purpose of simple spin representation*

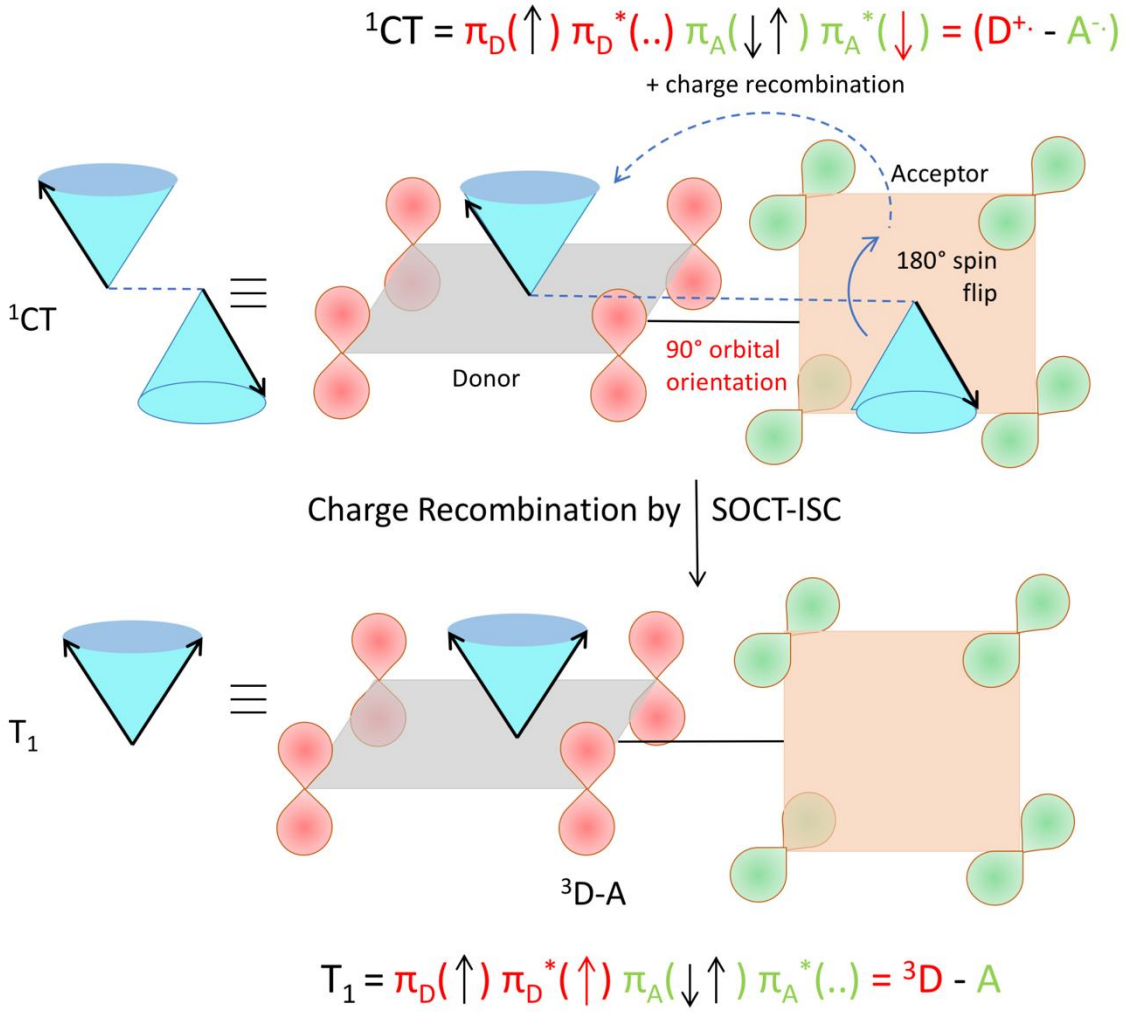

Figure 2.15. *Visualization of spin-orbit charge transfer inter system crossing (SOCT-ISC) within an orthogonal electron donor-acceptor compound. Within the singlet charge-transfer excited state (top), the transition between the singly occupied orthogonal acceptor π^*-orbital (green) and donor π-orbital (red, single occupation + empty π^*) provides the spin-orbit coupling to enable the simultaneous spin flip and produce the local triplet state excited state $^3(\pi\text{-}\pi^*)$ on the donor (bottom). Upon charge transfer accompanied by an electron spin flip, the orbital magnetic momentum change (of the orthogonal orbitals involved in the transition) compensates for change of electron spin magnetic momentum. The orthogonal orbital (nodal plane) relation in the transition is important. The T_+ (or T_-) level is populated specifically (and not the T_0 level, see also figure **2.13**). The red arrow in the two electron configurations depicts the flipping and transferring electron. A magnetic field is present in the z direction, for the purpose of simple spin representation.*

Considering that HFI and SOCT-ISC mechanisms can operate in one particular system at the same time, it is important to stress that HFI is a 'localized' interaction occurring between electron spin and nearby nuclear spins. As such, the timescale of this process will not depend on the distance (nor orientation) between the donor and acceptor unit. However, in the SOCT-ISC mechanism a coupling term is present, that will show a strong distance (and orientation) dependence.[68]

Further inspection of figure **2.15** shows two more aspects: without dephasing, the triplet level that is formed specifically by SOCT-ISC is the so-called T_+ (or the T_-) level. In the T_0 level the two electron-spins point in opposite directions and should have the same phase (see e.g. figure **2.13**, a result of spin dephasing; see also Ref. 16 page 147). Furthermore, the spin-orbit Hamiltonian will operate between the charge-transfer state (consisting of the 'electronically coupled' radical cation and radical anion) and a local triplet state that can be localized on the donor or the acceptor.

$$<{}^1\Psi_I{}^0 | H_{SO} | {}^3\Psi_F{}^0> = <{}^1D^{+\cdot}\text{-}A^{-\cdot}{}_I{}^0 | H_{SO} | {}^3\text{D-A}_F{}^0>$$

or

$$<{}^1\Psi_I{}^0 | H_{SO} | {}^3\Psi_F{}^0> = <{}^1D^{+\cdot}\text{-}A^{-\cdot}{}_I{}^0 | H_{SO} | \text{D-}{}^3\text{A}_F{}^0>$$

If the triplet is formed on the donor, the orbital symmetry of the radical anion of the acceptor will play a more important role (next to that of the donor triplet) for the magnitude of the spin-orbit coupling interaction matrix element. If the triplet is formed on the acceptor, the orbital symmetry of the radical cation of the donor (next to that of the acceptor triplet) will play a more dominant role in the transition.

As discussed in section 2, Weber and co-workers have been able to apply computational chemistry to determine important aspects for the triplet formation by charge recombination for compound **11** and **12**.[36] By using experimental data from charge-transfer absorption and charge-transfer emission properties they determined a rather large V_{DA} value of 0.16 eV (= 1290 cm^{-1}) for **12** (related to the charge separation). By using DFT methods (TD-DFT and the Dalton code) they were able to calculate the magnitude of the spin-orbit coupling interaction matrix element (SOCME) to be 2.37 cm^{-1} for compound **12**, and 0.37 cm^{-1} for compound **11**. These small interaction energies are enough to mediate charge recombination to the triplet (by

SOCT-ISC) on a ~1 ns timescale. So clearly is it possible nowadays to calculate the magnitude of the coupling that mediates TCR. This is also possible with ADF (see section **2.6**).

Although it is most certainly an oversimplification, we can apply a frontier molecular orbital description (FMO) as a starting point to identify the orbitals that mainly play a role in the triplet formation by charge recombination process. Such an approach results in the simplified orbital representation in figure **2.16**. By using such an FMO scheme,[69, 70, 71] we can identify that the TCR process will be an interaction between the HOMO of the acceptor and the HOMO of the donor. We refer here to the orbitals of the neutral system. In fact, the SOMO of the radical cation of the donor and the HOMO (below the SOMO) of the radical anion are the active orbitals, but for simplicity we consider the orbitals of the neutrals. We assume that the symmetry properties of these orbitals are similar.

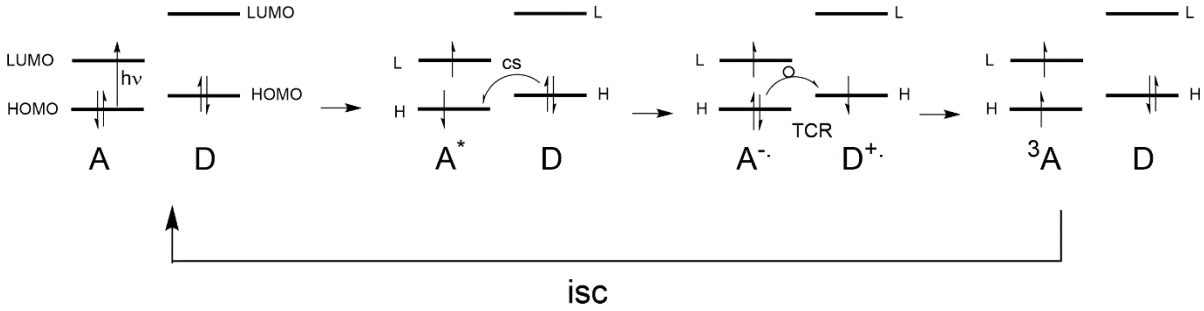

***Figure 2.16**. Frontier molecular orbital description of triplet formation by charge recombination in a donor (D) acceptor (A) system. Upon excitation of the acceptor (A^*), charge separation (CS) can occur to give the radical anion ($A^{-\cdot}$) and the radical cation ($D^{+\cdot}$). Now TCR (triplet formation by charge recombination) can occur via a charge transfer accompanied by a spin flip, leading to the triplet state of the acceptor (^3A). In an energy scheme, the triplet state is lower than the charge-transfer state (note the difference between "energy of state" and "energy of orbital"). The triplet state decays through intersystem crossing (ISC) back to the ground state. HOMO and LUMO levels are represented for the neutral starting systems.*

For the system studied by Mataga as well as for the BAD system **3** and the BODIPY dimer **d2** the HOMO of the donor together with the HOMO of the acceptor clearly show a special feature. Double orthogonality of the nodal planes is observed. Not only are the nodal planes related to the two molecular planes of donor and acceptor orthogonal, also the 'secondary' nodal planes of the orbitals are orthogonal! This was already stipulated by Mataga in 1981, but here we visualize these requirements for triplet formation by charge recombination (see Figure **2.17**). Note that for compound **4** (see Figure **2.3**) these requirements do not hold,

and that this compound does not show substantial TCR (as well as for compounds BB5 and BB6 in reference 34).

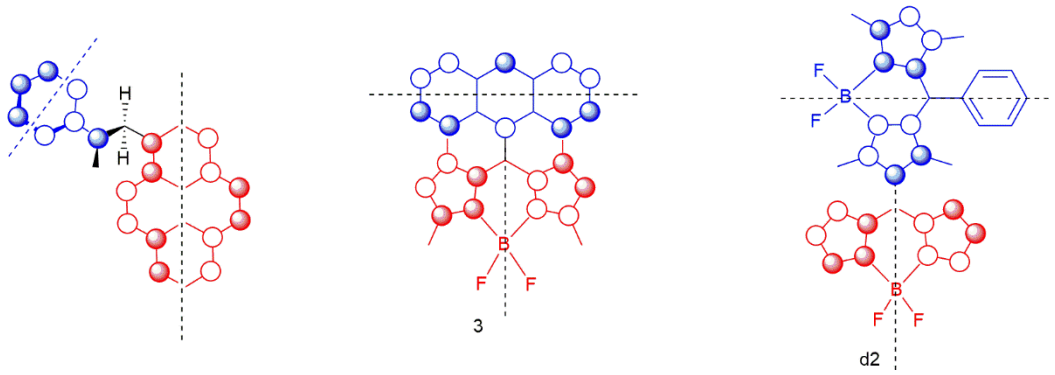

Figure 2.17*. Orbital representation of the HOMO of the electron-donor (in blue) and the HOMO of the electron-acceptor (in red). The black dotted lines represent the secondary orthogonal nodal plane. The first orthogonal nodal planes of the orbitals are the molecular planes of the donor unit and acceptor unit (with a ~90˚ angle between the π systems). Double orthogonality of the nodal planes is present. See figure* ***2.1*** *for a 3D model of the first molecule.* ***Note*** *that in* ***d2*** *there is a ~90˚ twist angle between the red part and the blue part. In the first molecule molecule both angles (between the molecular planes and the secondary nodal planes) are approaching 60˚. For* ***3*** *the angle is estimated to be between 78 and 85˚ (see ref. 31).*

A similar approach can be applied to systems in which the triplet is formed on the donor (like in the polymer fullerene blends discussed in section 4). Here however, the character of the LUMO of the donor and the LUMO of the acceptor will be the most significant (again referring to the orbitals of the neutral systems). This does imply that the energetics has to be such that TCR is possible, leading to triplet formation on the donor.

Hereby we have identified a unifying theme, that connects the early donor acceptor systems (in section 2) with the recent BODIPY work (in section 3): double orthogonality of the nodal planes. The key is not the ground state dipole moment, nor the transition dipole moment of the two separate transitions (CT and triplet), but the specific orbital symmetry properties. This fits the concept that the spin-orbit Hamiltonian operates between the initial and final state and has a maximum output when orbitals are orthogonal.

2.6. Conclusions and Outlook

Triplet formation by charge recombination has been observed in numerous molecular electron donor-acceptor systems.[72] However, examples of systems in which this process occurs well below a 10 ns timescale, are scarce. The recent intensive research on BODIPY systems has renewed the interest in triplet formation by charge recombination, as well the work on organic photovoltaic materials. The main viable mechanistic factors that play a role in the formation of triplet states in which the precursor state is not a locally excited singlet state, but a charged state, are proton hyperfine interactions (H-HFI) as well as spin-orbit coupling (SOCT-ISC). These two interactions can be quantified (see section 5). When we look at the various other possible mechanisms we see that they occur on a much longer timescale.

Triplet formation can occur by geminate (in molecular systems) or by non-geminate processes (in thin films). In long lived (geminate or non-geminate) charge-transfer states, HFI is inevitable and will lead to formation of triplet CT states through the localized interactions of nuclear spins and electron spin on a ~ 10 ns timescale. Electron donor acceptor systems that do not contain nuclear spins are so far unknown (to us). The triplet CT state can recombine fast to a local triplet state without spin-forbiddenness (*via* spin-allowed transitions), if the energetics allows this. However, in short lived singlet CT states, fast competitive spin-orbit coupling can lead to direct local triplet state formation on a ~ 40 ps timescale. The selection rules for triplet state formation become important and imply short distance and orthogonal orbitals, with double orthogonality of the nodal planes. As the origins of these interactions (HFI and SOCT-ISC) have a quantum-chemical basis these effects will ultimately be related to the nature of the Hamiltonian that couples the two states: a trivial assessment with complex consequences. With modern computational methods however, it is possible to calculate the so-called transfer integrals (or SOCME) between CT states and local triplet excited states, (also as a function of a rotating bond between donor and acceptor) for the SOCT-ISC mechanism. From several experimental studies, 60˚ angles between the nodal planes of the orbitals seems optimal. FMO analysis suggests that double orthogonality of the nodal planes is an important factor.

The physical and quantum chemical effects that play a role in the formation of local (excited) triplet states from charged states can be visualized by using a spin-vector description together with a molecular orbital representation. Thereby we can understand and describe these factors in a better way, expanding on the visualizations provided us by Turro.

We can exploit triplet formation by charge recombination by using it as an ‘alternative’ method to generate triplet states. This paper begs the question: What can the produced triplets be used

for? While there will likely be many applications in the photosciences, we have seen their application in PDT already. Can all dyads that undergo triplet charge recombination be used for Photodynamic Therapy? *In Vitro* tests can be carried out to determine the best candidates. After this, evaluation of their photosensitizer properties will have to be assessed. BODIPY's can also be attached to known photosensitizers to see what their capability as a singlet oxygen photosensitizer is. There is also an ideal situation that many types of dyads can use this triplet formation method that results in the next big photosensitizer that cannot only be used in photodynamic therapy but in many other photo-associated applications as well.

Applying the principles of triplet formation by charge recombination to photodynamic therapy not only implies optimizing the orientation of the donor and acceptor (and the nodal planes of their orbitals), but also the charge generation has to be optimal and the energy difference between the CT state and the triplet state has to be fine-tuned.

If we want to understand, control or predict charge recombination, we need to quantify the ^{1}CT $\rightarrow$ ^{3}CT interconversion characterized by T_2^* (and HFI) as well as the ^{1}CT $\rightarrow$ T_1 conversion characterized by the SOCME, the transfer integral for the SOCT-ISC mechanism. Both quantities can be determined experimentally[73] or with computational chemistry.[36, 59, 74, 75.]

List of Abbreviatons

T_+/ T_0/ T_-	Triplet excited state energy levels
τ	Lifetime (in seconds)
$\tau_{CR}(T)$	Time of formation of the triplet state corresponding to the decay time of the charge-transfer state
T	Triplet excited state
${}^{CR}k_T$	Rate of Triplet formation by charge recombination
DFT	Density Functional Theory
${}^3L_a$	triplet state with L_a symmetry using Platt's notation of the symmetry of the excited state of a molecule
π	pi orbital
π^*	pi* orbital
n	Lone pair molecular orbital
C_{60}	Fullerene
ns	Nanosecond
BAD	BODIPY-Anthracene dyad
CSS	Charge Separated State
CR	Charge Recombination
CS	Charge Separation
CT	Charge Transfer
${}^1O_2$	Singlet Oxygen
3D	Three Dimensional
EnT	Energy Transfer
ISC	Intersystem crossing
TD-DFT	Time-Dependent Density Functional Theory
τ_{CS}	Electron transfer time in a donor-acceptor dyad from the donor to the acceptor to form a Charge Separated State
τ_{CR}	Charge recombination time
DMJ	3,5-dimethyl-4-julolidine
NI	Naphthalene-1,8:4,5-bis(dicarboximide)
An	Anthracene
DMJ-An-NI	3,5-dimethyl-4-julolidine Naphthalene-1,8:4,5-bis(dicarboximide) triad with an Anthracene linker

$DMJ^{(+\cdot)}$-An-$NI^{(-\cdot)}$	Charge Separated State of DMJ-An-NI
ps	Picoseconds (10^{-12} seconds)
s^{-1}	Unit of rates of physical and chemical processes (per second)
SOCT-ISC	Spin-Orbit Charge-Transfer intersystem crossing
SOCME	Spin-orbit coupling matrix element
RP-ISC	Radical Pair intersystem crossing
EPR	Electron Paramagnetic Resonance spectroscopy
^{1}CSH	Charged-Shifted singlet state
^{3}LE	Localized-Excited triplet state
k_T	Rates of Triplet formation
SOMO	Singly occupied molecular orbital
HFI	Hyperfine Interactions
PS	Photosensitizer
PeT	Photoinduced electron transfer
TOL	Toluene
THF	Tetrahydrofuran
DCM	Dichloromethane
ACN	Acetonitrile
TA	Transient Absorption
BODIPY	Boron-dipyrromethene

2.7. References

[1] W. Rutsch, K. Dietliker, D. Leppard, M. Köhler, L. Misev, U. Kolczak and G. Rist, Recent development in photoinitiators, *Prog. Org. Coat.*, 1996, **27**, 227–239. DOI: 10.1021/jp001348j

[2] L. B. Rocha, F. Schaberle, J. M. Dąbrowski, S. Simões and L. G. Arnaut, Intravenous Single-Dose Toxicity of Redaporfin-Based Photodynamic Therapy in Rodents, *Int. J. Mol. Sci*., 2015, **16**, 29236–29249. doi:10.3390/ijms161226162

[3] M. Wainwright, Photodynamic antimicrobial chemotherapy (PACT), *J. Antimicrob. Chemother*., 1998, **42**, 13–28. doi: 10.1590/S0100-879X2010007500141

[4] A. van Dijken, J. J. A. M. Bastiaansen, N. M. M. Kiggen, B. M. W. Langeveld, C. Rothe, A. Monkman, I. Bach, P. Stössel and K. Brunner, Carbazole Compounds as Host Materials for Triplet Emitters in Organic Light-Emitting Diodes: Polymer Hosts for High-Efficiency Light-Emitting Diodes, *J. Am. Chem. Soc.*, 2004, **126**, 7718–7727. doi: 10.1021/ja049771j

[5] D. N. Congreve, J. Lee, N. J. Thompson, E. Hontz, S. R. Yost, P. D. Reusswig, M. E. Bahlke, S. Reineke, T. Van Voorhis and M. A. Baldo, External Quantum efficiency above 100% in a Singlet-Exciton-Fission—Based Organic Photovoltaic Cell, *Science*, 2013, **340**, 334–337. doi: 10.1126/science.1232994

[6] W. Shockley and H. J. Queisser, Detailed Balance Limit of Efficiency of *p-n* Junction Solar Cells, *J. Appl. Phys.*, 1961, **32**, 510–519. doi: 10.1063/1.1736034
[7] A. Rao, P. C. Y. Chow, S. Gélinas, C. W. Schlenker, C. -Z. Li, H. L. Yip, A. K. -Y Jen, D. S. Ginger and R. H. Friend, The role of spin in the kinetic control of recombination in organic photovoltaics, *Nature*, 2013, **500**, 435–439. doi: 10.1038/nature12339,.
[8] S. D. Dimitrov, S. Wheeler, D. Niedzialek, B. C. Schroeder, H. Utzat, J. M. Frost, J. Yao, A. Gillett, P. S. Tuladhar, I. McCulloch, J. Nelson and J. R. Durrant, Polaron pair mediated triplet generation in polymer/fullerene blends, *Nat. Commun*., 2015, **6**, 6501–6508. doi: 10.1038/ncomms7501
[9] F. Etzold, I. A. Howard, N Forler, A. Melnyk, D. Andrienko, M. R. Hansen and F. Laquai, Sub-ns triplet state formation by non-geminate recombination in PSBTBT:$PC_{70}BM$ and PCPDTBT:$PC_{60}BM$ organic solar cells, *Energy Environ. Sci.*, 2015, **8**, 1511–1522. doi: 10.1039/c4ee03630a
[10] I. A. Howard, N. C. Greenham, A. Abrusci, R. H. Friend and S Westenhoff, Charge Transfer and Charge Separation in Conjugated Polymer Solar Cells. Chapter 13, 531–561; in "Nanostructured conductive polymers", Eftekhari. A. (ed); Wiley 2010 (see especially page 555).
[11] D. W. Gehrig, Unraveling Efficiency-Limiting Processes in Organic Solar Cells by Ultrafast Spectroscopy – Impact of Chemical Structure and Morphology on Photophysics and Efficiency, PhD Dissertation, Mainz, 2015. page 185. http://pubman.mpdl.mpg.de/
[12] X. -K. Chen, T. Wang and J. -L. Brédas, Suppressing Energy Loss due to Triplet Exciton Formation in Organic Solar Cells: The Role of Chemical Structures and Molecular Packing, *Adv. Energy Mater*., 2017, **7**, 1602713–1602721. doi: 10.1002/aenm.201602713
[13] See for example: N. J. Turro, V. Ramamurthy and J. C. Scaiano, *Principles of Molecular Photochemistry: An Introduction*, University Science Books, 2009. Chapter 7; R. M. Williams, Introduction to Electron Transfer, https://doi.org/10.13140/RG.2.2.16547.30244; R. M. Williams, Introduction to Photo-induced Electron Transfer in "Mathematica"-V5. Classical Marcus Equation Calculator, https://doi.org/10.13140/RG.2.2.20531.89125/2 and references therein.
[14] M. Lor, J. Thielemans, L. Viaene, M. Cotlet, J. Hofkens, T. Weil, C. Hampel, K. Müllen, J. W. Verhoeven, M. Van der Auweraer and F. C. De Schryver, Photoinduced Electron Transfer in a Rigid First Generation Triphenylamine Core Dendrimer Substituted with a Peryleneimide Acceptor, *J. Am. Chem. Soc.*, 2002, **124**, 9918–9925. doi: 10.1021/ja020448v
[15] N. J. Turro, The triplet state, *J. Chem. Educ.*, 1969, **46**, 2–6.
[16] N. J. Turro, V. Ramamurthy and J. C. Scaiano, *Principles of Molecular Photochemistry: An Introduction*, University Science Books, 2009. Chapter 2 and 3.
[17] E. A. Margulies, J. L. Logsdon, C. E. Miller, L. Ma, E. Simonoff, R. M. Young, G. C. Schatz and M. R. Wasielewski, Direct Observation of a Charge-Transfer State Preceding High-Yield Singlet Fission in Terrylenediimide Thin Films, *J. Am. Chem. Soc.*, 2017, **139**, 663–671. doi: 10.1021/jacs.6b07721
[18] Y. Hou, X. Zhang, K. Chen, D. Liu, Z. Wang, Q. Liu, J. Zhao and A. Barbon, Charge separation, charge recombination, long-lived charge transfer state formation and intersystem crossing in organic electron donor/acceptor dyads, *J. Mater. Chem. C.*, 2019,**7**, 12048-12074. doi: 10.1039/C9TC04285G.
[19] T. Okada, I. Karaki, E. Matsuzawa, N. Mataga, Y. Sakata and S. Misumi, Ultrafast Intersystem Crossing in Some Intramolecular Heteroexcimers, *J. Phys. Chem.*, 1981, **85**, 3957–3960. doi: 10.1021/j150626a002
[20] R. M. Williams, J. M. Zwier and J. W. Verhoeven, Photoinduced Intramolecular Electron Transfer in a Bridged C_{60} (Acceptor)-Aniline (Donor) System; Photophysical Properties of the First "Active" Fullerene Diad, *J. Am. Chem. Soc.*, 1995, **117**, 4093–4099. doi: 10.1021/ja00119a025
[21] M. H. Lee, B. D. Dunietz and E. Geva, Calculation from First Principles of Intramolecular Golden-Rule Rate Constants for Photo-Induced Electron Transfer in Molecular Donor–Acceptor Systems, *J. Phys. Chem. C*, 2013, **117**, 23391–23401. doi: 10.1021/jp4081417
[22] P. Hudhomme and R. M. Williams, Energy And Electron Transfer In Photo- And Electro-Active Fullerene Dyads' in 'Fundamental and Applications of Carbon Nano Materials, World Scientific Publishing Company, 2011.

[23] M. T. Colvin, A. B. Ricks, A. M. Scott, D. T. Co and M. R. Wasielewski, Intersystem Crossing Involving Strongly Spin Exchange-Coupled Radical Ion Pairs in Donor–bridge–Acceptor Molecules, *J. Phys. Chem. A*, 2012, **116**, 1923–1930. doi: 10.1021/jp212546w

[24] H. van Willigen, G. Jones and M. S. Farahat, Time-Resolved EPR Study of Photoexcited Triplet-State Formation in Electron-Donor-Substituted Acridinium Ions, *J. Phys. Chem.*, 1996, **100**, 3312–3316. doi: 10.1021/jp953176+

[25] M. Wegner, H. Fischer, M. Koeberg, J. W. Verhoeven, A. M. Oliver, and M. N. Paddon-Row, Time-resolved CIDNP from photochemically generated radical ion pairs in rigid bichromophoric systems, *Chem. Phys.*, 1999, **242**, 227–234. doi: 10.1016/S0301-0104(99)00047-6

[26] M. R. Roest, A. M. Oliver, M. N. Paddon-Row and J. W. Verhoeven, Distance Dependence of Singlet and Triplet Charge Recombination Pathways in a Series of Rigid Bichromophoric Systems, *J. Phys. Chem. A*, 1997, **101**, 4867–4871. doi: 10.1021/jp970969i

[27] H. Imahori, K. Tamaki, D. M. Guldi, C. Luo, M. Fujitsuka, O. Ito, Y. Sakata and S. Fukuzumi, Modulating Charge Separation and Charge Recombination Dynamics in Porphyrin–Fullerene Linked Dyads and Triads: Marcus-Normal versus Inverted Region, *J. Am. Chem. Soc.*, 2001, **123**, 2607–2617. doi: 10.1021/ja003346i

[28] A. Loudet and K. Burgess, BODIPY Dyes and Their Derivatives: Syntheses and Spectroscopic Properties, *Chem. Rev*., 2007, **107**, 4891–4932. doi: 10.1021/cr078381n

[29] M. A. Filatov, S. Karuthedath, P. M. Polestshuk, H. Savoie, K. J. Flanagan, C. Sy, E. Sitte, M. Telitchko, F. Laquai, R. W. Boyle and M. O. Senge, Generation of Triplet Excited States via Photoinduced Electron Transfer in *meso*-anthra-BODIPY: Fluorogenic Response toward Singlet Oxygen in Solution and in Vitro, *J. Am. Chem. Soc.*, 2017, **139**, 6282–6285. doi: 10.1021/jacs.7b00551

[30] Z. Wang and J. Zhao, BODIPY–Anthracene Dyads as Triplet Photosensitizers: Effect of Chromophore Orientation on Triplet-State Formation Efficiency and Application in Triplet–Triplet Annihilation Upconversion, *Org. Lett*., 2017, **19**, 4492–4495. doi: 10.1021/acs.orglett.7b02047

[31] M. A. Filatov, S. Karuthedath, P. M. Polestshuk, S. Callaghan, K. J. Flanagan, M. Telitchko, T. Wiesner, F. Laquai and M. O. Senge, Control of triplet state generation in heavy atom-free BODIPY–anthracene dyads by media polarity and structural factors, *Phys. Chem. Chem. Phys.*, 2018, **20**, 8016–8031. doi: 10.1039/C7CP08472B

[32] X. -F. Zhang, X. Yang and B. Xu, PET-based bisBODIPY photosensitizers for highly efficient excited triplet state and singlet oxygen generation: tuning photosensitizing ability by dihedral angles, *Phys. Chem. Chem. Phys.*, 2017, **19**, 24792–24804. doi: 10.1039/C7CP02645E

[33] R. M. Williams, Distance and orientation dependence of photoinduced electron transfer through twisted, bent and helical bridges: A Karplus relation for charge transfer interaction, *Photochem. Photobiol. Sci*., 2010, **9**, 1018–1026. doi: 10.1039/C0PP00050G

[34] Y. Liu, J. Zhao, A. Iagatti, L. Bussotti, P. Foggi, E. Castellucci, M. Di Donato and K. -L. Han, A Revisit to the Orthogonal BODIPY Dimers: Experimental Evidence for the Symmetry Breaking Charge Transfer-Induced Intersystem Crossing, *J. Phys. Chem. C*, 2018, **122**, 2502–2511. doi: 10.1021/acs.jpcc.7b10213

[35] M. A. Filatov, S. Karuthedath, P. M. Polestshuk, S. Callaghan, K. J. Flanagan, T. Wiesner, F. Laquai and M. O. Senge, BODIPY-pyrene and perylene dyads as heavy atom-free singlet oxygen sensitizers, *ChemPhotoChem*., 2018, **20**, 8016–8031. doi: 10.1002/cptc.201800020

[36] Y. Hou, T. Biskup, S. Rein, Z. Wang, L. Bussotti, N. Russo, P. Foggi, J. Zhao, M. Di Donato, G. Mazzone and S. Weber, Spin–Orbit Charge Recombination Intersystem Crossing in Phenothiazine–Anthracene Compact Dyads: Effect of Molecular Conformation on Electronic Coupling, Electronic Transitions, and Electron Spin Polarizations of the Triplet States, *J. Phys. Chem. C*, 2018, **122**, 27850–27865. doi: 10.1021/acs.jpcc.8b08965

[37] Z. E. X. Dance, S. M. Mickley, T. M. Wilson, A. B. Ricks, A. M. Scott, M. A. Ratner and M. R. Wasielewski, Intersystem Crossing Mediated by Photoinduced Intramolecular Charge Transfer: Julolidine-Anthracene Molecules with Perpendicular pi Systems, *J. Phys. Chem. A*, 2008, **112**, 4194—4201. doi: 10.1021/jp800561g

[38] S. Weber, Transient EPR, *eMagRes*., 2017, **6**, 255–270. doi: 10.1002/9780470034590.emrstm1509

[39] J. T. Buck, A. M. Boudreau, A. DeCarmine, R. W. Wilson, J. Hampsey and T. Mani, Spin-Allowed Transitions Control the Formation of Triplet Excited States in Orthogonal Donor-Acceptor Dyads, *Chem.*, 2019, **5**, 138–155. doi: 10.1016/j.chempr.2018.10.001

[40] M. A. El-Sayed, Effect of spin orbit interactions on the dipolar nature of the radiative microwave zero-field transitions in aromatic molecules, *J. Chem. Phys*., 1974, **60**, 4502–4507. doi: 10.1063/1.1680930

[41] Z. E. X. Dance, Q. Mi, D. W. McCamant, M. J. Ahrens, M. A. Ratner and M. R. Wasielewski, Time-Resolved EPR Studies of Photogenerated Radical Ion Pairs Separated by *p*-Phenylene Oligomers and of Triplet States Resulting from Charge Recombination, *J. Phys. Chem.* B, 2006, **110**, 25163–25173. doi: 10.1021/jp063690n

[42] S. Callaghan, M. A. Filatov, H. Savoie, R. W. Boyle and M. O. Senge, In vitro cytotoxicity of a library of BODIPY-anthracene and -pyrene dyads for application in photodynamic therapy, *Photochem. Photobiol. Sci*., 2019, **18**, 495–504. doi: 10.1039/C8PP00008E

[43] J. Zhao, K. Chen, Y. Hou, Y. Che, L. Liu and D. Jia, Recent progress in heavy atom-free organic compounds showing unexpected intersystem crossing (ISC) ability, *Org. Biomol. Chem.*, 2018, **16**, 3692–3701. doi: 10.1039/C8OB00421H

[44] J. Zhao, K. Xu, W. Yang, Z. Wang and F. Zhong, The triplet excited state of BODIPY: formation, modulation and application, *Chem. Soc. Rev.*, 2015, **44**, 8904–8939. doi: 10.1039/C5CS00364D

[45] M. A. Filatov, Heavy-atom-free BODIPY photosensitizers with intersystem crossing mediated by intramolecular photoinduced electron transfer, *Org. Biomol. Chem.*, 2020. doi: 10.1039/C9OB02170A.

[46] P. C. Y. Chow, S. Gélinas, A. Rao and R. H. Friend, Quantitative Bimolecular Recombination in Organic Photovoltaics through Triplet Exciton Formation, *J. Am. Chem. Soc*., 2014, **136**, 3424−3429. doi: 10.1021/ja410092n

[47] Y. Tamai, K. Tsuda, H. Ohkita, H. Benten and S. Ito, Charge-carrier generation in organic solar cells using crystalline donor polymers, *Phys. Chem. Chem. Phys*., 2014, **16**, 20338–20346. doi: 10.1039/c4cp01820f

[48] M. C. Scharber, C. Lungenschmied, H. -J. Egelhaaf, G. Matt, M. Bednorz, T. Fromherz, J. Gao, D. Jarzab and M. A. Loi, Charge transfer excitons in low band gap polymer based solar cells and the role of processing additives, *Energy Environ. Sci.*, 2011, **4**, 5077–5083. doi: 10.1039/c1ee02181h

[49] R. Haberkorn, M. E. Michel-Beyerle and R. A. Marcus, On spin-exchange and electron-transfer rates in bacterial photosynthesis, *Proc. Natl Acad. Sci*. USA, 1979, **76**, 4185–4188. doi: 10.1073/pnas.76.9.4185

[50] D. W. Gehrig, I. A. Howard and F. Laquai, Charge Carrier Generation Followed by Triplet State Formation, Annihilation, and Carrier Recreation in PDBTTT-C/$PC_{60}BM$ Photovoltaic BlendsBlends, *J. Phys. Chem. C*, 2015, **119**, 13509–13515. doi: 10.1021/acs.jpcc.5b03467

[51] J. R. Ochsmann, D. Chandran, D. W. Gehrig, H. Anwar, P. K. Madathil, K. -S. Lee and F. Laquai, Triplet State Formation in Photovoltaic Blends of DPP-Type Copolymers and $PC_{71}BM$, *Macromol. Rapid Commun*., 2015, **36**, 1122–1128. doi: 10.1002/marc.201400714

[52] R. M. Williams, H. -C. Chen, D. Di Nuzzo, S. C. J. Meskers, and R. A. J. Janssen, Ultrafast charge and triplet state formation in Diketopyrrolopyrrole Low Band Gap Polymer/ Fullerene blends: influence of Nanoscale Morphology of Organic Photovoltaic Materials on charge recombination to the Triplet State, *J. Spectrosc.*, 2017, 6867507. doi: 10.1155/2017/6867507

[53] R. M. Williams, N. Vân Anh and I. H. M. van Stokkum, Triplet Formation by Charge Recombination in Thin Film Blends of Perylene Red and Pyrene: Developing a Target Model for the Photophysics of Organic Photovoltaic Materials, *J. Phys. Chem. B*, 2013, **117**, 11239–11248. doi: 10.1021/jp402086p

[54] C. M. Kirk, ESR studies of radical ions, PhD thesis, University of Canterbury 1975.

[55] B. G. Segal, M. Kaplan and G. K. Fraenkel, Measurement of *g* Values in the Electron Spin Resonance Spectra of Free Radicals, *J. Chem. Phys.*, 1965, **43**, 4191–4200. doi: 10.1063/1.1696676

[56] B. M. Latta and R. W. Taft, Substituent Effects on the Hyperfine Splitting Constants of N,N-Dimethylaniline Cation Radicals, *J. Am. Chem. Soc.*, 1967, **89**, 5172—5178. doi: 10.1021/ja00996a017

[57] V. I. Krinichnyi and E. I. Yudanova, Light-Induced EPR Study of Charge Transfer in P3HT/$PC_{71}BM$ Bulk Heterojunctions, *J. Phys. Chem. C*, 2012, **116**, 9189–9195. doi: 10.1021/jp2120516

[58] V. I. Krinichnyi and E. I. Yudanova, Influence of morphology of low-band-gap PCDTBT:$PC_{71}BM$ composite on photoinduced charge transfer: LEPR spectroscopy study, *Synth. Met.*, 2015, **210**, 148—155. doi: 10.1016/j.synthmet.2015.09.019

[59] S. A. J. Thomson, J. Niklas, K. L. Mardis, C. Mallares, I. D. W. Samuel and O. G. Poluektov, Charge Separation and Triplet Exciton Formation Pathways in Small-Molecule Solar Cells as Studied by Time-Resolved EPR Spectroscopy, *J. Phys. Chem. C*, 2017, **121**, 22707–22719. doi: 10.1021/acs.jpcc.7b08217

[60] J. W. Verhoeven, On the role of spin correlation in the formation, decay, and detection of long-lived, intramolecular charge-transfer states, *J. Photochem. Photobiol.*, 2006, **7**, 40–60. doi: 10.1016/j.jphotochemrev.2006.04.001

[61] K. Maeda, K. B. Henbest, F. Cintolesi, I. Kuprov, C. T. Rodgers, P. A. Liddell, D. Gust, C. R. Timmel and P. J. Hore, Chemical compass model of avian magnetoreception, *Nature*, 2008, **453**, 387–390. doi: 10.1038/nature06834.

[62] E. L. Frankevich, A. A. Lymarev, I. Sokolik, F. E. Karasz, S. Blumstengel, R. H. Baughman and H. H. Hörhold, Polaron-pair generation in poly(phenylene vinylenes), *Phys. Rev. B*, 1992, **46**, 9320–9324. doi: 10.1103/PhysRevB.46.9320

[63] D. Veldman, S. M. A. Chopin, S. C. J. Meskers, M. M. Groeneveld, R. M. Williams and R. A. J. Janssen, Triplet Formation Involving a Polar Transition State in a Well-Defined Intramolecular Perylenediimide Dimeric Aggregate, *J. Phys. Chem. A*, 2008, **112**, 5846–5857. doi: 10.1021/jp8022524

[64] M. Kállay, K. Németh and P. R. Surján, Triplet State Characteristics of Higher Fullerenes, *J. Phys. Chem. A*, 1998, **102**, 1261–1273. doi: 10.1021/jp972739+

[65] D. Beljonne, Z. Shuai, G. Pourtois and J. L. Bredas, Spin−Orbit Coupling and Intersystem Crossing in Conjugated Polymers: A Configuration Interaction Description, *J. Phys. Chem. A*, 2001, **105**, 3899––3907. doi: 10.1021/jp010187w

[66] M. A. El-Sayed, Triplet state. Its radiative and nonradiative properties, *Acc. Chem. Res.*, 1968, **1**, 8–16. doi: 10.1021/ar50001a002

[67] N. J. Turro, V. Ramamurthy, and J. C. Scaiano, *Principles of Molecular Photochemistry: An Introduction*, University Science Books, 2009. Chapter 5, page 284. Note that the second representation in Figure 5.9(a) (top line) on page 285 is not correct: a $^1(n,\pi^*)$ is depicted (should be a $^1(\pi,\pi^*)$).

[68] B. Hu, L. Yan and M. Shao, Magnetic-Field Effects in Organic Semiconducting Materials and Devices, *Adv. Mater.*, 2009, **21**, 1500–1516. doi: 10.1002/adma.200802386

[69] R. M. Williams, M. Koeberg, J. M. Lawson, Y.-Z. An, Y. Rubin, M. N. Paddon-Row and J. W. Verhoeven, Photoinduced Electron Transfer to C_{60} across Extended 3- and 11-Bond Hydrocarbon Bridges: Creation of a Long-Lived Charge-Separated State, *J. Org. Chem.*, 1996, **61**, 5055–5062. doi: 10.1021/jo960678q

[70] M. N. Paddon-Row, Electron and Energy Transfer, *in* Stimulating Concepts in Chemistry, VCH, Weinheim, 2000, pp. 267– 291.

[71] R. M. Williams, A highly soluble asymmetric perylene-bis(dicarboximide)-acceptor system incorporating a methylene bridged methoxybenzene-donor: solvent dependence of charge transfer interactions, *Turk. J. Chem.*, 2009, **33**, 727–737. doi: 10.3906/kim-0811-33

[72] S. I. van Dijk, P. G. Wiering, C. P. Groen, A. M. Brouwer, J. W. Verhoeven, W. Schuddeboom and J. M. Warman, Solvent-dependent switching between two dipolar excited states in a rigidly extended trichromophoric system, *J. Chem. Soc. Faraday Trans.*, 1995, **91**, 2107–2114. doi: 10.1039/FT9959102107

[73] D. Veldman, S. M. A. Chopin, S. C. J. Meskers and R. A. J. Janssen, Enhanced Intersystem Crossing via a High Energy Charge Transfer State in a Perylenediimide−Perylenemonoimide Dyad, *J. Phys. Chem. A*, 2008, **112**, 8617–8632. doi: 10.1021/jp805949r

[74] P. K. Samanta, D. Kim, V. Coropceanu and J.-L. Brédas, Up-Conversion Intersystem Crossing Rates in Organic Emitters for Thermally Activated Delayed Fluorescence: Impact of the Nature of Singlet vs Triplet Excited States, *J. Am. Chem. Soc.*, 2017, **139**, 4042–4051. doi: 10.1021/jacs.6b12124

[75] P. A. B. Haase, M. Repisky, S. Komorovsky, J. Bendix and S. P. A. Sauer, Relativistic DFT Calculations of Hyperfine Coupling Constants in 5d Hexafluorido Complexes: $[ReF_6]^{2-}$ and $[IrF_6]^{2-}$, *Chem. - Eur. J.*, 2018, **24**, 5124–5133. doi: 10.1002/chem.201704653

Photo-activated thin films of porphyrinoids for reactive oxygen species generation[‡]

Abstract

This chapter discusses the synthesis and photophysical studies, in both solution and thin film, of free base 5,10,15,20-tetra-(4-hexyloxyphenyl)porphyrin. The porphyrin was synthesized *via* modified Adler-Longo conditions. This porphyrin was then studied *via* UV-Vis spectroscopy, and steady-state and time-resolved photoluminescence spectroscopy. A thin film was cast on quartz glass *via* spin coating and *via* vapour-phase deposition. The fluorescence lifetime of the porphyrin in a solid film, as well as the detection of singlet oxygen generated by the film using a water-soluble singlet oxygen probe, are reported.

[‡]The content of this chapter has been submitted to the Journal of Porphyrins and phthalocyanines.

3.1. Introduction

The first written accounts of Photodynamic Therapy (PDT) were reported at the end of the 19th century.[1] Back then, it was coined as 'phototherapy'[2] and has since been developed to treat early stage tumors,[3] dermatological conditions[4] and microbial infections (Antimicrobial Photodynamic Therapy).[5] PDT requires the presence of molecular oxygen ($^3O_2$), a photosensitizer (PS) and light to form singlet oxygen ($^1O_2$) that is responsible for the desired therapeutic effect. The 'ideal PS' is highly sought after and its properties are described in reviews by Callaghan and Senge, and by Abrahamse and Hamblin (see also section **1.4.4**).[1, 6] Some of these properties include efficient triplet excited state formation with an excitation wavelength in the region of 650–850 nm (known as the therapeutic window), possessing a sufficiently long triplet lifetime, and generating high yields of singlet oxygen and Reactive Oxygen Species (ROS). Following irradiation of a PS, its singlet state is populated. This singlet state can then undergo intersystem crossing (ISC) to form the triplet state. The triplet state can interact with $^3O_2$ to form $^1O_2$ (Figure **3.1**), which can destroy cancer cells or microbial cells.

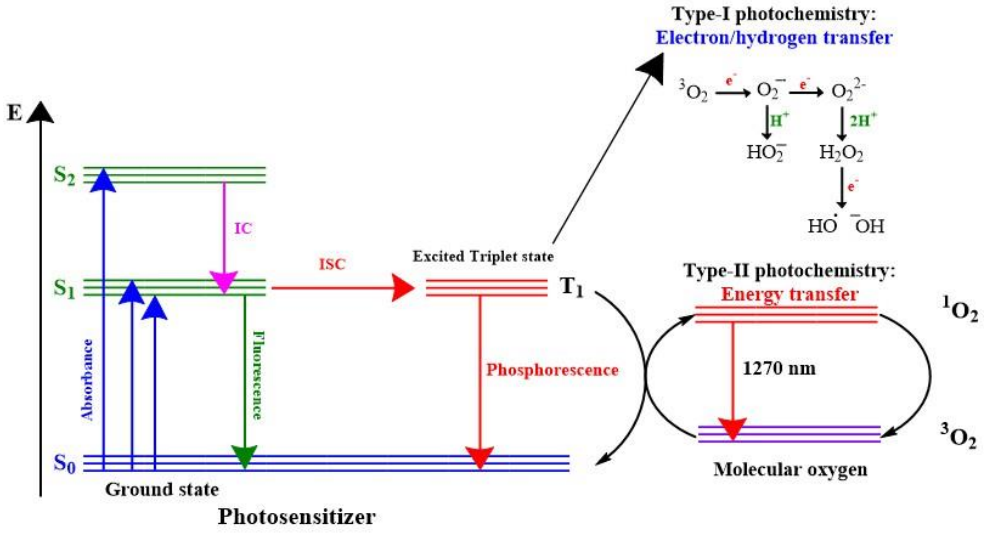

Figure 3.1. *Jablonski energy diagram showing how the photosensitizer is excited to the singlet state (S_1), followed by population of the excited triplet state by intersystem crossing (ISC) and the triplet state interacting with molecular oxygen to form cytotoxic singlet oxygen.*[7]

Antimicrobial Photodynamic Therapy (APDT) is the light treatment against harmful micro-organisms and has been applied in the clinics for almost thirty years.[8] It has been used to treat skin infections,[9] oral infections in dentistry[10] and more recently, it has been investigated as an alternative pest management in agriculture.[11] In order for the PSs to treat the microbial infections in the clinic, they have to be physically applied to the surface of the infected areas.

Furthermore, PSs have been incorporated into thin films for their uses as photodetectors and sensors.[12, 13]

The PS used in this study is the 5,10,15,20-tetra-(4-hexyloxyphenyl)porphyrin (**THOPP**), that was synthesized for the first time in 1993 by Shimizu *et al.*[14] It was recently shown that introducing a Zn(II) metal ion into the core of the **THOPP** macrocycle allowed an electroluminescence process to occur in thin films.[15] Furthermore, Shimizu and coworkers described the mesomorphic phase transitions of *meso*-tetra-(4-alkoxyphenyl)porphyrins with differing chain lengths.[14] **THOPP** appeared in numerous papers that reported on volumetric properties of porphyrins,[16] oxygen sensing,[17] fluorescence and FTIR analysis,[18] mesogenic properties of porphyrin liquid crystals,[19] and organic-inorganic surfaces in thin films.[20]

Since thin films containing *meso*-tetra-(4-alkoxyphenyl)porphyrins can exhibit luminescence,[15, 18] investigations were conducted to determine whether it is also possible to create singlet oxygen, *via* light excitation, in the thin film. Herein, the synthesis of a *meso*-tetra-(hexyloxyphenyl)porphyrin, **THOPP**, and its photophysical properties in solution, as well as in thin films, are described for application in photomedicine.

3.2. Results and Discussion

3.2.1. Synthesis and characterization

THOPP was synthesized (Figure **3.2**) *via* a modified literature procedure (see supplementary information for full synthetic procedure and characterization data - figures **S3.1**–**S3.6**).[15] The photophysical properties of **THOPP** were studied in solution and in a thin film. Results are summarized into tables **3.1**–**3.4** and commercially available 5,10,15,20-tetraphenylporphyrin (**TPP**) was used as a reference for properties in solution (see structure of **TPP** in Figure **3.2**).

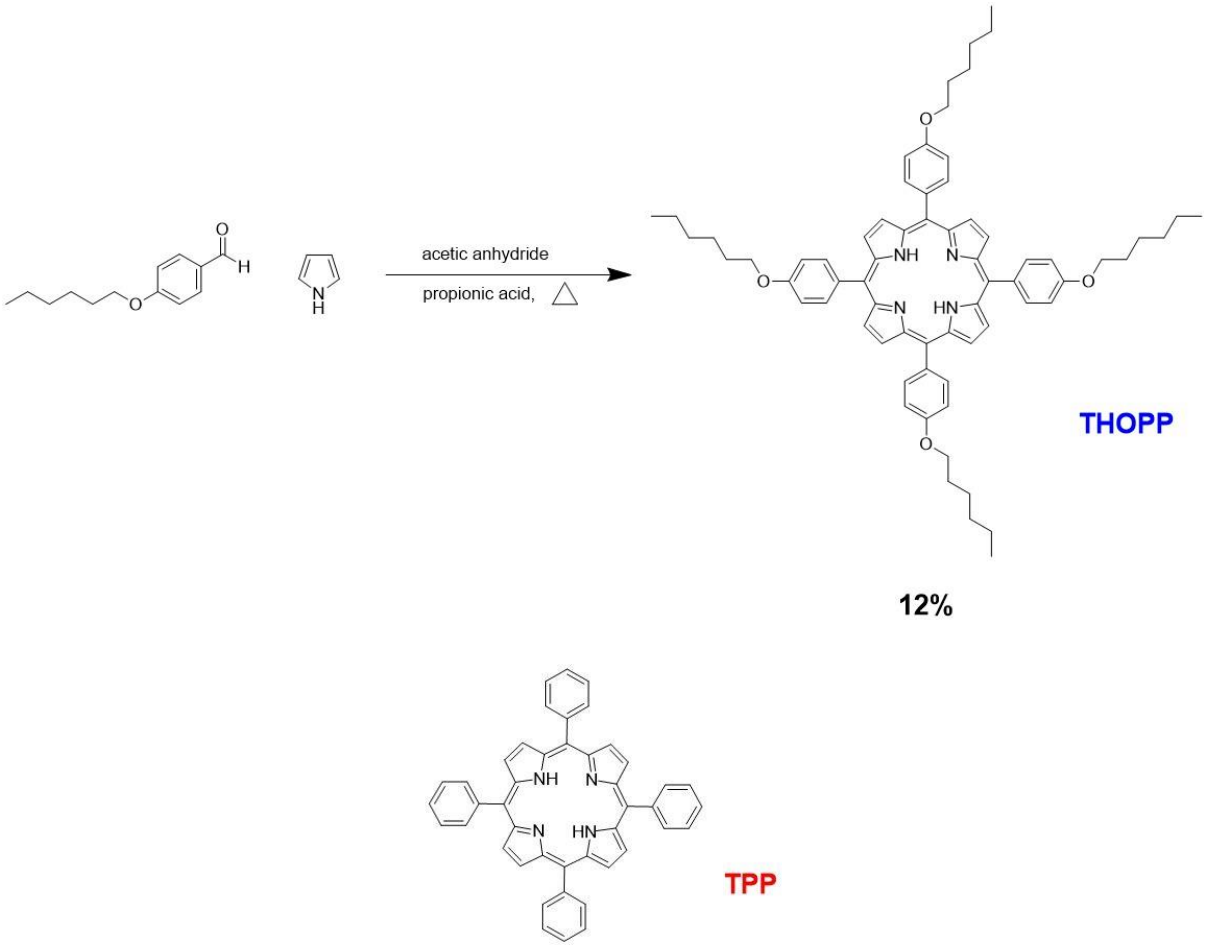

Figure 3.2. (Top): *Reaction scheme for the synthesis of 5,10,15,20-tetra-4-hexyloxyphenylporphyrin (**THOPP**) and **(Bottom):** chemical structure of 5,10,15,20-tetraphenylporphyrin (**TPP**).*[15]

3.2.2. Photophysical characterization

3.2.2.1. Solution properties

UV-Vis spectra of **THOPP** and **TPP** in chloroform ($CHCl_3$) (Figures **3.3** and **3.4**) are characteristic of free base porphyrins with an intense Soret band at 423 nm and 418 nm, respectively (Table **3.1**).[24, 30] These Soret bands both bear shoulders with maxima at 400 nm and four Q-bands (Q-band maxima are summarized in Table **3.1**). **THOPP** shows a small peak at 450 nm that corresponds to partial protonation of the porphyrin by the $CHCl_3$ solvent.[21] For this reason and for the determination of the triplet lifetime, **THOPP** was also studied in tetrahydrofuran (THF; see UV-Vis spectrum in Figure **S3.7**). Upon changing the solvent from $CHCl_3$ to THF, the Soret band shifts towards the blue region by 2 nm (see Table **3.1**). No partial protonation was observed, the Q-bands absorbed less light (as indicated by their reduced molar absorption coefficients), and they were shifted to the blue region by a max of 3 nm.

The UV-Vis spectrum of **TPP** in $CHCl_3$ also shows evidence of partial protonation by the acidity of the $CHCl_3$ solvent, as it has a small peak at approx. 440 nm. **THOPP** undergoes a bathochromic shift (4–9 nm) of all bands, compared to **TPP**. This is most likely due to the presence of electron-donating hexyloxy chains on the *para*-position of the phenyl rings. This structural difference therefore causes a shift towards the red region of the UV-Vis spectrum. The photoluminescence spectra were recorded in toluene and $CHCl_3$ to determine the fluorescence quantum yield (Φ_f) and the singlet oxygen quantum yield (Φ_Δ), respectively. In Figure **3.5**, it shows that the energy of the first excited state, S_1, of **THOPP** is 654 nm and 648 nm for **TPP**. The energy of the S_1 ($E(S_1)$) slightly lower for **THOPP** than for **TPP** and thus explains the bathochromic shift observed in the UV-Vis spectrum of **THOPP**, compared to **TPP**.

The concentration of **THOPP** in the UV-Vis spectrum was 2.3 μM (Figure **3.3**), while that of **TPP** in Figure **3.4** was 1.6 μM. Despite the higher concentration of **THOPP**, its Soret band absorbs less than **TPP** as shown by its lower molar absorption coefficient (Table **3.1** and in Figures **3.4** and **3.5**). However, the Q-bands of **THOPP** absorb more and their intensity ratio is different compared to **TPP** in $CHCl_3$. The intensity of these bands of **THOPP** in decreasing order, from longer to shorter wavelengths (low energy to high energy), are: $Q_{IV} > Q_{III} > Q_I > Q_{II}$. In **TPP**'s UV-Vis spectrum, the Q-bands decrease in order of: $Q_{IV} > Q_{III} > Q_{II} > Q_I$, with the Q_{IV}-peak much more intense than the others. This intense peak is followed by minor decreases in intensity from the Q_{III} to Q_I in the UV-Vis spectrum of TPP. However, **THOPP** shows a gradual decrease from Q_{IV} to Q_{III}, followed by a large decrease to the Q_{II}. Surprisingly,

the intensity almost doubles from the Q_{II} to Q_I in the UV-Vis spectrum of **THOPP**. These differences in the intensity ratio and position of the Q-bands are accredited to the molecular structure. Previous reports of **THOPP** show identical UV-Vis spectra, only differing slightly (Soret and Q-band experience shifts of 1–4 nm) due to the different solvents used.[17, 22]

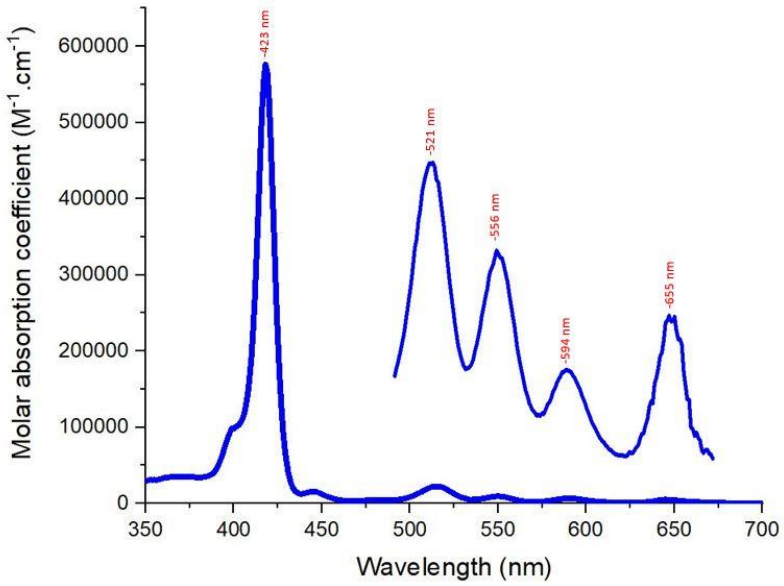

Figure 3.3. *UV-Vis spectrum of* ***THOPP****, in* $CHCl_3$*, using a molar absorption coefficient scale. The concentration of* ***THOPP*** *was 2.3* μM *and the spectrum was recorded at room temperature.*

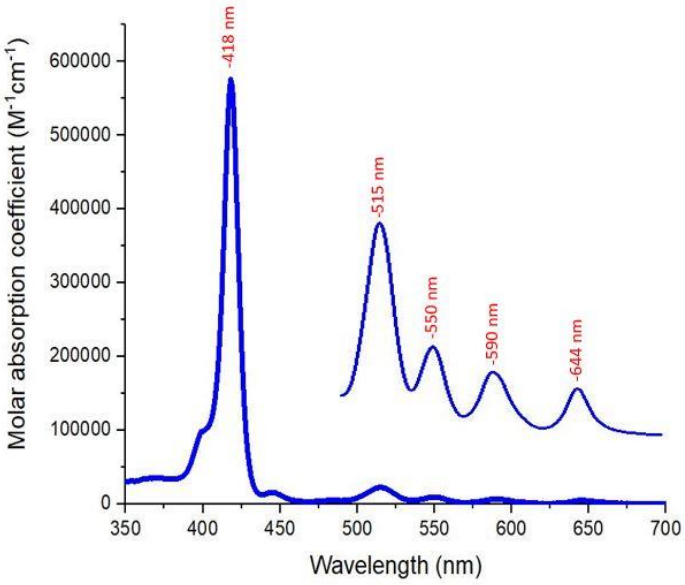

Figure 3.4. *UV-Vis spectrum of* ***TPP****, in* $CHCl_3$*, using a molar absorption coefficient scale. The concentration of* ***TPP*** *was 1.6* μM *and the spectrum was recorded at room temperature.*

Table 3.1. *UV-Vis absorption data of the PSs,* ***THOPP*** *and* ***TPP****. The concentration was 2.3 μM for* ***THOPP*** *in $CHCl_3$, 2.2 μM for* ***THOPP*** *in THF, and 1.6 μM for* ***TPP*** *in $CHCl_3$. Values in brackets refer to the log of the molar absorption coefficient (ε).*

PS	Sh [a] (λ/nm)	Soret band (λ/nm)	Q-bands (λ/nm)				Q_y / Soret [b]
			Q_{IV} [c]	Q_{III} [d]	Q_{II} [e]	Q_I [f]	
THOPP – $CHCl_3$	400	423 (5.65)	521 (4.40)	556 (4.32)	594 (4.14)	655 (4.20)	0.02
THOPP - THF	400	421 (5.64)	518 (4.16)	554 (4.02)	596 (3.56)	654 (3.84)	0.02
TPP – $CHCl_3$	400	418 (5.76)	515 (4.35)	550 (3.97)	590 (3.82)	644 (3.69)	0.02

[a] Sh = shoulder that appears beside Soret band; [b] Ratio of the intensity of the Q_{III} band compared to the Soret band; [c] Q_{IV} = Qy(1,0) peak; [d] Q_{III} = Qy(0,0) peak; [e] Q_{II} = Qx(1,0) peak; [f] Q_I = Qx(0,0) peak.

The overlap of the absorption and emission spectra for **THOPP** and **TPP** in $CHCl_3$ are shown below. This overlap determines the experimental energy of the singlet excited state ($E(S_1)$; Figure **3.5**). This figure shows the wavelength at which the normalized absorption spectrum overlaps with the normalized emission spectrum. The $E(S_1)$ of **THOPP** in $CHCl_3$ is 654 nm and for **TPP** in $CHCl_3$, the $E(S_1)$ is 648 nm. This result is in close agreement with the literature value of 646 nm of **TPP**.[28]

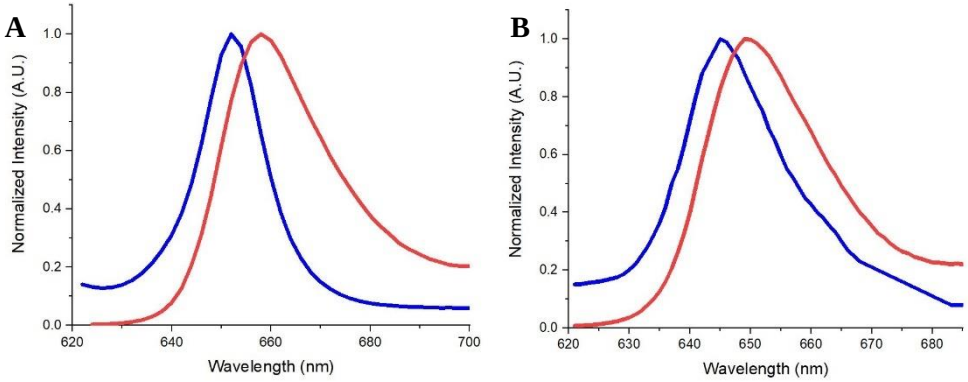

Figure 3.5. (A): THOPP's *normalized absorption (blue) and emission spectra (red) in $CHCl_3$. $E(S_1)$ of* ***THOPP*** *= 654 nm.* ***(B): TPP's*** *normalized absorption (blue) and emission spectra (red) in $CHCl_3$. $E(S_1)$ of* ***TPP*** *= 648 nm.*

Furthermore, the emission spectra of **THOPP** and **TPP** in $CHCl_3$ at room temperature are shown in Figure **3.6**. The emission maxima of **THOPP** appear at 655 nm and 725 nm. The former (Em1 as shown in Table **3.2**) is approximately three times more intense than the latter emission maximum (Em2). The fluorescence of **THOPP** in THF was also conducted (Figure **S3.8**). The position of the emission maxima, and the overall emission shape, remain unchanged

upon changing the solvent from $CHCl_3$ to THF. Furthermore, the Φ_f remains unchanged (Table **3.2**). **TPP** exhibits emission maxima at 649 nm and 718 nm in $CHCl_3$ (Figure **3.6**). All solutions (**TPP** in $CHCl_3$, and **THOPP** in $CHCl_3$ and THF) were excited at 518 nm and the absorbance at this wavelength was 0.1. **TPP**'s emission spectrum appears to have a more bimodal distribution shape as the Em1 emission band is almost 1.6 times more intense than the Em2 peak. **TPP**'s emission spectrum is overall less intense than **THOPP**. The **THOPP** emission profile reported here is slightly different compared to previous reports in the same solvent. Also, the Φ_f (**THOPP**) in this report is larger than previously reported (0.22 vs 0.13) by Şen *et al*.[18] and the τ_s reported herein is twice as long compared to that reported by Şen and coworkers.

Table 3.2. *Photophysical properties of* ***THOPP*** *in THF and* $CHCl_3$*, and* ***TPP*** *in* $CHCl_3$*.*

PS	Em1 [a] (nm)	Em2 [a] (nm)	SS [b] (cm^{-1})	Φ_f [c]	Φ_Δ [d]	τ_s (ns) [e]	τ_T (ns) [f]	τ_T (µs) [g]	
								τ1	τ2
THOPP – $CHCl_3$ [h]	655	725	70	0.22	0.44	- [i]	- [i]	- [i]	- [i]
THOPP – THF [j]	655	725	70	0.22	- [i]	9.4 ± 0.9	330 ± 4.5	297	46
TPP – $CHCl_3$ [h]	649 [h]	718 [h]	120 [h]	0.11 [h]	0.55 [h]	10.6 ± 0.3 [k]	480 [k]	385 [k]	*

[a] According to the emission spectra, Em1 = first emission peak [λ_{em} $Q_x(0,0)$] and Em2 = second emission peak [λ_{em} $Q_x(0,1)$]; [b] The Stokes shift (SS) that was calculated from the corresponding UV-Vis and emission spectra; [c] Φ_f = fluorescence quantum yield calculated using TPP (0.11) as a reference in toluene;[24] [d] Φ_Δ = singlet oxygen quantum yield was calculated using TPP (0.55) as a reference in $CHCl_3$;[23] [e] τ_s = singlet state lifetime in air (equilibrated), given in nanoseconds; [f] τ_T (ns) = triplet state lifetime in air (equilibrated), given in nanoseconds; [g] τ_T (µs) = triplet state lifetime in oxygen-free solution (given in microseconds), the triplet state lifetime in the oxygen-free solution undergoes bi-exponential decay giving two lifetimes, τ1 and τ2, given in microseconds; [h] in $CHCl_3$ solvent; [i] data not available; [j] in THF solvent; [k] literature values in DMF solvent;[22] ******* *no triplet-triplet annihilation reported in literature, it decays mono-exponentially, thus yielding one triplet lifetime.*

Figure **3.6** displays the fluorescence quantum yield (Φ_f) of **THOPP** in $CHCl_3$ and it was determined using **TPP** in toluene as a reference (0.11).[24] The fluorescence of **TPP** is lower than that of **THOPP** (Figure **3.6**). The Φ_Δ of **THOPP** in $CHCl_3$ was calculated using **TPP** in $CHCl_3$ as a reference (0.55).[23] The higher Φ_f in **THOPP** is compensated by the decreased singlet oxygen quantum yield of **THOPP** (0.44; Figure **3.7**). Therefore, the quantum yields confirm that intersystem crossing (ISC) in **TPP** is faster than in **THOPP**.

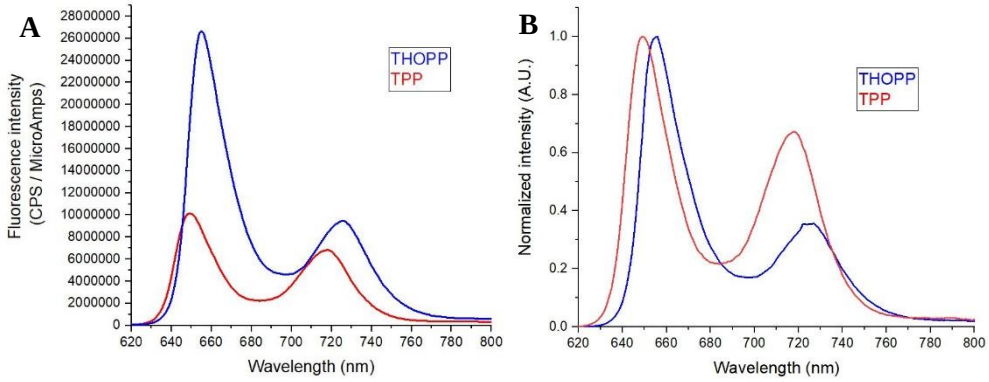

***Figure 3.6. (A)**: Fluorescence spectra of **THOPP** (blue) and **TPP** (red) in $CHCl_3$ using **TPP** in toluene (0.11) as a reference (Excitation wavelength = 518 nm and absorbance of both samples at this wavelength was 0.1).[24] The fluorescence quantum yield obtained for **THOPP** was 0.22. **(B)**: Normalized fluorescence emission spectra of **THOPP** (blue) and **TPP** (red) in $CHCl_3$.*

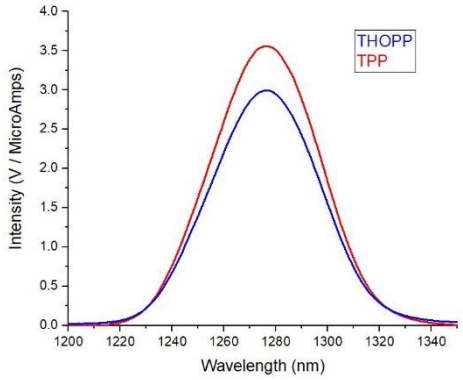

***Figure 3.7.** Singlet oxygen emission of **THOPP** (blue) and **TPP** (red) in $CHCl_3$ using **TPP** in $CHCl_3$ as a reference (0.55).[23] Excitation wavelength = 521 nm and the obtained singlet oxygen quantum yield was 0.44.*

In figure **3.8**, the nanosecond transient experiment of aerated **THOPP** in THF is reported. The experiment was first conducted in $CHCl_3$, however the sample decomposed after excitation by the pump laser (see experimental details). There was no decomposition observed in THF and the decay curve of this aerated sample is fitted mono-exponentially. The oxygen-free sample of **THOPP** in THF decays bi-exponentially (Table **3.2** and Figure **S3.9**). This indicates that triplet-triplet annihilation is predominantly occurring and this decay undergoes second order decay kinetics. There is a slow and fast component observed and the slow component likely corresponds to the intrinsic lifetime of the triplet excited state of **THOPP** in oxygen-free THF (see section **3.5.1.1** for experimental details). The fast component would then correspond to triplet-triplet annihilation occurring (Table **3.2**). The lifetime of **TPP** in DMF

was reported to be slightly longer than that of **THOPP** in THF (Table **3.2**).[22] This correlates well with the singlet oxygen quantum yield of **THOPP** (Figure **3.7**): the shorter triplet lifetime of **THOPP** produces a lower singlet oxygen yield.

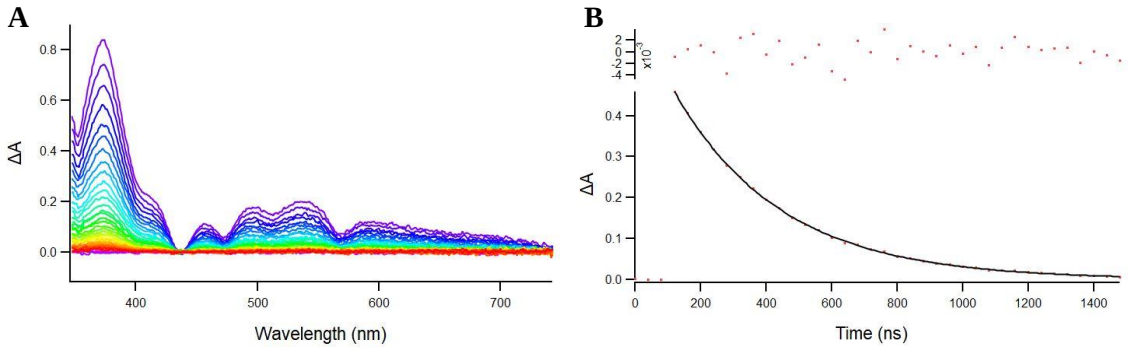

Figure 3.8. *(**A**): Nanosecond transient absorption spectrum of **THOPP** in THF (in air). λ_{ex} = 518 nm, incremental time delay = 40 ns. (**B**): Decay kinetics trace at 517 nm. Decay curve is fitted mono-exponentially and the obtained triplet lifetime is 330 ns. On the top, weighted residuals are presented.*

Table **3.2** reports a bi-exponential fit of the triplet decay data, however, a more appropriate model is second order decay kinetics. The observed triplet lifetime (T_1) is influenced by the triplet state being quenched by oxygen in solution, as well as by triplet-triplet annihilation (k_{TT}), and by the intrinsic triplet decay (k_0). Within the triplet-triplet annihilation process, the diffusion rate of the molecules in the triplet excited state, as well as their concentration at time zero (C_0; influenced by laser-power), plays an important role due to bimolecular collisional quenching.[25, 26]

The complex decay of triplet states and their interaction with oxygen also implies that singlet oxygen emission is due to a process with second order decay kinetics. This means that it can be fitted *via* a bi-exponential decay, as the concentration of the triplet at time 0 (C_0 in equations below) and the concentration of oxygen in solution, are of importance. The triplet decay can be fitted by a mono-exponential function if the interaction with oxygen is fast. Furthermore, it is clear that total removal of oxygen is not straightforward, indicated also by the fact that the singlet oxygen emission quantum yield remained virtually the same upon prolonged bubbling with argon. These effects have also been noted by others.[37]

By using second order decay kinetics at room temperature in THF, we obtain an intrinsic triplet lifetime of τ^0_T = 566 µs, and a triplet-triplet annihilation rate constant of k_{TT} = 9.1×10^9 $M^{-1}s^{-1}$. This is close to the diffusion rate in THF, which is 1.3×10^{10} at 293 K. For

pristine **C60** in toluene[27] at room temperature, $\tau^0_T \geq 280$ µs, with a $k_{TT} \geq 4.8 \times 10^9$ $M^{-1}s^{-1}$ was reported. The intrinsic triplet state lifetime τ^0_T of **TPP** is reported to be 1500 µs at 293 K.[28] This implies that the values reported here are within the range of expectation.

The (partly spectrally integrated) data vs time (*t*) was fitted with a home-made Igor procedure describing the following function:

$$\Delta A(t) = \frac{C_0 k_0}{k_0 e^{(k_0 t)} + k_{TT} C_0 (e^{(k_0 t)} - 1)}$$

Perhaps superfluous to note, this is mathematically equivalent to

$$\Delta A(t) = \frac{C_0 e^{-(k_0 t)}}{1 + C_0 (k_{TT}/k_0)(1 - e^{(k_0 t)})}$$

as well as

$$\Delta A(t) = \frac{C_0 k_0}{e^{(k_0 t)}(C_0 k_{TT} + k_0) - C_0 k_{TT}}$$

as used by others.[28, 29]

The concentration of the triplet excited state at time zero (C_0) was estimated by using the absorbance of the sample, the starting concentration, the excited volume (and depth) as well as the number of photons per pulse and was estimated to be 3.26×10^{-6} M. Based on the molar absorption coefficient of the triplet state of **TPP** at 790 nm of 6000 $M^{-1}cm^{-1}$, a concentration of triplet excited state at time zero (C_0) of 8.3×10^{-6} M was estimated. It has to be noted that the exact outcome of the fitting procedure is rather sensitive to the C_0 value, but within reasonable limits of the C_0 value (between 10% and an absolute maximum of 100% of the ground state concentration, 3.26×10^{-5} M). The variation of the outcome (of k_{TT}) is then a factor of ten.

Interestingly, and quite surprisingly, it has been reported that THF can react with singlet oxygen to form **THF-singlet oxygen adducts**.[29] Therefore, it is possible that the THF solvent slightly affects the triplet lifetime obtained. However, the reaction conditions reported in the paper by Sagadevan *et al*. show that these adducts are unlikely to form in our TA measurements. In particular, this paper reported reaction conditions of 2 hours irradiation with a blue LED light source (460 nm, 40 mW/cm^2). Our experiments were only 40 minutes in

length with a pulsed laser (517 nm, 9 mW), which is too short for **THF-singlet oxygen adduct** formation.

The singlet excited state of **THOPP** decays mono-exponentially in THF (Figure **3.9**). This S_1 lifetime is 9.33 ns and is almost 6 times longer than the Zn(II) derivative of this compound (1.51 ns in THF).[15] However, the freebase of **THOPP** has a slightly shorter S_1 lifetime than **TPP** in DMF (10.6 ns).[22] The reduced S_1 lifetime is due to the increased rate of ISC associated with the Zn(II) in the macrocycle. Thus, the competitive relationship between fluorescence to the ground state and intersystem crossing to the triplet state, from the singlet excited state, is evident here.

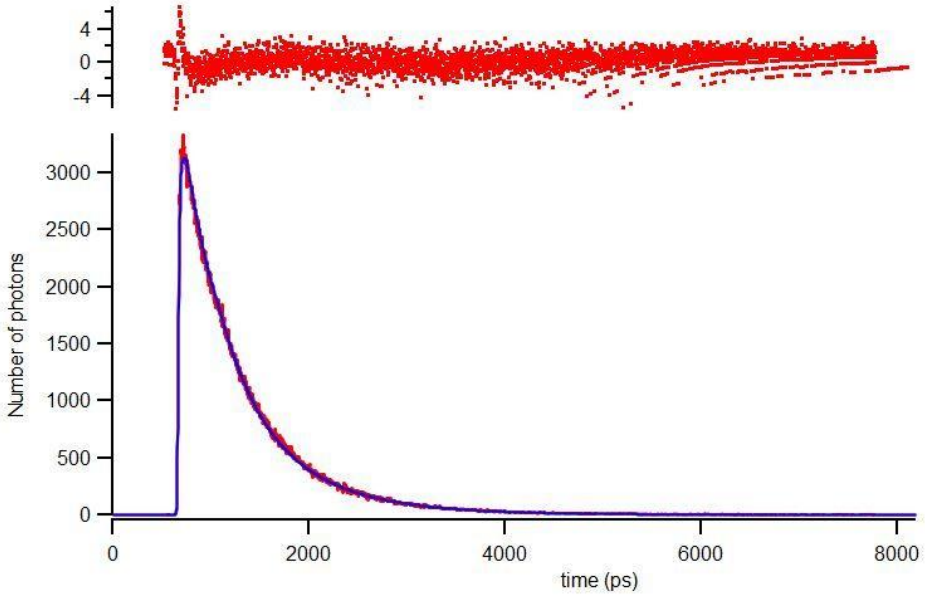

Figure 3.9. *Time-correlated single photon counting (TC-SPC) spectrum of* ***THOPP*** *in THF. Excitation wavelength = 560 nm. Emission wavelength = 650 nm. The absorbance was 0.05 at the excitation wavelength. Laser power is 0.44 mW and at this power,* ***THOPP*** *decayed mono-exponentially, the S_1 lifetime is 9.33 ns. On the top, weighted residuals are presented.*

.

3.2.2.2. Solid film properties

THOPP in THF (10 mg mL^{-1}) was spin coated to make a thin film on quartz glass. The UV-Vis spectrum was recorded (Figure **3.10**) and the data is summarized in Table **3.3**.

Film UV-Vis spectra

Some differences were observed between the UV-Vis spectra of **THOPP** in solution and in the film. The major difference observed in the thin film spectrum (Figure **3.10**) is a large 19 nm shift of the Soret band in the thin film to the near-IR regions (Table **3.3**). Other small deviations are seen in the positions of the Q-bands with the largest difference observed in the Q_{II} band (hypsochromic shift of 5 nm). In terms of band characteristics, the Q-bands of **THOPP** in the film are approximately the same width as in solution (approximately 40 nm for Q_{IV}). Furthermore, there is a higher Q_{III} to Soret band ratio in the film compared to solution (Q_{III} / Soret = 0.12 vs 0.02).

Compared to the **Zn(II)THOPP** in a thin film,[15] there are four Q-bands in the free base porphyrin film due to the absence of a metal in the core (2 Q-bands), which is known to occur because of symmetry.[30] The Soret band in the Zn(II) species is slightly blue-shifted (438 nm) compared to the free-base counterparts (440 nm), with the Q-bands of the Zn(II) species appear at 560 nm and 602 nm.[15]

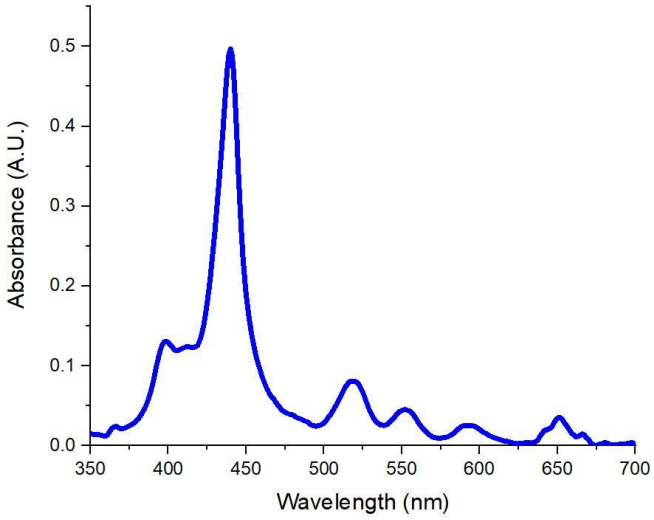

Figure 3.10. *UV-Vis spectrum of* ***THOPP*** *thin film spin coated onto quartz glass.*

Table 3.3. *UV-Vis absorption data of* ***THOPP*** *in a thin film obtained via spin coating.*

PS	Soret band (λ/nm)	Sh [a] (λ/nm)	Q-bands (λ/nm)				Q_y / Soret [b]
			Q_{IV} [c]	Q_{III} [d]	Q_{II} [e]	Q_I [f]	
THOPP	440	400	519	551	591	651	0.12

[a] Sh = shoulder that appears beside Soret band; [b] ratio of the intensities of the $Q_y(0,0)$ and Soret band of the porphyrin in the film; [c] Q_{IV} = $Q_y(1,0)$ peak; [d] Q_{III} = $Q_y(0,0)$ peak; [e] Q_{II} = $Q_x(1,0)$ peak; [f] Q_I = $Q_x(0,0)$ peak.

The excitation wavelength used for the emission spectrum of the **THOPP** thin film is 440 nm and the porphyrin emission is visible in the 600–800 nm region approximately (as seen in figure **3.11**). Interestingly, there is a sharp emission peak that arises at 741 nm which does not appear in solution. This peak most likely appears due to the presence of J-aggregates in the film.[31, 32, 33] The presence of aromatic groups at the *meso* positions in porphyrins has been reported to cause the formation of J-aggregates.[34, 35] The peak, at 741 nm, can be removed by making thin films *via* vapour-phase deposition (see Figure **3.15**). It is generally more intense than the Em2 peak. There is almost no Stokes shift in the film compared to the solution and this differs in the Zn(II) species,[27] where there is the presence of a meaningful Stokes shift. In a **THOPP** solution, there is a presence of a monomeric form in the emission spectrum. Whereas this "aggregation" peak in the emission spectrum of the **THOPP** film, suggests that the porphyrin forms J-aggregates in the film.

Table 3.4 *Photophysical properties of* ***THOPP*** *thin films obtained by spin coating (SC) and vapour-phase deposition (VP).*

PS	Em1 [a]	Em2 [a]	Em3 [b]	SS (cm^{-1}) [c]	S_1 lifetime (ns) [d]			
					Full power [e]		Half power [e]	
					τ1 (Amp) [f]	τ2 (Amp) [f]	τ1 (Amp) [f]	τ2 (Amp) [f]
THOPP SC	651	719	741	0	0.745 (0.51)	0.239 (0.49)	0.749 (0.42)	0.368 (0.58)
THOPP VP	648	714	- [g]	0	- [h]	- [h]	- [h]	- [h]

[a] According to the emission spectra, Em1 = first emission peak [λ_{em} $Q_x(0,0)$] and Em2 = second emission peak [λ_{em} $Q_x(0,1)$], Excitation wavelength = 440 nm and emission was measured in nm; [b] Em3 = peak that appears at 741 nm that is due to the formation of a J-aggregate in the film; [c] SS = The Stokes shift was calculated from the corresponding UV-Vis and emission spectra; [d] The film of ***THOPP*** *undergoes a bi-exponential decay at both full and half power, due to singlet-singlet annihilation, see Figure* ***3.12****; [e] The laser power was changed from full power to half power and it was measured as 0.44 mW and 0.22 mW, respectively; [f] Amp. = amplitude associated with values for bi-exponential fitting. [g] No J-aggregate in THOPP film achieved by vapour-phase deposition (VP); [h] No data available.*

Emission spectra of films

Figure **3.11** shows the emission spectrum of **THOPP** on a quartz film that was obtained *via* spin coating. The emission is similar to that observed in solution, however there is a large peak at 741 nm that is due to the formation of J-aggregates in the thin film (see below).

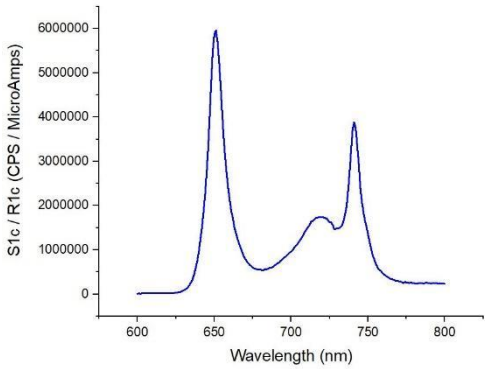

Figure 3.11. *Emission spectrum of spin coated* ***THOPP*** *thin film on quartz glass. Excitation wavelength= 440 nm.*

Porphyrin aggregation: J-band emission

The sharp features of the new emission band (at 741 nm) in the films are reminiscent of J-band emission.[34] In fact, a very similar emission band has been attributed to such phenomenon before for TPPS type molecules,[35, 36] as well as other porphyrins[37, 38, 39] and ZnTPP.[40]

Fluorescence lifetime determination using time-correlated single photon counting (TC-SPC)

Figure **3.12** shows the fits of the S_1 decay kinetics of **THOPP** in THF, and in a thin film at full laser power and half laser power (0.44 mW and 0.22 mW, respectively). The S_1 decay spectra in solution is shown above (Figure **3.9**) and that of the film at both full and half power are in the SI (Figures **S3.10** and **S3.11**).

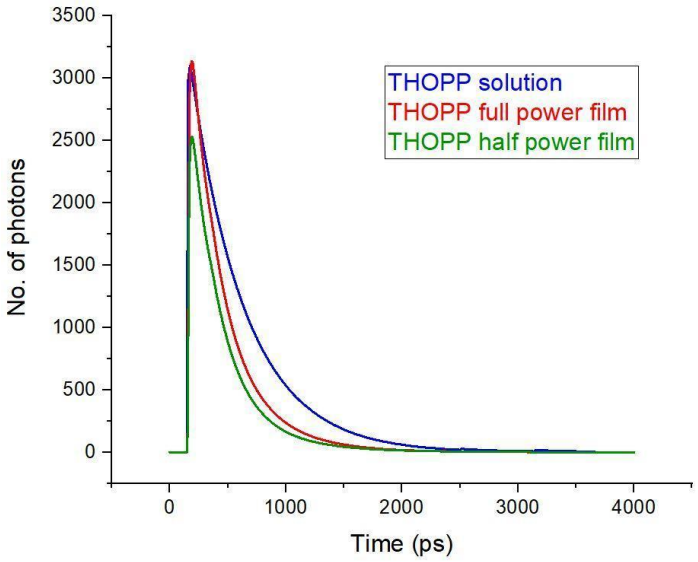

Figure 3.12. *Time-correlated single photon counting (TC-SPC) fitted spectrum of* ***THOPP*** *in THF solution (blue) and a thin film, at a full laser power (red) and half laser power (green). Excitation wavelength = 560 nm. Emission wavelength = 650 nm. The absorbance was 0.05 at the excitation wavelength for all species. Full power includes the laser power being at 0.44 mW while at half power, the laser power is 0.22 mW.*

THOPP in solution has a much longer S_1 lifetime than in the film, as clearly shown above as it decays slower than that of the film (Figure **3.12**). Within the film, the laser power does not appear to have much effect on the lifetime (Table **3.4**). Intuitively, the τ_2 is longer in the half-power (approx. 0.1 ns longer) as the weaker laser power causes depopulation of the S_1 state at a slower rate. In the thin film, the singlet decays *via* bi-exponential decay kinetics in both laser power conditions applied (100% and 50%). The lifetime of **THOPP** at full laser power (0.44 mW) in the film is 0.745 ns. Reducing the laser power to half power (0.22 mW) yields a S_1 lifetime of 0.749 ns. The second lifetime obtained from the bi-exponential fitting is likely due to singlet-singlet annihilation. To our knowledge, this is the first reported fluorescence lifetime of this porphyrin in a solid thin film.

Porphyrin film: Singlet oxygen detection

In order to measure the singlet oxygen production of **THOPP** in a solid film, a solvent or medium is needed to detect the singlet oxygen generated. The main reason for this is that the emission intensity of singlet oxygen depends on its steady state concentration present in a particular solvent.[41] In the above spectra and discussion (Figures **3.10**–**3.12**), the UV-Vis and emission spectra are conducted in air. Attempts were conducted to measure singlet oxygen

emission in air using these films (obtained *via* spin coating), however there was no signal detected. Moreover, even though the singlet oxygen lifetime is sufficiently long in organic solvents,[42] it was found that the porphyrin thin films obtained by spin coating dissolves in organic solvents. Thus, an aqueous solvent, a reliable method to detect singlet oxygen, and films that are stable in aqueous media, were needed.

A water-soluble singlet oxygen probe called AquaSpark, that has an emission maximum at 515 nm, is an ideal candidate (see mechanism of emission in figure **3.13**).[43]

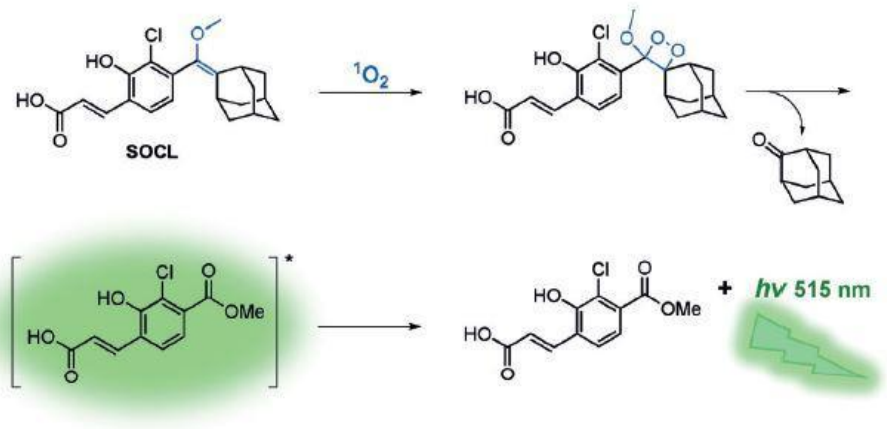

Figure 3.13. *Mechanism of AquaSpark probe (**SOCL**) reacting with singlet oxygen to give emission at 515 nm.*[43]

This probe has been shown to be selective towards singlet oxygen compared to other reactive oxygen species.[43] New films, that are stable in aqueous media, were made using a modified vapour-phase deposition technique (see experimental section: solid thin films for protocol) and its photophysical properties were determined. The UV-Vis spectrum of this new film is shown below (Figure **3**.**14**) and the data is summarized in Table **3**.**5**.

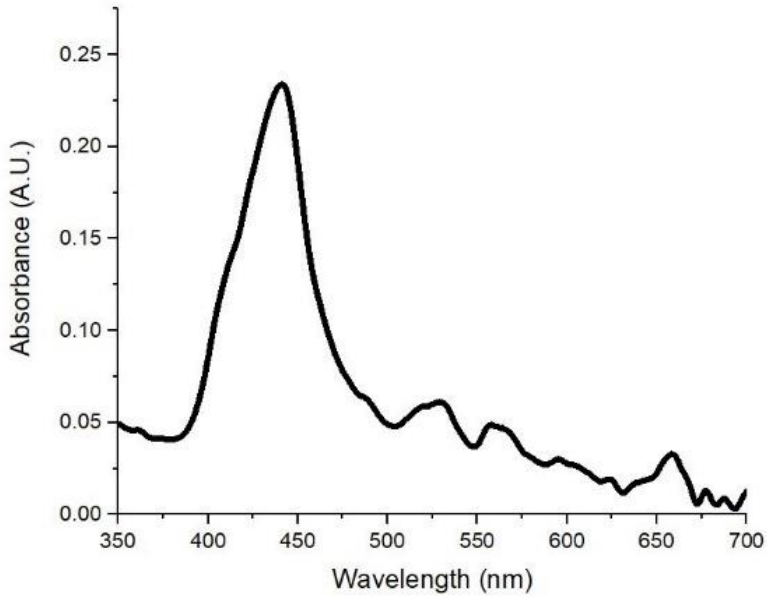

Figure 3.14. *UV-Vis spectrum of* ***THOPP*** *thin film on quartz glass made by vapour-phase deposition.*

Table 3.5. *UV-Vis absorption data of* ***THOPP*** *in a thin film obtained via vapour-phase deposition.*

PS	Soret band (λ/nm)	Q-bands (λ/nm)				Q_y / Soret [a]
		Q_{IV} [b]	Q_{III} [c]	Q_{II} [d]	Q_I [e]	
THOPP	440	528	556	601	661	0.15

[a] *Ratio of the intensity of the $Q_y(0,0)$ band compared to the Soret band;* [b] $Q_{IV} = Q_y(1,0)$ *peak;* [c] $Q_{III} = Q_y(0,0)$ *peak;* [d] $Q_{II} = Q_x(1,0)$ *peak;* [e] $Q_I = Q_x(0,0)$ *peak.*

From the UV-Vis spectrum of the thin film made by vapour-phase deposition, there is a profile similar to that observed in solution and in the films made by spin coating (see figures **3.3** and **3.10**). The spectrum has the characteristics of a porphyrin: a large Soret band and four small Q-bands. The Q-bands are visible and compared to the spin coated thin film, the Soret band is less intense compared to the Q-bands and all of the peaks appear to be red-shifted by at least 5 nm. This newly formed film was excited with 418 nm light and an emission spectrum was recorded (see figure **3.15**). Compared to the films made by spin coating, there is no J-band observed in these films (peak at 741 nm). Clearly, J-aggregates are formed during the spin coating process, but not *via* the vapour-phase deposition technique.

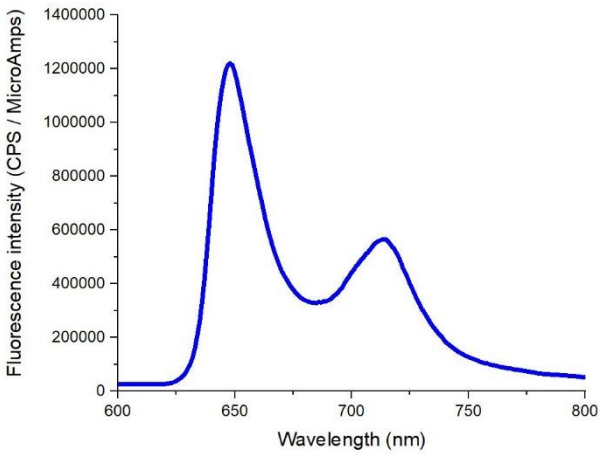

Figure 3.15. *Emission spectrum of a* ***THOPP*** *thin film on quartz glass made by vapour-phase deposition. Excitation wavelength = 418 nm.*

Table 3.6. *Emission data of a* ***THOPP*** *thin film obtained via vapour-phase deposition.*

PS	Em1 [a]	Em2 [a]
THOPP	648	714

[a] *According to the emission spectra, Em1 = first emission peak [λ_{em} $Q_x(0,0)$] and Em2 = second emission peak [λ_{em} $Q_x(0,1)$], Excitation wavelength = 418 nm.*

The **THOPP** thin film was placed in a large cuvette containing the AquaSpark solution and an emission spectrum was obtained (see figure **3.16**).

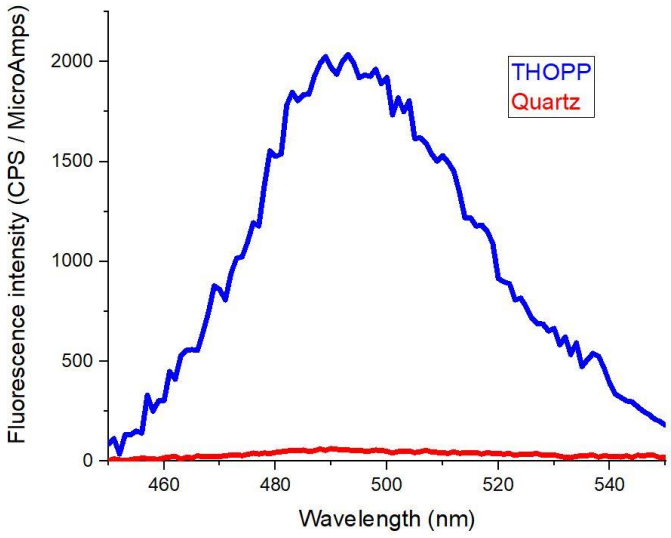

Figure 3.16. *Singlet oxygen detection via AquaSpark probe after exciting the* ***THOPP*** *PS in a thin film. The reference is a quartz plate in AquaSpark probe solution. Excitation wavelength = 650 nm.*

This showed that the **THOPP** photosensitizer (PS), even in a thin film, is capable of producing singlet oxygen. The only difference between the **THOPP** thin film and the quartz plate was the presence of the PS. The excitation wavelength used was 650 nm. This was chosen as the production of singlet oxygen *via* near IR light is highly sought after for photo medical applications. The near IR light can penetrate deep into the human tissue to activate the PS in the thin film that can be present on an implant and produce $^1O_2$ for antimicrobial effects.

3.3. Conclusion

THOPP was synthesized, and its photophysical properties were determined in solution, using **TPP** as a reference. While **THOPP** produces a slightly smaller amount of singlet oxygen compared to **TPP** (0.44 and 0.55 in $CHCl_3$, respectively), a novel approach to apply **THOPP** as a photosensitizer is to include it in a thin film. Due to its long alkyl tails, the film formation is improved. The fluorescence emission and lifetimes in the film are a lot shorter than in solution and the reported fluorescence lifetime of **THOPP** in a film, as well as its singlet oxygen emission, are reported herein. The future potential impact of this is that the water-resistant **THOPP** thin film can be activated using near IR light. The near IR light can penetrate deep within human tissue to produce singlet oxygen that can kill cancer or bacteria in the body. This can be envisaged as a novel way to clean an implant: **THOPP** can produce the singlet oxygen that would kill the bacteria that are accumulating at the implant.

3.4. Experimental

The synthesis was carried out in the laboratories of Porphychem, Dijon, France.

3.4.1. Synthesis[15]

4-Hexyloxybenzaldehyde (5.00 mL, 4.96 g, 24.04 mmol, 1.00 eq.), 2.6 ml freshly distilled pyrrole (2.60 mL, 2.51 g, 37.48 mmol, 1.56 eq.) and 1 mL acetic anhydride was dissolved in 100 mL propionic acid. The reaction mixture was stirred under reflux conditions at 130°C for 4 hours. The reaction mixture was cooled slowly to room temperature. The reaction mixture was then filtered and the filtrate was washed with methanol. The crude product was then recrystallized using a 1:1 $CHCl_3$:MeOH mixture and the product was filtered. The product was washed with methanol and allowed to dry overnight to obtain a crystalline purple solid (**1.17 g**, **12% yield**). ^{1}H NMR (500 MHz, $CDCl_3$): δ -2.73 (s, 2 H, 2 x NH), 1.00 (t, 12 H, 4 x CH_3),

1.48 (m, 16 H, 8 x CH_2), 1.64 (m. 8 H, 4 x CH_2), 1.97 (m, 8 H, 4 x CH_2), 4.23 (t, 8 H, 4 x CH_2), 7.29 (d, 8 H, 8 x Ar-H), 8.11 (d, 8 H, 8 x Ar-H), 8.85 (s, 8 H, 8 x Ar-H) ppm. ^{13}C NMR (600 MHz, $CDCl_3$): δ13.14, 22.72, 25.94, 29.50, 31.75, 68.35, 112.71, 119.82, 134.48, 135.61, 158.98 ppm. UV-Vis (THF) λ_{max} (log ε) (ε, mM^{-1} cm^{-1}): 421 (438.5), 518 (13.4), 552 (9.3), 597 (1.4), 652 (13.6). HRMS (MALDI): Calcd for $C_{82}H_{75}N_6NaO_7S_2$: *m/z* 1342.3713 ($[M]^+$). Found: *m/z* 1015.518 ($[M]^+$).

3.4.2. Photophysical characterization in solution

Materials and techniques

The photophysical characterization was conducted in $CHCl_3$ and THF (spectroscopy grade, supplier = Merck).

Absorption and photoluminescence spectra

Both UV-Vis absorption spectra and fluorescence emission spectra were recorded at 21°C. UV-Vis absorption spectra were measured in quartz cuvettes (1 cm path-length, Hellma) using a HP/Agilent 8453 UV-Vis and Shimadzu UV2700 spectrophotometer. Fluorescence emission spectra were recorded on a SPEX Fluorolog 3 fluorometer. In this fluorometer, double grating monochromators are used in the excitation and emission channels. A Xenon arc lamp (450 W, Osram) is the excitation light source, and a Peltier cooled photomultiplier tube (R636-10, Hamamatsu) is the detector. The fluorescence signal from the fluorophores in solution is collected in a right-angle geometry, and the fluorescence spectra are corrected for fluctuations of the excitation source flux and for the wavelength dependence of the detection sensitivity. The absorbance for photoluminescence spectra was approximately 0.1 for solution.

Fluorescence and Singlet Oxygen Quantum yields

Both quantum yields were determined using the SPEX fluorolog 3 fluorometer relative to a fluorescent/singlet oxygen standard of a known quantum yield. From here, the integrated emission spectra of the unknown sample are compared with that of the standard under the same absorbance conditions (absorbance = 0.1) at the same excitation wavelength. The integrated emission spectra are corrected for the skewed baselines where appropriate.

For these measurements, dilute solutions with absorbances of approximately 0.1 at one of the Q-bands in the absorption spectrum were used. Absorption and emission spectra (both fluorescence and singlet oxygen) were measured using 3.0 ml of the sample and standard solutions in 1 x 1 cm optical path length quartz cells. The quantum yields were calculated using the equation **3.1** [44] below:

$$Q_x = Q_r[A_r(\lambda_r)/A_x(\lambda_x)][I(\lambda_r)/I(\lambda_x)][(n_x)^2/(n_r)^2](D_x/D_r) \quad \textbf{(Equation 3.1)}$$

Where Q_x = the desired quantum yield (fluorescence or singlet oxygen) of the unknown sample; Q_r = the (fluorescence of singlet oxygen) quantum yield of the known sample according to literature; $A_r(\lambda_r)$ = absorbance of the reference at the excitation wavelength; $A_x(\lambda_x)$ = absorbance of the unknown sample at the excitation wavelength; $I(\lambda_r)$ = relative intensity of the exciting light of a known reference at wavelength λ; $I(\lambda_x)$ = relative intensity of the exciting light of an unknown sample at wavelength λ; n_x = refractive index of the solvent that the unknown sample is dissolved in; n_r = refractive index of the solvent that the known sample is dissolved in; D_x = integrated area under the corrected emission spectrum of the unknown sample; D_r = integrated area under the corrected emission spectrum of the known sample. In both cases, the integrated area was corrected for the skewed baseline (if present), thereby lowering the area under the emission curve. The data was analyzed using the Origin program and excel.[45] **Note:** For singlet oxygen measurements, the unknown and reference sample must be in the same solvent.

Nanosecond transient absorption spectra

Triplet state lifetimes were determined by means of nanosecond time-resolved absorption spectroscopy using an EKSPLA NT342B laser system in which the third harmonic of a Nd:YAG laser system (355 nm) was used to pump an OPO (to give λ_{ex} = 517 nm, pulse width which has an adjustable gate width of minimal 2.9 ns and laser power range of 1–3 mJ per pulse). This setup is described in full detail in the literature.[46] The data was analyzed using Igor 7 Pro (Wavemetrics, Lake Oswego, OR, USA).[47] The absorbances of the solutions used were approximately 0.5. For the oxygen-free solution, the solution was bubbled with argon for 1–2 hours prior to laser excitation *via* this setup.

Time correlated single photon counting spectra

Time-resolved emission measurements were performed on a picosecond single photon counting setup. The excitation wavelength (560 nm) is generated by the output of a fully automatic tunable Ti:sapphire laser (Chameleon Ultra, Coherent). This source produces a sub-picosecond excitation pulse, (full-width half-maximum, FWHM). The repetition rate is decreased from the fundamental 80 MHz to a lower value (usually 8 MHz) using a pulse picker (Pulse Select, APE). After second harmonic generation (SHG), a dichroic mirror is used to separate the doubled light which is directed to the sample. Fundamental light is guided *via* a delay line to a fast photodiode (PD) and used as a reference pulse. The emission is collected at a 'magic angle' (54.7^o) and focused onto a multichannel plate photomultiplier tube (MCP-PMT, R3809U-50, Hamamatsu) through a single-grating monochromator (Newport Cornerstone 260, f=250mm, grating 300ln/mm blaze 422 or grating 300ln/m blaze 750nmM20, Carl Zeiss, 600 lines/mm). Although the excitation source produces sub-picosecond pulses, the electronics and the detector cause a broadening of the signal and are the limiting factor of the time resolution. The overall instrument response function (IRF) was 20 ps (FWHM) for the

solution of the measured compound, which is measured from a dilute scattering solution (Ludox) at the excitation wavelength.

3.4.3. Solid thin films

Precleaning

Three square quartz glass slides (see provider and description below) were washed with a brush, soap and water in a beaker. The slides were then placed into a Teflon substrate holder using forceps. The glass slides in the substrate holder were submerged in deionized water before sonication for 15 minutes. The water was then replaced by acetone and the beaker was further sonicated for 15 minutes. The acetone was replaced by isopropanol and further sonicated for 15 minutes. The glass slides were allowed to dry. Compressed air was used to accelerate the drying process. The glass slides were then placed back into the substrate holder and were placed inside a UV-ozone photoreactor for 30 minutes.

Provider and description of thin films

Provider: Präzisions Glas & Optik GmbH;

Description: 2.5 x 2.5 cm^2 quartz glass substrates with a thickness of 1.1 mm - CNC precision-cut, no bevel.

Spin coating procedure for thin film formation

Three quartz glass slides were cleaned with the precleaning technique as described above. Almost immediately after being removed from the UV-ozone photoreactor, the slides were then mounted on the spin coating machine, (Delta 10, Ble Laboratory Equipment GmbH). The vacuum was switched on to approximately 0.6 bar. The spin speed, spinning time and acceleration settings were set. 10 mg/ml **THOPP** samples were prepared, sonicated and filtered into a sample vial. They would then be drawn into a syringe (0.3 ml) per slide. They would then be spun to form films.

Vapour-phase deposition procedure for thin film formation

Three glass slides were cleaned with the precleaning technique as described above. Almost immediately after being removed from the UV-ozone photoreactor, 10 mg of the **THOPP** porphyrin was then placed at the bottom of a 100 ml two-neck round bottom flask. A slide was then carefully placed to be over the porphyrin solid. The flask was carefully attached to a Schlenk line and the pressure of the system inside the flask was reduced to 10^{-4} mbar. The solid was then heated slowly from 250^{o}C to 400^{o}C using a heat gun or until the solid had been vaporized and formed a layer on the slide. The slide was then allowed to cool to room temperature to create a water stable thin film.

Absorption and photoluminescence spectra of thin films

Both UV-Vis absorption spectra and fluorescence emission spectra were recorded at 21^{o}C and on a thin film support. The instruments were then used as described in section **3.4.2**.

Time correlated single photon counting of a thin film

The time-resolved emission measurements were performed as described above in section **3.4.2**. The differences were that the film was placed on a thin film support and the overall instrument response function (IRF) was 8 ps (FWHM) for the thin film.

AquaSpark™ 515 Singlet Oxygen Probe

This singlet oxygen probe was supplied by Carbosynth and a 50 ml 2 μM AquaSpark PBS solution was made. For measuring singlet oxygen, the excitation wavelength used was 650 nm and emission was observed from 450 nm to 550 nm, using the same settings as the fluorescence emission spectra. The film was placed into a large cuvette (20 ml capacity) and the THOPP film was excited in the presence of the AquaSpark probe. A quartz slide was used as a reference.

3.5. Supplementary Information

3.5.1. Synthesis and characterization

The porphyrin, 5,10,15,20-tetra-(4-hexyloxyphenyl)porphyrin (**THOPP**), was synthesized according to the protocol described in 3.4.1.[15]

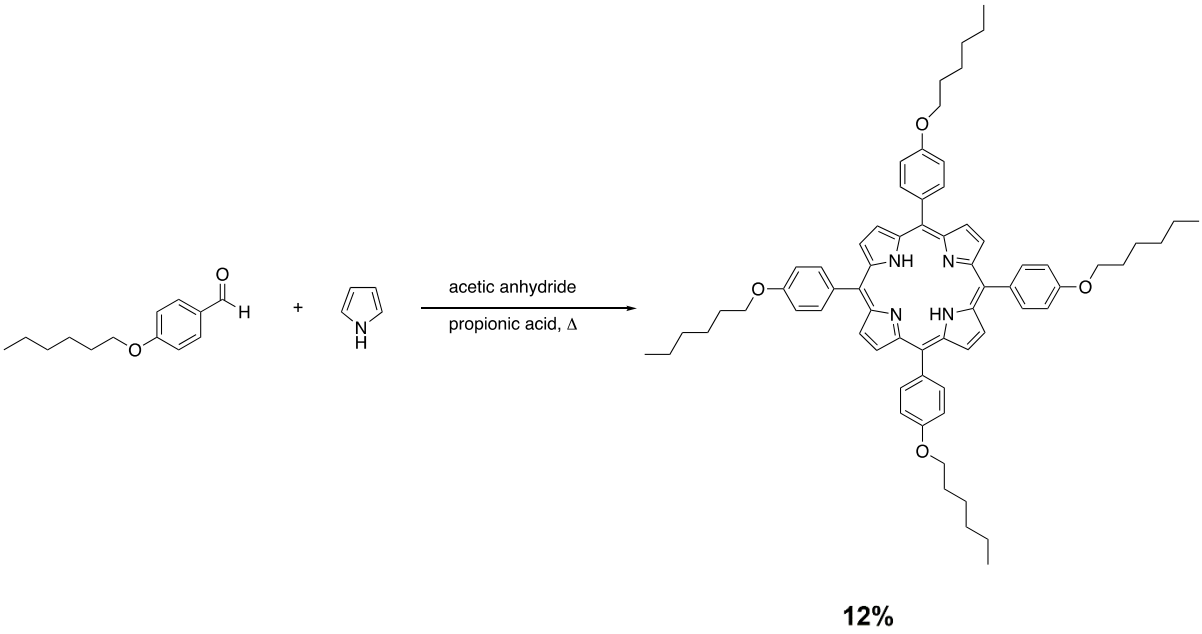

Figure S3.1. *Reaction scheme of 5,10,15,20-tetra-(4-hexyloxyphenyl)porphyrin (**THOPP**).*[15]

Synthesis of THOPP and characterization

The synthesis of this A_4 *meso*-substituted porphyrin was in a slightly lower yield, compared to literature.[15] This can be explained by the large increase in scale of the reaction and **THOPP** was fully characterized using ^{1}H and ^{13}C NMR, Mass spectroscopy, UV-Vis Spectroscopy and HPLC (Figures **S3.2**–**S3.6)**. The ^{1}H NMR spectrum (Figure **S3.1**) is pure according to literature.[15] The only difference is at the peak 1.64 ppm, there are 12 protons instead of 8 and this is likely due to the water in the humid atmosphere. There is another small peak at around 2.2 ppm. The ^{13}C spectrum (Figure **S3.3**) is out of phase and cannot be fully corrected however it is not that significant. There are two carbons missing from the spectrum: the alpha- and beta-carbon in the pyrrole moieties of the porphyrin macrocycle. This has also been reported in the literuature.[15] The β carbons have been reported for this compound, however though the peak is very broad and has a low intensity.

The MALDI TOF mass spectrum of **THOPP** (Figure **S3.4**) shows two peaks at: 1015 ($M+H^+$) and 226 (HABA matrix). In figure **S3.5**, the $M+H^+$ peak is the most intense and it has been previously reported that mass peaks of M+6 occur in porphyrins.[48]

The HPLC analysis shows that there are no impurities in the product. There were no other peaks present apart from that shown in Figure **S3.6**. The product was dissolved in $CHCl_3$ and injected into the HPLC normal phase column (stationary phase = SiO_2 and mobile phase = $CHCl_3$) to determine purity. The elution time of the product was 2.94 minutes. There were no products or impurities that eluted off during HPLC indicating the product is 99.9% pure.

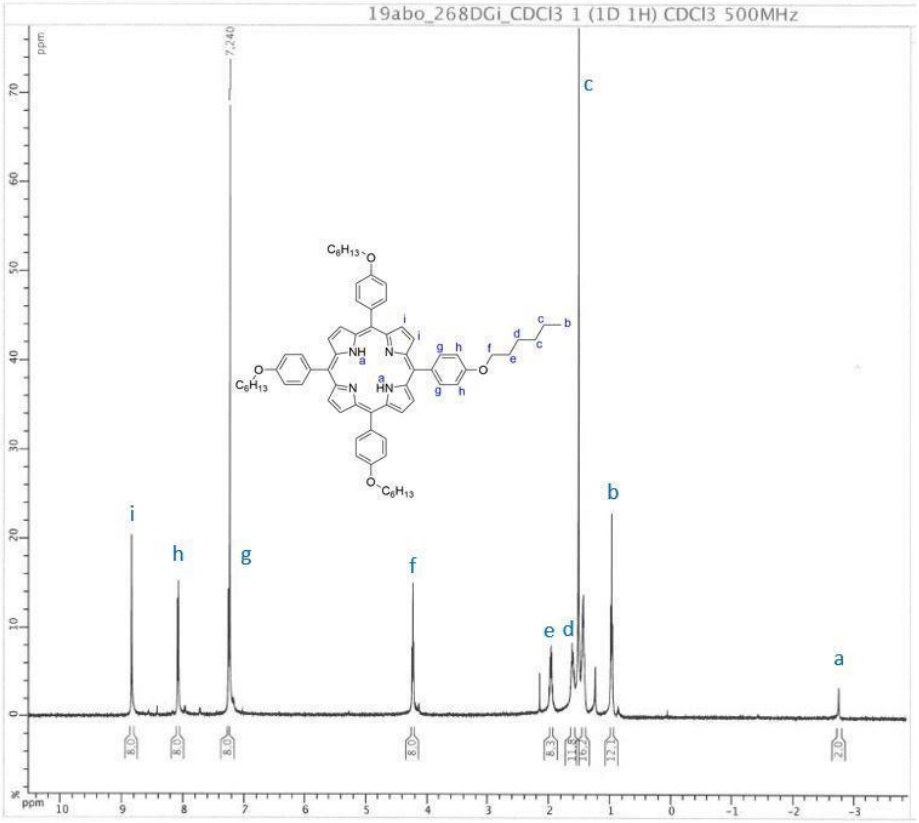

Figure S3.2. *Fully integrated ^1H NMR spectrum of* ***THOPP****, dissolved in deuterated chloroform ($CDCl_3$), with the structure and the labels for the protons in the structure.*

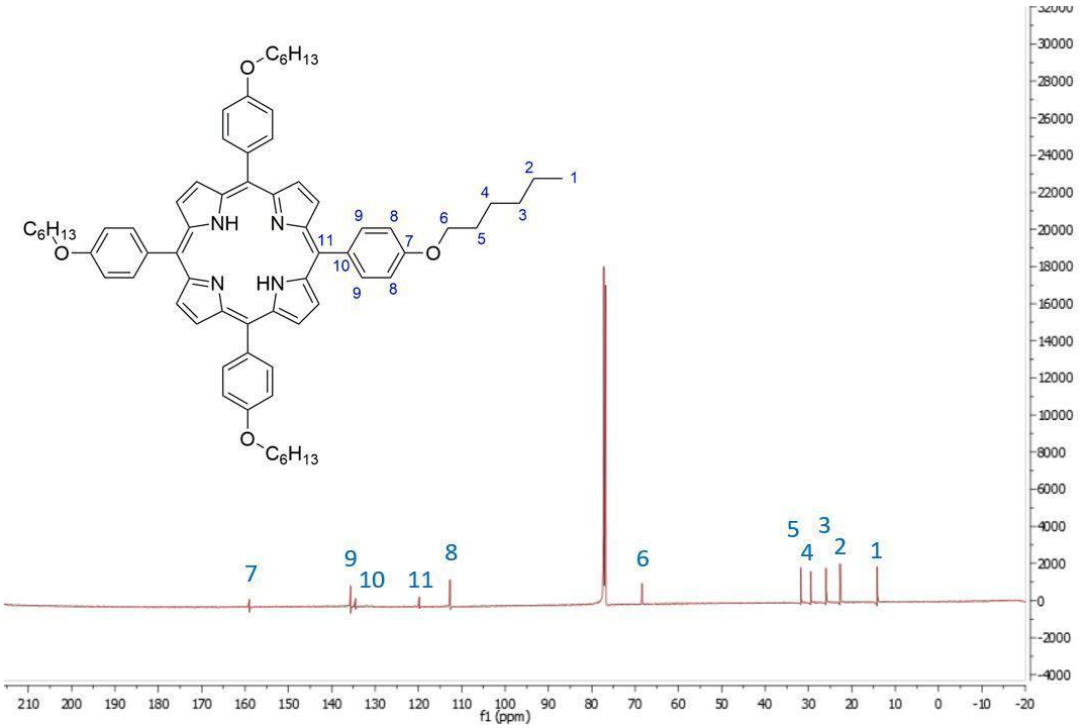

Figure S3.3. *^{13}C NMR spectrum of **THOPP**, dissolved in deuterated chloroform ($CDCl_3$), with the structure and the labels for the carbons in the structure.*

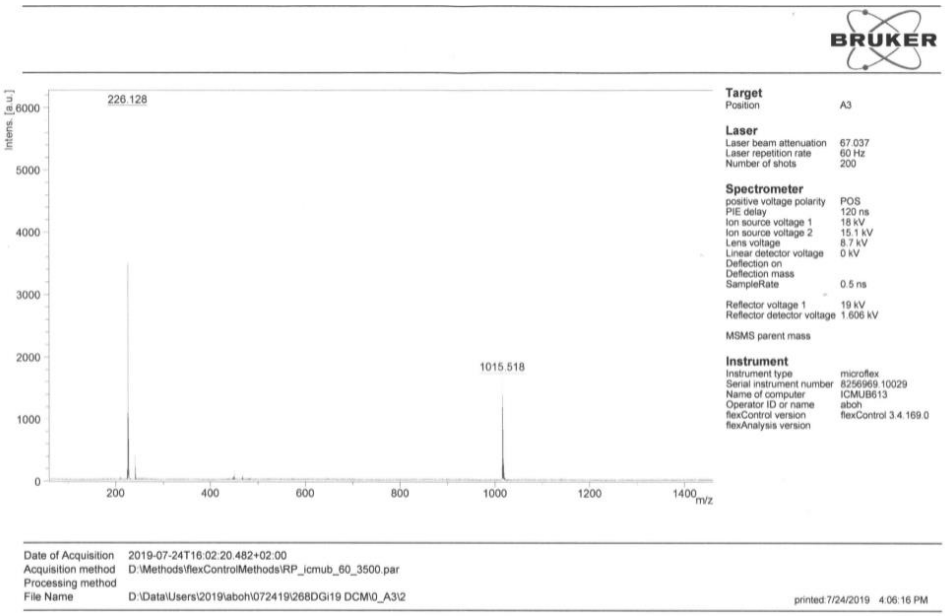

Figure S3.4. *Mass spectrum of **THOPP** using MALDI-TOF dissolved in dichloromethane (CH_2Cl_2).*

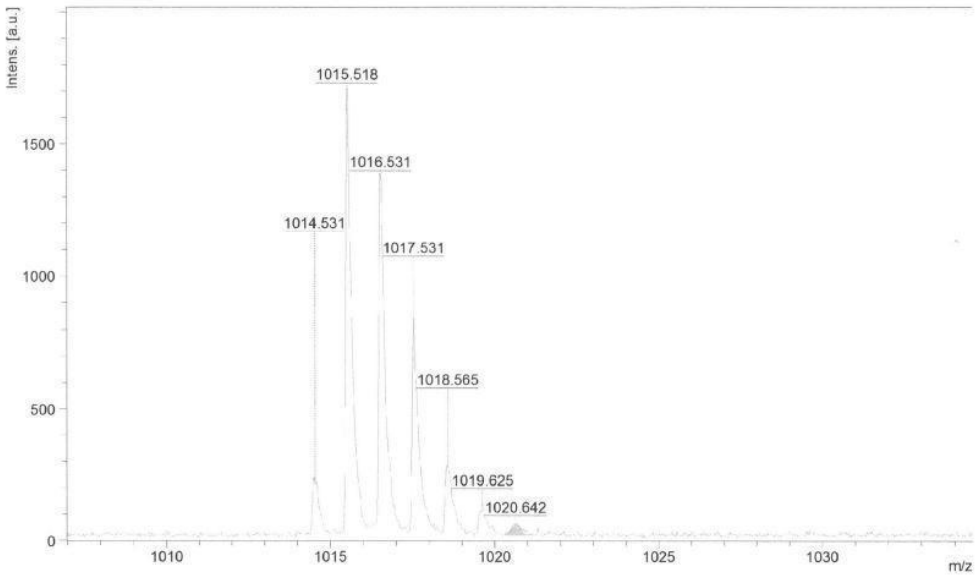

Figure S3.5. *Mass spectrum zoom, using MALDI-TOF displaying the isotope pattern of* ***THOPP****, dissolved in dichloromethane (CH_2Cl_2).*

Chromatogram and Result:

Injection Details

Injection Name:	**268DGi19**	*Run Time (min):*	**10.00**
Vial Number:	**GE2**	*Injection Volume:*	**10.00**
Injection Type:	**Unknown**	*Channel:*	**UV_VIS_2**
Calibration Level:		*Wavelength:*	**420**
Instrument Method:	**Standard_CHCl3_modified**	*Bandwidth:*	**4**
Processing Method:	**Standard Processing Method**	*Dilution Factor:*	**1.0000**
Injection Date/Time:	**25/juil./19 16:00**	*Sample Weight:*	**1.0000**

Chromatogram

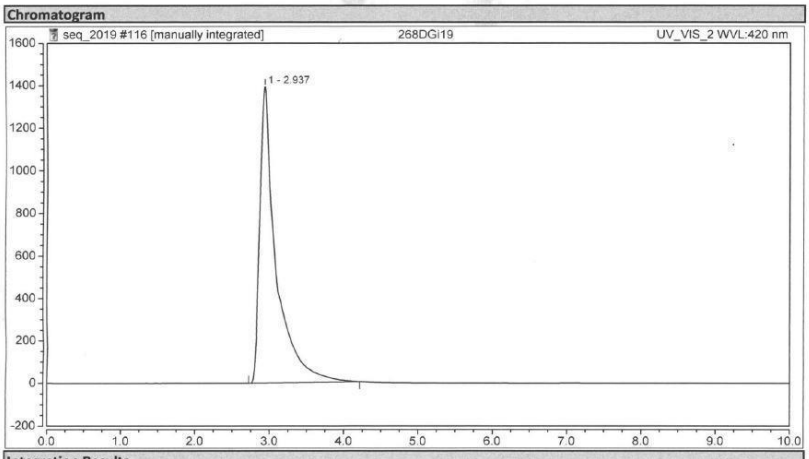

Integration Results

No.	Peak Name	Retention Time min	Area mAU*min	Height mAU	Relative Area %	Relative Height %	Amount n.a.
1		2.937	353.045	1394.164	100.00	100.00	n.a.
Total:			**353.045**	**1394.164**	**100.00**	**100.00**	

Figure S3.6. *HPLC analysis of* ***THOPP*** *using normal stationary phase silica column, dissolved in $CHCl_3$.*

3.5.2. Photophysical characterization

3.5.2.1. Solution

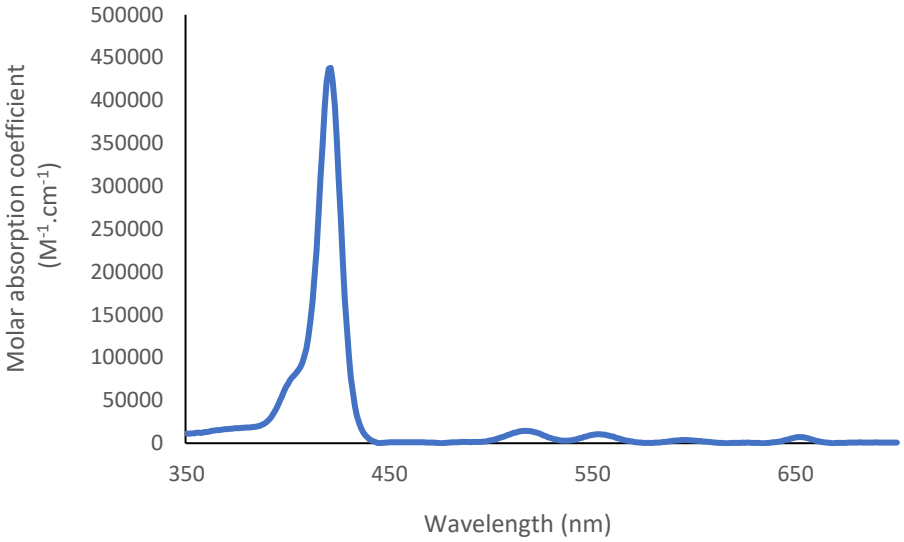

Figure S3.7. *UV-Vis spectrum of* ***THOPP*** *at room temperature, dissolved in THF. The concentration of THOPP in the THF solution was 2.2 µM. The y axis is a molar absorption coefficient scale.*

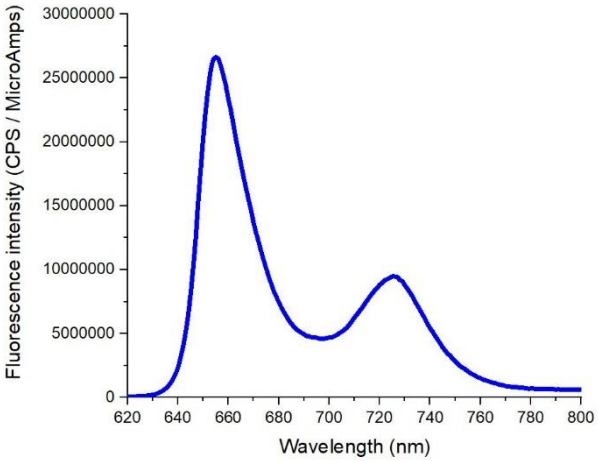

Figure S3.8. *Emission spectrum of* ***THOPP*** *at room temperature in THF, after excitation at 518 nm. The absorbance of the solution at 518 nm was 0.1.*

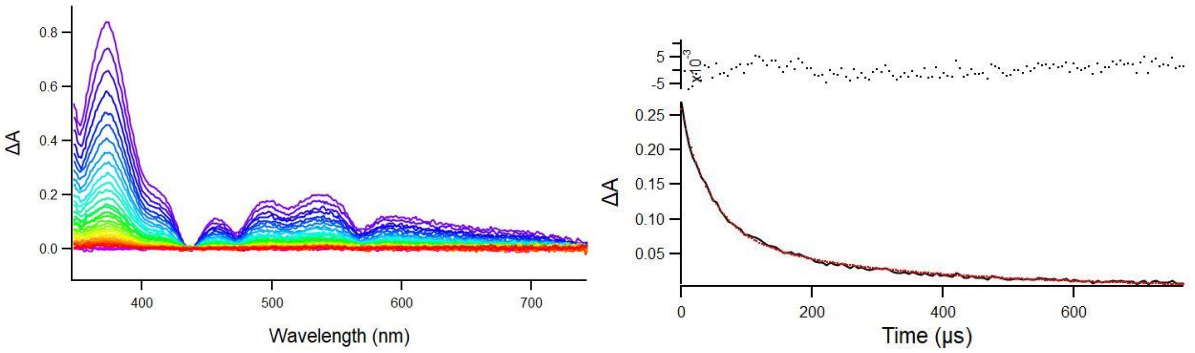

Figure S3.9. *(Left): Nanosecond transient absorption spectrum of* ***THOPP*** *in THF (in oxygen-free solution). Excitation wavelength = 517 nm, incremental time delay = 6 μs. (Right): Decay kinetics trace at 517 nm. The decay curve was decayed bi-exponentially and the obtained triplet lifetime was 297 ± 30 μs. On the top, weighted residuals are presented.*

3.5.2.2. Thin film

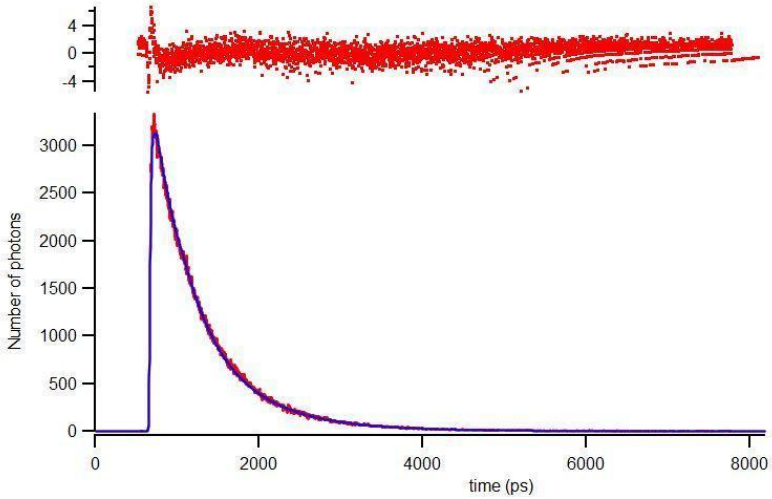

Figure S3.10. *Time-correlated single photon counting spectrum of* ***THOPP*** *in a thin film (at full laser power). Excitation wavelength = 560 nm. Emission wavelength = 650 nm. The absorbance was 0.05 at the excitation wavelength (560 nm). Laser power is 0.44 mW and* ***THOPP*** *decays bi-exponentially in this film at this laser power. The S_1 lifetime in these conditions is 0.745 ns. On the top, weighted residuals are presented.*

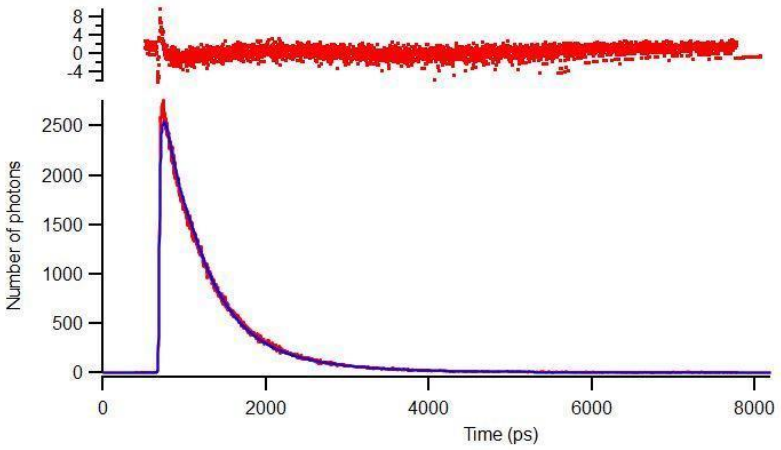

Figure S3.11. *Time-correlated single photon counting spectrum of* ***THOPP*** *in a thin film (at half laser power). Excitation wavelength = 560 nm. Emission wavelength = 650 nm. The absorbance was 0.05 at the excitation wavelength (560 nm). Laser power is 0.22 mW and* ***THOPP*** *decays bi-exponentially in this film at this laser power. The* S_1 *lifetime in these conditions is 0.749 ns. On the top, weighted residuals are presented.*

3.6. References

[1] S. Callaghan and M. O. Senge, The good, the bad and the ugly – controlling singlet oxygen through design of photosensitizers and delivery systems for photodynamic therapy, *Photochem. Photobiol. Sci.*, 2018, **17**, 1490–1514. doi: 10.1039/C8PP00008E
[2] N. R. Finsen, La Photothérapie, Georges Carré et C. Naud, 1899, Paris.

[3] P. Agostinis, K. Berg, K. A. Cengel, T. H. Foster, A. W. Girotti, S. O. Gollnick, S. M. Hahn, M. R. Hamblin, A. Juzeniene, D. Kessel, M. Korbelik, J. Moan, P. Mroz, D. Nowis, J. Piette, B. C. Wilson and J. Golab, Photodynamic Therapy Of Cancer: An Update, *CA Cancer J. Clin.*, 2011, **61**, 250–281. doi: 10.3322/caac.20114.
[4] K. Kalka, H. Merk and H. Mukhtar, Photodynamic therapy in dermatology, *J. Am. Acad. Dermatol*., 2000, **42**, 389–413. doi: 10.1016/s0190-9622(00)90209-3
[5] M. Wainwright, Photoantimicrobials and PACT: what's in an abbreviation?, *Photochem. Photobiol. Sci*., 2019, **18**, 12–14. doi: 10.1039/C8PP00390D
[6] H. Abrahamse and M. R. Hamblin, New photosensitizers for photodynamic therapy, *Biochem. J*., 2016, **473**, 347–364. doi: 10.1042/BJ20150942
[7] J. M. Dąbrowski, B. Pucelik, A. Regiel-Futyra, M. Brindell, O. Mazuryk, A. Kyzioł, G. Stochel, W. Macyk and L. G. Arnaut, Engineering of relevant photodynamic processes through structural modifications of metallotetrapyrrolic photosensitizers, *Coord. Chem. Rev.*, 2016, **325**, 67–101. doi: 10.1016/j.ccr.2016.06.007
[8] F. Cieplik, D. Deng, W. Crielaard, W. Buchalla, E. Hellwig, A. Al-Ahmad and T. Maisch, Antimicrobial Photodynamic Therapy – What We Know and What We Don't, *Crit. Rev. Microbiol.,* 2018, **44**, 571–589. doi: 10.1080/1040841X.2018.1467876.

[9] M. Wainwright, The Problem with Dyes in Infection Control, *Dyes Pigm.*, 2017, **146**, 402–407. doi: 10.1016/j.dyepig.2017.07.042.

[10] H. Gursoy, C. Ozcakir-Tomruk, J. Tanalp and S. Yilmaz, Photodynamic Therapy in Dentistry: A Literature Review, *Clin. Oral Investig.*, 2013, **17**, 1113–1125. doi: 10.1007/s00784-012-0845-7.

[11] V. Ambrosini, M. Issawi, V. Sol and C. Riou, Photodynamic Inactivation of Botrytis Cinerea by an Anionic Porphyrin: An Alternative Pest Management of Grapevine, *Sci. Rep.*, 2020, **10**, 17438. doi: 10.1038/s41598-020-74427-9.

[12] A. W. Utari, B. Purnama and K. Abraha, Utilization of Natural Porphyrin Thin Films as a Photosensitizer for Photodetectors, *Adv. Mater. Res.*, 2014, **896**, 187–191. doi: 10.4028/www.scientific.net/AMR.896.187.

[13] B. Long, O. Bakr and F. Stellacci, Reversible Aggregation of Porphyrins in the Solid State, *J. Exp. Nanosci.*, 2008, **3**, 53–60. doi: 10.1080/17458080802073091.

[14] Y. Shimizu, M. Miya, A. Nagata, K. Ohta, I. Yamamoto and S. Kusabayashi, Mesomorphic phase transitions of tetraphenylporphyrins with four long aliphatic chains, *Liq. Cryst*., 1993, **14**, 795–805. doi: 10.1080/02678299308027756
[15] A. Charisiadis, A. Bagaki, E. Fresta, K. T. Weber, G. Charalambidis, C. Stangel, A. G. Hatzidimitriou, P. A. Angaridis, A. G. Coutsolelos and R. D. Costa, Peripheral Substitution of Tetraphenyl Porphyrins: Fine-Tuning Self-Assembly for Enhanced Electroluminescence, *ChemPlusChem*., 2017, **82**, 1–13. doi: 10.1002/cplu.201700416
[16] W. Zielenkiewicz, G. L. Perlovich, G. E. Nikitina and O. A. Golubchikov, Volumetric Properties of Methyl, tert-Butyl, and Alkoxy Derivatives of Tetraphenylporphyrin in Benzene Solution, *J. Solution Chem.*, 1997, **26**, 633–679. doi: 10.1007/BF02767620
[17] S. Z. Topal, M. Z. Ongu, E. Önal, K. Ertekin and C. Hirel, Hyperporphyrin effect on oxygen sensitivity of free meso-tetraphenylporphyrins, *Dyes Pigm.*, 2017, **144**, 102–109. doi: 10.1016/j.dyepig.2017.05.022

[18] P. Şen, C. Hirel, C. Andraud, C. Aronica, Y. Bretonnière, A. Mohammed, H. Ågren, B. Minaev, V. Minaeva, G. Baryshnikov, H. -H. Lee, J. Duboisset and M. Lindgren, Fluorescence and FTIR Spectra Analysis of Trans-A2B2-Substituted Di- and Tetra-Phenyl Porphyrins, *Materials*, 2010, **3**, 4446–4475. doi: 10.3390/ma3084446

[19] P. Bhyrappa, C. Arunkumara, B. Varghesea, D. S. S. Rao and S. K. Prasad, Synthesis and mesogenic properties of β-tetrabrominated tetraalkyloxyporphyrins, *J. Porphyr. Phthalocyanines*, 2008, **12**, 54–64. doi: 10.1142/S108842460800008X

[20] N. Minamijima, N. Furuta, S. Wakunami and T. Mizutani, Functionalization of Silica Surface by Tetrahydroxyporphyrin via SiO Linkages, *Bull. Chem. Soc. Jpn.*, 2011, **84**, 794–801. doi: 10.1246/bcsj.20100317

[21] T. Bruhn and C. Brückner, The Origin of the Absorption Spectra of Porphyrin N- and Dithiaporphyrin S-Oxides in Their Neutral and Protonated States, *Phys. Chem. Chem. Phys.*, 2015, **17**, 3560–3569. doi: 10.1039/C4CP04675G

[22] B. Röder, M. Büchner, I. Rückmann and M. O. Senge, Correlation of photophysical parameters with macrocycle distortion in porphyrins with graded degree of saddle distortion, *Photochem. Photobiol. Sci*., 2010, **9**, 1152–1158. doi: 10.1039/C0PP00107D

[23] L. M. Mazur, T. Roland, S. Leroy-Lhez, V. Sol, M. Samoc, I. D.W. Samuel and K. Matczyszyn, Efficient Singlet Oxygen Photogeneration by Zinc Porphyrin Dimers upon One- and Two-Photon Excitation, *J. Phys. Chem*., 2019, **123**, 4271–4277. doi: 10.1021/acs.jpcb.8b12561

[24] P. G. Seybold and M. Gouterman, Porphyrins: XIII: Fluorescence spectra and quantum yields, *J. Mol. Spectrosc*., 1969, **31**, 1–13. doi: 10.1016/0022-2852(69)90335-X

[25] T. N. Singh-Rachford and F. N. Castellano, Photon upconversion based on sensitized triplet–triplet annihilation, *Coord. Chem. Rev*., 2010, **254**, 2560–2573. doi: 10.1016/j.ccr.2010.01.003

[26] Z. Wang, M. Ivanov, Y. Gao, L. Bussotti, P. Foggi, H. Zhang, N. Russo, B. Dick, J. Zhao, M. Di Donato, G. Mazzone, L. Luo and M. Fedin, Spin–Orbit Charge-Transfer Intersystem Crossing (ISC) in Compact Electron Donor–Acceptor Dyads: ISC Mechanism and Application as Novel and Potent Photodynamic Therapy Reagents, *Chem. – Eur. J*., 2020, **26**, 1091–1102. doi: 10.1002/chem.201904306

[27] T. W. Ebbesen, K. Tanigaki and S. Kuroshima, Excited-state properties of C_{60}, *Chem. Phys. Lett.*, 1991, **181**, 501–504. doi: 10.1016/0009-2614(91)80302-E

[28] M. Montalti, A. Credi, L. Prodi and M. T. Gandolfi, Handbook of Photochemistry, CRC Press, 2006.

[29] A. Sagadevan, K. C. Hwang and M. -D. Su, Singlet oxygen-mediated selective C–H bond hydroperoxidation of ethereal hydrocarbons, *Nat. Commun.*, 2017, **8**, 1–8. doi: 10.1038/s41467-017-01906-5

[30] M. Gouterman, Spectra of Porphyrins*, *J. Mol. Spectrosc.*, 1961, **6**, 138–163. doi: 10.1016/0022-2852(61)90236-3

[31] M. Kasha, In Spectroscopy of the Excited State.; Di Bartolo, B., Ed.; Plenum Press: New York, 1975, p 340.

[32] B. Dong, C. H. Galka, L. H. Gade, L. Chi and R. M. Williams, Hydrogen-bond Assisted Formation of Rod Shaped Organic Nanocrystals: Control of the Aggregational State and Structural Elucidation, *Nanopages*, 2006, **3**, 325–338. doi: 10.1556/NANO.1.2006.3.4

[33] F. Würthner, T. E. Kaiser and C. R. Saha-Möller, J Aggregates: From Serendipitous Discovery to Supramolecular Engineering of Functional Dye Materials, *Angew. Chem. Int. Ed*., 2011, **50**, 3376–3410. doi: 10.1002/anie.201002307

[34] N. Keller, M. Calik, D. Sharapa, H. R. Soni, P. M. Zehetmaier, S. Rager, F. Auras, A. C. Jakowetz, A. Görling, T. Clark and T. Bein, Enforcing Extended Porphyrin J-Aggregate Stacking in Covalent Organic Frameworks, *J. Am. Chem. Soc.*, 2018, **140**, 16544–16552. doi: 10.1021/jacs.8b08088.

[35] N. Venkatramaiah, B. Ramakrishna, R. Venkatesan, F. A. Almeida Paz and J. P. C. Tomé, Facile synthesis of highly stable BF3-induced meso-tetrakis (4-sulfonato phenyl) porphyrin (TPPS4)-J-aggregates: structure, photophysical and electrochemical properties, *New J. Chem.*, 2013, **37**, 3745–3754. doi: 10.1039/C3NJ00482A

[36] L. L. Liu, Y. F. Zhao and W. J. Jin, Investigation on the effect of water on the spectroscopic behaviors of TPPS in acidic imidazolium-based ionic liquids, *J. Porphyr. Phthalocyanines*, 2012, **16**, 1132–1139. doi: 10.1142/S1088424612501118
[37] C. -P. Jellen and H. Bettermann, Unusual emissions from low-concentrated porphyrin solutions, *Spectrochim. Acta. A. Mol. Biomol. Spectrosc.*, 2003, **59**, 463–470. doi: 10.1016/s1386-1425(02)00214-7
[38] H. Ma, S. Sun, X. Chen, D. Wu, P. Zhu, B. Du and Q. Wei, Spectroscopic studies of aggregation behavior of meso -tetra(4-hydroxyphenyl)porphyrin in aqueous AOT solution, *J. Porphyr. Phthalocyanines*, 2008, **12**, 101–108. doi: 10.1142/S1088424608000133
[39] Q. Han, C. Wang, Z. Li, J. Wu, P. K. Liu, F. Mo and Y. Fu, Multifunctional Zinc Oxide Promotes Electrochemiluminescence of Porphyrin Aggregates for Ultrasensitive Detection of Copper Ion, *Anal. Chem.*, 2020, **92**, 3324–3331. doi: 10.1021/acs.analchem.9b05262
[40] I. B. Zakharova, M. A. Elistratova, N. M. Romanov and O. E. Kvyatkovskii, Specific Features of the Electron Structure of ZnTPP Aggregated Forms: Data of Optical Measurements and Quantum-Chemical Calculations, *Semiconductors*, 2018, **52**, 1708–1714. doi: 10.1134/S1063782618130237
[41] N. Hananya, O. Green, R. Blau, R. Satchi-Fainaro and D. Shabat, A Highly Efficient Chemiluminescence Probe for the Detection of Singlet Oxygen in Living Cells, *Angew. Chem. Int. Ed.*, 2017, **56**, 11793–11796. doi: 10.1002/anie.201705803.

[42] F. Wilkinson, W. P. Helman and A. B. Ross, Rate constants for the decay and reactions of the lowest electronically excited singlet state of molecular oxygen in solution. An expanded and revised compilation, *J. Phys. Chem. Ref. Data*, 1995, **24**, 663–677. doi: 10.1063/1.555965
[43] N. Hananya, O. Green, R. Blau, R. Satchi-Fainaro and D. Shabat, A Highly Efficient Chemiluminescence Probe for the Detection of Singlet Oxygen in Living Cells, *Angew. Chem. Int. Ed.*, 2017, **56**, 11793–11796. https://doi.org/10.1002/anie.201705803.

[44] J. N. Demas and G. A. Crosby, The Measurement of Photoluminescence Quantum Yields. A Review, *Am. J. Phys. Chem.*, 1971, **75**, 991–1024. doi: 10.1021/j100678a001
[45] Origin, Version 2018b. OriginLab Corporation, Northampton, MA, USA.
[46] T. Kumpulainen, B. H. Bakker, M. Hilbers and A. M. Brouwer, Synthesis and Spectroscopic Characterization of 1,8-Naphthalimide Derived “Super” Photoacids, *J. Phys. Chem. B.*, 2015, **119**, 2515–2524. doi: 10.1021/jp508334s
[47] Igor Pro (Wavemetrics, Lake Oswego, OR, USA).
[48] M. K. Green, C. J. Medforth, C. M. Muzzi, D. J. Nurco, K. M. Shea, K. M. Smith, C. B. Lebrilla and J. A. Shelnutt, Application of matrix-assisted laser desorption/ionization Fourier transform massspectrometry to the analysis of planar porphyrins and highly substituted nonplanar porphyrins, *Eur. Mass Spectrom.*, 1997, **3**, 439–451. doi: 10.1255/ejms.178

Lignin conjugates of porphyrins and cyanine dyes for biomedical applications

Abstract

This chapter describes the synthesis and photophysical studies conducted on lignin-containing compounds. Lignin is a polymer that is produced annually in millions of tons as a side product in the paper industry. It has been recently shown that lignin can be functionalized to produce singlet oxygen for photomedical applications. Herein, lignin was covalently attached to cyanine dyes (lignin-cyanine conjugate) to investigate the photophysical effect of lignin attachment on the cyanine dye upon near IR light excitation (700–800 nm). In parallel, lignin was attached to porphyrins, macrocycles that absorb in the UV, visible and near IR region (300–700 nm), to investigate whether there is enhanced photophysical activity for application in photodynamic therapy. The lignin polymer, of one of the lignin-porphyrin compounds, was acetylated.

The synthesis and photophysical studies are split into two sections: **lignin-cyanine** and **lignin-porphyrin** conjugates. In the latter section, the discussion is further divided into two subsections (**TCPP** and ***m*-CPTPP**). It is shown that lignin attachment does not substantially modify the photophysical properties of the cyanine and porphyrin chromophores.

4.1. Introduction

Lignin is a naturally occurring organic polymer that has attracted huge interest in the last decade for its potential use to make high value-added chemicals.[1] Every year, 98% of the 55–70 million tons of lignin that is produced is directly combusted for energy production.[2] Once extracted from nature using the 4 different processes: Sulfite, Kraft, Organosolv and Soda (see chapter **1**, table **1.2**),[3] there are functional groups that are available for functionalization. These include aliphatic and aromatic hydroxy moieties, *via* the three main mono-lignols: *p*-coumaryl, coniferyl and sinapyl alcohols (see figure **4.1**).[4]

Figure 4.1. *Chemical structures of mono-lignols highlighting the aromatic and aliphatic hydroxyl groups that are available for functionalization.*[3]

Since 2018, it has been known that upon acetylation of the OH groups in the mono-lignols of lignin, there is an enhanced production of singlet oxygen.[5] Acetylated lignin has been made into acetylated lignin nanoparticles that, when containing porphyrins, exhibit antibacterial activity.[6, 7] Acetylated lignin is thus a potential bio-photosensitizer and even without acetylation, lignin exhibits low cytotoxicity, is biodegradable and possesses antioxidant, antimicrobial, anti-inflammatory and UV-blocking properties.[8] Furthermore, lignin extracts appear to have promising natural anti-cancer and anti-oxidant agents.[9] Interestingly, preliminary studies indicate a potential application of lignin-type structures (similar to those in Figure **4.1**) for treating thrombosis and obesity.[10] Due to its array of impressive properties and the large quantity of lignin available each year, there is a huge potential for the creation of new highly valuable compounds for photo-medicine, as well as many other applications.[11] Once lignin has been extracted, it can be used without any chemical modification, by incorporation into a matrix as a delivery system. Chemical functional groups can also be attached to it, to give new or improved properties.[12, 13] Overall, researchers

worldwide have thus far found various applications in medicine and environmental sciences for lignin.[14, 15, 16]

Porphyrin macrocycles are the most commonly studied photosensitizers in relation to photodynamic therapy.[17] They can absorb light in the wavelength region of 350–700 nm, depending on peripheral substitution.[18] While their use as first generation photosensitizers saw great initial success in early clinical trials in the 1980s,[19] problems began to arise. Improvements needed to be made that included enhanced tumor selectivity, absorption at longer wavelengths for greater tissue penetration, reduced aggregation in aqueous media, etc.[5, 6, 7, 8, 20, 21, 22] Therefore, in order to further improve these macrocycles as photosensitizers, chemical modifications and delivery systems with improved photodynamic efficacy are highly sought after.

Near IR cyanine dyes are highly desirable for fluorescence imaging as well as the eradication of cancer tissues.[23] These dyes can absorb light from 750–900 nm and target cancer cells which makes them ideal candidates for photosensitizers. Unfortunately, these compounds exhibit rather low singlet oxygen quantum yields (<0.08) and have thus not been considered as novel PSs.[31] However, they have been considered as 'potential PDT tools' and have been investigated for their potential in photodynamic therapy.[24] Halogenation, metal atom incorporation, synthesis of emulsions and conjugations have been the main source of enhanced photodynamic therapy in these cyanine dyes. While the use of the heavy-atom effect to increase the singlet oxygen quantum yield of these cyanine dyes has been successful,[25] there are drawbacks of the heavy-atom effects in photosensitizers.[26] The presence of a heavy atom can dramatically increase the cost of producing these photosensitizers, reduce solubility and introduce unwanted side effects.[27]

Therefore, we pursue a heavy-atom free approach that involves the kraft lignin-cyanine and -porphyrin conjugates. Herein, the synthesis and photophysical studies of these conjugate systems for their application in photomedicine are reported.

4.2. Synthesis

4.2.1. Lignin-cyanine

Extending the conjugation of commercially available **IR-783** cyanine dye, by adding a 4-mercapto-benzoic acid group (Figure **4.2**), was achieved in a quantitative yield (>99%) *via* mild reaction conditions under argon for approximately 24 hours. This high-yielding S_N2 reaction involved the 4-mercaptobenzoic acid as the nucleophile, the chlorine atom of the cyanine as the leaving group on the electrophile, and resulted in the **IR-783-SPA** product. Kraft lignin (**KL-2** in Marchand *et al.*)[5] was then covalently attached to the available carboxylic acid functionality *via* a modified Mitsunobu reaction, to create a lignin-cyanine dye conjugate, called **IR-783-SPA-lignin**.[28, 29] The synthetic characterization is in the supplementary section of this chapter (Figures **S4.18**–**S4.20**).

The determination of the weight percentage of the cyanine in this lignin-cyanine conjugate (**IR-783-SPA**) was determined using the procedure described in section **4.5.1** of this chapter. It was estimated that 12% of the mass weight of the **IR-783-SPA-lignin** is made up of the **IR-783-SPA**. The rest of this conjugate is made up of the lignin polymer. Since **IR-783-SPA-lignin** is formed in a quantitative yield, we can assume that 12% of the mass weight is made up of the **IR-783-SPA** cyanine. Thus, 88% of the mass weight is made up of the lignin. Therefore, using the calculations described in section **4.5.1**, there are estimated to be 20 repeating units of lignin monomer in the **IR-783-SPA** conjugate.

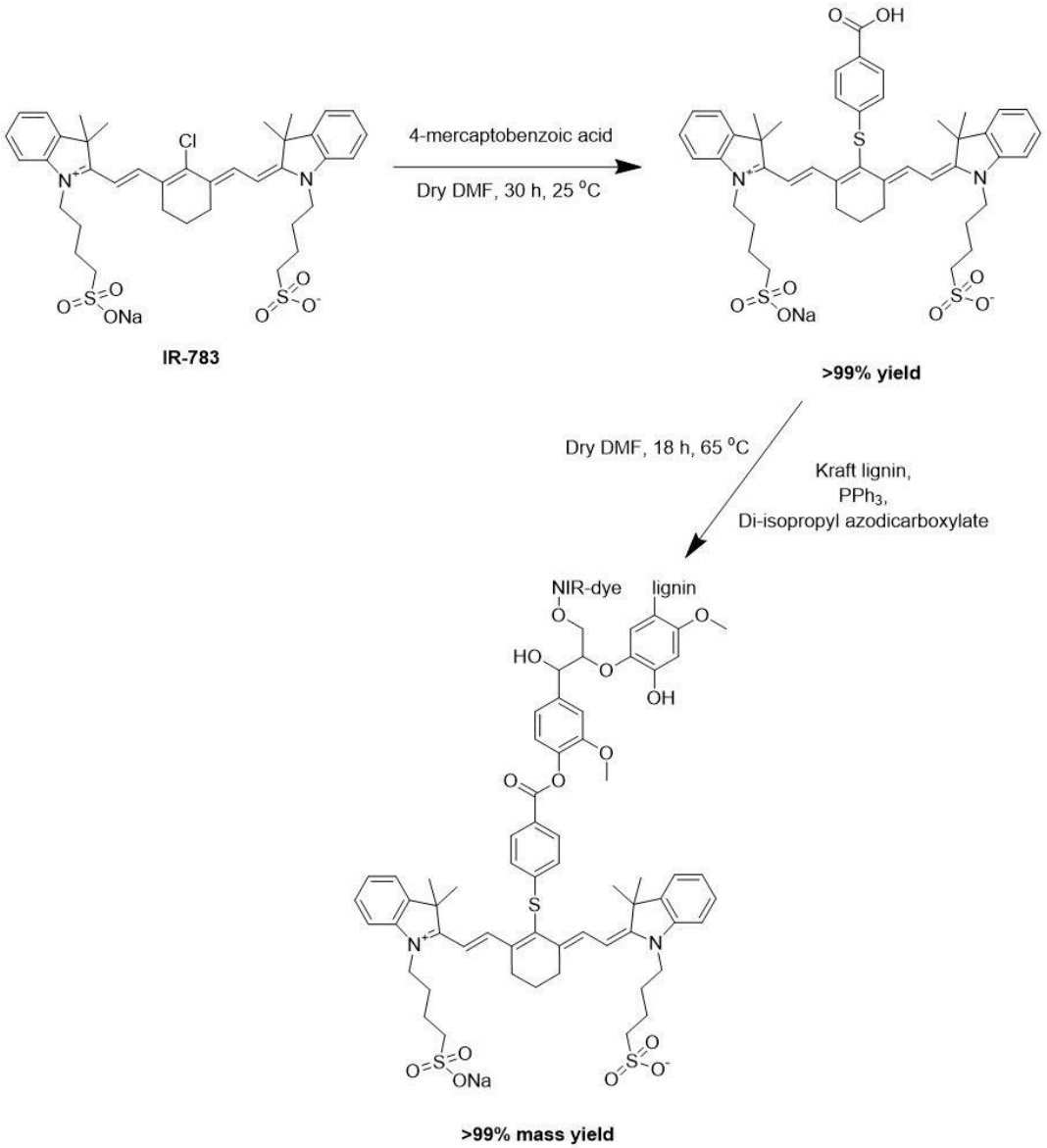

Figure 4.2. *Reaction scheme of the modification of* ***IR-783*** *to form* ***IR-783-SPA,*** *followed by its attachment to kraft lignin to form* ***IR-783-SPA-lignin****.*[29]

4.2.2. Lignin-porphyrin

4.2.2.1. Tetra-carboxyphenylporphyrin (TCPP)

The second group of reactions involve the esterification of the commercially available 5,10,15,20-tetra-(4-carboxyphenyl)porphyrin (**TCPP**) with kraft lignin *via* a modified Mitsunobu reaction. This was conducted using identical conditions as the lignin-cyanine conjugate (Figure **4.3**).[29] This product was obtained in an excellent yield and the lignin moiety of this product was further acetylated with the aim of improving the photophysical properties of the system.[5] It has been shown in the literature that

acetylation of lignin increases the singlet oxygen production compared to that of non-acetylated kraft lignin.

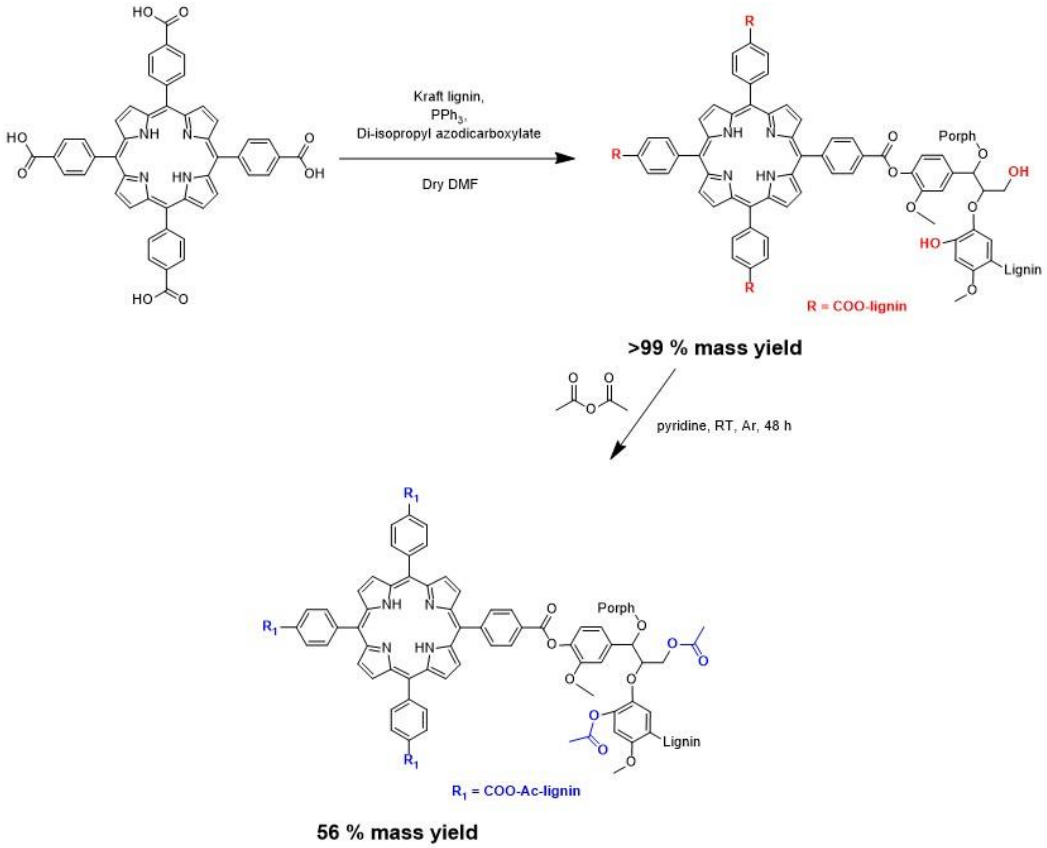

Figure 4.3. *Reaction scheme of 5,10,15,20-(4-kraft lignin-carboxyphenyl)-porphyrin conjugate (**TCPP-lignin**) and the subsequent acetylation of the lignin moiety (**TCPP-Ac-lignin**).*[5, 29] ****Note:** Both structures **TCPP-lignin** and **TCPP-Ac-lignin** are tetra-substituted structures that have been abbreviated for clarity.*

Observing the IR spectrum of **TCPP** (Figure **4.4**), the presence of the carboxyl groups on the *para*-phenyl groups of the porphyrin are visible. The peaks at 3000 cm^{-1} correspond to C=O stretch of carboxylic acid and peak at approx. 3700 cm^{-1} represents the hydroxyl O-H stretch, respectively. Following on from here, the IR spectrum of **TCPP-lignin** is as expected. The attachment of the porphyrin to lignin has led to the disappearance of the peak O-H peak at 3700 cm^{-1} and led to the appearance of a large band at 3300 cm^{-1}. This new peak likely represents the mono-lignol hydroxyphenyl groups (Figure **4.1**). Moving on to the IR spectrum of **TCPP-Ac-lignin**, these lignin O-H groups have been largely reduced due to the presence of acetyl groups (peaks at 1760 cm^{-1} and C=O peaks at approx. 2900 cm^{-1}).

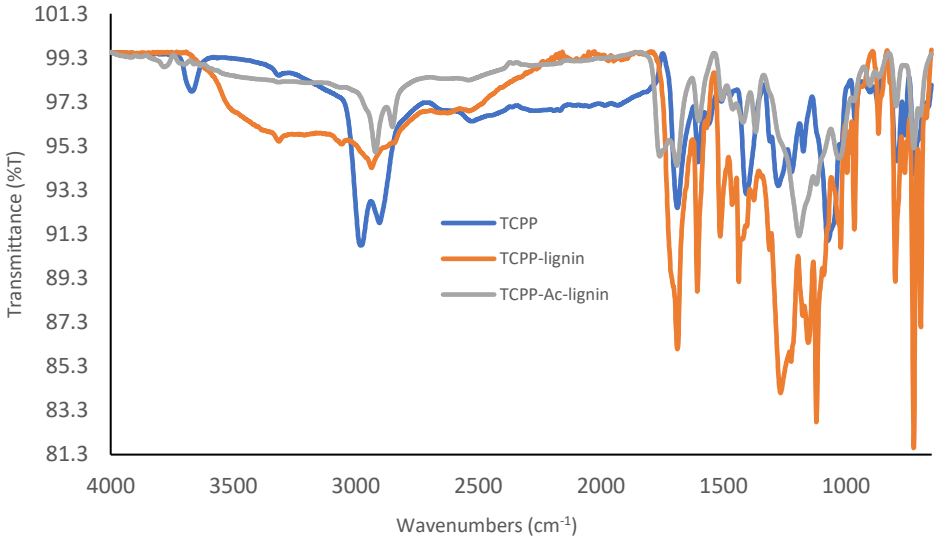

Figure 4.4. *IR spectra of* ***TCPP*** *(blue)* ***TCPP-lignin*** *(orange), and* ***TCPP-Ac-lignin*** *(grey).*

Therefore, these IR spectra indicate the formation of **TCPP-lignin** and **TCPP-Ac-lignin**. The rest of the spectra is provided in the supplementary section (Figures **S4.22**–**S4.25**).

4.2.2.2. Mono-carboxyphenyl-triphenylporphyrin (*m*-CPTPP)

To see the effect an A_3B porphyrin system would have on the photophysics, another porphyrin was applied, 5-(4-carboxyphenyl)-10,15,20-triphenylporphyrin (***m*-CPTPP)**. As well as having fewer sites of attachment (1 carboxyl group in ***m*-CPTPP** versus four in **TCPP**), the system resembles a dyad system (1-part porphyrin: 1-part lignin) as opposed to a pentad system (as seen in **TCPP-lignin**). The commercially available 5-(4-carboxyphenyl)-10,15,20-triphenylporphyrin was covalently attached to kraft lignin *via* the reaction conditions described in figures **4.5**. This lignin-porphyrin system was obtained *via* the same modified Mitsunobu reaction conditions.[29] The grafting percentage of the porphyrin in this lignin-porphyrin conjugate (***m*-CPTPP**) was determined using the procedure in section **4.5.1** of this chapter. It was estimated that 26% of the mass of this ***m*-CPTPP-lignin** conjugate consists of the ***m*-CPTPP** porphyrin. From here, the degree of polymerization was then estimated to be approximately five repeating lignin units.

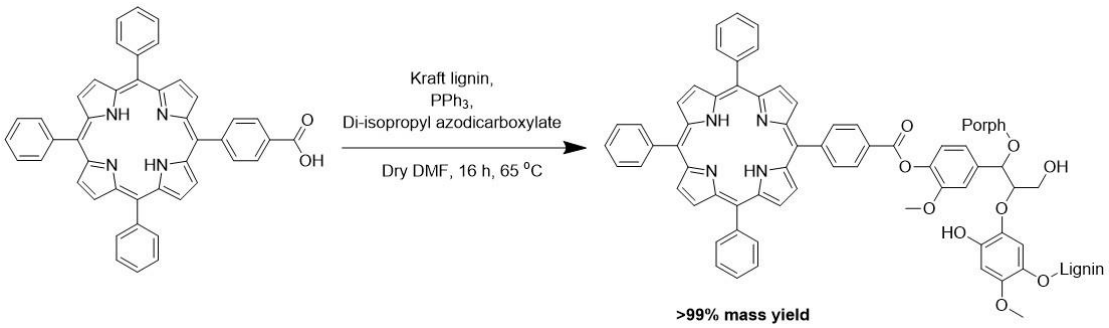

Figure 4.5. *Reaction scheme of 5-(4-kraft lignin-phenyl)-10,15,20-triphenylporphyrin conjugate (**m-CPTPP-lignin**).*[29]

Attempts to acetylate the lignin-cyanine conjugate (**IR-783-SPA-lignin**) and the monocarboxyphenyl-lignin conjugate (***m*-CPTPP-lignin**) were conducted. However, after characterization, it was shown that the desired acetylated products did not form. The rest of the synthetic details for the *m*-**CPTPP-lignin** compound are shown in Figures **S4.26–S4.28**.

The synthetic details and spectra are shown below (section **4.5.1** and section **4.5.3**). The photophysical properties of these compounds were then determined for their application as novel photosensitizers in photodynamic therapy (see section **4.3**).

As a reference for the photophysical studies, kraft lignin and acetylated kraft lignin was also studied as a comparison, using Zn(II) phthalocyanine as a reference (Figure **4.6**). These were previously synthesized by previous lab members according to literature.[5] The Zn(II) phthalocyanine reference was chosen as it was used before, as seen in Marchand *et al.*[5]

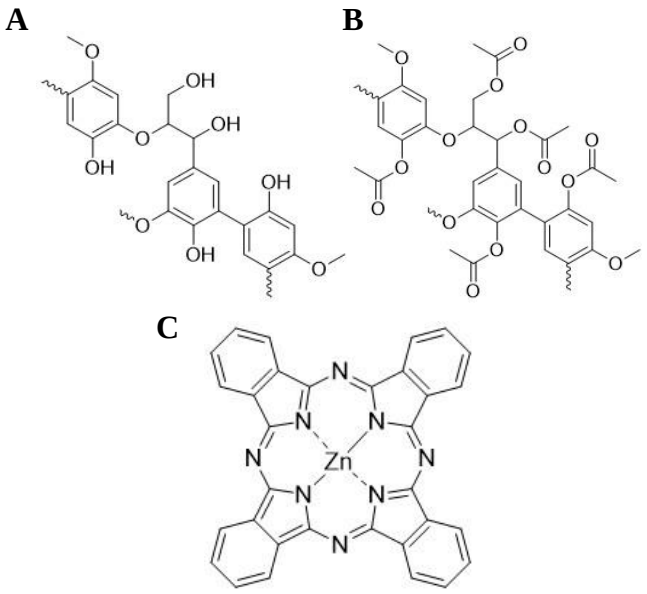

Figure 4.6. *Chemical structures of* ***(A)****: Kraft lignin (****KL****);* ***(B)****: Acetylated kraft lignin (Ac-KL) and* ***(C)****: Zn(II) phthalocyanine.*

4.3. Photophysical studies

As mentioned in the abstract, the first section (section **4.3.1**) will be devoted to the photophysical characterization of the lignin-cyanine conjugates.

4.3.1. Lignin-cyanine conjugates

The UV-vis spectra of the lignin-cyanine conjugate (**IR-783-SPA-lignin**) and it's starting materials (**IR-783** and **IR-783-SPA**), in methanol (MeOH), are provided in the supplementary information (Figure **S4.1**) and the data are summarized in Table **4.1**. Replacing the mercaptobenzoic acid group for the chlorine atom on the **IR-783** dye extended the π-system, and the absorption maximum was shifted from 783 nm to 799 nm (16 nm). Lignin attachment to this dye did not further red shift the absorption band, it had the opposite effect. It shifted the peak by 3 nm (from 799 nm to 796 nm), which could be due to the hindered rotation of the mercaptobenzoic acid moiety, by the lignin polymer.[30]

Table 4.1. *UV-visible absorption maxima data of* ***IR-783****,* ***IR-783-SPA*** *and* ***IR-783-SPA-lignin*** *in methanol (MeOH).*

PS	**λ/nm**	
	Shoulder [a]	**main band**
IR-783	700	783
IR-783-SPA	727	799
IR-783-SPA-lignin	732	796

[a] These peaks were determined as the shoulders of the main cyanine peak and have a margin of error of ± 5 nm.

In Table **4.2**, the photophysical properties (fluorescence maxima, stokes shift, fluorescence quantum yield, fluorescence (singlet) lifetime and singlet oxygen quantum yield) are summarized (see experimental part in chapter **3** for protocols). The fluorescence and singlet oxygen quantum yields of indocyanine green (**ICG**) in MeOH were used as references (see **Table 4.2** for values, figure **4.7** for chemical structures and figures **4.8** and **4.9** for photoluminescence spectra).[31]

Table 4.2. *Photophysical properties of* ***IR-783****,* ***IR-783-SPA*** *and* ***IR-783-SPA-lignin*** *in MeOH.*

PS	**λ_{em} $Q_x(0,0)$ (nm)**	**λ_{em} $Q_x(0,1)$ (nm)**	**SS (cm^{-1}) [a]**	**Φ_f [b]**	**τ_s (ns) [c]**	**Φ_Δ [d]**
IR-783	802	889	303	0.10 ± 0.01	0.56 ± 0.02	0.004 ± 0.001
IR-783-SPA	882	900	350	0.06 ± 0.01	0.47 ± 0.1	0.006 ± 0.001
IR-783-SPA-lignin	823	899	412	0.07 ± 0.01	0.52 ± 0.3 [e] / 0.47 ± 0.2	0.006 ± 0.001

[a] The Stokes shift (SS) was calculated from the corresponding UV-Vis and emission spectra; [b] *Fluorescence quantum yield. Excitation wavelength = 727 nm and reference = Indocyanine green (**ICG**; Φ_f = 0.08);*[31] [c] *Singlet state lifetime in air solution (equilibrated).* ***IR-783*** *and* ***IR-783-SPA*** *are fitted via a mono-exponential decay, whilst* ***IR-783-SPA-lignin*** *is fitted via a bi-exponential decay. Excitation wavelength is 720 nm and emission wavelength is 800 nm;* [d] *Singlet oxygen quantum yield. Excitation wavelength = 727 nm and reference = **ICG** (Φ_Δ = 0.008).*[3131] [e] *This is the proposed singlet lifetime for* ***IR-783-SPA****.*

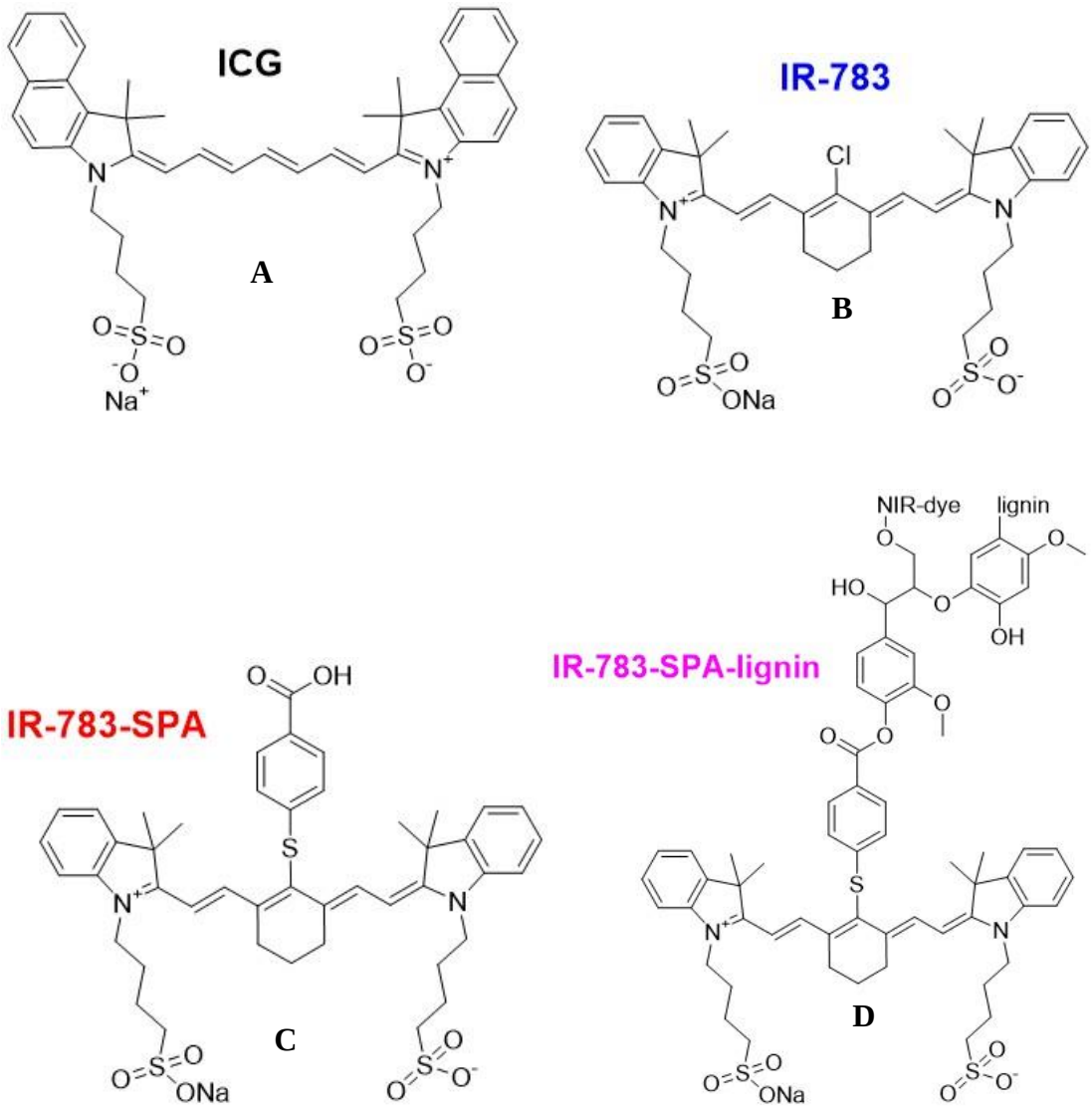

Figure 4.7. *Chemical structures of (**A**): Indocyanine green (**ICG**); (**B**): **IR-783**; (**C**): **IR-783-SPA**; (**D**): **IR-783-SPA-lignin**.*

When comparing the Φ_f of **IR-783-SPA** and **IR-783-SPA-lignin** against that of **ICG** in MeOH, the fluorescence is almost 50% less when replacing the chlorine atom on **IR-783** with the mercaptobenzoic acid moiety (Figures **4.7** and **4.8** and table **4.2**). From here, the fluorescence is slightly enhanced upon attachment of the lignin to the cyanine dye *via* an ester bond. In terms of the singlet oxygen produced (Φ_Δ), **IR-783-SPA** produces almost twice as much $^1O_2$ than **IR-783** (Figure **4.9**). This singlet oxygen producing capacity is retained in **IR-783-SPA** when lignin is attached to this cyanine (Table **4.2**; see chapter **3** for quantum yield determination method).

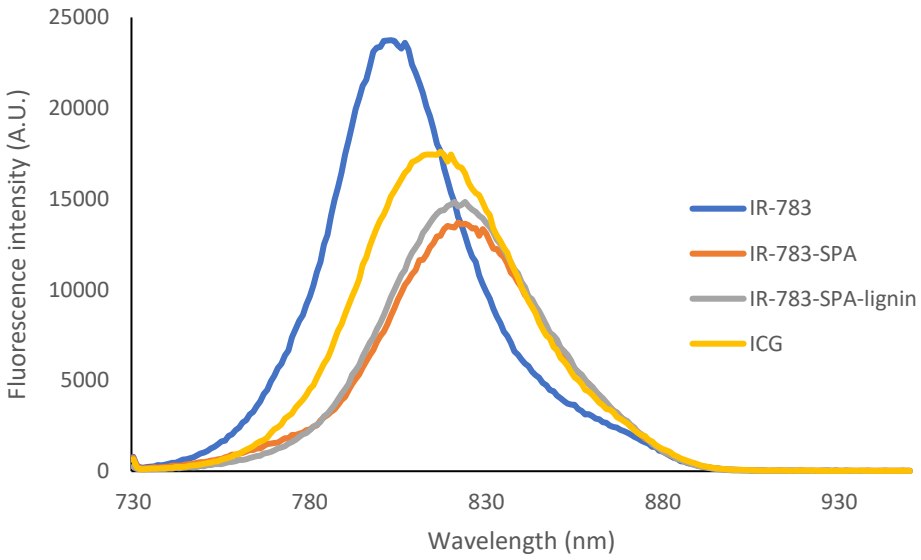

Figure 4.8. *Fluorescence spectra of* ***IR-783*** *(blue),* ***IR-783-SPA*** *(orange),* ***IR-783-SPA-lignin*** *(grey) and the reference* ***ICG*** *(yellow;* Φ_f *= 0.08) in MeOH.*[31] *Excitation wavelength = 727 nm. Concentrations of each solution measured are: 1.9 µM (****IR-783****), 2.8 µM (****IR-783-SPA****), 2.3 µM (****IR-783-SPA****; assuming ε of* ***IR-783-SPA-lignin*** *= that of* ***IR-783-SPA****) and 1.4 µM (****ICG****).*

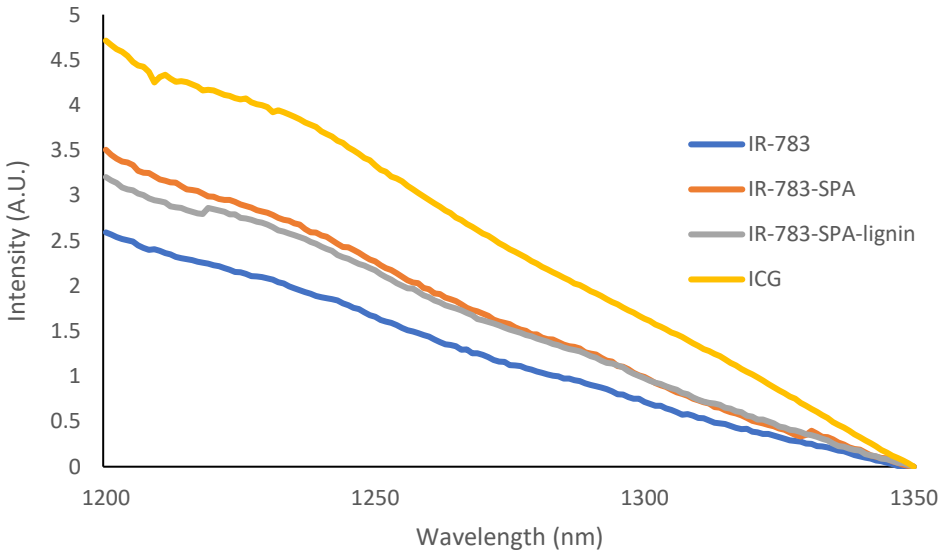

Figure 4.9. *Singlet oxygen emission spectra of* ***IR-783*** *(blue),* ***IR-783-SPA*** *(orange),* ***IR-783-SPA-lignin*** *(grey) and reference* ***ICG*** *(yellow,* Φ_Δ *= 0.008) in MeOH.*[3131] *Excitation wavelength = 727 nm. Tailing of the* ***IR-783*** *fluorescence emission is evident and obscures the singlet oxygen emission. Concentrations of each solution measured are: 6.4 µM (****IR-783****), 4.5 µM (****IR-783-SPA****), 3.9µM (****IR-783-SPA****; assuming ε of* ***IR-783-SPA-lignin*** *= that of* ***IR-783-SPA****) and 3.6 µM (****ICG****).*

Attempts to determine the triplet lifetimes of **IR-783**, **IR-783-SPA** and **IR-783-SPA-lignin** in MeOH were conducted using nanosecond transient absorption spectroscopy. However, the limit of the Ekspla laser was 700 nm and was thus unable to excite the cyanine dye. According to the literature, it was found that numerous reports have reported on cyanines being weak $^1O_2$ generators.[32, 33] Thus, it would suggest that once the light is absorbed by the cyanine, the molecule is promoted to a singlet excited state. There is most likely a small intersystem crossing quantum yield ($\boldsymbol{\Phi_{ISC}}$) and thus, a preference to return to the ground state *via* radiative (fluorescence) and non-radiative decays (photo-switches) must exist.[34]

The fluorescence lifetimes of **IR-783**, **IR-783-SPA** and **IR-783-SPA-lignin** were determined in MeOH *via* time-correlated single photon counting (TC-SPC). They follow the same trend as the $\boldsymbol{\Phi_f}$: (see table **4.2** and figure **S4.2**–**S4.4**) **IR-783** > **IR-783-SPA-lignin** > **IR-783-SPA**.[35]

In summary, modification of the **IR-783** dye to form **IR-783-SPA**, very slightly reduces the fluorescence of the cyanine dye and does not significantly increase the singlet oxygen production. Further attachment of lignin does not significantly introduce any major changes.

4.3.2. Lignin-porphyrin conjugates

The next set of compounds studied are the lignin-porphyrin conjugates. These compounds are split up into two subsets: the tetra-carboxyphenylporphyrin-lignin conjugate (**TCPP**) subset and the mono-carboxyphenyl-triphenylporphyrin-lignin conjugate (***m*-CPTPP**) subset.

4.3.2.1. TCPP

The chemical structures for this subset of compounds, and the reference for measuring the fluorescence quantum yield, 5,10,15,20-tetraphenylporphyrin (**TPP**), are given in figure **4.10**.

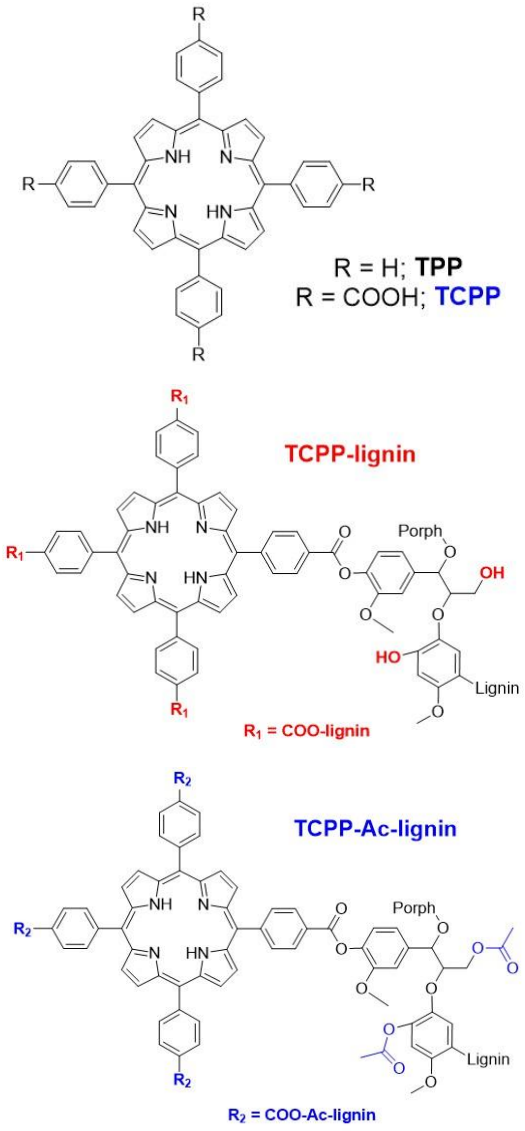

Figure 4.10. *Chemical structures of (**Top**): R = H: 5,10,15,20-tetraphenylporphyrin (**TPP**), R = COOH: **TCPP**; (**Middle**): **TCPP-lignin**; (**Bottom**): **TCPP-Ac-lignin**.*

The UV-vis spectra of the porphyrin-acetylated kraft lignin conjugate (**TCPP-Ac-lignin**) and its starting materials (**TCPP-lignin** and **TCPP**) are provided in the supplementary information (Figure **S4.5**) and the data are summarized in Table **4.3**. In Table **4.4**, the photophysical properties (fluorescence maxima, stokes shift, fluorescence and singlet oxygen quantum yield, and singlet and triplet lifetimes) are summarized.

The UV-Vis spectra of the **TCPP** subset are consistent and possess the known Soret band (at approximately 400–420 nm) and four Q-bands (stretching from 500–700 nm; table **4.3**).[18] The lignin moiety is known to absorb strongly from 250–400 nm and can reach as far as 500 nm, depending on concentration.[36]

The fluorescence quantum yield of **TPP** in toluene was used as a reference (0.11) to determine the fluorescence in these **TCPP** conjugates (Figures **4.10** and **4.11**; Table **4.4**).[37] In order to determine the singlet oxygen quantum yield in MeOH, **Rose Bengal** was used as a reference (structure in Figure **4.12**).[38] The triplet lifetime was calculated using nanosecond transient absorption (ns-TA) spectroscopy in MeOH, and the singlet lifetimes were calculated using (TC-SPC) in the same solvent (See figures **S4.6**–**S4.11** for spectra).

Table 4.3. *UV-visible absorption maxima data of* ***TCPP****,* ***TCPP-lignin*** *and* ***TCPP-Ac-lignin*** *in MeOH.*

PS	Lignin maxima (λ/nm)	B-band (λ/nm)	Q-bands (λ/nm)				Q_{III}/B
			Q_{IV} [a]	Q_{III} [a]	Q_{II} [a]	Q_I [a]	
TCPP	- [c]	415	513	547	588	645	0.04
TCPP-lignin	282	415	513	547	589	645	0.03
TCPP-Ac-lignin	- [d]	415	513	548	589	645	0.03

[a] $Q_{IV} = Q_y(1,0)$ peak; $Q_{III} = Qy(0,0)$, $Q_{II} = Q_x(1,0)$ and $Q_I = Q_x(0,0)$; [b] Ratio of the intensities of the Q_{III} and Soret (B) bands; [c] no lignin in this compound therefore no lignin peak; [d] Difficult to determine peak maximum as there is a broad band.

Table 4.4. *Photophysical properties of* ***TCPP***, ***TCPP-lignin*** *and* ***TCPP-Ac-lignin*** *in MeOH.*

PS	Em1 [a]	Em2 [b]	SS [c]	Φ_f [d]	τ_s [e]				Φ_Δ [f]	τ_T [g]
TCPP	647	714	48	0.07 ± 0.01	11.9 ± 0.3	5.8 ± 1.7	2.3 ± 0.7	0.9 ± 0.5	0.66 ± 0.03	252 ± 32
TCPP-lignin	647	714	48	0.08 ± 0.01	12.2 ± 0.6	5.8 ± 1.3	2.9 ± 0.6	1.0 ± 0.5	0.53 ± 0.02	234 ± 26
TCPP-Ac-lignin	647	713	48	0.10 ± 0.01	12.9 ± 1.3	6.3 ± 0.5	2.4 ± 0.5	0.9 ± 0.6	0.56 ± 0.03	276 ± 45

*[a] λ_{em} $Q_x(0,0)$ (**Em1**) = 1st emission maximum; [b] λ_{em} $Q_x(0,1)$ (**Em2**) = 2nd emission maximum. Both given in nm; [c] The Stokes shift (SS) was calculated, in wavenumbers (cm^{-1}) from the corresponding UV-Vis and emission spectra; [d] Fluorescence quantum yield calculated in MeOH using **TPP** in toluene as reference (0.11).[37] Excitation wavelength is 548 nm; [e] Singlet excited state lifetime, given in nanoseconds, measured using TC-SPC, Excitation wavelength is 418 nm and emission wavelength is 650 nm. These fluorescence decays were fitted tetra exponentially; [f] Singlet oxygen quantum yield calculated in MeOH using Rose Bengal as a reference (0.80).[38] Excitation wavelength is 548 nm; [g] Triplet state lifetime in air (equilibrated), given in nanoseconds. Excitation wavelength is 515 nm.*

Φ_f follows a trend where the porphyrin (**TCPP**) is the least fluorescent molecule in this subset and lignin attachment to this porphyrin seems to marginally increase this fluorescence, followed by a further slight increase once the lignin moiety is acetylated. The presence of the lignin polymer is likely to play a role in slightly increasing this fluorescence. This observation regarding the trends of the Φ_f is further backed up by the fluorescence lifetimes: the higher the Φ_f, the longer the fluorescence lifetime. The fluorescence lifetime decays *via* tetra-exponential decay kinetics (see chapter **3** for further information). Thus the longest lifetime obtained, of the four lifetimes from the tetra-exponential fit, is likely the fluorescence lifetime associated with the porphyrin (Table **4.4**). Except **TCPP**, other lifetimes that appear in the decay of the singlet state of **TCPP-lignin** and **TCPP-Ac-lignin** are likely present due overlapping lignin emission from the different types of lignin segments, or even possibly from different lignin polymer configurations (long polymer chains/short polymer chains/dimers/oligomers).[5] In **TCPP** (Figure **4.10**), vibrational relaxation to the Q-bands of the porphyrin, polarity of the MeOH solvent 'inducing conformational changes' and energy transfer are likely reasons for this tetra-exponential fluorescence decay (Figures **S4.6**–**S4.8**).[39, 40, 41] In toluene, **TPP** showed

a lifetime of 14.7 (± 0.1) ns in toluene.[42] Therefore, these lifetimes for the **TCPP** series are within the region of expectation.

In terms of the singlet oxygen quantum yields, **TCPP** has the highest $\boldsymbol{\Phi_\Delta}$ (see chapter **3** for procedure used to calculate the yields). In figure **4.12**, the singlet oxygen emission spectra of the **TCPP** subset are very noisy and less intense compared to the compounds of the ***m*-CPTPP** subset (see chemical structure in figure **4.13**). The less intense signal, that possesses a high signal to noise ratio, of the $^1O_2$ emission in MeOH is likely due to its shorter $^1O_2$ lifetime in this solvent compared to that in chloroform (10 μs vs 0.25 ms, respectively).[43] Thus, the singlet oxygen emission is harder to detect in MeOH.

Lignin attachment to this porphyrin appears to slightly reduce the $\boldsymbol{\Phi_\Delta}$. This could be explained by the strong antioxidant behavior of lignin that could quench the $^1O_2$ produced.[44] Furthermore, lignin likely acts as a shield-like physical barrier that envelopes the porphyrin and is another potential reason for the reduction in singlet oxygen produced. This "shielding effect" is somewhat hindered upon acetylation of the lignin moiety and could be due to hydrophobic/apolar interactions of **TCPP** porphyrin and the acetylated lignin (in **TCPP-Ac-lignin**), compared to lignin.

This increase in $\boldsymbol{\Phi_\Delta}$ from the **TCPP-lignin** to the **TCPP-Ac-lignin** is not significant enough to conclude that the acetyl groups on lignin increase the singlet oxygen production. In 2018, our group published an article reporting the increase of the $\boldsymbol{\Phi_\Delta}$ of lignin upon acetylation.[5] It was noticed that upon acetylation of the lignin by itself, the singlet oxygen production increased. This was further proven in section **4.3.3** of this chapter as acetylated lignin has a higher $\boldsymbol{\Phi_\Delta}$ than lignin by itself (see table **4.8**). Thus, it was expected that the acetylation of **TCPP-lignin** would induce a higher singlet oxygen production than observed.

The triplet lifetimes were then measured using nanosecond transient absorption spectroscopy. There were no significant differences in the lifetimes (Table **4.4**). The triplet decay and transient absorption spectra of the triplet excited states are included in the supplementary information section (Figures **S4.9**–**S4.11**).

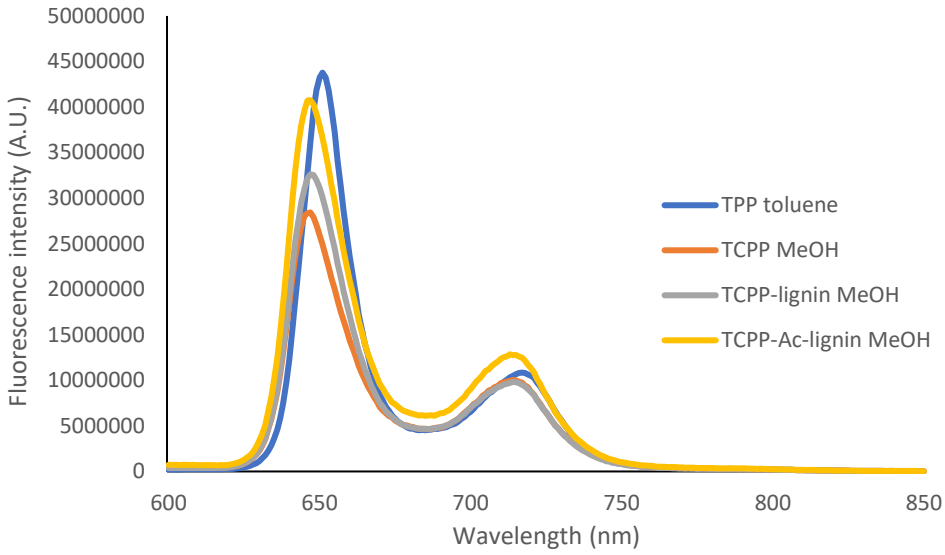

Figure 4.11. *Fluorescence spectra of* ***TPP in toluene*** *(blue),* ***TCPP*** *in MeOH (orange),* ***TCPP-lignin*** *in MeOH (grey) and* ***TCPP-Ac-lignin*** *in MeOH (yellow). Excitation wavelength = 548 nm and reference for quantum yield calculation is* ***TPP*** *in toluene (*$\boldsymbol{\Phi_f}$ *= 0.11).*[37] *Concentrations of each solution measured are: 12 µM (****TPP****), 28 µM (****TCPP****), 24 µM (****TCPP-lignin****; assuming ε of* ***TCPP-lignin*** *= that of* ***TCPP****) and 17 µM (****TCPP-Ac-lignin****; assuming ε of* ***TCPP-Ac-lignin*** *= that of* ***TCPP****).*

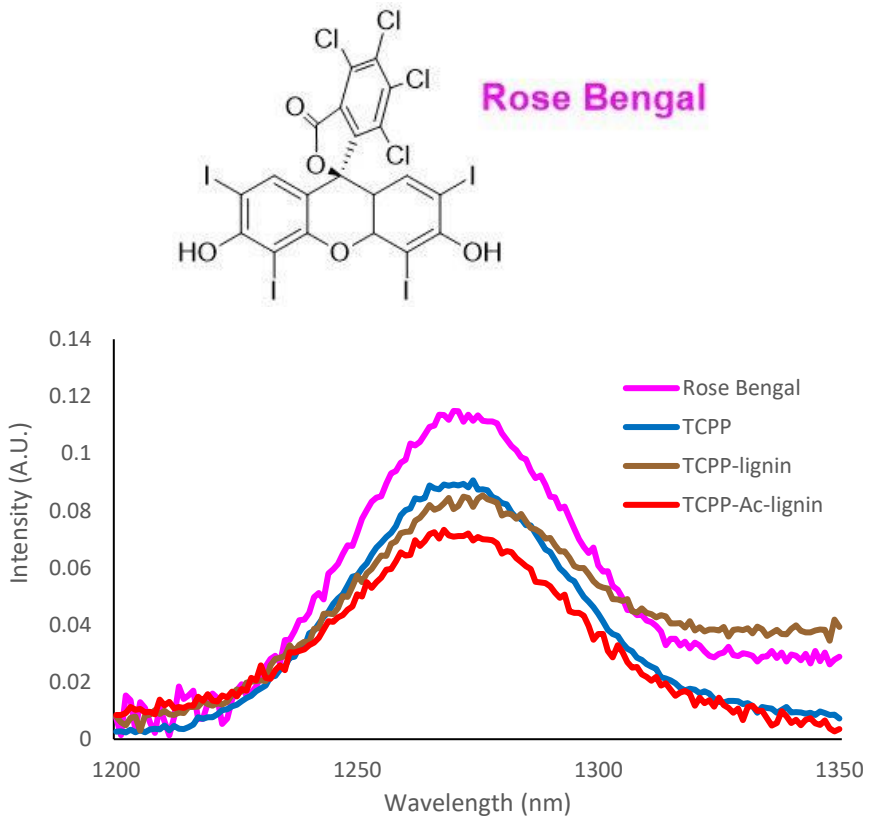

Figure 4.12. (Top): *Rose Bengal chemical structure;* ***(Bottom):*** *Singlet oxygen emission spectra of* ***Rose Bengal*** *(pink),* ***TCPP*** *(blue),* ***TCPP-lignin*** *(brown) and* ***TCPP-Ac-lignin*** *(red) in MeOH. Excitation wavelength = 548 nm and reference is Rose Bengal in methanol (*Φ_Δ *= 0.80).*[3838] *Concentrations of each solution measured are: 40 µM (****TCPP****), 25 µM (****TCPP-lignin****; assuming ε of* ***TCPP-lignin*** *= that of* ***TCPP****), 30 µM (****TCPP-Ac-lignin****; assuming ε of* ***TCPP-Ac-lignin*** *= that of* ***TCPP****) and 13.5 µM (****Rose Bengal****).*

4.3.2.2. *m*-CPTPP

The chemical structures of this subset of the lignin-porphyrin conjugates (***m*-CPTPP**) are shown in Figure **4.13**.

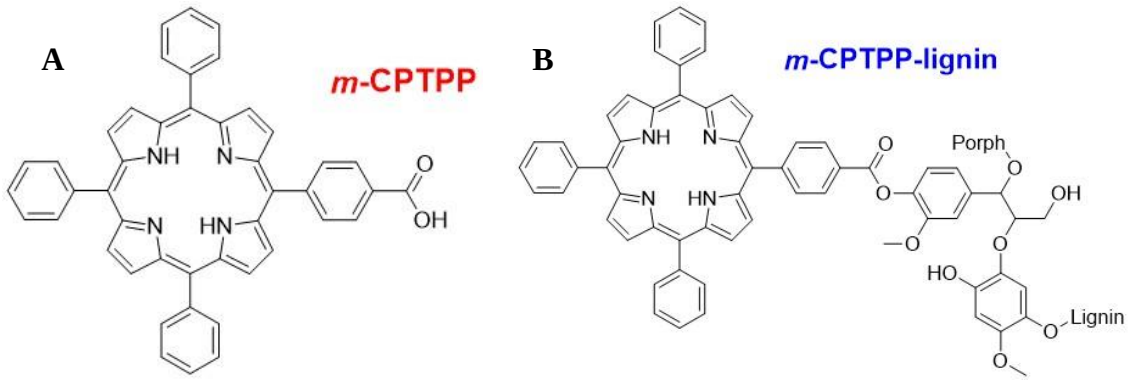

Figure 4.13. *Chemical structures of (****A****):* ***m-CPTPP*** *and (****B****):* ***m-CPTPP-lignin****.*

The UV-vis spectra of this mono-carboxyphenylporphyrin-lignin conjugate (***m*-CPTPP-lignin**) and its starting material (***m*-CPTPP**) are provided in the supplementary information (Figure **S4.12**) and the data are summarized in Table **4.5**. In Table **4.6**, the photophysical properties (fluorescence maxima, stokes shift, singlet and triplet lifetimes, fluorescence and singlet oxygen quantum yield) are summarized.

Table 4.5. *UV-visible absorption data of* ***m-CPTPP- lignin*** *and* ***m-CPTPP*** *in* $CHCl_3$.

PS	Lignin maxima (λ/nm)	B-band (λ/nm)	Q-bands (λ/nm)				Q_{III} / B
			Q_{IV} [a]	Q_{III} [a]	Q_{II} [a]	Q_I [a]	
***m*-CPTPP**	- [b]	419	515	551	589	645	0.03
***m*-CPTPP-lignin**	- [c]	419	514	550	589	645	0.04

[a] *Q_{IV} = $Q_y(1,0)$ peak; Q_{III} = $Qy(0,0)$, Q_{II} = $Q_x(1,0)$ and Q_I = $Q_x(0,0)$;* [b] *Ratio of the intensities of the Q_{III} and Soret (B) bands;* [b] *There is no lignin in this compound therefore there is no lignin peak;* [c] *Difficult to determine peak maximum as there is a broad band.*

Table 4.6. *Photophysical properties of* ***m-CPTPP*** *and* ***m-CPTPP-lignin***.

PS	λ_{em} $Q_x(0,0)$ (nm) [a]	λ_{em} $Q_x(0,1)$ (nm) [a]	SS (cm^{-1}) [b]	Φ_f [c]	τ_s (ns) [d]	Φ_Δ [e]	τ_T (ns) [f]
***m*-CPTPP**	648	714	72	0.08 ± 0.01	10.3 ± 0.4	0.67 ± 0.03	248 ± 32
***m*-CPTPP-lignin**	648	715	72	0.08 ± 0.01	10.4. ± 0.4	0.60 ± 0.04	239 ± 21

[a] *Emission spectra were determined in chloroform;* [b] *The Stokes shift (SS) was calculated from the corresponding UV-Vis and emission spectra;* [c] *Fluorescence quantum yield calculated in chloroform using* ***TPP*** *in toluene as reference (Φ_f = 0.11).*[37] *Excitation wavelength is 548 nm;* [d] *Singlet excited state lifetime measured in tetrahydrofuran (THF) using TC-SPC; Excitation wavelength is 418 nm and emission wavelength is 650 nm. These fluorescence decays were fitted mono-exponentially;* [e] *Singlet oxygen quantum yield calculated in chloroform using* ***TPP*** *as a reference (Φ_Δ = 0.55).*[45] *Excitation wavelength is 548 nm;* [f] *Triplet lifetime in air (equilibrated) measured in THF using ns-TA spectroscopy, excitation wavelength is 513 nm.*

The UV Vis data shown in Table **4.5** is characteristic of the typical porphyrin compounds and the lignin-porphyrin compound as seen above (**TCPP** subset, Table **4.3**). As seen in Table **4.6**, the overall fluorescence remains the same, and singlet oxygen production is

slightly decreased upon lignin attachment to the porphyrin. The singlet and triplet lifetimes of ***m*-CPTPP** and ***m*-CPTPP-lignin** were determined (Figures **S4.13–S4.16**) and appear to not significantly differ from each other.

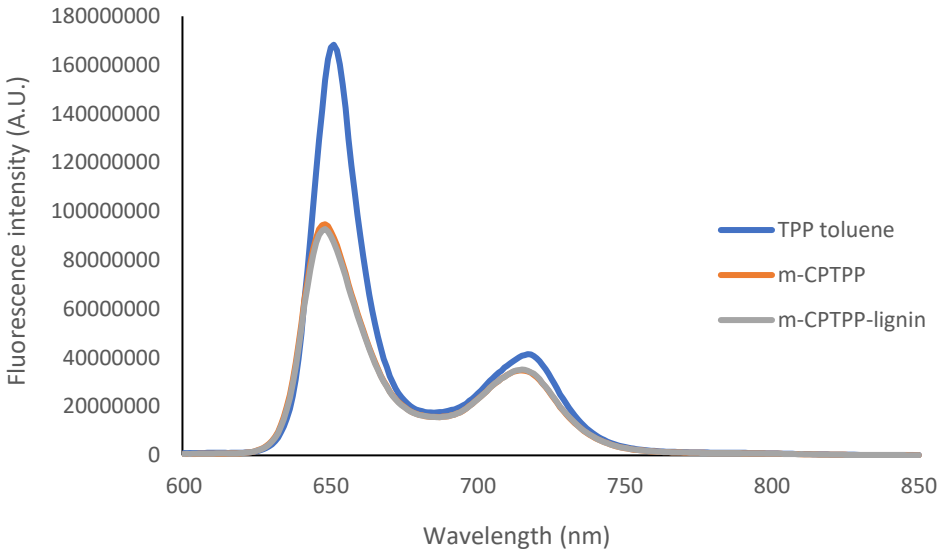

Figure 4.14. *Fluorescence emission spectra of* ***m-CPTPP*** *(orange) and* ***m-CPTPP-lignin*** *(grey) in* $CHCl_3$ *versus the reference* ***TPP*** *(blue) in toluene.*[37] *Excitation wavelength = 548 nm. Concentrations of each solution measured are: 10 µM (****TPP****), 14 µM (****m-CPTPP****) and 14 µM (****m-CPTPP-lignin****; assuming ε of* ***m-CPTPP-lignin*** *= that of* ***m-CPTPP****).*

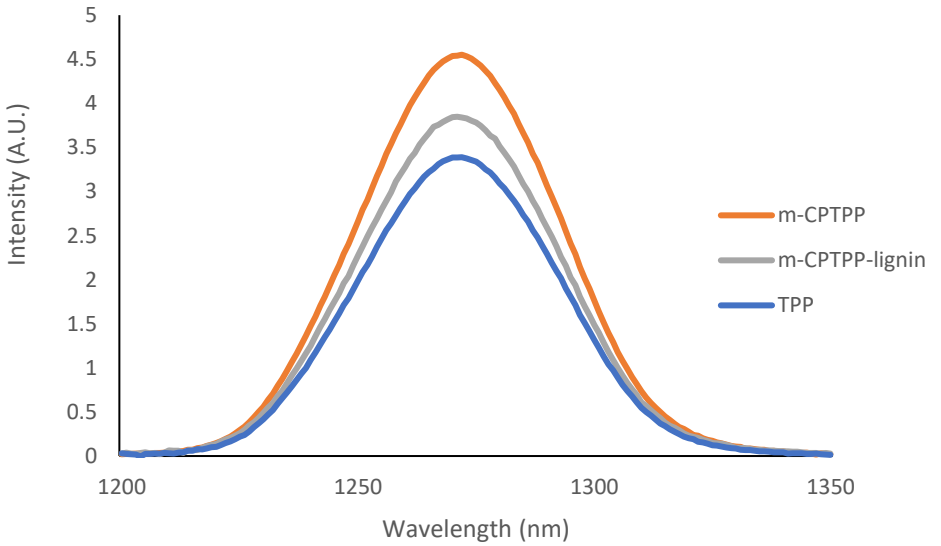

Figure 4.15. *Singlet oxygen emission spectra of* ***m-CPTPP*** *(blue) and* ***m-CPTPP-lignin*** *(orange) in* $CHCl_3$*. The reference used was TPP in* $CHCl_3$ *(*Φ_Δ *= 0.55).*[45] *Excitation wavelength = 548 nm. Concentrations of each solution measured are: 12 µM (****TPP****), 14 µM (****m-CPTPP****) and 14 µM (****m-CPTPP-lignin****; assuming ε of* ***m-CPTPP-lignin*** *= that of* ***m-CPTPP****)*

4.3.3. Lignin and acetylated lignin

In order to quantify the impact of combining lignin to known fluorophores and singlet oxygen generators (cyanines and porphyrins, respectively), the photophysical properties of lignin and acetylated kraft lignin were determined.

Firstly, the UV-Vis of kraft lignin, acetylated kraft lignin and the reference (Zn(II) phthalocyanine) was determined (see Figure **4.16**). From the spectra and based on the structure of these aromatic lignin polymers, they absorb light in the UV region (200–400 nm).

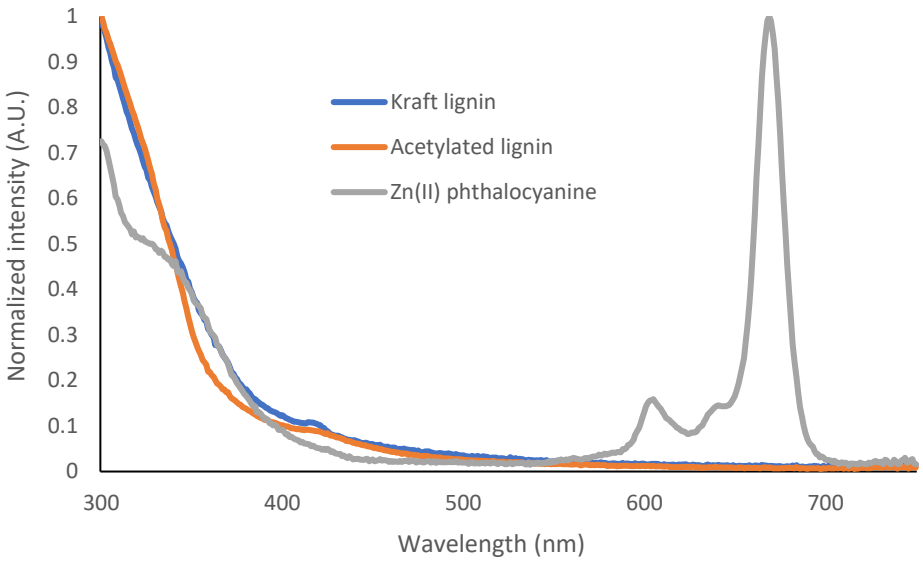

Figure 4.16. *UV-Vis spectra of* ***kraft lignin*** *(blue),* ***acetylated kraft lignin*** *(orange) and* ***Zn(II) Phthalocyanine*** *(grey) in N,N-dimethylformamide (DMF).*

The photoluminescence properties of these lignin compounds were then quantified (Table **4.8**). It follows the same trend as the **TCPP** section where the acetylated lignin has a higher fluorescence and a slightly higher overall singlet oxygen production (Figure **4.17** and **4.18**, respectively). Thus, it can be concluded that the acetylation of kraft lignin increases the fluorescence and the singlet oxygen quantum yield.

Table 4.8. *Photophysical properties of* ***Kraft lignin*** *and* ***acetylated kraft lignin*** *in DMF.*

PS	Em (nm) [a]	Φ_f [c]	Φ_Δ [d]
Kraft lignin	389	0.04	0.17 ± 0.05
Acetylated kraft lignin	412	0.09	0.21 ± 0.05

[a] *Emission maximum in emission spectrum;* [b] *The Stokes shift (SS) calculated from the corresponding UV-Vis and fluorescence spectra.* [c] *Fluorescence quantum yield calculated using Zn(II) phthalocyanine (**Zn(II)Pc**; Φ_f = 0.17 ± 0.03) as a reference in DMF.*[46] *Excitation wavelength = 350 nm;* [d] *Singlet oxygen quantum yield was calculated using Zn(II) phthalocyanine (**Zn(II)Pc**; Φ_Δ = 0.55) as a reference in DMF. Excitation wavelength = 350 nm.*[5]

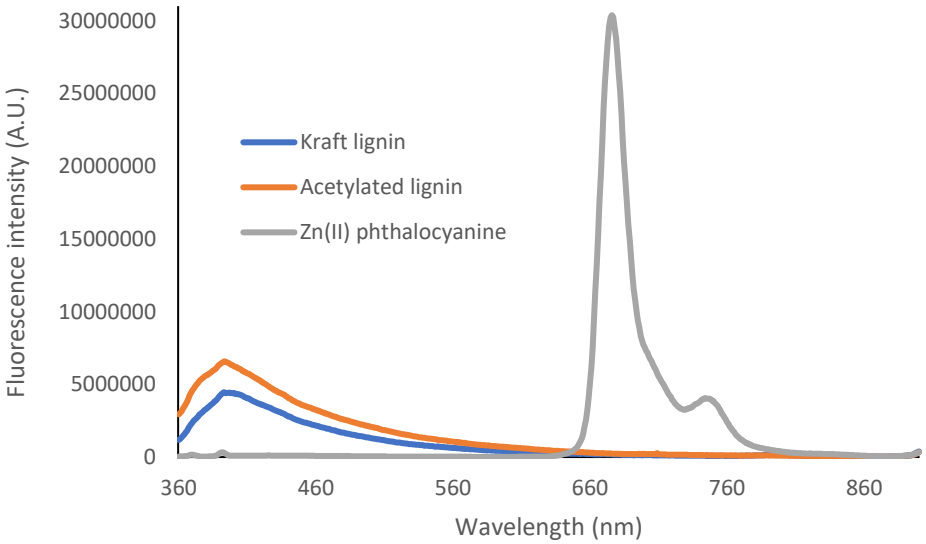

Figure 4.17. *Fluorescence spectra of* ***kraft lignin*** *(blue),* ***acetylated kraft lignin*** *(orange) and* ***Zn(II) phthalocyanine*** *(grey) in DMF. Reference is Zn(II) phthalocyanine in DMF (Φ_f = 0.17 ± 0.03). Excitation wavelength is 350 nm.*[46]

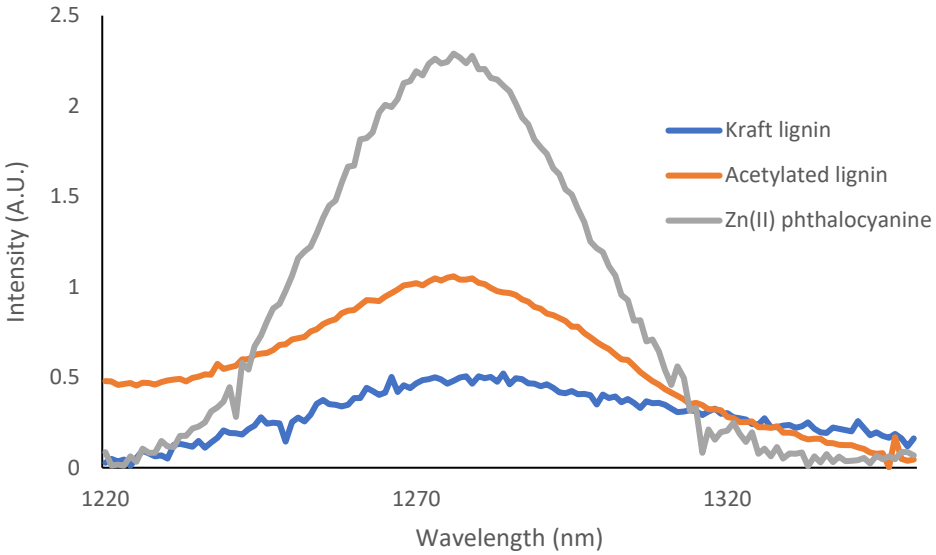

Figure 4.18. *Singlet oxygen spectra of* ***Kraft lignin*** *(blue),* ***Acetylated kraft lignin*** *(orange) and* ***Zn(II) Phthalocyanine*** *(grey) in DMF. Reference is Zn(II) phthalocyanine in DMF (*$\boldsymbol{\Phi_\Delta}$ *= 0.55). Excitation wavelength is 350 nm.*[5]

4.4. Conclusion

Novel lignin systems were synthesized with excellent yields and the porphyrin based systems exhibited efficient activity as novel $^1O_2$ photosensitizers. Lignin was introduced to improve three types of chromophores: a modified commercially available near-IR cyanine dye (**IR-783-SPA**), tetra-4-carboxyphenylporphyrin (**TCPP**) and mono-carboxyphenyl-triphenylporphyrin (***m*-CPTPP**), for their application in photodynamic therapy. Furthermore, the acetylation of the lignin moiety in **TCPP-lignin**, thus creating **TCPP-Ac-lignin**, further enhanced the singlet oxygen generation and the fluorescence. The **IR-783** based system shows negligible singlet oxygen emission.

Future work

In order to further investigate the photochemical mechanisms in these lignin conjugates, it is of interest to further investigate the excited state dynamics upon light excitation. This can be done by exciting the lignin moiety at 280 nm, for example, and observing the fluorescence of the fluorophores (cyanine and porphyrins) in both non-covalent and covalent systems. This can be conducted using TC-SPC and femtosecond transient absorption spectroscopy.

Furthermore, nano-particle formation is possible from these conjugates to enhance water solubility and improve their physicochemical properties as novel photosensitizers. The

compounds discussed in this chapter can be now investigated for their application against cancer, microbial infections *in vitro* and in the environment. In future work, it would be quite interesting to compare these compounds with their nanoparticle counterparts and see what effect lignin, acetylated lignin and their nanoparticles have in biological applications.

4.5. Supplementary information

4.5.1. Experimental procedures

Synthesis of **sodium 4-((E)-2-((E)-2-(2-((4-carboxyphenyl)thio)-3-((E)-2-(3,3-dimethyl-1-(4-sulfonatobutyl)-3H-indol-1-ium-2-yl)vinyl)cyclohex-2-en-1-ylidene)ethylidene)-3,3-dimethylindolin-1-yl)butane-1-sulfonate (IR-783-SPA)**: IR-783 (158 mg, 0.211 mmol, 1.00 eq.) and 4-mercaptobenzoic acid (176 mg, 1.14 mmol, 5.40 eq.) were dissolved in 7 mL dry DMF in a 100 mL three-neck round bottom flask with a stirrer bar. The mixture was allowed to stir at ambient temperature (21°C) for 24 hours under argon. The reaction was monitored *via* TLC analysis (eluent = 8/2 CH_2Cl_2/MeOH). The dark green reaction mixture was then purified *via* a flash column with an eluent gradient of 95/5 dichloromethane/methanol to 8/2 dichloromethane/methanol. The product was obtained as a dark green powder/crystalline solid (**183 mg, 0.210 mmol, >99% yield**). R_f = 0.1 (8/2 dichloromethane/methanol). ^{1}H NMR (DMSO-d_6, 500 MHz): δ (ppm) = 12.85 (br s, 1 H, 1 x COOH), 8.54 (d, *J* = 14.0 Hz, 2 H, 2 x Ar-H), 7.86 (d, *J* = 8.5 Hz, 2 H, 2 x Ar-H), 7.52 (d, *J* = 7.8 Hz, 2 H, 2 x Ar-H), 7.44 (d, *J* = 8.0 Hz, 2 H, 2 x Ar-H), 7.38 (dd, *J* = 6.3, 8.8 Hz, 4 H, 4 x Ar-H), 7.22 (t, *J* = 7.5, 7.5 Hz, 2 H, 2 x vinyl H), 6.40 (d, *J* = 14.3 Hz, 2 H, 2 x vinyl H), 4.18 (t, *J* = 7.5, 6.5 Hz, 4 H, 2 x CH_2), 2.81 (t, *J* = 6.3, 6.3 Hz, 4 H, 2 x CH_2), 1.95 (t, *J* = 6.0, 6.0 Hz, 2 H, 1 x CH_2), 1.68–1.82 (m, *J* = 6.8, 9.0, 6.8, 7.3, 7.5, 14.0, 8.0, 8.3, 6.3 Hz, 8 H, 4 x CH_2), 1.39 (s, 12 H, 4 x CH_3). ^{13}C NMR (DMSO-d_6, 500 MHz): δ (ppm) = 171.8 (**C_{COOH}**), 166.6 (**C_1**), 162.2 (**C_{10}**), 146.9 (**C_{17}**), 144.5 (**C_4**), 142.0 (**C_5**), 141.0 (**C_6**), 133.2 (**C_{12}**), 130.3 (**C_{11}**), 128.4 (**C_2**), 125.2 (**C_3**), 124.8 (**C_{16}**), 122.3 (**C_{13}**), 111.5 (**C_{15}**), 101.9 (**C_{14}**), 50.6 (**C_9**), 48.6 (**C_8**), 43.6 (**C_{18}**), 35.7 (**C_{21}**), 27.0 (**C_{19}**), 26.0 (**C_{20}**), 25.8 (**C_7**), 22.4 (**C_{22}**), 20.3 (**C_{23}**). UV-Vis (MeOH) λ_{max} (log ε) = 798 nm (3.32). IR (cm^{-1}) = 3054, 2964, 2923, 2861.

Synthesis of IR-783-SPA-kraft lignin conjugate (IR-783-SPA-lignin):[29] IR-783-SPA (100 mg, 0.11 mmol, 1.00 eq.), kraft lignin (190 mg) and triphenylphosphine (260 mg, 0.99 mmol, 9.00 eq.) were dissolved in 15 mL dry DMF in a 50 mL two-neck round bottom flask. The mixture was stirred to dissolve all solids and then di-isopropylazodicarboxylate (0.1 mL, 100 mg, 0.51 mmol, 4.64 eq.) was added to the reaction mixture. The reaction mixture was allowed to stir under argon at 65°C for 18 hours. After cooling the reaction to room temperature, the contents were transferred to membranes to undergo dialysis for 48 hours before freeze drying for 72 hours to obtain a dark green powder (**310 mg, >99% mass yield**). ^{1}H NMR (DMSO-d_6, 500 MHz): δ (ppm) = 12.86 (br s, $H_{lignin\text{-}COOH}$), 8.54 (d, *J* = 14.0 Hz, 2 H, 2 x Ar-H), 7.85–7.88 (d, *J* = 8.5 Hz, 2 H, 2 x Ar-H), 7.60–7.70 (m, *J* = 7.0, 6.5, 8.9, 8.3, 4.5, 7.3 Hz, 22 H, 22 x H_{lignin}), 7.53–7.58 (m, *J* = 4.3, 4.3, 2.5, 5.0, 3.0, 3.5, 7.5 Hz, 14 H, 14 x H_{lignin}), 7.52 (d, *J* = 7.8 Hz, 2 H, 2 x Ar-H), 7.44 (d, *J* = 8.0 Hz, 2 H, 2 x Ar-H), 7.38 (dd, *J* = 6.3, 8.8 Hz, 4 H, 4 x Ar-H), 7.20–7.26 (m, *J* = 4.0, 3.8, 4.5, 7.3, 7.3, Hz, 4 H, 4 x Ar-H), 6.40 (d, *J* = 14.3 Hz, 2 H, 2 x H_{vinyl}), 4.18 (t, *J* = 7.5, 6.5 Hz, 4 H, 2 x CH_2), 3.50–3.90 (br s, 31 H, 31 x H_{lignin}), 2.81 (t, *J* = 6.3, 6.3 Hz, 4 H, 2 x CH_2), 1.95 (t, *J* = 6.0, 6.0 Hz, 2 H, 1 x CH_2), 1.68–1.83 (m, *J* = 6.8, 9.0, 6.8, 7.3, 7.5, 14.0, 8.0, 8.3, 6.3 Hz, 8 H, 4 x CH_2), 1.39 (s, 12 H, 4 x CH_3). ^{13}C NMR (DMSO-

d_6, 500 MHz): δ (ppm) = 171.8 (**C_{COOR}**), 166.6 (**C_1**), 146.9 (**C_2**), 144.5 (**C_3**), 142.8 (**C_4**), 142.0 (**C_5**), 141.0 (**C_6**), 133.2 (**C_7**), 133.0 (**C_{Li}**), 132.2 (**C_{Li}**), 131.9 (**C_{Li}**), 131.9 (**C_{Li}**), 131.7 (**C_{Li}**), 131.6 (**C_{Li}**), 131.4 (**C_{Li}**), 131.3 (**C_{Li}**), 130.3 (**C_{Li}**), 128.7 (**C_{Li}**), 128.6 (**C_{Li}**), 128.4 (**C_{Li}**) 127.7 (**C_{20}**), 125.2 (**C_{21}**), 124.9 (**C_{22}**), 122.2 (**C_{23}**), 111.5 (**C_{24}**), 101.9, (**C_{25}**) 55.5 (**C_{Li}**), 50.6 (**C_{27}**), 48.6 (**C_{28}**), 43.7 (**C_{29}**), 27.0 (**C_{30}**), 26.0 (**C_{31}**), 25.8 (**C_{32}**), 22.4 (**C_{33}**). UV-Vis (DMSO) λ_{max} = 265 and 811 nm. IR (cm^{-1}) = 3369, 2933.

Synthesis of 5,10,15,20-Tetra-(4-kraft lignin-carboxyphenyl)porphyrin conjugate (TCPP-lignin):[29] 5,10,15,20-tetra-(4-carboxyphenyl)porphyrin (TCPP, 310 mg, 0.39 mmol, 1.00 eq.), kraft lignin (490 mg) and triphenylphosphine (280 mg, 1.06 mmol, 2.72 eq.) were dissolved in 15 mL dry DMF in a 100 mL three-neck round bottom flask using the stirrer bar. Once this mixture was dissolved, di-isopropylazodicarboxylate (0.2 mL, 210 mg, 1.02 mmol, 2.62 eq.) was added into the side neck *via* a syringe. The mixture was stirred under argon at 65°C for 16 hours. After cooling to room temperature, the mixture was transferred to membranes to undergo dialysis for 48 hours before being freeze dried for 36 hours. The product was obtained as a **brown powder** (**880 mg, >99% mass yield**). ^{1}H NMR (DMSO-d_6, 500 MHz): δ (ppm) = 13.26 (s, 4 H, 4 x $COOH_{lignin}$), 8.86 (s, 8 H, 8 x $H_{β\text{-pyrrole}}$), 8.34–8.41 (dd, *J* = 8.0, 8.5 Hz, 16 H, 4 x $H_{2, 3, 5, 6\text{-aryl}}$), 7.60–7.65 (m, *J* = 7.3, 4.7, 7.3 Hz, 19 H, 19 x H_{lignin}), 7.53–7.58 (m, *J* = 5.1, 7.5, 4.5, 3.5 Hz, 13 H, 13 x H_{lignin}), 6.38–7.25 (br s, 17 H, 17 x H_{lignin}), 3.53–3.94 (br s, 22 H, 22 x H_{lignin}), -2.92 (s, 2 H, 2 x N-H). ^{13}C NMR (DMSO-d_6, 500 MHz): δ (ppm) = 167.3 (**C_1**), 162.2 (**C_{Li}**), 156.1 (**C_{Li}**), 145.4 (**C_4**), 134.4 (**C_5**), 133.0 (**C_{Li}**), 132.2 (**C_{Li}**), 131.9 (**C_{Li}**), 131.9 (**C_{Li}**) 131.4 (**C_{Li}**), 131.4 (**C_{Li}**), 130.4 (**C_{Li}**), 128.7 (**C_{Li}**), 128.6 (**C_{13}**), 127.8 (**C_{14}**), 119.2 (**C_{15}**), 67.6 (**C_{Li}**), 55.5 (**C_{Li}**), 35.7 (**C_{Li}**), 30.7 (**C_{Li}**), 21.8 (**C_{Li}**). UV-Vis (DMSO) λ_{max} = 288, 421, 516, 551, 590 and 646 nm. IR (cm^{-1}) = 3314, 3056, 2936.

Synthesis of 5,10,15,20-Tetra-(4-acetylated-kraft lignincarboxyphenyl)porphyrin conjugate (TCPP-Ac-lignin):[5] TCPP-lignin (55 mg) was dissolved in Ac_2O/dry pyridine (10 mL, 1/1 v/v) in a three-neck 100 mL round bottom flask with a stirrer bar under argon. The solution was stirred at room temperature (21°C) for 48 hours. After 48 hours, the reaction was transferred into 100 mL HCl 1 M and washed with 50 mL deionized water. The precipitate was dissolved in chloroform and washed with 3 x 100 mL deionized H_2O. The organic phase was dried over $MgSO_4$, filtered into a new pre-weighed round bottom flask and evaporated to obtain a **brown solid** (**31 mg, 56% mass yield**). ^{1}H NMR (DMSO-d_6, 500 MHz): δ (ppm) = 12.96 (s, 4 H, 4 x $COOH_{lignin}$), 8.87 (s, 8 H, 8 x $H_{β\text{-pyrrole}}$), 8.32–8.44 (dd, *J* = 8.0, 8.5 Hz, 16 H, 4 x $H_{2, 3, 5, 6\text{-aryl}}$), 7.59–7.70 (m, *J* = 7.3, 4.7, 7.3 Hz, 16 H, 16 x H_{lignin}), 7.50–7.58 (m, *J* = 5.1, 7.5, 4.5, 3.5 Hz, 10 H, 10 x H_{lignin}), 2.14–2.31 (br s, 15 H, 5 x $CH_{3\text{-acetyl}}$), 1.85–2.00 (br s, 15 H, 5 x $CH_{3\text{-acetyl}}$), -2.92 (s, 2 H, 2 x N-H). ^{13}C NMR (DMSO-d_6, 500 MHz): δ (ppm) = 167.9 (**C_{COOR}**), 145.9 (**C_1**), 135.0 (**C_2**), 133.7 (**C_{Li}**), 132.7 (**C_{Li}**), 132.5 (**C_{Li}**), 132.5 (**C_{Li}**), 132.0 (**C_7**), 131.0 (**C_{Li}**), 129.2 (**C_9**), 128.4 (**C_{10}**), 119.8 (**C_{11}**), 29.5 (**C_{Li}**), 28.7 (**C_{Li}**). IR (cm^{-1}) = 2920 (acetyl C-H stretch), 2851 (acetyl C-H stretch), 1760 (acetyl C=O stretch).

Synthesis of 5-(4-kraft lignin-phenyl)-10,15,20-triphenylporphyrin conjugate (*m*-CPTPP-lignin):[29] 5-(4-carboxyphenyl)-10,15,20-triphenylporphyrin (110 mg, 0.16 mmol, 1.00 eq.), kraft lignin (190 mg) and triphenylphosphine (160 mg, 0.60 mmol, 3.75 eq.) were dissolved in 20 mL dry DMF in a 50 mL two-neck round bottom flask, under argon and containing a stir bar. Once dissolved, di-isopropyl-azodicarboxylate (0.10 mL, 100 mg, 0.51 mmol, 3.40 eq.) was added dropwise to the reaction *via* the side neck. The reaction was allowed to stir at 65°C for 17 hours under argon. Once cooled to room temperature, the mixture was transferred, *via* a pipette, to membranes to undergo dialysis for 48 hours and freeze dried for 72 hours to obtain a **brown powder** (**320 mg, >99% mass yield**). ^{1}H NMR (DMSO-d_6, 500 MHz): δ (ppm) =

13.30 (br s, 1 H, 1 x $H_{lignin\text{-}COOH}$), 8.84 (s, 8 H, 8 x $H_{\beta\text{-}pyrrole}$), 8.33–8.40 (dd, *J* = 8.3, 12, 8.3 Hz, 4 H, 2 x $Aryl_{2,6}$-H + 2 x $Aryl_{3,5}$-H), 8.23 (d, *J* = 5.8 Hz, 6 H, 6 x $Aryl_{2,6}$-H), 7.81–7.88 (m, *J* = 6.0, 6.8, 7.5, 6.3, 9.0 Hz, 9 H, 9 x $Aryl_{3,4,5}$-H), 7.53–7.65 (m, *J* = 7.3, 5.0, 6.8, 3.0, 4.0, 3.0, 8.3, 3.8 Hz, 16 H, 16 x H_{lignin}), 6.38–7.27 (br s, 5 x H_{lignin}), 3.48–3.95 (br s, 9 H, 9 x H_{lignin}), -2.92 (s, 2 H, 2 x $N_{pyrrole}$-H). ^{13}C NMR (DMSO-d_6, 500 MHz): δ (ppm) = 167.4 (**C_{COOR}**), 145.6 (**C_1**), 141.1 (**C_2**), 134.3 (**C_3**), 134.1 (**C_4**), 133.0 (**C_5**), 132.2 (**C_6**), 131.9 (**C_7**), 131.4 (**C_8**), 130.3 (**C_9**), 128.6 (**C_{10}**), 128.0 (**C_{11}**), 127.8 (**C_{12}**), 126.9 (**C_{13}**), 120.2 (**C_{14}**), 120.1 (**C_{15}**), 118.6 (**C_{16}**), 79.1 (**C_{17}**), 55.5 (**C_{18}**), 21.8 (**C_{19}**). IR (cm^{-1}) = 3675, 3315, 2988, 2972, 2902, 1688. UV-Vis (DMSO) λ_{max} = 288, 419, 514, 550, 589 and 645 nm.

Component analysis of lignin-containing conjugates

A small amount of sample of the product was weighted, dissolved and diluted. UV-Vis was used to determine the concentration of chromophore (cyanine or porphyrin) in solution. (Molar absorption coefficients of lignin-containing conjugates were assumed to be the same as the pristine chromophores). This concentration was used to calculate the number of moles of chromophore in the sample and thereby the weight contribution.

The rest of the weight of the sample is therefore attributed to the lignin. Assuming the same number of moles of lignin-oligomer in the sample (corrected for the mono- or tetra-functionalization of the chromophore), the average molecule weight of the attached lignin oligomers was determined. For a typical monomeric unit 317 g/mol was used.

Using the Beer-Lambert law,[47] the concentration in moles per litre (mol/L) was obtained using equation **4.1**.

$$A = \varepsilon . C . l \qquad \text{(Equation } \mathbf{4.1}\text{)}$$

Where A = absorbance, ε = molar absorption coefficient ($M^{-1}.cm^{-1}$), C = concentration (M) and l = path length (1 cm).

Photophysical characterization

For all UV-Vis spectra, photoluminescence and nanosecond absorption spectroscopy shown, the instrumentation used is detailed in Chapter **3** (section **3.4.2**).

4.5.2. Supplemental spectra

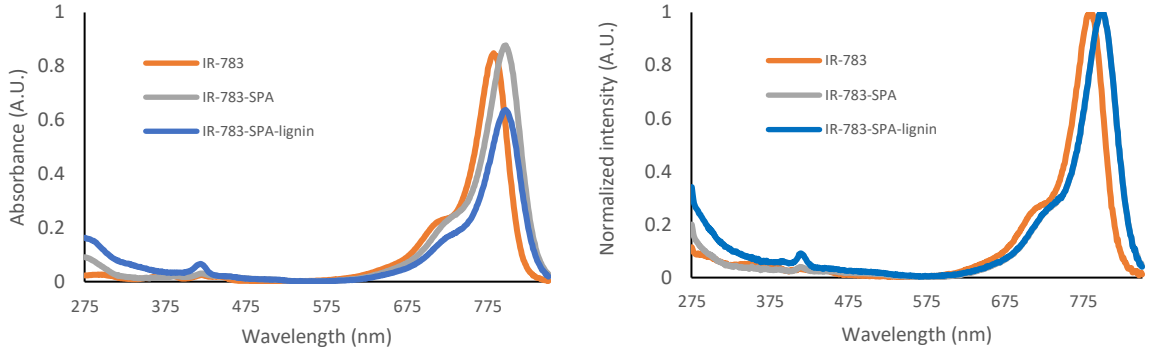

Figure S4.1. (A): *UV-Vis spectra of* ***IR-783*** *(orange),* ***IR-783-SPA*** *(grey) and* ***IR-783-SPA-lignin*** *(blue) in MeOH;* ***(B):*** *Normalized UV-Vis spectra of* ***IR-783*** *(orange),* ***IR-783-SPA*** *(grey) and* ***IR-783-SPA-lignin*** *(blue) in MeOH.*

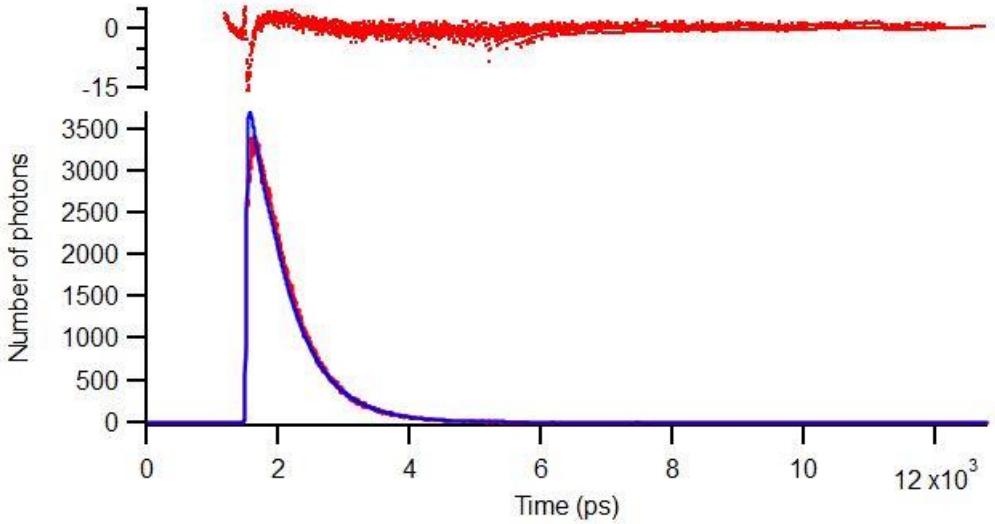

Figure S4.2. *Time-correlated single photon counting (TC-SPC) spectrum of* ***IR-783*** *in MeOH. Excitation wavelength = 720 nm and emission wavelength = 800 nm. Absorbance = 0.2 at the excitation wavelength. Laser power = 0.44 mW and the decay curve is fitted mono-exponentially. Singlet lifetime = 0.56 ± 0.02 ns. IRF = 40 ps. On the top, weighted residuals are presented.*

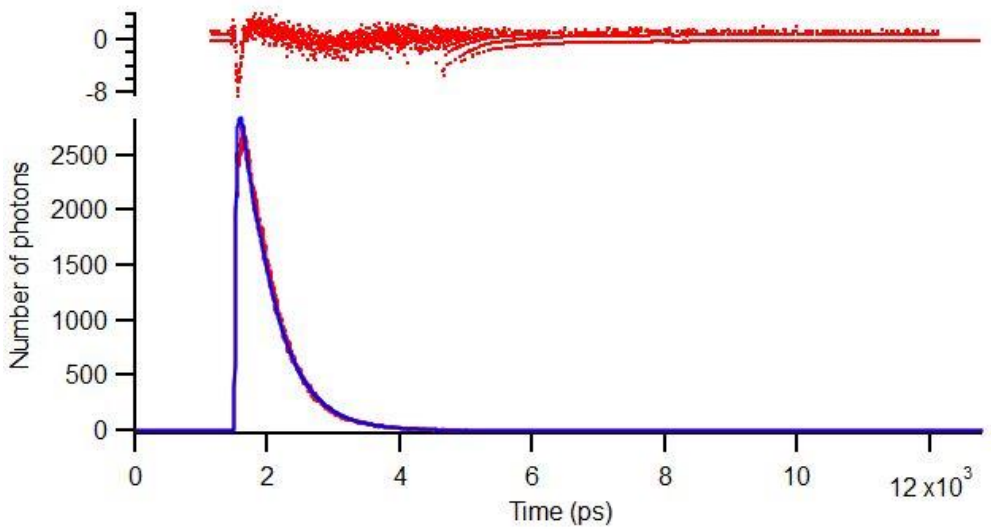

Figure S4.3. *TC-SPC spectrum of* ***IR-783-SPA*** *in MeOH. Excitation wavelength = 720 nm and emission wavelength = 800 nm. Absorbance = 0.2 at the excitation wavelength. Laser power = 0.44 mW and the decay curve is fitted mono-exponentially Singlet lifetime = 0.47 ± 0.1 ns. IRF = 40 ps. On the top, weighted residuals are presented.*

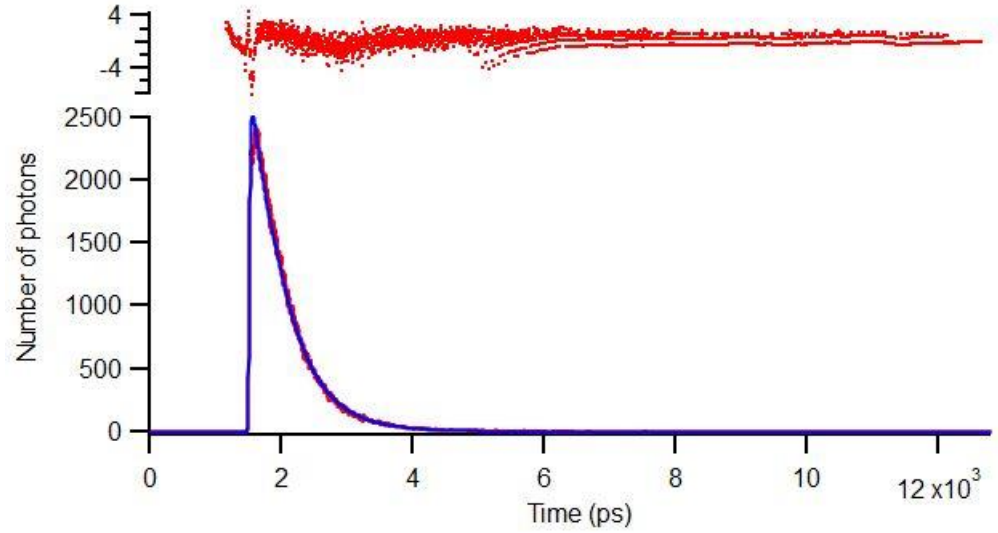

Figure S4.4. *TC-SPC spectrum of* ***IR-783-SPA-lignin*** *in MeOH. Excitation wavelength = 720 nm and emission wavelength = 800 nm. Absorbance = 0.2 at the excitation wavelength. Laser power = 0.44 mW and the decay curve is fitted bi-exponentially. Singlet lifetime of the cyanine = 0.52 ± 0.3 ns (Amplitude = 2081) and τ_2 = 0.47 + 0.2 ns (Amplitude = 2001). IRF = 40 ps. On the top, weighted residuals are presented.*

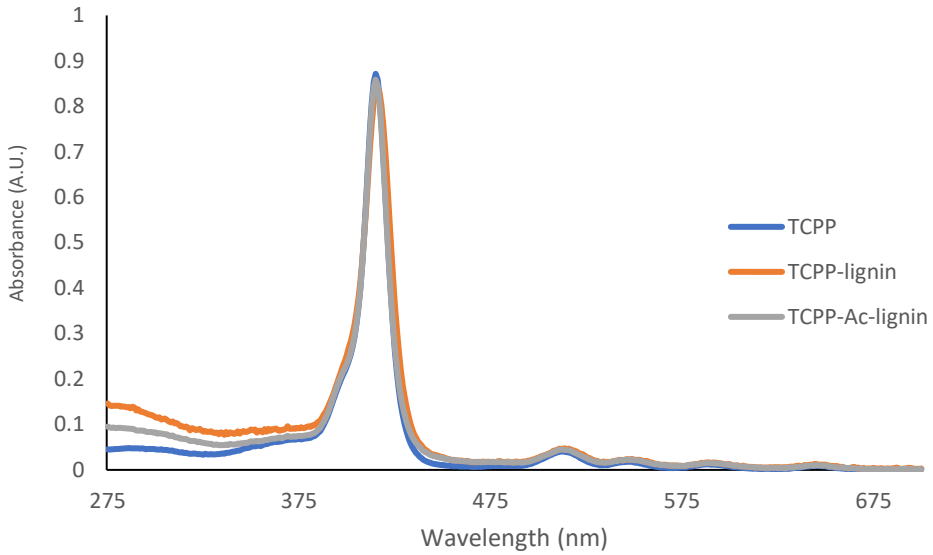

Figure S4.5. *UV-Vis spectra at room temperature of* ***TCPP*** *(blue),* ***TCPP-lignin*** *(orange) and* ***TCPP-Ac-lignin*** *(grey) in MeOH.*

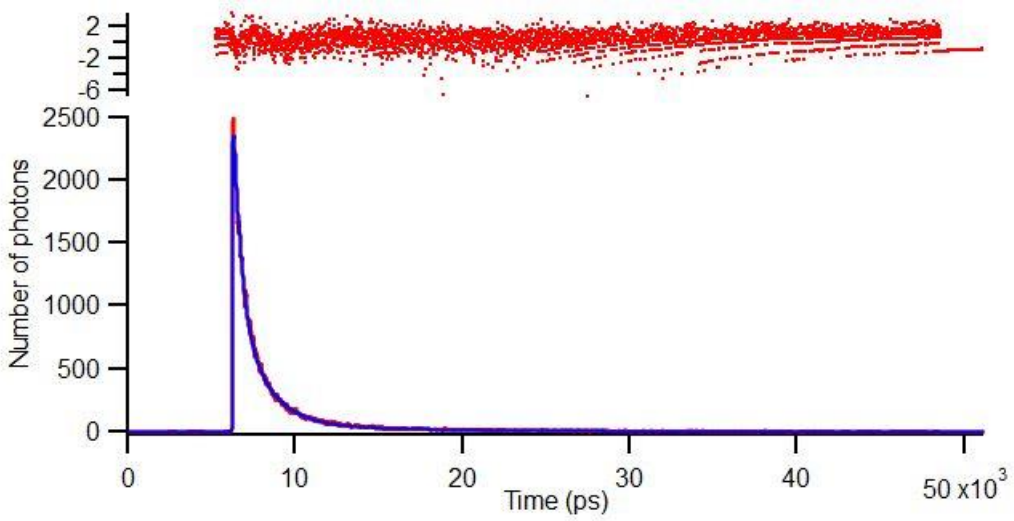

Figure S4.6. *TC-SPC spectrum of* ***TCPP*** *in MeOH. Excitation wavelength = 415 nm and emission wavelength = 650 nm. Absorbance = 0.2 at the excitation wavelength and laser power is 0.44 mW.* ***TCPP*** *decays tetra-exponentially. Singlet lifetime (τ_1) of the porphyrin = 11.9 $\pm$ 0.3 ns (Amplitude = 312). Other lifetimes obtained are: τ_2 = 5.8 + 1.7 ns (Amplitude = 623), τ_3 = 2.3 + 0.7 ns (Amplitude = 1246) and τ_4 = 0.9 + 0.5 ns (Amplitude = 1447). Weighted residuals are shown on the top of the graph. IRF = 50 ps.*

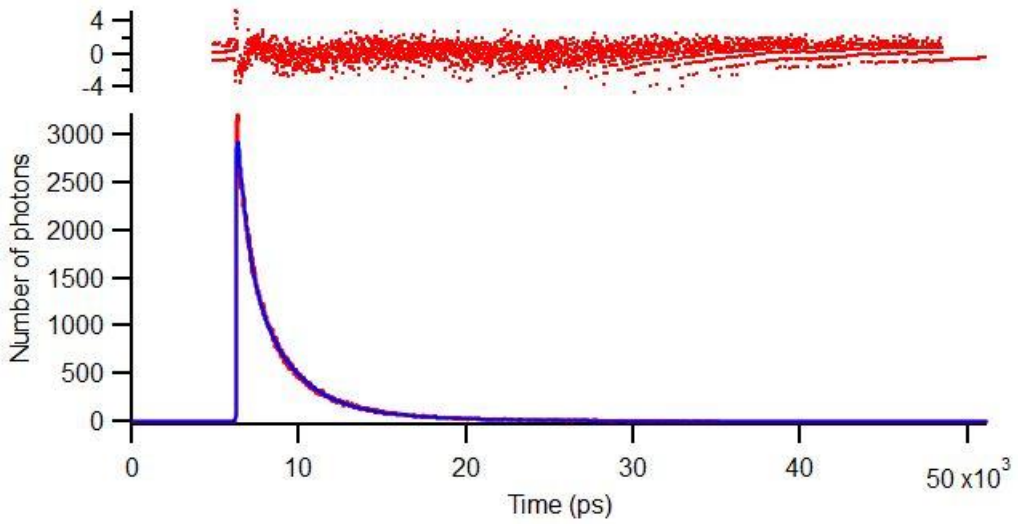

Figure S4.7. *TC-SPC spectrum of* ***TCPP-lignin*** *in MeOH. Excitation wavelength = 420 nm and emission wavelength = 650 nm. The absorbance was 0.15 at the excitation wavelength and laser power is 0.44 mW.* ***TCPP-lignin*** *decays tetra-exponentially. Singlet lifetime (τ_1) of the porphyrin = 12.2 $\pm$ 0.6 ns (Amplitude = 403). Other lifetimes obtained are: τ_2 = 5.8 + 1.3 ns (Amplitude = 805), τ_3 = 2.9 + 0.6 ns (Amplitude = 1610) and τ_4 = 1.0 + 0.5 ns (Amplitude = 3220). Weighted residuals are shown on the top of the graph. IRF = 50 ps.*

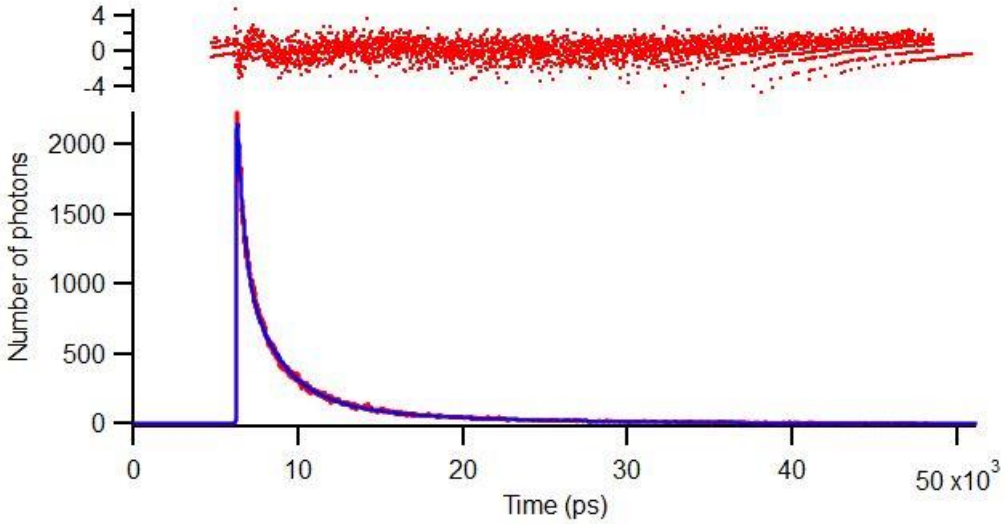

Figure S4.8. *TC-SPC spectrum of* ***TCPP-Ac-lignin*** *in MeOH. Excitation wavelength = 420 nm. Emission wavelength = 650 nm. The absorbance was 0.15 at the excitation wavelength and laser power is 0.44 mW.* ***TCPP-Ac-lignin*** *decays tetra-exponentially.*

Singlet lifetime (τ_1) of the porphyrin = 12.9 $\pm$ 1.3 ns (Amplitude = 54). Other lifetimes obtained are: τ_2 = 6.3 + 0.5 ns (Amplitude = 168), τ_3 = 2.4 + 0.5 ns (Amplitude = 1011) and τ_4 = 0.9 + 0.5 ns (Amplitude = 1342). Weighted residuals are shown on the top of the graph. IRF = 50 ps.

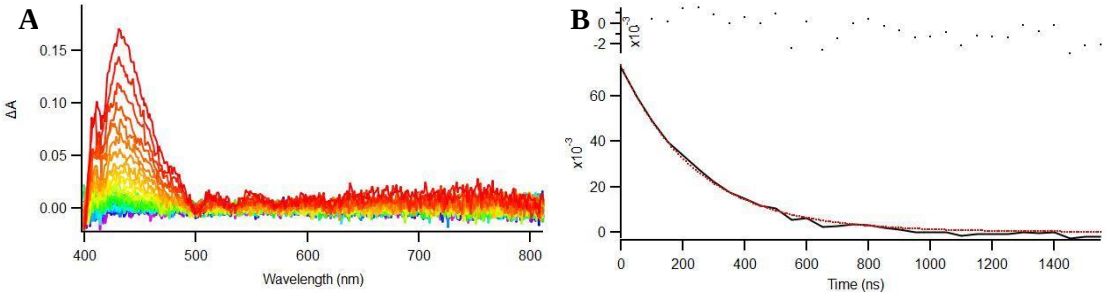

***Figure S4.9. (A)**: Nanosecond transient absorption spectrum of **TCPP** in MeOH (in air). λ_{ex} = 515 nm, incremental time delay = 50 ns. **(B)**: Decay kinetics trace at 515 nm. Decay curve is fitted mono-exponentially and the obtained triplet lifetime (T_1) is 252± 32 ns. Weighed residuals are shown on the top of the graph.*

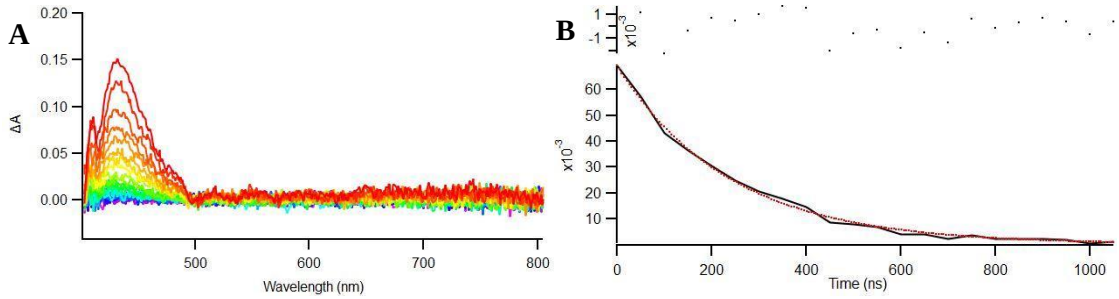

***Figure S4.10. (A)**: Nanosecond transient absorption spectrum of **TCPP-lignin** in MeOH (in air). λ_{ex} = 515 nm, incremental time delay = 50 ns. **(B)**: Decay kinetics trace at 515 nm. Decay curve is fitted mono-exponentially and the obtained triplet lifetime (T_1) is 234 ± 26 ns. Weighed residuals are shown on the top of the graph.*

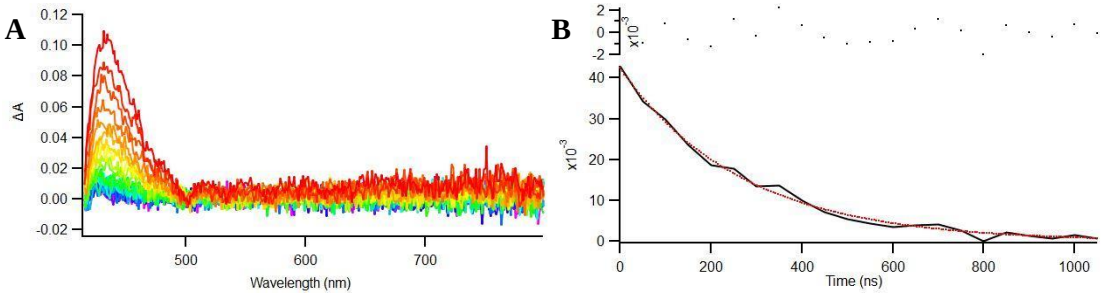

***Figure S4.11. (A)**: Nanosecond transient absorption spectrum of **TCPP-Ac-lignin** in MeOH (in air). λ_{ex} = 515 nm, incremental time delay = 50 ns. **(B)**: Decay kinetics trace at 515 nm. Decay curve is fitted mono-exponentially and the obtained triplet lifetime (T_1) is 276 ± 45 ns. Weighed residuals are shown on the top of the graph.*

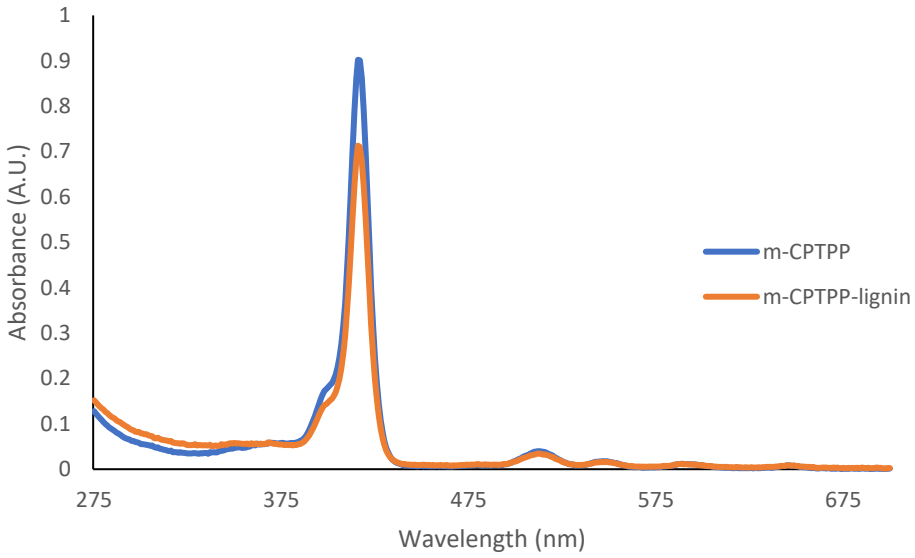

Figure S4.12. *UV-Vis spectra at room temperature of* ***m-CPTPP*** *(blue) and* ***m-CPTPP-lignin*** *(orange) in chloroform ($CHCl_3$).*

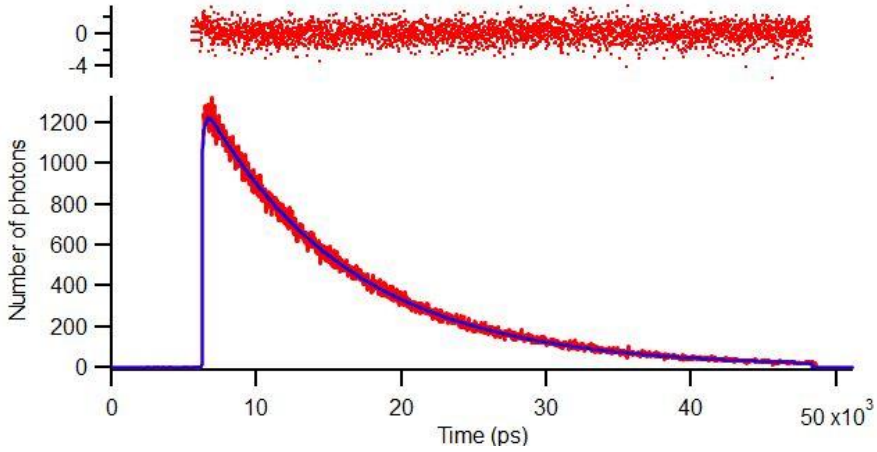

Figure S4.13. *TC-SPC spectrum of* ***m-CPTPP*** *in tetrahydrofuran (THF). Excitation wavelength = 420 nm and emission wavelength = 650 nm. The absorbance was 0.15 at the excitation wavelength and laser power is 0.44 mW.* ***m-CPTPP*** *decays mono-exponentially and the S_1 lifetime in these conditions is 10.3 ± 0.4 ns. Weighted residuals are shown on the top of the graph. IRF = 50 ps.*

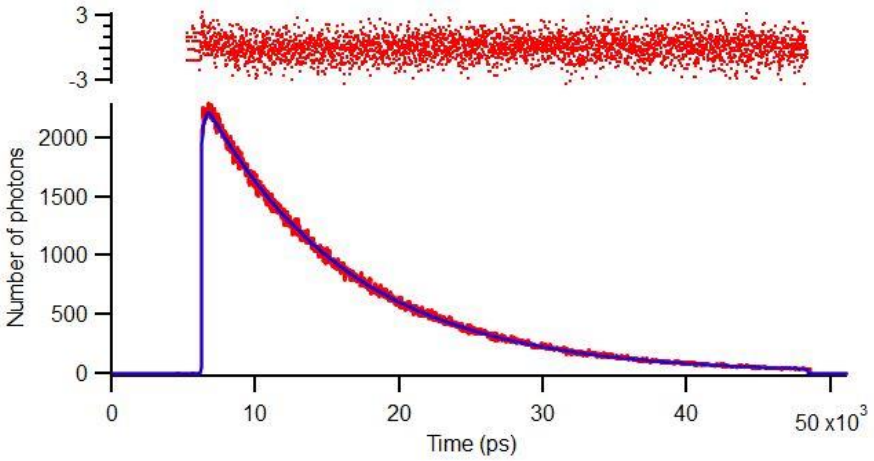

Figure S4.14. *TC-SPC spectrum of* ***m-CPTPP-lignin*** *in THF. Excitation wavelength = 420 nm and emission wavelength = 650 nm. The absorbance was 0.15 at the excitation wavelength and laser power is 0.44 mW.* ***m-CPTPP-lignin*** *decays mono-exponentially and the S_1 lifetime in these conditions is 10.4 ± 0.4 ns. Weighted residuals are shown on the top of the graph. IRF = 50 ps.*

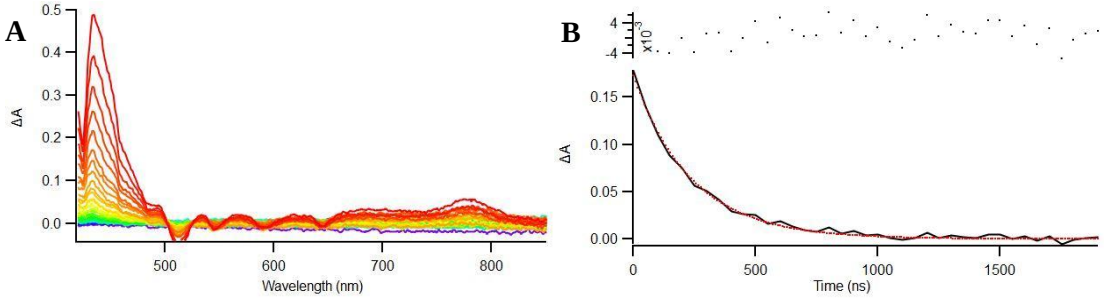

Figure S4.15. (A)*: Nanosecond transient absorption spectrum of* ***m-CPTPP*** *in THF (in air). λ_{ex} = 513 nm, incremental time delay = 50 ns.* ***(B)****: Decay kinetics trace at 513 nm. Decay curve is fitted mono-exponentially and the obtained triplet lifetime (T_1) is 248 ns. Weighed residuals are shown on the top of the graph.*

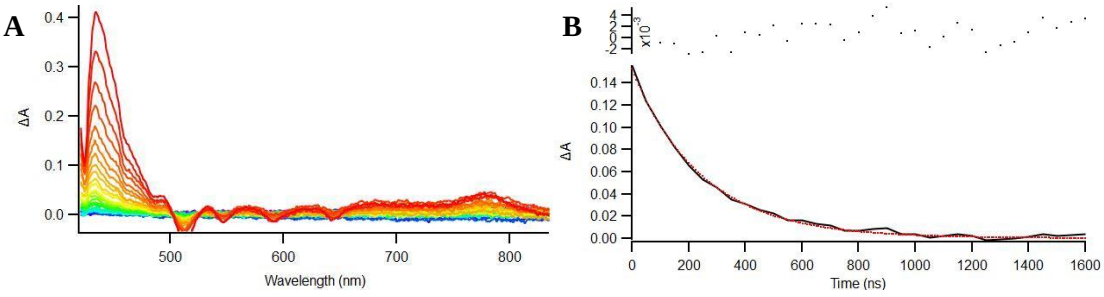

Figure S4.16. (A)*: Nanosecond transient absorption spectrum of* ***m-CPTPP-lignin*** *in THF (in air). λ_{ex} = 513 nm, incremental time delay = 50 ns.* ***(B)****: Decay kinetics trace at 513 nm. Decay curve is fitted mono-exponentially and the obtained triplet lifetime (T_1) is 239 ns. Weighed residuals are shown on the top of the graph.*

4.5.3. Synthetic characterization

4.5.3.1. Lignin-cyanine synthetic characterization

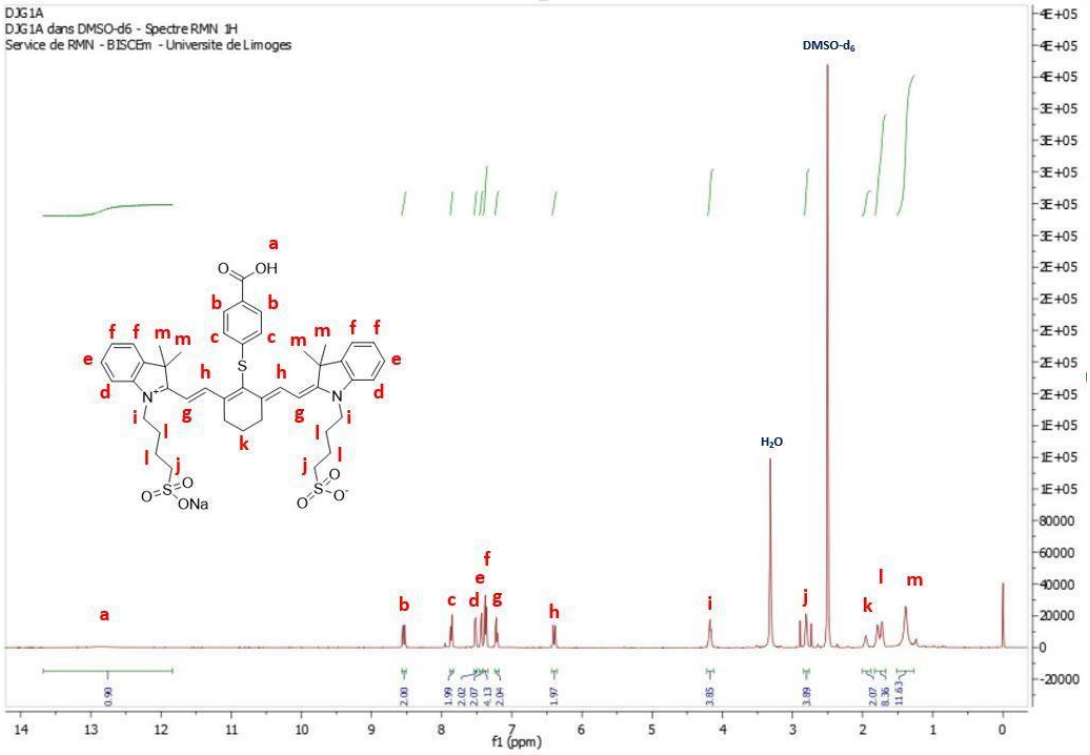

Figure S4.17. *Fully Integrated ^{1}H NMR spectrum at room temperature of* ***IR-783-SPA****, in DMSO-d_6, with the structure and labels for the protons in the structure.*

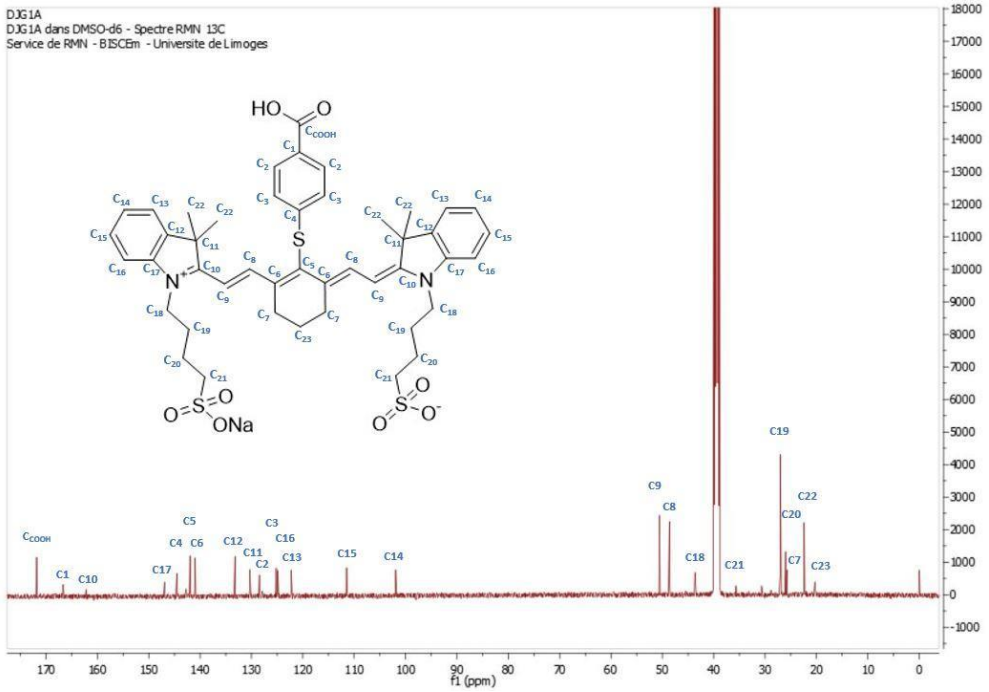

Figure S4.18. *^{13}C NMR spectrum at room temperature of sodium* ***IR-783-SPA*** *in DMSO-d_6, with the structure and labels for the carbons in the structure.*

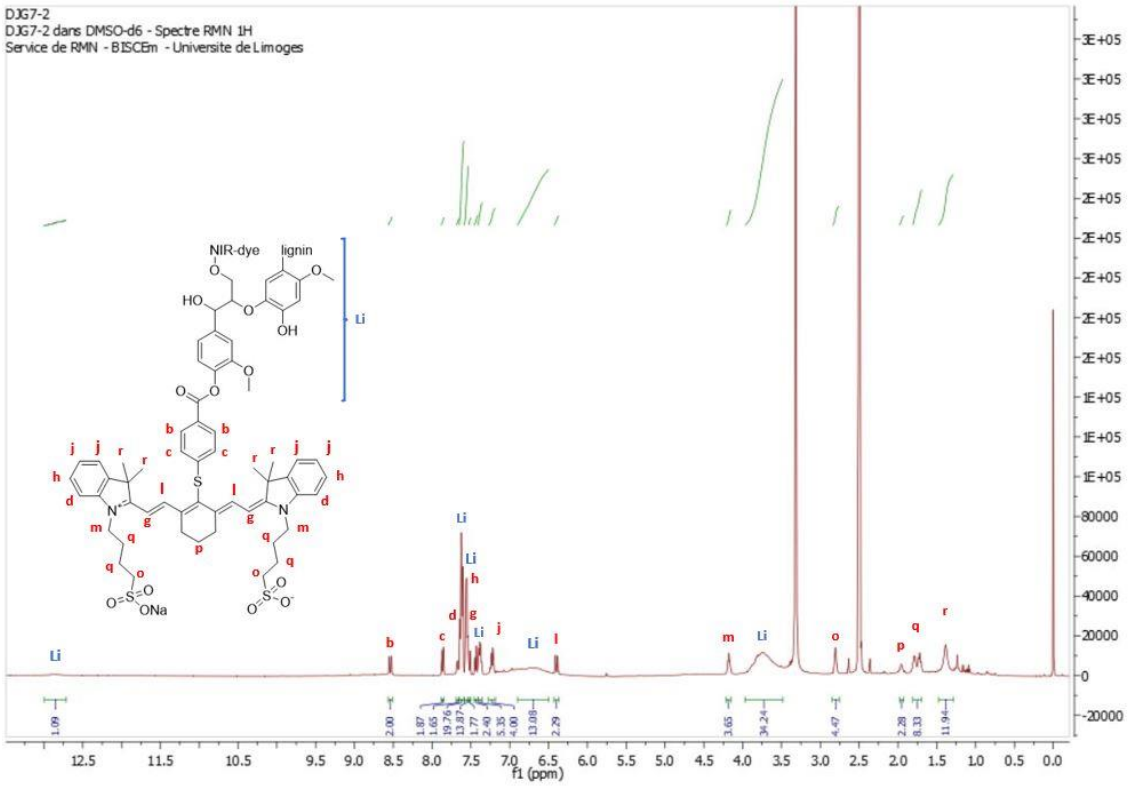

Figure S4.19. *Fully Integrated ^{1}H NMR spectrum at room temperature of* ***IR-783-SPA-lignin*** *in DMSO-d_6, with labels in spectrum indicating which protons belong to the* ***IR-783-SPA*** *moiety and which belong to kraft lignin.* ***Note:*** *Li = protons that belong to lignin. The two big peaks at 3.3 and 2.50 ppm correspond to water and DMSO-d_6, respectively.*

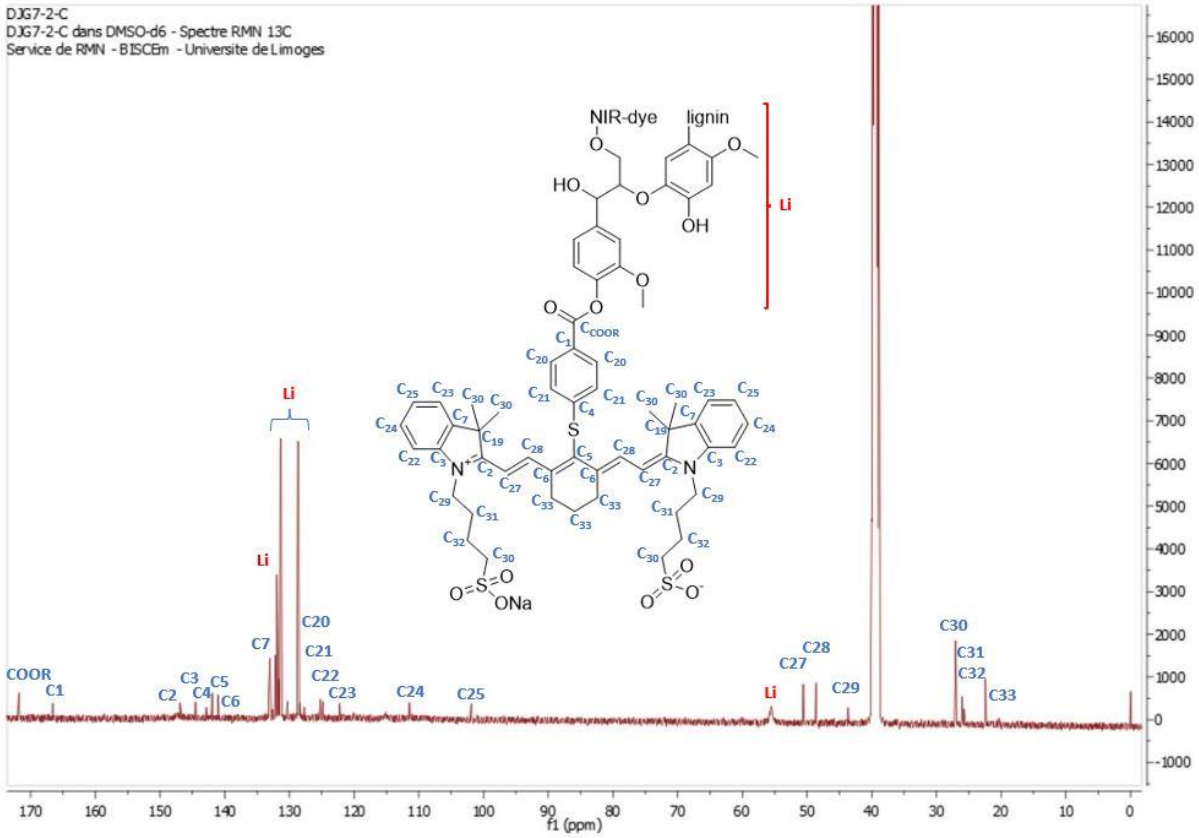

Figure S4.20. *^{13}C NMR spectrum at room temperature of* ***IR-783-SPA-lignin*** *in DMSO-d6, with labels in spectrum indicating which carbons belong to the* ***IR-783-SPA*** *moiety and which belong to kraft lignin.* ***Note:*** *Li = carbons that belong to lignin.*

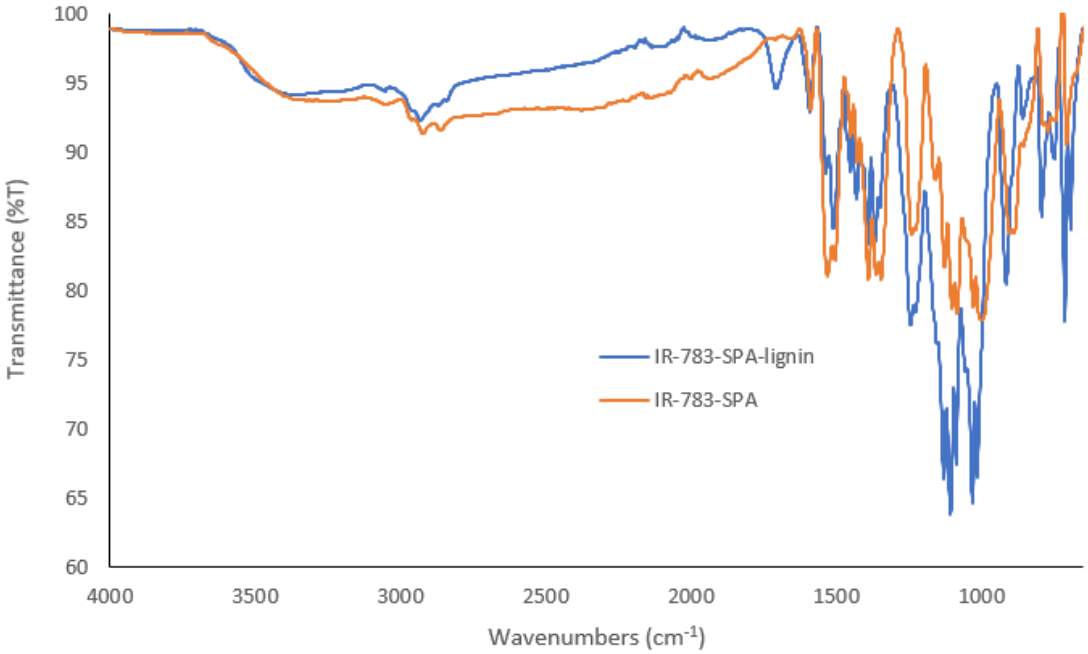

Figure S4.21. *IR spectrum at room temperature of* ***IR-783-SPA-lignin*** *(blue) and* ***IR-783-SPA*** *(orange).*

4.5.3.2. TCPP-lignin synthetic characterization

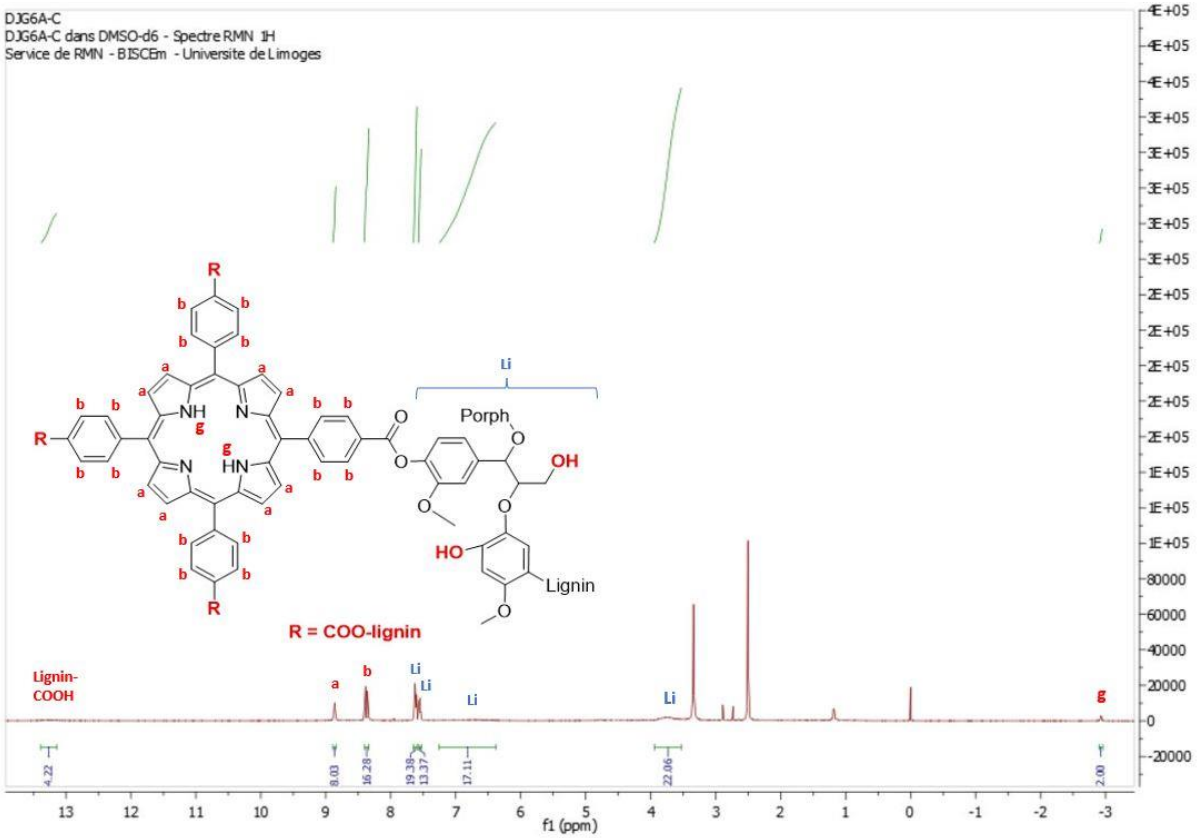

Figure S4.22. *Fully Integrated* ^{1}H *NMR spectrum at room temperature of* ***TCPP-lignin****, in DMSO-*d_6*, with the labels for the protons in the structure and those for lignin are indicated with a "Li".*

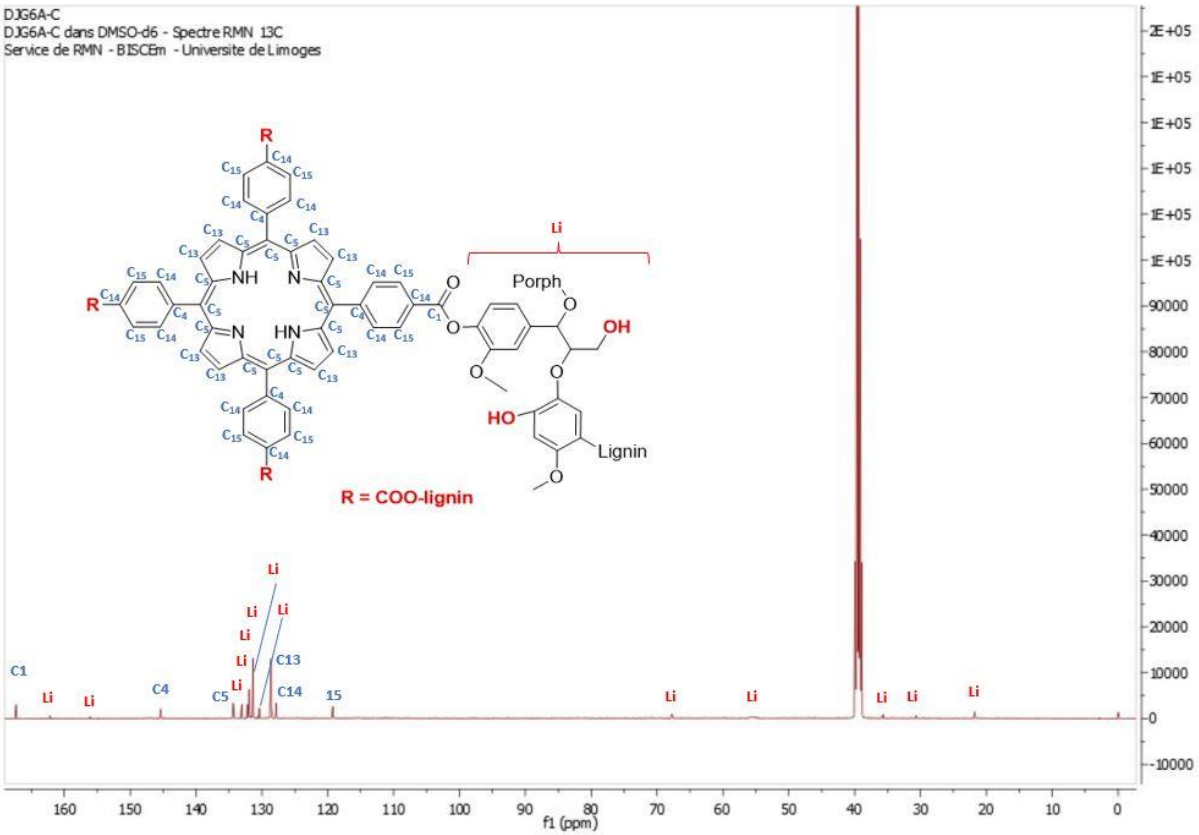

Figure S4.23. *^{13}C NMR spectrum at room temperature of* ***TCPP-lignin*** *in DMSO-d_6, with the structure and the labels of the carbons on the structure and those for lignin denoted with a "Li".*

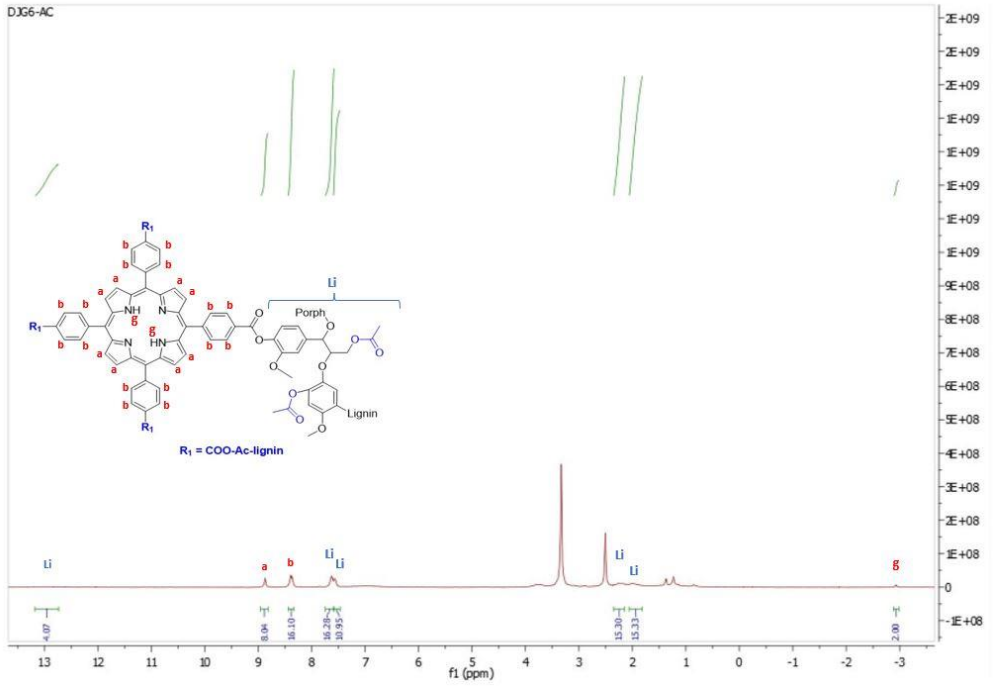

Figure S4.24. *Fully Integrated ^{1}H NMR spectrum at room temperature of* ***TCPP-Ac-lignin****, in DMSO-d_6, with the labels for the protons in the structure and those that are present due to lignin are labelled "Li".*

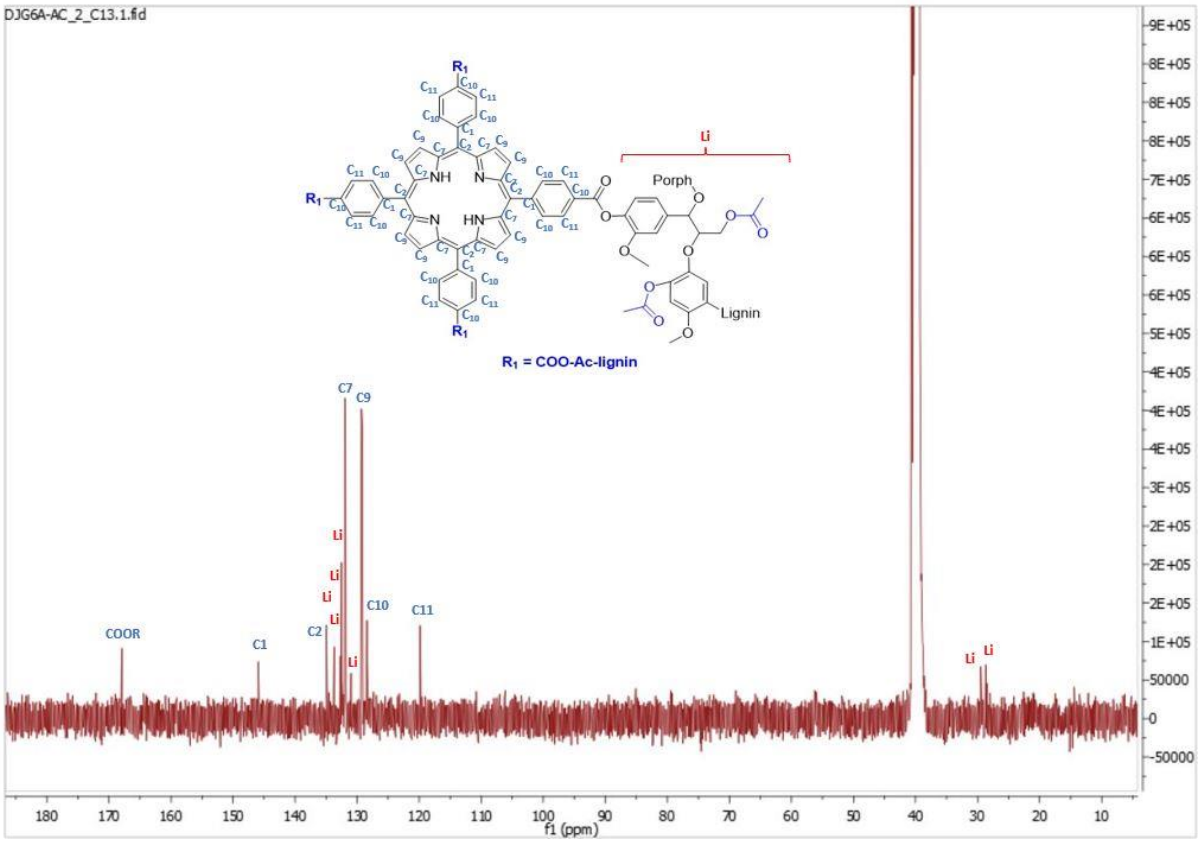

Figure S4.25. *^{13}C NMR spectrum at room temperature of* ***TCPP-Ac-lignin****, in DMSO-d_6, with the labels for the carbons in the structure. Carbons that belong to lignin are labelled with a "Li".*

4.5.3.3. *m*-CPTPP lignin conjugate

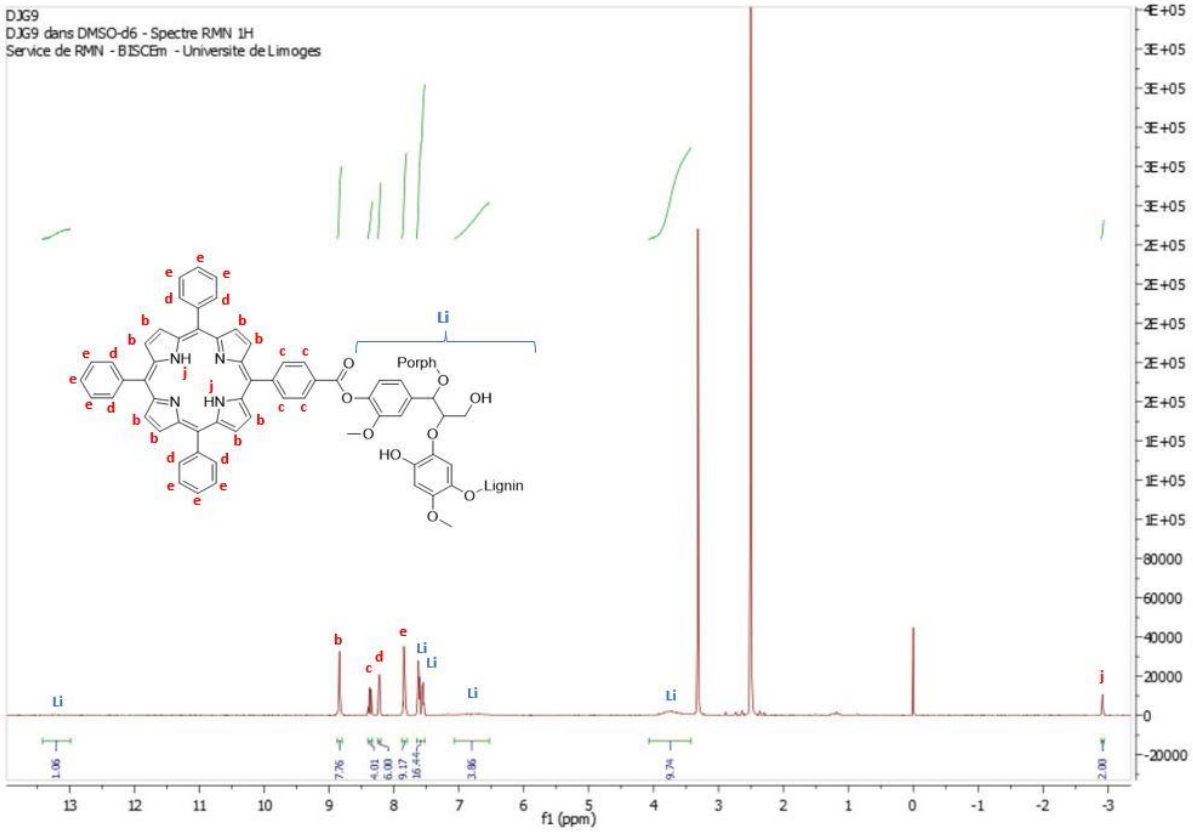

Figure S4.26. *^{13}C NMR spectrum at room temperature of* ***m-CPTPP-lignin*** *in DMSO-d_6, with the labels of the protons on the structure. Those that belong to lignin are labelled with a "Li".*

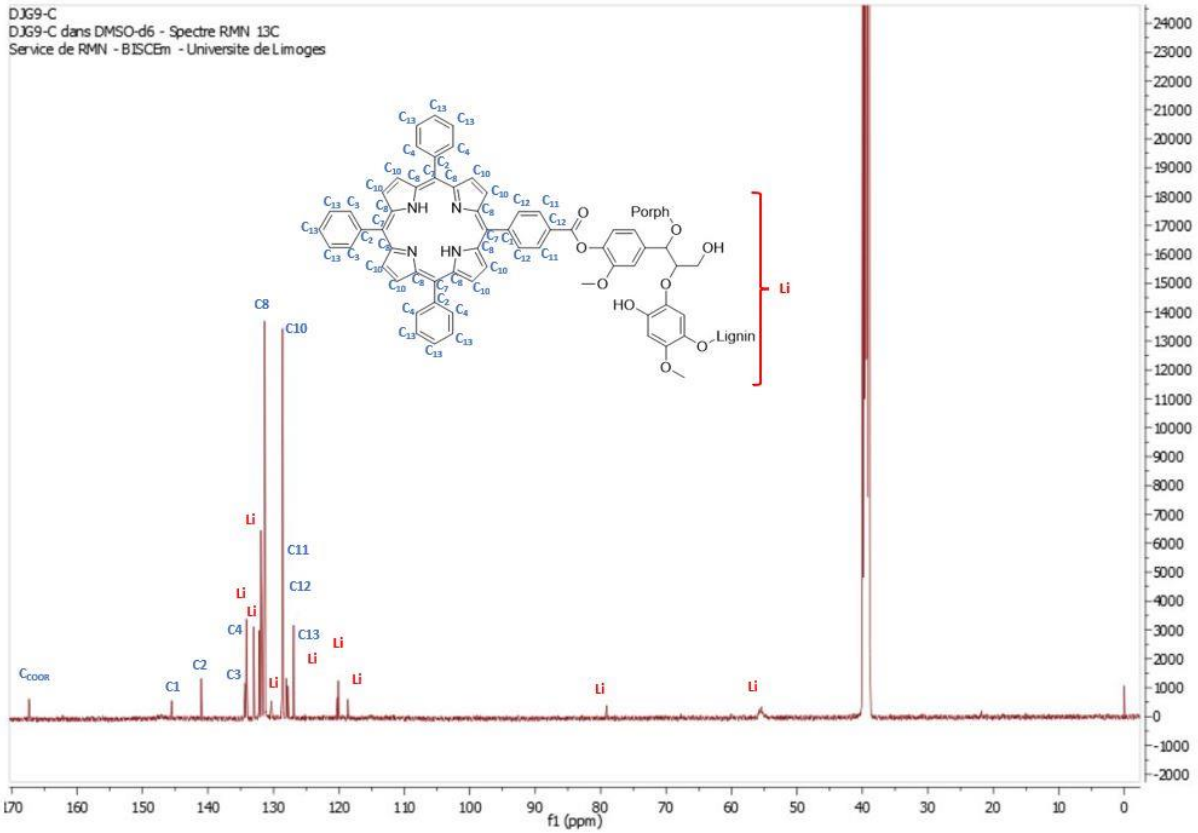

Figure S4.27. *^{13}C NMR spectrum at room temperature of* ***m-CPTPP-lignin*** *in DMSO-d_6, with the labels of the carbons on the structure. Those that belong to lignin are labelled with a "Li".*

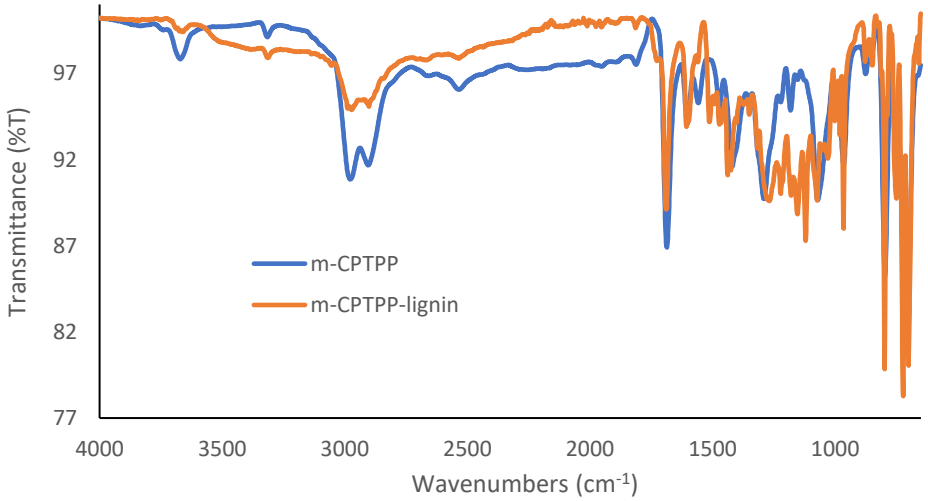

Figure S4.28. *IR spectrum of* ***m-CPTPP*** *(blue) and* ***m-CPTPP-lignin*** *(orange).*

4.6. References

[1] V. K. Ponnusamy, D. D. Nguyen, J. Dharmaraja, S. Shobana, J. R. Banu, R. G. Saratale, S. W. Chang and G. Kumar, A Review on Lignin Structure, Pretreatments, Fermentation Reactions and Biorefinery Potential, *Bioresour. Technol.*, 2019, **271**, 462–472. doi: 10.1016/j.biortech.2018.09.070.
[2] S. Stefan and M. Schubert. Softwood Lignin Self-Assembly for Nanomaterial Design, *Biomacromolecules*, 2017, **18**, 2649–2653. doi: 10.1021/acs.biomac.7b00822.
[3] B. Wang, D. Sun, H. -M. Wang, T. -Q. Yuan and R. -C. Sun, Green and Facile Preparation of Regular Lignin Nanoparticles with High Yield and Their Natural Broad-Spectrum Sunscreens, *ACS Sustain. Chem. Eng.*, 2019, **7**, 2658–2666. doi: 10.1021/acssuschemeng.8b05735.
[4] J. C. del Río, J. Rencoret, A. Gutiérrez, T. Elder, H. Kim and J. Ralph, Lignin Monomers from beyond the Canonical Monolignol Biosynthetic Pathway: Another Brick in the Wall, *ACS Sustain. Chem. Eng.*, 2020, **8**, 4997–5012. doi: 10.1021/acssuschemeng.0c01109.
[5] G. Marchand, C. A. Calliste, R. M. Williams, C. Mclure, S. Leroy-Lhez and V. Villandier, Acetylated Lignins: A potential Bio-Sourced Photosensitizer, *ChemistrySelect*, 2018, **3**, 5512–5516. doi: 10.1002/slct.201801039.
[6] N. Maldonado-Carmona, G. Marchand, N. Villandier, T.-S. Ouk, M. M. Pereira, M. J. F. Calvete, C. A. Calliste, A. Żak, M. Piksa, K. J. Pawlik, K. Matczyszyn and S. Leroy-Lhez, Porphyrin-Loaded Lignin Nanoparticles Against Bacteria: A Photodynamic Antimicrobial Chemotherapy Application, *Front. Microbiol.*, 2020. doi: 10.3389/fmicb.2020.606185.
[7] N. Maldonado-Carmona, T.-S. Ouk, N. Villandier, C. A. Calliste, M. J. F. Calvete, M. M. Pereira and S. Leroy-Lhez, Photophysical and Antibacterial Properties of Porphyrins Encapsulated inside Acetylated Lignin Nanoparticles, *Antibiotics*, 2021, **10**, 513–538. doi: 10.3390/antibiotics10050513.
[8] G. Marchand, G. Fabre, N. Maldonado-Carmona, N. Villandier and S. Leroy-Lhez, Acetylated Lignin Nanoparticles as a Possible Vehicle for Photosensitizing Molecules, *Nanoscale Adv.*, 2020, **2**, 5648–5658. doi: 10.1039/D0NA00615G.
[9] A. Barapatre, K. R. Aadil, B. N. Tiwary and H. Jha, In Vitro Antioxidant and Antidiabetic Activities of Biomodified Lignin from Acacia Nilotica Wood, *Int. J. Biol. Macromol.*, 2015, **75**, 81–89. doi: 10.1016/j.ijbiomac.2015.01.012.
[10] M. P. Vinardell and M. Mitjans, Lignins and Their Derivatives with Beneficial Effects on Human Health, *Int. J. Mol. Sci*., 2017, **18**, 1219–1233. doi: 10.3390/ijms18061219.
[11] H. dos Santos Abreu, A. M. D. Nascimento and M. A. Maria. Lignin Structure And Wood Properties, *Wood Fiber Sci.*, 1999, **31**, 426–433.
[12] S. Laurichesse and L. Avérous, Chemical modification of lignins: Towards biobased polymers, *Prog. Polym. Sci.*, 2013, **39**, 1266–1290. doi: 10.1016/j.progpolymsci.2013.11.004.
[13] R. Kumar, A. Butreddy, N. Kommineni, P. G. Reddy, N. Bunekar, C. Sarkar, S. Dutt, Y. K. Mishra, D. Oupicky and A. Kaushik, Lignin: Drug/Gene Delivery and Tissue Engineering Applications, *Int. J. Nanomedicine*, 2021, **16**, 2419–2441. doi: 10.2147/IJN.S303462.
[14] M. H. Sipponen, H. Lange, C. Crestini, A. Henn and M. Österberg, Lignin for Nano- and Microscaled Carrier Systems: Applications, Trends, and Challenges, *ChemSusChem.*, 2019, **12**, 2039–2054. doi: 10.1002/cssc.201900480.
[15] P. Figueiredo, K. Lintinen, J. T. Hirvonen, M. A. Kostiainen and H. A. Santos, Properties and chemical modifications of lignin: Towards lignin-based nanomaterials for biomedical applications, *Prog. Mater. Sci*., 2018, **93**, 233–269. doi: 10.1016/j.pmatsci.2017.12.001.
[16] S. Iravani and R. S. Varma, Greener synthesis of lignin nanoparticles and their applications, *Green Chem.*, 2020, **22**, 612–636. doi: 10.1039/C9GC02835H.
[17] J. Kou, D. Dou and L. Yang, Porphyrin Photosensitizers in Photodynamic Therapy and Its Applications, *Oncotarget*, 2017, **8**, 81591–81603. doi: 10.18632/oncotarget.20189.
[18]R. Giovannetti, The Use of Spectrophotometry UV-Vis for the Study of Porphyrins. doi: 10.5772/38797
[19] J. D. Spikes, New Trends in Photobiology: Chlorins as Photosensitizers in Biology and Medicine, *J. Photochem. Photobiol. B, Biol.*, 1990, **6**, 259–274. doi: 10.1016/1011-1344(90)85096-F.

[20] J. Bedwell, P. T. Chatlani, A. J. MacRobert, J. E. Roberts, H. Barr, J. Dillon and S. G. Bown, Enhanced Tumour Selectivity of Photodynamic Therapy in the Rat Colon Using a Radioprotective Agent, *Photochem. Photobiol.*, 1991, **53**, 753–756. doi: 10.1111/j.1751-1097.1991.tb09888.x.
[21] L. B. Josefsen and R. W. Boyle, Photodynamic Therapy: Novel Third-Generation Photosensitizers One Step Closer?, *Br. J. Pharmacol.*, 2008, **154**, 1–3. doi: 10.1038/bjp.2008.98.
[22] J. Sobczyński, H. H. Tønnesen and S. Kristensen, Influence of Aqueous Media Properties on Aggregation and Solubility of Four Structurally Related Meso-Porphyrin Photosensitizers Evaluated by Spectrophotometric Measurements, *Die Pharmazie*, 2013, **68**, 100–109. doi: 10.1691/ph.2013.2130.
[23] T. Duong, X. Li, B. Yang, C. Schumann, H. A. Albarqi, O. Taratula and O. Taratula, Phototheranostic Nanoplatform Based on a Single Cyanine Dye for Image-Guided Combinatorial Phototherapy, *Nanomedicine Nanomed-Nanotechnol.*, 2017, **13**, 955–963. doi: 10.1016/j.nano.2016.11.005.
[24] N. Lange, W. Szlasa, J. Saczko and A. Chwiłkowska, Potential of Cyanine Derived Dyes in Photodynamic Therapy, *Pharmaceutics*, 2021, **13**, 818–834. Doi: 10.3390/pharmaceutics13060818.
[25] J. Atchison, S. Kamila, H. Nesbitt, K. A. Logan, D. M. Nicholas, C. Fowley, J. Davis, B. Callan, A. P. McHale, J. F. Callan, Iodinated cyanine dyes: a new class of sensitisers for use in NIR activated photodynamic therapy (PDT), *Chem. Commun.*, 2017, **53**, 2009–2012. doi: 10.1039/C6CC09624G.
[26] M. A. Filatov, Heavy-Atom-Free BODIPY Photosensitizers with Intersystem Crossing Mediated by Intramolecular Photoinduced Electron Transfer, *Org. Biomol. Chem.*, 2019, **18**, 10–27. doi: 10.1039/C9OB02170A.
[27] D. J. Gibbons, A. Farawar, P. Mazzella, S. Leroy-Lhez and R. M. Williams, Making Triplets from Photo-Generated Charges: Observations, Mechanisms and Theory, *Photochem. Photobiol. Sci.*, 2020, **19**, 136–158. doi: 10.1039/C9PP00399A.
[28] O. Mitsunobu and M. Yamada, Preparation of Esters of Carboxylic and Phosphoric Acid via Quaternary Phosphonium Salts, *Bull. Chem. Soc. Jpn.*, 1967, **40**, 2380–2382. doi: 10.1246/bcsj.40.2380.
[29] H. -Y. TSE, S. -C. Cheng, C. S. Yeung, C. -Y. Lau, W. -H. Wong, C. Dong and S. -Y. Leu, Development of a Waste-Derived Lignin-Porphyrin Bio-Polymer with Enhanced Photoluminescence at High Water Fraction with Wide PH Range and Heavy Metal Sensitivity Investigations. *Green Chem.* 2019, **21**, 1319–1329. doi: 10.1039/C8GC02904K.
[30] D. J. Stewart, M. J. Dalton, S. L. Long, R. Kannan, Z. Yu, T. M. Cooper, J. E. Haley and L. -S. Tan, Steric Hindrance Inhibits Excited-State Relaxation and Lowers the Extent of Intramolecular Charge Transfer in Two-Photon Absorbing Dyes, *Phys. Chem. Chem. Phys.*, 2016, **18**, 5587–5596. doi: 10.1039/C5CP07716H.
[31] N. S. James, Y. Chen, P. Joshi, T. Y. Ohulchanskyy, M. Ethirajan, M. Henary, L. Strekowsk and R. K. Pandey, Evaluation of Polymethine Dyes as Potential Probes for near Infrared Fluorescence Imaging of Tumors: Part – 1, *Theranostics*, 2013, **3**, 692–702. doi: 10.7150/thno.5922.
[32] D. S. Conceição, D. P. Ferreira and L. F. V. Ferreira, Photochemistry and Cytotoxicity Evaluation of Heptamethinecyanine Near Infrared (NIR) Dyes, *Int. J. Mol. Sci.*, 2013, **14**, 18557–18571. doi: 10.3390/ijms140918557.
[33] E. Delaey, F. van Laar, D. De Vos, A. Kamuhabwa, P. Jacobs and P. de Witte, A Comparative Study of the Photosensitizing Characteristics of Some Cyanine Dyes, *J. Photochem. Photobiol. B, Biol.*, 2000, **55**, 27–36. doi: 10.1016/S1011-1344(00)00021-X.
[34] G. T. Dempsey, M. Bates, W E. Kowtoniuk, D. R. Liu, R. Y. Tsien and X. Zhuang, Photoswitching Mechanism of Cyanine Dyes." *J. Am Chem. Soc.*, 2009, **131**, 18192–18193. doi: 10.1021/ja904588g.
[35] W. J. Akers, M. Berezin, H. Lee and S. Achilefu, Predicting in Vivo Fluorescence Lifetime Behavior of Near-Infrared Fluorescent Contrast Agents Using in Vitro Measurements, *J. Biomed. Opt.*, 2008, **13**, 054042. doi: 10.1117/1.2982535.
[36] A. Skulcova, V. Majova, M. Kohutova, M. Grosik, J. Sima, and M. Jablonsky, UV/Vis spectrometry as a quantification tool for lignin solubilized in deep eutectic solvents, *BioRes.*, 2017, **12**, 6713–6722. doi: 10.15376/biores.12.3.6713-6722
[37] P. G. Seybold and M. Gouterman, Porphyrins. XIII: Fluorescence Spectra and Quantum Yields, *J. Mol. Spectrosc.*, 1969, **31**, 1–13. doi: 10.1016/0022-2852(69)90335-X.

[38] P. Wang, F. Qin, Z. Zhang and W. Cao, Quantitative Monitoring of the Level of Singlet Oxygen Using Luminescence Spectra of Phosphorescent Photosensitizer, *Opt. Express*, 2015, **23**, 22991–23003. doi: 10.1364/OE.23.022991.
[39] D. L. Akins, S. Özçelik, H. -R. Zhu and C. Guo, Fluorescence Decay Kinetics and Structure of Aggregated Tetrakis(p-Sulfonatophenyl)Porphyrin, *J. Phys. Chem*., 1996, **100**, 14390–14396. doi: 10.1021/jp961013v.
[40] J. S. Baskin, H. -Z. Yu and A. H. Zewail, Ultrafast Dynamics of Porphyrins in the Condensed Phase: I. Free Base Tetraphenylporphyrin, *J. Phys. Chem. A*, 2002, **106**, 9837–9844. doi: 10.1021/jp020398g.
[41] M. Y. Berezin and S. Achilefu, Fluorescence Lifetime Measurements and Biological Imaging, *Chem. Rev.*, 2010, **110**, 2641–2684. doi: 10.1021/cr900343z.
[42] S. Gentemann, C. J. Medforth, T. P. Forsyth, D. J. Nurco, K. M. Smith, J. Fajer and D. Holten, Photophysical Properties of Conformationally Distorted Metal-Free Porphyrins. Investigation into the Deactivation Mechanisms of the Lowest Excited Singlet State, *J. Am. Chem. Soc.*, 1994, **116**, 7363–7368. doi: 10.1021/ja00095a046.
[43] F. Wilkinson, W. P. Helman and A. B. Ross, Rate constants for the decay and reactions of the lowest electronically excited singlet state of molecular oxygen in solution. An expanded and revised compilation, *J. Phys. Chem. Ref. Data*, 1995, **24**, 663-677. doi: 10.1063/1.555965
[44] Z. Mahmood, M. Yameen M. Jahangeer, M. Riaz, A. Ghaffar and I. Javid, Lignin as Natural Antioxidant Capacity. Lignin - Trends and Applications. *IntechOpen*, 2018. doi: 10.5772/intechopen.73284.
[45] L. M. Mazur, T. Roland, S. Leroy-Lhez, V. Sol, M. Samoc, I. D.W. Samuel and K. Matczyszyn, Efficient Singlet Oxygen Photogeneration by Zinc Porphyrin Dimers upon One- and Two-Photon Excitation, *J. Phys. Chem. B*, 2019, **123**, 4271–4277. doi: 10.1021/acs.jpcb.8b12561.
[46] A. Ogunsipe, D. Maree and T. Nyokong, Solvent Effects on the Photochemical and Fluorescence Properties of Zinc Phthalocyanine Derivatives, *J. Mol. Struct.*, 2003, **650**, 131–140. doi: 10.1016/S0022-2860(03)00155-8.
[47] R. W. Ricci, M. Ditzler and L. P. Nestor, Discovering the Beer-Lambert Law, *J. Chem. Educ.*, 1994, **71**, 983–985. doi: 10.1021/ed071p983.

Free base porphyrin-cyanine conjugates for photomedicine[‡]

Abstract

Cyanines are well known for their ability to absorb near IR light and to accumulate in cancer cells. Porphyrins are known photosensitizers that can absorb UV, visible and near IR light and show photodynamic anticancer effects. The synthesis, characterization and photophysical properties of a novel free base porphyrin-cyanine conjugate called **TPPO-IR-783** (**TOI**) is reported. The conjugation of these two units can hold strong potential for near IR fluorescence image guided photodynamic therapy. This novel compound was characterized by NMR, UV-Vis, MS and FT-IR techniques. Excited state properties were studied in various solvents of different polarity. The fluorescence greatly depends on the solvent, however, this is not the case for singlet oxygen. Singlet oxygen emission is only observed in tetrahydrofuran (THF), comparing 8 different polar, non-polar and medium polarity solvents. This novel type of photosensitizer has the ability to produce singlet oxygen and could target cancer cells owing to its porphyrin and cyanine moieties.

[‡]A manuscript based on this chapter is in preparation.

5.1. Introduction – Porphyrins and heptamethine cyanine dyes

Porphyrins and heptamethine cyanine dyes are well known fluorophores that have been used in a plethora of applications and disciplines (structures in Figure **5.1**).[1, 2, 3] While these uses range from anti-cancer agents in medicine to organic solar cells, it is those that are related to photomedicine that are of importance herein.

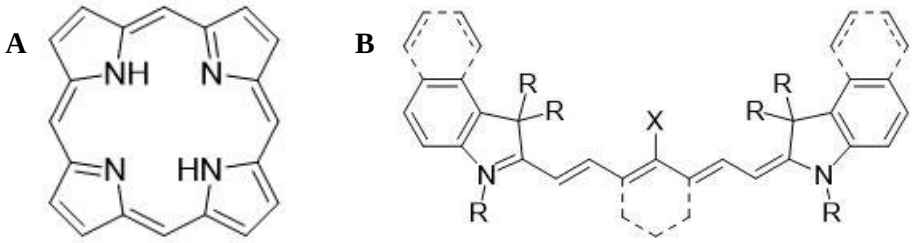

Figure 5.1. *Chemical structures of* ***(A)****: an unsubstituted porphyrin and* ***(B)*** *a cyanine dye.*

While these cyanine dyes have been reported to have anticancer, antibacterial and antifungal effects, they do not appear to have a direct reactive oxygen species based photodynamic effect.[4, 5, 6] However, cyanine dyes were reported to have harmful effects on HeLa cells after light exposure.[7] Delaey *et al.* describe that while the production of singlet oxygen is low, there is a "photo dependent biological activity." It is known that these compounds do not produce triplet states with efficient yields, nor produce singlet oxygen. However, they do have desirable effects in photomedicine.[8] They can be used as molecules that can target cancer tumors and can allow for intraoperative imaging.[9] The imaging is possible as these molecules are fluorophores that can absorb harmless near-IR light at 800 nm.[10] Further understanding of the photophysical properties of porphyrin-cyanine conjugates could have many benefits for photodynamic and related therapies.[8]

Porphyrins are tetrapyrrolic macrocycles that can absorb light in the UV, visible and near IR region (see structure in figure **5.1**).[11] They are well known for their capability to produce singlet oxygen in an efficient manner.[12] Conjugation of porphyrins and cyanines has been demonstrated in the literature and the resulting molecules have been investigated for their application in optimizing light dosimetry for improved photodynamic therapy of cancer.[13] Further studies have been conducted, including a photophysical study of a triad conjugate that consisted of two zinc porphyrins covalently bound to a cyanine dye (see figure **5.2**).[14] Upon excitation of the porphyrin by two-photon absorption, intramolecular energy transfer from the porphyrin to the cyanine is observed.

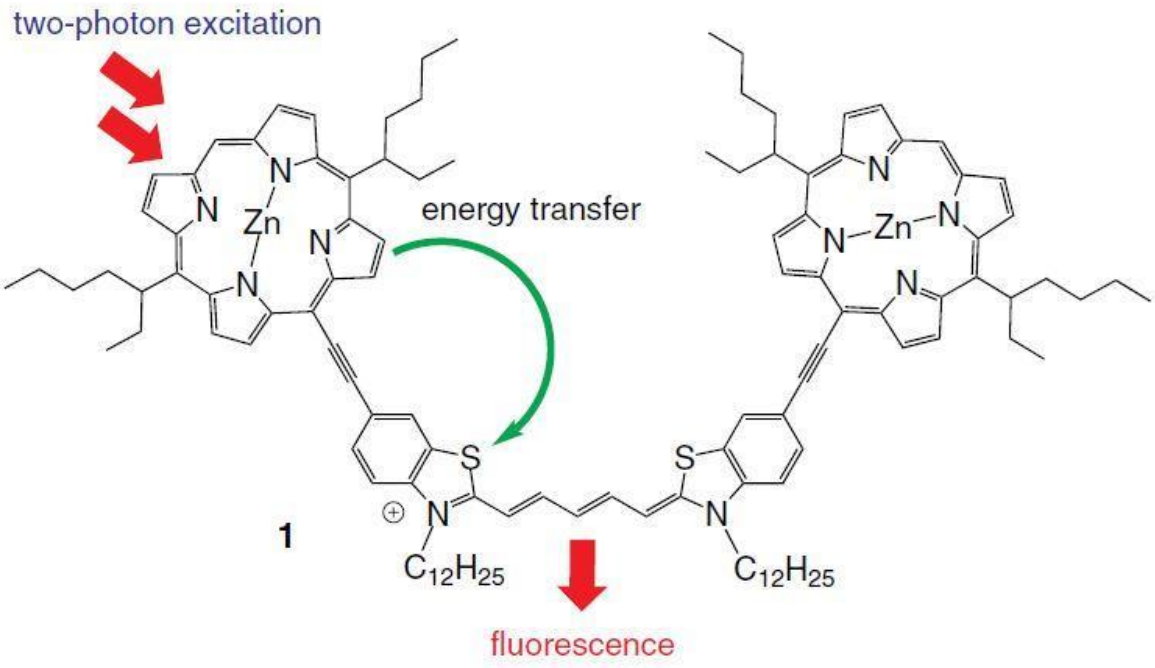

Figure 5.2. *Chemical structure of a triad conjugate, containing two zinc porphyrins covalently attached to a near IR cyanine dye. Once the porphyrin is excited, there is energy transfer to the cyanine followed by fluorescence of the cyanine reported by Ogawa et al.*[14]

To our knowledge, there have been no studies on the photophysical properties of a heavy atom-free (metal free) A_3B porphyrin-cyanine conjugate. For clarity, "A_3B" denotes the substitution pattern on the meso-substituents on the porphyrin: 3 "A" substituents and 1 "B" substituent. In **TPPOH** (Figure **5.3**), A = phenyl group and B = 4-hydroxyphenyl group. Similar porphyrin-cyanine conjugates have been synthesized and have shown self-aggregation properties that form micelles and have potential applications in drug delivery.[15] However, they have not shown singlet oxygen production. Herein, we demonstrate the synthesis and photophysical properties of a novel porphyrin-cyanine conjugate that produces singlet oxygen in tetrahydrofuran (THF) solvent (see structure in Figure **5.3**).

5.2. Synthetic reaction schemes

The porphyrin-cyanine conjugate was synthesized by combining a 5-(4-hydroxyphenyl)porphyrin (**TPPOH**) and a commercially available cyanine **IR-783** (Figure **5**.**3**). The first reaction involves the formation of the A_3B **TPPOH** porphyrin macrocycle *via* modified Adler-Longo conditions.[16] The 5,10,15,20-tetraphenylporphyrin is the main side-product in this reaction but it can be removed by repeated column chromatography and the desired **TPPOH** product was obtained in a **6%** yield (see figures **S5.1**–**S5.5** for spectra and section **5**.**5** for synthetic details).

After purification, the porphyrin was dissolved in N, N-dimethylformamide (DMF) and reacted with the commercially available cyanine dye, **IR-783**, in an S_N2 type reaction, using NaH as the base. The strong base deprotonated the phenoxy proton of the **TPPOH** porphyrin to form the phenoxy anion. This anion then attacks the cyanine electrophile to form the porphyrin-cyanine conjugate, **TPPO-IR-783** (**TOI**), in a high **84%** yield. The full synthetic procedure modified from literature is described in section **5.5.1** (spectra are included in the supplementary information, Figures **S5.6**, **S5.7**, and **S5.9**).[17]

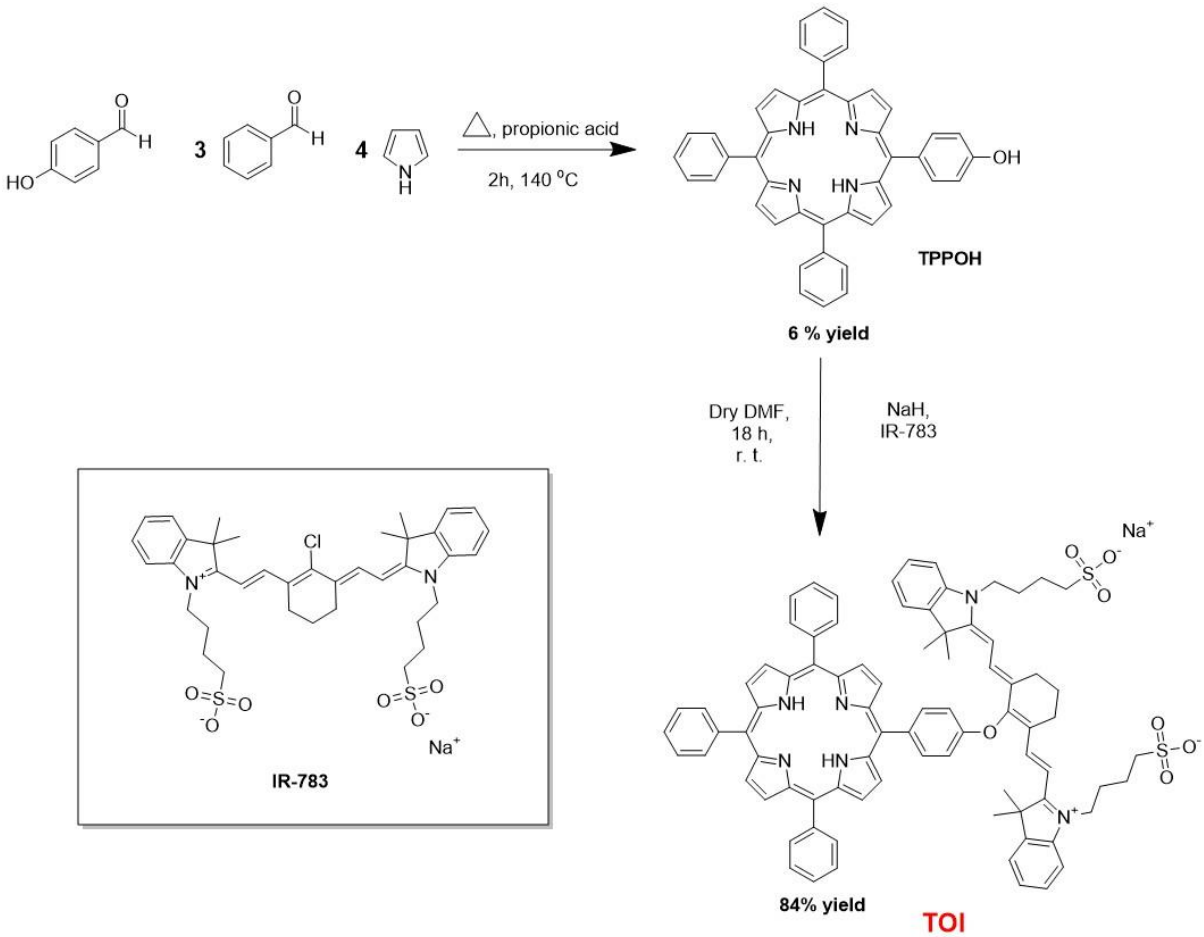

Figure 5.3. *Reaction scheme of the of 5-(4-hydroxyphenyl)-10,15,20-triphenylporphyrin (**TPPOH**), followed by the substitution reaction with the commercially available cyanine dye **IR-783**, to form the porphyrin-cyanine conjugate, **TPPO-IR-783 (TOI**).*

5.3. Photophysical studies of the porphyrin-cyanine conjugate - TPPO-IR-783

For the photophysical studies, the porphyrin-cyanine conjugate was analyzed in solution at room temperature *via* UV-Vis spectroscopy, photoluminescence spectroscopy, nanosecond and femtosecond transient absorption spectroscopy (ns-TA and fs-TA, respectively).

5.3.1. UV-Vis spectroscopy

The UV-Vis spectrum of **TOI** in tetrahydrofuran (THF) and methanol (MeOH; see data in table **5.2**; Figure **5.4**) was compared with its starting materials **TPPOH** in THF and **IR-783** in MeOH (see structures in Figure **5.3**). The data is described in Table **5.1**

Table 5.1. *UV-visible absorption data of* ***TOI*** *in THF and MeOH versus starting materials* ***TPPOH*** *in THF and* ***IR-783*** *in MeOH. Values in brackets refer to the log of the molar absorption coefficient (ε).*

PS	B-band (λ/nm) [a]	Porphyrin Q-bands (λ/nm) [b]				Sh [c]	MB [d]	Q_{III} / B [e]	MB / B [f]
		Q_{IV} [b]	Q_{III} [b]	Q_{II} [b]	Q_{I} [b]				
TOI – THF	417 (4.65)	514 (3.32)	548 (3.05)	5.94 (2.99)	651 (3.29)	714 (3.79)	780 (4.42)	0.02	0.58
TOI - MeOH	414 (4.64)	514 (3.29)	548 (2.98)	590 (2.91)	649 (3.26)	705 (3.77)	772 (4.42)	0.02	0.59
TPPOH [g]	417 (5.69) [g]	513 (4.33) [g]	549 (4.06) [g]	591 (3.82) [g]	650 (3.73) [g]	-	-	0.02	-
IR-783 [h]	-	-	-	-	-	708 (4.75) [g]	782 (5.35) [g]	-	-

[a] B-band is the Soret band of the porphyrin; [b] The maxima of the porphyrin Q-bands. $Q_{IV} = Q_y(1,0)$, $Q_{III} = Q_y(0,0)$, $Q_{II} = Q_x(1,0)$, and $Q_I = Q_x(0,0)$; [c] ***IR-783*** *shoulder (sh) band maximum; [d]* ***IR-783*** *main band (MB) maximum. [e] Ratio of the intensities of the Q_{III} and Soret (B) bands; [f] Intensity ratio of cyanine main band to that of the Soret band; [g] Dissolved in THF; [h] Dissolved in methanol (MeOH).*

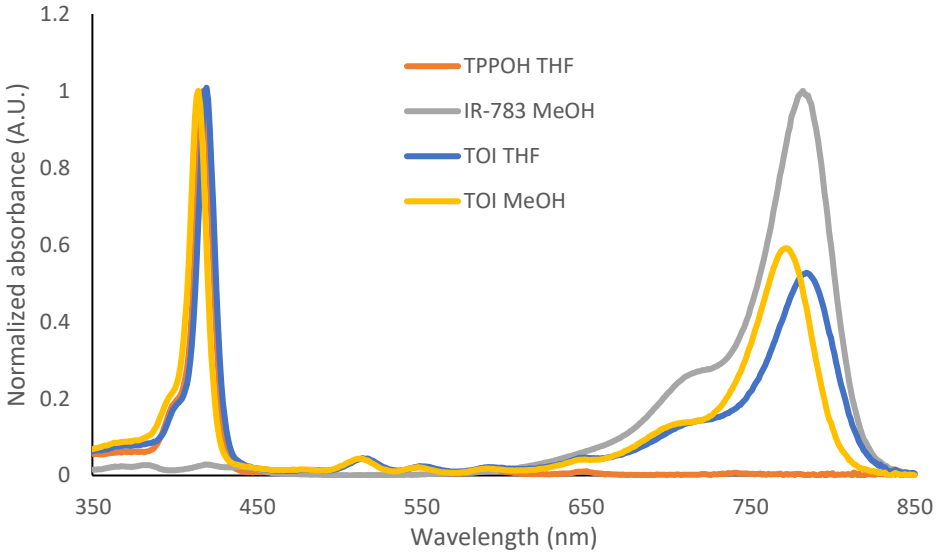

Figure 5.4. *Normalized UV-Vis spectra at room temperature of the the porphyrin starting material* ***TPPOH*** *(orange) in THF,* ***IR-783*** *(grey) in MeOH, porphyrin-cyanine conjugate* ***TOI*** *in THF (blue) and MeOH (yellow).*

Comparing the UV-Vis spectra of the **TOI** to the starting materials, it is clear that the spectral shapes are very similar. Table **5.1** shows a difference in molar absorption coefficients. A potential reason for this difference is the perturbation of the π-system, implying a strong

interaction between the two units in **TOI**. It is unlikely that the reason for this reduction is due to aggregation as there are no signs of aggregation in the UV-Vis (Figure **5.4**).[22]

In articles published Ventura *et al.*[18] and Lee *et al.*[19] porphyrins that were attached to π-extended systems (like Figure **5.5**) also showed a reduced molar absorption coefficient in comparison with the parent porphyrin.[18]

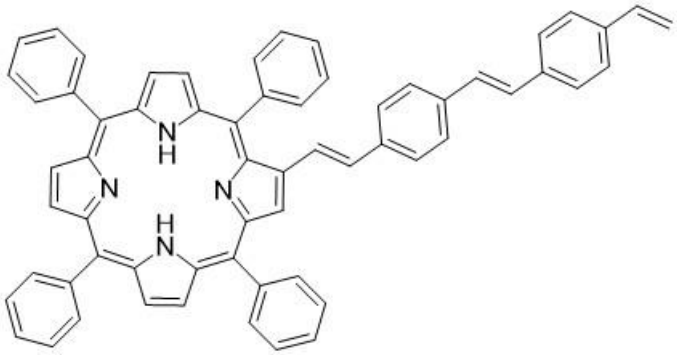

Figure 5.5. *Chemical structure of π-extended porphyrin that was reported by Ventura et al. to have a lower molar absorption coefficient (ε(438 nm) = 159,000 $M^{-1}{\cdot}cm^{-1}$).*[18]

This agrees with the work of Pandey *et al.* on related systems in which the distance was varied between two similar units (e.g. comparing their compounds **3** and **7**).[20] Additional work from Pandey and co-workers[21] implies that when attached to other chemical structures for use as a photosensitizer, the Soret band of porphyrin-type molecules decreased. Moreover, articles published by Lee *et al.* and Ventura *et al.*, reported similar reductions of molar absorption coefficients of porphyrins upon conjugation. This could be due to the breaking of the symmetry of the porphyrin. This would lead to the redistribution of the oscillator strengths that results in a lowering intensity of the absorption bands of the porphyrin moiety.

In the UV-Vis spectrum of the conjugate in THF, there is no evidence of aggregation (Figure **5.4**).[11, 22] The Soret band, four Q-bands of the porphyrin and the cyanine profile (700–800 nm) are observed. In the porphyrin moiety, the five (Soret and four Q-bands) absorption maxima remain the same upon direct conjugation to the cyanine dye, or by shift a maximum of 3 nm. In the cyanine moiety, the shoulder is slightly red-shifted by 6 nm and the main band is blue-shifted by 2 nm. Altogether, both porphyrin and cyanine moieties are clearly visible in the spectra.

Dissolving **TOI** in different solvents led to similar spectra (Figure **5.6** and Table **5.2**). However, the conjugate absorbed more due to its higher ε in $CHCl_3$ than the majority of the

solvents (Figure **S5.8** and Table **5.2**). The molar absorption coefficient was a lot less in phosphate-buffered solution (PBS) likely due to aggregation (Table **5.2** and Figure **S5.10**).

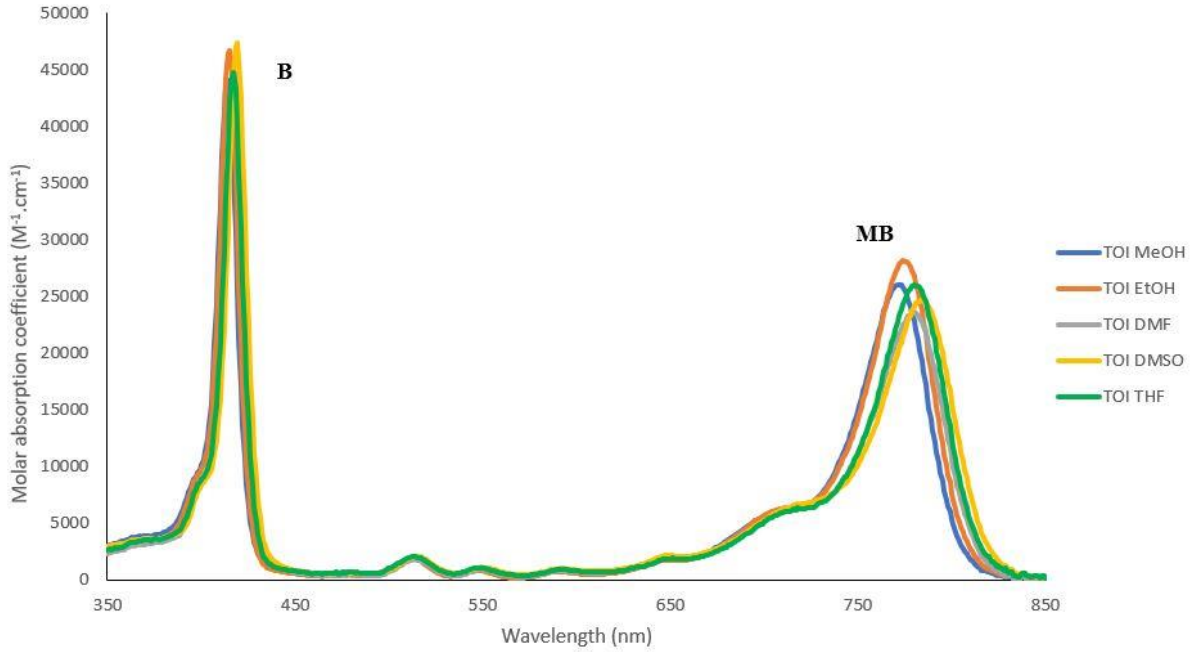

Figure 5.6. *UV-Vis spectra at room temperature of* ***TOI****, using the molar absorption coefficient scale, in five different solvents: MeOH (blue), ethanol (EtOH; orange), DMF (grey), dimethyl sulfoxide (DMSO; yellow), and THF (green).* ***Note:*** *The Soret band (B) of the porphyrin and main cyanine band (MB) of the cyanine dye are clearly labelled. Concentrations of each are equal to 17 µM.*

When dissolved in the solvents listed in table **5.2**, the maximum of the Soret band shifts within a wavelength range between 414 and 422 nm. The positions of the Q-bands differ by a maximum of 5 nm in all of the solvents with the cyanine shoulder shifting the most. This is also due to the difficulty in assigning this shoulder to a wavelength, whereas the main cyanine band is clearly defined and shifts by 15 nm depending on the solvent. However, the ground state of the dyad appears to be only slightly polar as there are no large shifts in ground state properties due to the polarity of the solvent (except PBS in Figure **S5.8** where aggregation is clearly visible).[23]

Table 5.2. *UV-visible absorption maxima data of* ***TOI*** *in seven different solvents: MeOH, EtOH, DMF, DMSO, THF, chloroform ($CHCl_3$) and PBS. Values in brackets refer to the log of the molar absorption coefficient.*

Solvent	SP [a]	B-band (λ/nm) [b]	Porphyrin Q-bands (λ/nm) [c]				Sh [d]	MB [e]	Q_{III} / B [f]	MB/ B [g]
			Q_{IV} [c]	Q_{III} [c]	Q_{II} [c]	Q_I [c]				
MeOH	+	414 (4.64)	514 (3.29)	548 (2.98)	590 (2.91)	649 (3.26)	705 (3.77)	772 (4.42)	0.02	0.59
EtOH	+	415 (4.67)	514 (3.28)	548 (2.95)	590 (2.89)	649 (3.26)	710 (3.80)	774 (4.45)	0.02	0.60
DMF	+	417 (4.65)	514 (3.27)	548 (2.97)	593 (2.93)	649 (3.31)	711 (3.78)	780 (4.37)	0.02	0.53
DMSO	+	419 (4.68)	514 (3.33)	549 (3.05)	593 (3.01)	649 (3.34)	713 (3.81)	784 (4.39)	0.02	0.52
THF	0	417 (4.65)	514 (3.32)	548 (3.05)	594 (2.99)	651 (3.29)	714 (3.79)	780 (4.42)	0.02	0.58
$CHCl_3$	0	419 (4.72)	514 (3.34)	552 (3.03)	590 (2.94)	649 (3.19)	715 (3.79)	781 (4.55)	0.02	0.67
PBS	+	4.22 (4.29)	517 (3.26)	553 (2.93)	595 (2.90)	652 (3.40)	729 (3.91)	787 (3.97)	0.04	0.48

[a] Solvent polarity (SP): "+" = polar and "0" = moderate polarity; [b] B-band is the Soret band of the porphyrin; [c] The Q-bands of the porphyrin: Q_{IV} = Qy(1,0) peak, Q_{III} = Qy(0,0) peak, Q_{II} = Qx(1,0) peak, Q_I Qx(0,0) peak; [d] cyanine shoulder (sh) band maximum; [e] cyanine main band (MB) maximum. [f] Ratio of the intensities of the Q_{III} and Soret (B) bands; [g] Ratio of the intensities of the main cyanine band (MB) and the Soret (B) bands.

5.3.2. Photoluminescence – Fluorescence emission and singlet oxygen emission spectroscopy

Photoluminescence spectroscopy studies were conducted to quantify the fluorescence observed and the singlet oxygen produced. The separate moieties were excited in MeOH and the fluorescence was monitored. The excitation wavelengths chosen were 548 nm and 727 nm, respectively (Figure **5.6**).

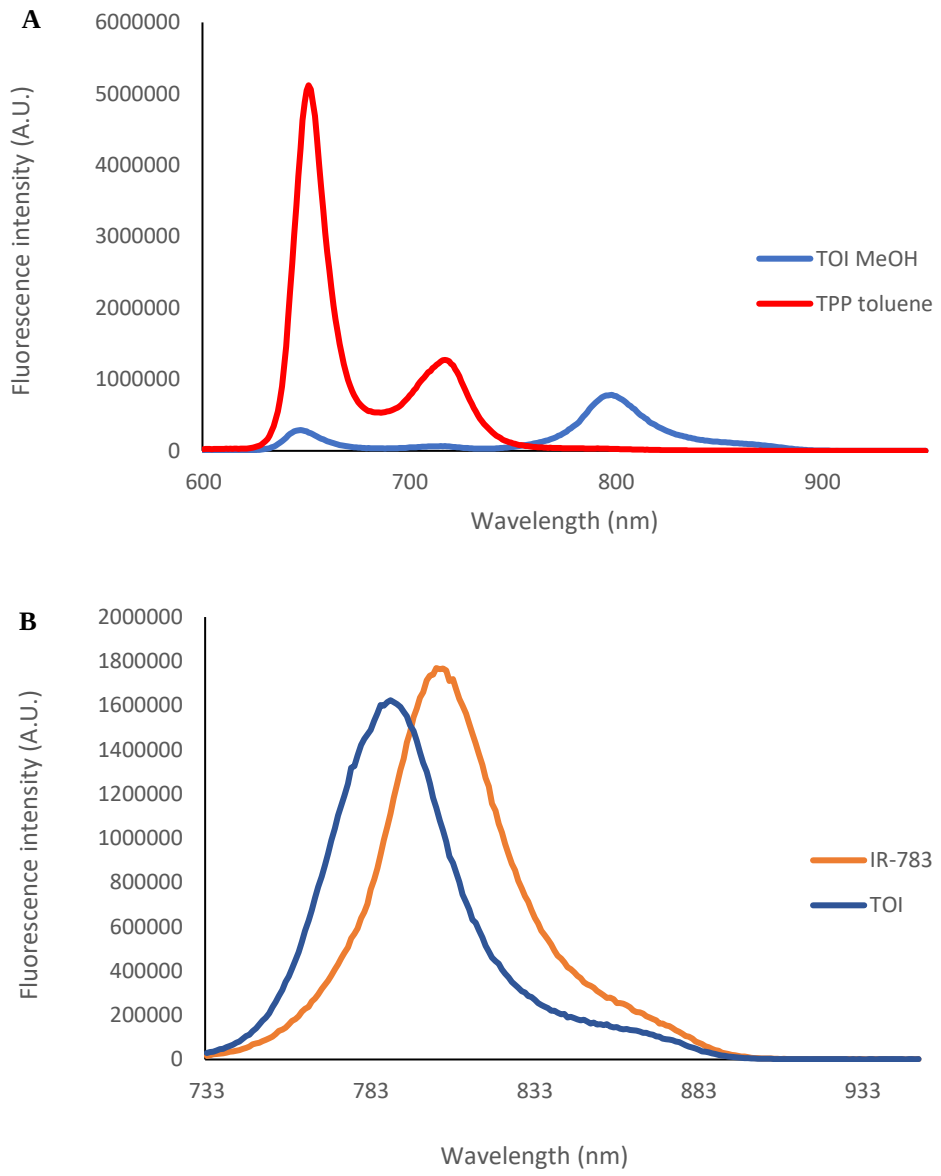

***Figure 5.6. (A)**: Fluorescence spectrum of **TOI** (blue) in MeOH vs 5,10,15,20-tetraphenylporphyrin (**TPP**; red) in toluene (Φ_f = 0.11). Excitation wavelength = 548 nm.[24]; **(B)**: Fluorescence spectrum of **TOI** (blue) in MeOH vs **IR-783** (orange) in MeOH (Φ_f = 0.08).[30] Excitation wavelength = 727 nm.*

Upon excitation of the porphyrin moiety of the conjugate (at 548 nm), there is fluorescence emission of the porphyrin and cyanine (fluorescence quantum yield (Φ_f) = 0.05; see table **5.3** and figure **5.6**). This fluorescence is less than that of the starting materials, **TPPOH** and **IR-783**, separately (Φ_f values of 0.10 and 0.08, respectively).[30] Furthermore, excitation of the cyanine moiety (727 nm) yields only the cyanine fluorescence.

It is of interest to excite the conjugate using near IR light as this type of light allows ideal penetration depth in human tissue.[25, 26] The fluorescence of the **TOI** conjugate was

monitored and compared upon 548 nm (visible light) and 727 nm (near IR light) excitation to determine if intramolecular photochemical mechanisms differ (Figure **5.7**; see section **5.3.3**: ns- and fs-TA spectroscopy sections below for further discussion).

As already mentioned, excitation of the porphyrin moiety (548 nm) results in fluorescence of the cyanine and porphyrin. Excitation of the cyanine subunit (at 727 nm) gives solely the fluorescence of the cyanine. Surprisingly, excitation of the PS at 548 nm results in the reddest shifted cyanine emission maximum (798 nm, Table **5.3**). Excitation at 727 nm results in a 789 nm emission maximum (Table **5.3** and figure **5.7**). The likely reason for this blue shifted emission of the near-IR light excitation is the inner filter effect.[27] The emission of the **TOI** conjugate is reabsorbed again by the conjugate in solution due to the proximity of emission (800 nm) and main absorption band (see table **5.2**). The concentrations were largely different in both: 0.1 mM at 727 nm and 0.4 mM at 548 nm, and is yields different inner filter effects that likely result in different emission maxima.

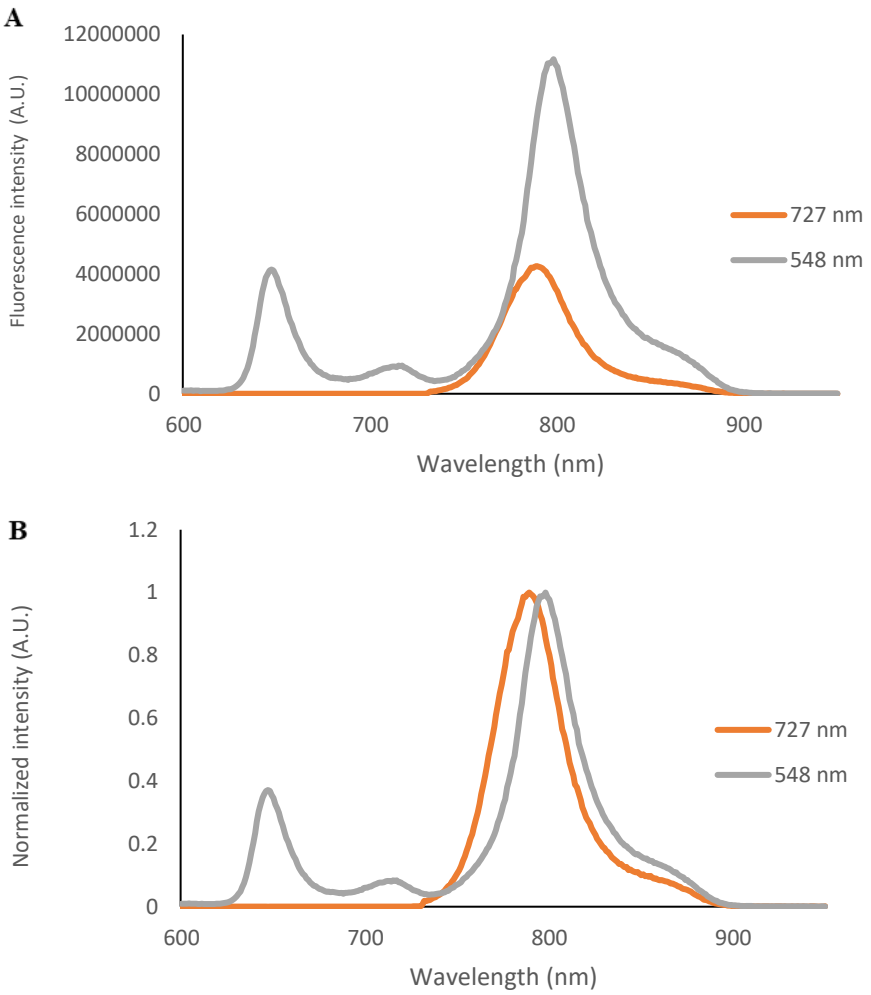

Figure 5.7. (A): *Fluorescence emission spectra at room temperature of* ***TOI*** *in MeOH with excitation at* ***548 nm*** *(grey) and* ***727 nm*** *(orange). The emission spectra are absorption-corrected for the excitation wavelength;* ***(B):*** *Normalized fluorescence emission spectra at room temperature of* ***TOI*** *in MeOH with excitation at* ***548 nm*** *(grey), and* ***727 nm*** *(orange). Concentrations = 0.1 mM at 727 nm and 0.4 mM at 548 nm excitation.*

Since the excitation of the porphyrin moiety yielded fluorescence of both moieties within the structure (dual fluorescence),[28] it was decided to further investigate the excited state decay pathways at this excitation wavelength (548 nm). Upon dissolving the **TOI** conjugate in different solvents that have different polarities, different fluorescence intensities are observed (Figure **5.8**). The fluorescence data is summarized in Table **5.3**.

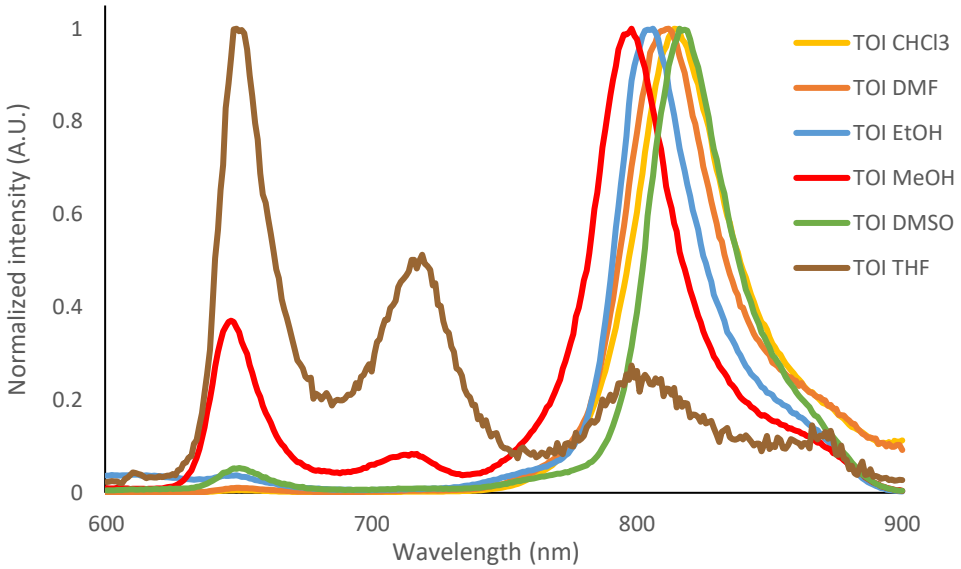

Figure 5.8. *Normalized fluorescence emission spectra at room temperature of* ***TOI*** *in $CHCl_3$ (yellow), DMF (orange), EtOH (blue), MeOH (red), DMSO (green) and THF (brown. Excitation at 548 nm. Reference is* ***TPP*** *in toluene (Φ_f = 0.11).*[24] *Concentrations of* ***TOI*** *= 58 µM ($CHCl_3$), 62 µM (DMF), 146 µM (EtOH), 71 µM (MeOH), 126 µM (DMSO) and 22 µM (THF).*

From the normalized emission spectra above (Figure **5.8**), the fluorescence of **TOI** in THF results in mainly very weak porphyrin fluorescence, and a small amount of cyanine fluorescence. The fluorescence in other solvents was mainly from the cyanine moiety. Concerning the cyanine maxima in the other solvents in Figure **5.8**, there is no red shift of the emission in the most polar solvents (EtOH and MeOH). However, due to the different concentrations in each solvent, the inner filter effect could be playing a role in their emission maxima.[27] This is clearly seen when **TOI** is dissolved in MeOH, the emission maximum is blue shifted compared to that of THF.

When dissolved in $CHCl_3$ and DMF, the fluorescence quantum yield of **TOI** is greatly increased (0.39 and 0.17, respectively, using TPP in toluene as a reference, $\mathbf{\Phi_f}$ = 0.11).[24] However, in EtOH and MeOH, the fluorescence is greatly reduced to <0.01 and 0.05, respectively. Similar low $\mathbf{\Phi_f}$ are also observed in dimethylsulfoxide (DMSO) and tetrahydrofuran (THF), which are <0.01.

Therefore, increasing the solvent polarity generally decreases the fluorescence. There are two exceptions to this rule: **TOI** in DMF and THF. Therefore, due to this conjugate having a solvent-dependent fluorescence, it is likely that there is some intramolecular photoinduced electron transfer from the porphyrin to the cyanine (see section **5.3.3** for further discussion).[34]

Table 5.3. *Fluorescence emission properties of* ***TOI*** *in MeOH, EtOH, DMF, DMSO, THF and* $CHCl_3$.

Solvent	Porphyrin [a]		Cyanine [b]		SS (cm^{-1}) [e]		Φ_f [f]
	λ_{em} Qx(0,0) (nm)	λ_{em} Q_x(0,1) (nm)	λ_{em} (nm) [c]	λ_{em} (nm) [d]	P	C	
MeOH	647	715	798	860	0	422	0.05 [j]
EtOH	649	719	806	854	0	513	<0.01
DMF	650	715	812	873	24	505	0.17
DMSO	650	- [g]	816	862	24	500	<0.01
THF	649	719	798	- [g]	0	289	<0.01
$CHCl_3$	651	719	814	876	0	273	0.39

[a] Fluorescence emission maxima that correspond to the porphyrin moieties; [b] Fluorescence emission maxima that correspond to the cyanine moieties; [c] Cyanine main band fluorescence emission maximum; [d] Shoulder band fluorescence maximum; [e] The Stokes shift (SS) was calculated from the corresponding UV-Vis and emission spectra of the porphyrin (P) and cyanine (C) moiety; [f] Fluorescence quantum yield calculated using ***TPP*** *in toluene as a reference (0.11). Excitation wavelength = 548 nm;[24] [g] No peak visible.*

Regarding singlet oxygen emission, all solvents listed in tables **5.2**–**5.4** were used in determining whether there was singlet oxygen production in these solvents, however, there was only singlet oxygen production in THF. **TOI** was also dissolved in non-polar solvents like cyclohexane, pentane and toluene, however there was still no singlet oxygen production. Upon exciting the porphyrin moiety of **TOI** in THF solvent, singlet oxygen production was observed (Figure **5.9**). There was no singlet oxygen production upon excitation of the cyanine moiety with near-IR light (700–800 nm) as also checked, in THF, with the AquaSpark singlet oxygen probe (see Chapter **3** for details).[29] It is difficult to find a reference for singlet oxygen production in THF using excitation at 548 nm. Thus, the conjugate was excited at the Soret band at 400 nm in THF (Figure **5.9**), using phenalenone as a reference, and was found to have a singlet oxygen quantum yield (Φ_Δ) of 0.23 $\pm$ 0.03 in THF (see Table **5.4**).[32]

Table 5.4. *Photophysical properties of* ***TOI*** *in THF,* ***IR-783*** *in MeOH and* ***TPPOH*** *in $CHCl_3$ and THF.*

PS	Porphyrin [a]		Cyanine [b]		SS (cm^{-1}) [c]		Φ_f [d]	Φ_Δ [e]	τ_T [f] (ns)
	λ_{em} Qx(0,0) (nm)	λ_{em} Q_x(0,1) (nm)	λ_{em} (nm)	λ_{em} (nm)	P [c]	C			
TOI	649	719	798	- [g]	0	289	<0.01 [h]	0.23 ± 0.03 [i]	327 ± 7 [j]
TPPOH [k]	651	718	- [l]	- [l]	47	-	0.10 [h]	0.72 [m]	312 ± 8 [j]
IR-783	- [l]	- [l]	802	899	- [l]	319	0.08 [n]	<0.01 [n]	- [o]

[a] Fluorescence emission maxima that correspond to the porphyrin moieties; [b] Fluorescence emission maxima that correspond to the cyanine moieties; [c] The Stokes shift (SS) was calculated from the corresponding UV-Vis and emission spectra, porphyrin (P) and cyanine (C); [d] Fluorescence quantum yield; [e] Singlet oxygen quantum yield; [f] τ_T (ns) = triplet state lifetime in air (equilibrated); [g] No clear maximum observed; [h] This fluorescence quantum yield was calculated using ***TPP*** *in toluene as a reference (0.11). Excitation wavelength = 548 nm;[24] [i] This singlet oxygen quantum yield was calculated using phenalenone as a reference (0.96 ± 0.02).[32] Excitation wavelength = 400 nm; [j] This triplet excited state decay was fitted mono-exponentially; [k]* ***TPPOH*** *was dissolved in $CHCl_3$ except for triplet lifetime determination (dissolved in THF); [l] Not applicable; [30] [m] Singlet oxygen quantum yield of* ***TPPOH*** *was calculated in $CHCl_3$ using TPP in $CHCl_3$ (0.55) as a reference and excitation wavelength = 548 nm;[31] [n] Literature value;[24] [o] Not measured as the limit of the laser is at 700 nm.*

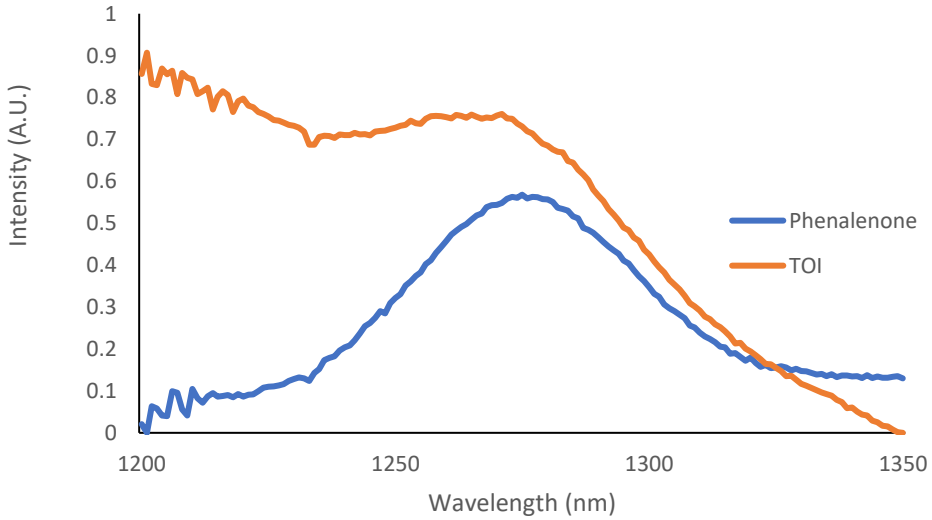

Figure 5.9. *Singlet oxygen emission spectrum of* ***TOI*** *(orange) and* ***phenalenone*** *(blue) in THF (0.96± 0.02) in THF. Excitation wavelength used is 400 nm.[32]*

The production of $^1O_2$ in THF is a somewhat surprising result since there is no production of singlet oxygen in any other solvents tested, especially with solvents wherein the lifetime of singlet oxygen is longer.[33] The singlet oxygen emission in figure **5.9** gives strong evidence for the presence of a triplet state in THF. It has already been determined that the fluorescence of this conjugate in THF is low (< 0.01). Thus, since the fluorescence is quenched, other excited state dynamics were investigated. Upon porphyrin excitation, fluorescence could occur from the porphyrin to the cyanine since there is solvent dependent fluorescence. It is therefore hypothesized that there could be triplet formation *via* charge recombination occurring (see mechanism in figure **5.10**).

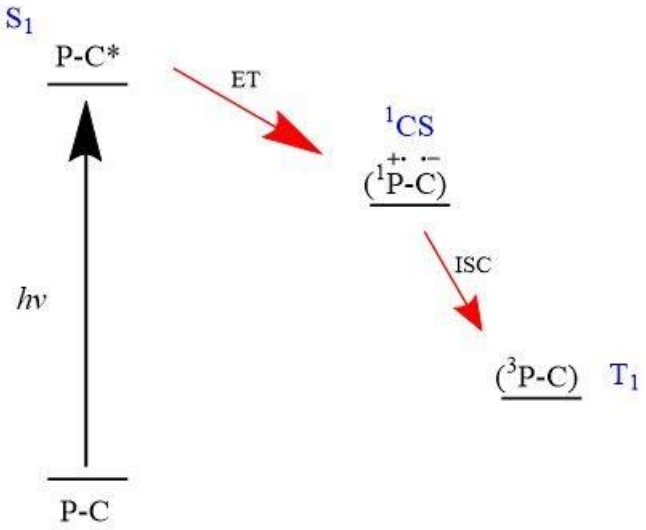

Figure 5.10. *Simplified Jablonski diagram of the triplet formation by charge recombination process that could be occurring within the* ***TOI (P-C)*** *conjugate.[34] Firstly, there is absorption of the P-C conjugate via excitation of the porphyrin moiety to the singlet excited state (S_1, P-C*). Then, there is electron transfer (ET) via manipulation of the solvent polarity to go to the charge separated state (CS). From here, there is an intersystem crossing mechanism to go to the triplet state.*

In general, manipulation of the solvent polarity encourages photoinduced charge transfer.[35] Excitation of the porphyrin subunit in the conjugate likely creates a charge transfer state. When the porphyrin-cyanine is in the singlet excited state (S_1), electron transfer can occur from the porphyrin donor to the cyanine acceptor forming a charge separated (CS) or transfer (CT) state. From here, this state can undergo intersystem crossing to arrive at the triplet state. In the review that is discussed in chapter **2**,[34] the type of intersystem crossing that allows triplet formation from the CT state is called spin-orbit charge transfer intersystem crossing (SOCT-ISC). In theory, once an orthogonal dyad is in the CT state, there is a large change in orbital

angular momentum of this state, that must be compensated by a fast spin flip to conserve the overall angular momentum of the system.[34, 36] Thus, intersystem crossing (SOCT-ISC) must occur due to the orthogonality of a dyad in a CT state. However, transient absorption experiments need to be conducted in order to investigate what is the most likely photochemical mechanism that occurs (see section **5.3.3**).

5.3.3. Transient Absorption spectroscopy

Nanosecond transient absorption spectroscopy was conducted to determine the triplet lifetime of **TOI** in THF and obtain more information about the excited state pathways. Since singlet oxygen production was observed in THF, the conjugate was excited at 548 nm and 650 nm in THF for ns-TA spectroscopy (Figure **5.11** and **5.12**, respectively). The difference between the intensity (y-axis) of the TA graphs is due to the differing absorbances of the two sites of excitation. The limit of the Ekspla laser was 700 nm and thus it was not possible to conduct ns-TA spectroscopy on the cyanine moiety of the conjugate (see UV vis spectrum of **TOI** in Figure **5.5**).

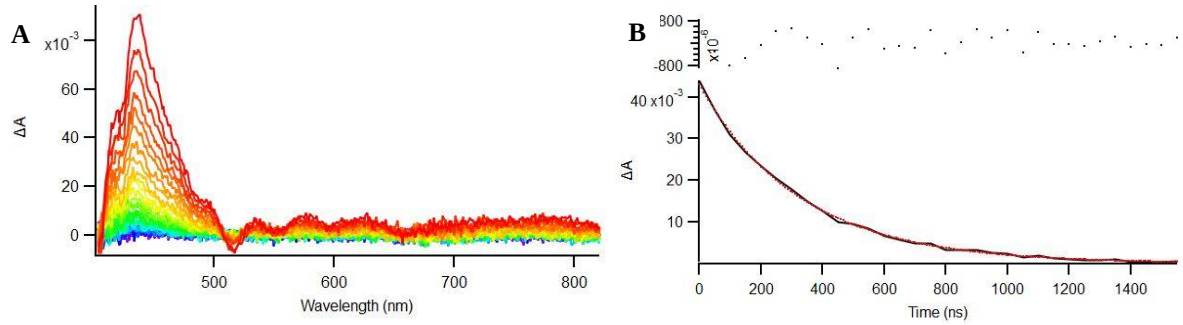

Figure 5.11. (A): *Ns-TA spectrum of* ***TOI*** *in THF (in air);* ***(B):*** *Decay spectrum of* ***TOI*** *in THF (in air). Excitation wavelength is 548 nm. Incremental delay = 50 ns.* τ_T *= 327* $\pm$ *7 ns.*

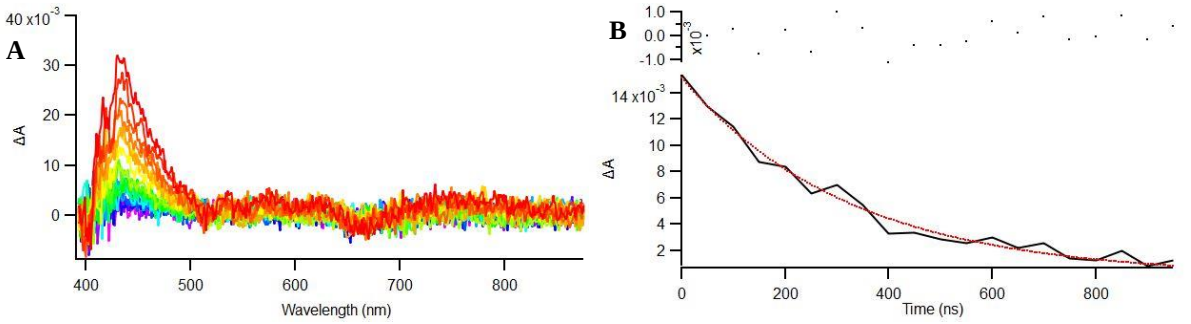

Figure 5.12*. (A):* *Ns-TA spectrum of* ***TOI*** *in THF (in air);* ***(B):*** *Decay spectrum of* ***TOI*** *in THF. Excitation wavelength is 650 nm. Incremental delay = 50 ns.* τ_T *= 321* $\pm$ *24 ns.*

The TA spectrum recorded shows evidence of the triplet state of the porphyrin subunit that belongs to the **TOI** conjugate. The same profile was observed upon excitation of this conjugate in THF with 650 nm light. This profile is almost identical to that of the transient absorption spectrum of the **TPPOH** starting material in THF (Figure **S5.11** and Table **5.4**).

Femtosecond transient absorption spectroscopy

Femtosecond transient absorption (fs-TA) spectroscopy data of **TOI** in THF as a solvent (with 515 nm excitation) shows the presence of five components (as analyzed with Glotaran with a sequential model).[37] The first component of the normalized evolution associated difference spectra (black spectrum in figure **5.13**) shows clear features of the singlet excited state of the porphyrin moiety (with ground state bleaching at 514, 555 and 610 nm and excited state absorption peaking around 690 nm).

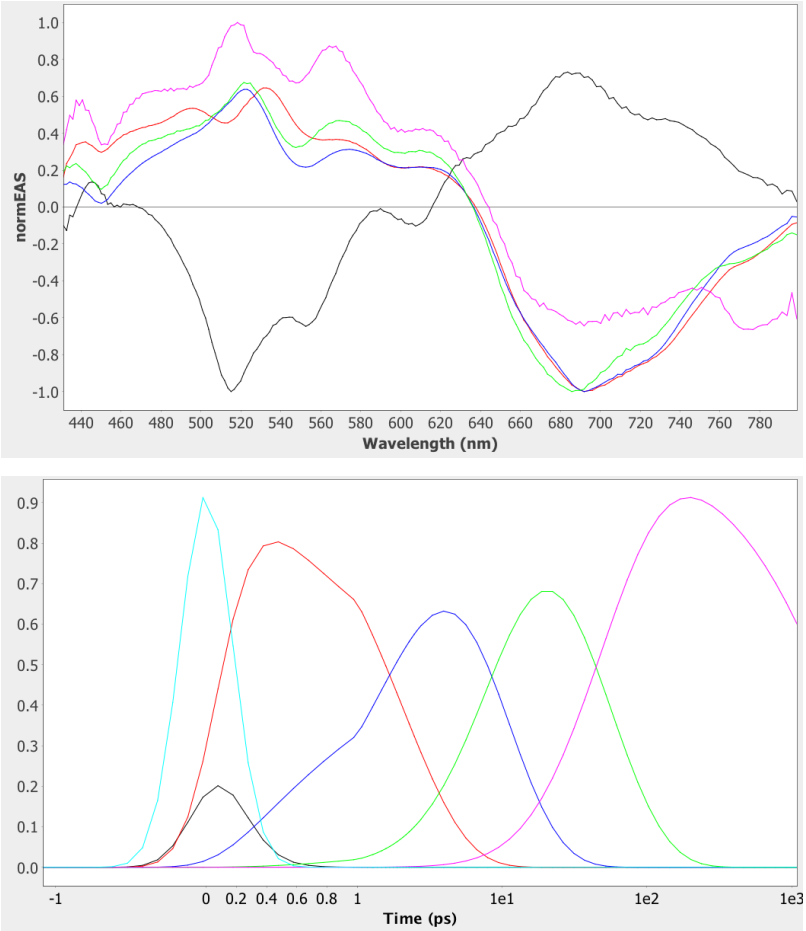

***Figure 5.13. (Top)**: Femtosecond transient absorption data of **TOI** in THF as the solvent obtained upon analysis (EAS = evolution associated difference spectra). Excitation wavelength = 515 nm; (**Bottom**): Graph highlighting the time scale and relative concentrations (intensity) of the photochemical species depicted in top figure, that play a role in the conjugate in THF after excitation at 515 nm.*

This first species (black line) converts with a rate of around 10^{13} s^{-1} (~100 fs) to the species which belongs to the red spectrum. This excited state clearly is cyanine based, as the bleaching at 690 nm is evident. This implies that after selective porphyrin excitation, energy transfer occurs to the cyanine dye with a rate of about 10^{13} s^{-1}. After 2 ps (5×10^{11} s^{-1}), the excited state represented by the blue spectrum is formed. This species is also cyanine based (as evidenced by the ground-state bleach at 690 nm, but relative to the red species, bleaching bands at 555 and 610 nm develop (biting out of the broader positive excited state absorption of the cyanine dye) indicating a state in which the porphyrin is also participating. We attribute this to charge transfer: in the charge transfer state both chromophores display a ground state bleaching. The next two processes occurring with decay times of 8.5 and 48 ps (green and pink spectra, respectively) give rise to a negative band at 780 nm, and have features of the blue spectrum (their precursor state). At earlier times, this negative 780 nm band of the ground state bleaching of the cyanine is obscured by positive excited state absorption of the porphyrin. Solvation (8.5 ps), followed by a slight conformation change of the dyad, involving one of the charged ionic side groups, is an option for last 48 ps process. The last state has decay-time of at least 2 ns.

The ns-TA presented above in this section (Figures **5.11** and **5.12**), shows the presence of a long-lived triplet state present on the porphyrin units (rather similar to the ns-TA of **TPPOH –** see Figure **S5.11**, as well as that of **THOPP** in chapter **3**). It would appear that the longer-lived species (pink spectrum) must convert to this porphyrin triplet on a slower, ~10 ns timescale.

Ns-TA spectroscopy was performed, once again, on the **TOI** conjugate in THF. The porphyrin moiety was excited at 514 nm and the incremental delays were 1 ns in order to see a more complete picture (Top and middle graph in figure **5.14**). A second spectrum with longer incremental delays (20 ns), shows that the triplet forms as shown in the bottom graph in Figure **5.14** (peak at 440 nm in bottom graph).

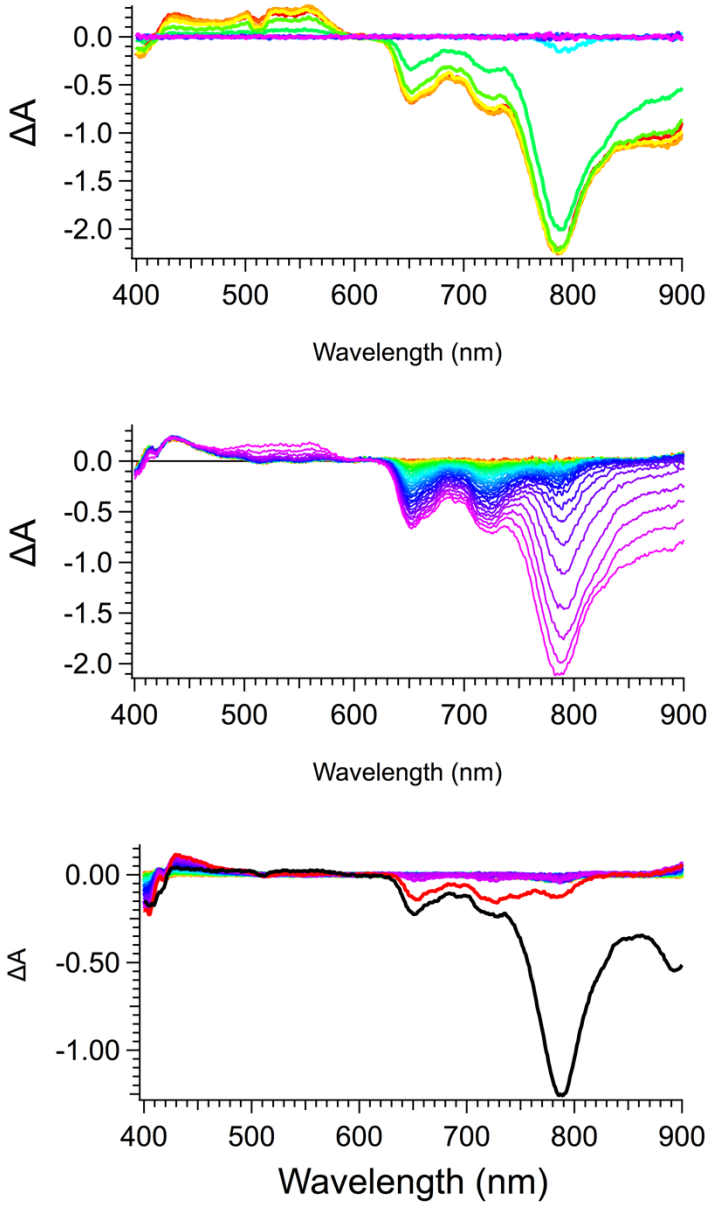

Figure 5.14. (Top & middle): *Ns-TA spectrum of* ***TOI*** *in THF (in air). Excitation wavelength is 514 nm. Incremental delay = 1 ns, traces follow a rainbow color-scheme (violet to red).* ***Top****: traces of the first 10 ns after excitation;* ***middle****: traces of the following times, from 10 ns to 50 ns* ***(Bottom):*** *Ns-TA spectrum of* ***TOI*** *in THF (in air). Excitation wavelength is 514 nm. Incremental delay = 20 ns. First trace is black, second trace is red. Others follow rainbow color-scheme.*

The ns-TA shown in figure **5.14**, together with the fs-TA data, show a complex photophysical decay pathway. It is clear that porphyrin excitation leads to excited state formation on the cyanine, but the final triplet state is localized on the porphyrin. There are no features present of this porphyrin triplet state within the first 1 ns (see fs-TA). The black and

red traces in figure **5.14** (bottom) show the relatively slow formation of the triplet of the porphyrin within ~20 ns. The excited state of the cyanine is formed very fast, has initial emission, but at around a time of 5 ns, has lost its emission, but is still ground state bleached. This latter aspect indicates charge transfer or cyanine triplet state formation (figure **5.14**, top and middle). Since intrinsic triplet state formation of the cyanine dye is unconventional, triplet-triplet energy transfer (from a cyanine triplet to the porphyrin triplet) is unlikely. The SOCT-ISC mechanism is a good option to clarify the complex behavior, but clearly more research is needed to obtain strong arguments supporting this hypothesis. The ns-TA equipment has a gate of 2.9 ns, therefore this data deviates from the fs-TA observations.

It has to be realized that **TOI** is a tetra-ionic compound. Whereas the sodium sulfonate tail can easily form solvent separated ions, the positive charge on the cyanine dye can be delocalized within the conjugated cyanine system. This positive charge is more likely to be influenced by ion-pairing with its internal counter ion, the sulfonate anion group. Furthermore, a meticulous inspection shows that formally a charge shift reaction from the cyanine to the porphyrin is considered, as the photoinduced electron transfer step. Thus potential disrupted ion paring can couple to the photoinduced charge shift reaction, in which a positive charge moves, under the influence of light, from the cyanine dye to the porphyrin unit forming a neutral cyanine radical.

5.4. Conclusion

The synthesis and the photophysical studies of a novel porphyrin-cyanine conjugate, **TOI**, for photomedicine is described herein. Following conjugation of the cyanine to the porphyrin, the systems are strongly perturbed. The excited state dynamics of this conjugate involve: energy transfer from the porphyrin to the cyanine, possible photoinduced electron transfer from the porphyrin to the cyanine (formally a charge shift reaction, obtained *via* manipulation of the solvent polarity), triplet excited state formation of the porphyrin and singlet oxygen generation in THF.

Future studies

It has been hypothesized that this conjugate undergoes triplet formation *via* charge recombination in THF. However, further experiments need to be conducted to clarify the photochemical pathways in this conjugate following porphyrin excitation. Direct triplet formation *via* porphyrin excitation is still an option, however, determination of the redox

potential in THF and evaluation of the level of charge transfer state would provide further clarity. This equation estimates the free energy change between a locally excited state and a radical ion pair state, and would hopefully clarify whether photoinduced electron transfer occurs.

Furthermore, in terms of optimal structure design, this molecule has limitations for its photodynamic therapy. It is poorly water solubility and as a low singlet oxygen production. Further modifications could be made to this structure or to the structural design of the next porphyrin-cyanine PS in the future. This could include adding more sulfonate groups to make it water soluble and introducing a metal into the porphyrin center to increase its singlet oxygen production. However, as mentioned in the review in Chapter **2**, metals or heavy atoms leads to more rapid triplet decay to the ground state, makes the molecule more expensive to make and could introduce unwanted toxicity when testing this conjugate for its biological activity. Moreover, the aim is to investigate whether triplet formation by charge recombination is possible in a heavy atom-free porphyrin-cyanine conjugate. In terms of further experiments that are envisaged for the future: femtosecond transient absorption spectroscopy can be investigated further and computational tools can also be utilized to predict triplet formation *via* charge recombination pathways. It is possible to calculate the photoinduced electron transfer using Marcus theory and triplet forming mechanism using Time Dependent Density Functional Theory (TD-DFT) calculations using the quantum chemical program Amsterdam Density Functional (ADF). Overall, these structural modifications and computational tools could aid in optimizing the structural design of a porphyrin-cyanine PS that can be used in photomedicine.

5.5. Experimental procedures

5.5.1. Synthetic reaction schemes

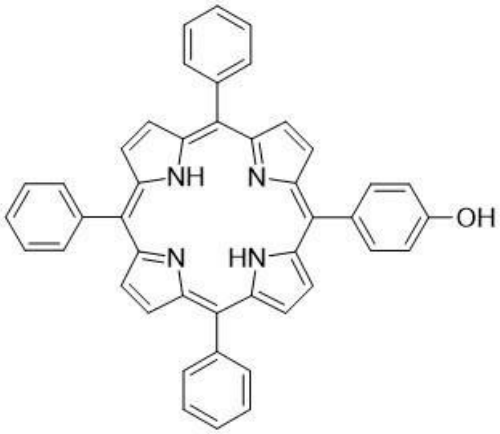

Synthesis of **5-(4-hydroxyphenyl)-10,15,20-triphenylporphyrin (TPPOH)**: 4-hydroxybenzaldehyde (3.52 g, 28.8 mmol, 1.00 eq.) was dissolved in 200 mL propionic acid. The mixture was then stirred and benzaldehyde (8.80 mL, 9.15 g, 86.2 mmol, 3.01 eq.) was added to the flask dropwise *via* the side neck using a dropping funnel. The mixture was allowed to stir at 140 ^{o}C reflux for 30 minutes. Pyrrole (7.74 g, 8.0 mL, 115 mmol, 4.00 eq.) was added dropwise to the reaction while stirring. The reaction was allowed to stir at reflux (140 ^{o}C) for another 90 minutes. After cooling to room temperature, the mixture was allowed to cool slowly to room temperature. 70 mL cold methanol was added to the reaction mixture and the porphyrin was allowed to recrystallize overnight. This mixture was then filtered using a fritz funnel. The precipitate was washed with methanol and the purple crystalline crude product was purified using column chromatography (eluent gradient of 1/1 chloroform/petroleum ether to 100% chloroform) to obtain a **crystalline purple solid** (**600 mg, 1.73 mmol, 6% yield).** R_f = 0.33 ($CHCl_3$); ^{1}H NMR ($CDCl_3$, 500 MHz): δ (ppm) = 8.87 (d, *J* = 4.5 Hz, 2 H, 2 x $H_{\beta\text{-pyrrolic}}$), 8.83 (s, *J* = 23.9 Hz, 6 H, 6 x $H_{\beta\text{-pyrrolic}}$), 8.21 (d, *J* = 6.3 Hz, 6 H, 3 x $H_{2,6\text{-phenyl}}$), 8.04 (d, *J* = 8.5 Hz, 2 H, $H_{3,5\text{-aryl}}$), 7.75 (m, 7.5, 9.3, 7.3, 6.5 Hz, 9 H, 3 x $H_{3,4,5\text{-phenyl}}$), 7.16 (d, *J* = 8.4 Hz, 2 H, 1 x $H_{2,6\text{-aryl}}$), 5.13 (br s, 1 H, Ar-OH), -2.74 (s, 2 H, 2 x N-H). ^{13}C NMR ($CDCl_3$, 500 MHz): δ (ppm) = 155.4 (**C_{OH}**), 142.2 (**C_3**), 135.7 (**C_4**), 134.6 (**C_5**), 131.1 (**C_8**), 127.7 (**C_1**), 126.7 (**C_6**), 120.1 (**C_2**), 113.7 (**C_7**)**.** UV-Vis (THF) λ_{max} (log ε) = 418 (5.97), 515 (4.54), 550 (4.20), 592 (3.87) and 649 nm (3.74). IR (cm^{-1}) = 3501, 3315, 2921, 2902. HRMS (MALDI) *m/z* calcd. for $C_{44}H_{30}N_4O$ (M^+): 630.74; found 630.30.

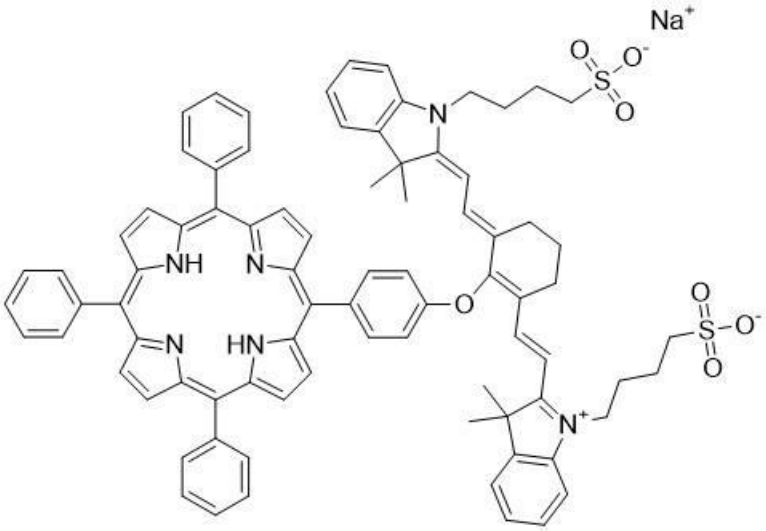

TPPOH (102 mg, 0.16 mmol, 1.00 eq.) was dissolved in 15 mL dry DMF under argon in a 25 mL two-neck round bottom flask with a stirrer bar. 7 mg **NaH** (60 % oil solution, 0.175 mmol, 1.09 eq.) was then added and the solution was allowed to stir under room temperature (21°C) for 30 minutes under argon. The reaction mixture turned from a dark violet to a dark green solution. **IR-783** (118 mg, 0.16 mmol, 1.00 eq.) was then added and the reaction was allowed to stir under ambient temperature in the dark for 18 hours under argon. The solution was then transferred to a round bottom flask and 70 mL diethyl ether was added to allow to precipitate the desired product. The suspension was then centrifuged at 7,000 g for 10 minutes. After removing the supernatant, the solid was washed with 100 mL diethyl ether. A dark crude solid was obtained after removing the diethyl ether *in vacuo* and it was purified using solid deposition column chromatography (dissolving crude product and Florisil® in a 1:1 w/w mixture in dichloromethane and evaporating the solvent) using an eluent: dichloromethane/ethanol/methanol 7/1/2 (V/V/V). The desired **TPPO-IR-783** was obtained as a dark solid (181 mg, 0.13 mmol, 84% yield). R_f = 0.42 (7/1/2 dichloromethane/ethanol/methanol). ^{1}H NMR (DMSO-d_6, 500 MHz): δ (ppm) = 8.82 (dd, *J* = 5.0, 7.0 Hz, 8 H, 6 x $H_{\beta\text{-pyrrolic}}$), 8.67 (d, *J* = 4.5 Hz, 2 H, 2 x $H_{\beta\text{-pyrrolic}}$), 8.25 (d, *J* = 10.0 Hz, 2 H, 2 x C-$H_{aromatic}$), 8.20 (dd, *J* = 7.5, 5.0, 7.5 Hz, 6 H, 3 x $H_{2,6\text{-phenyl}}$), 8.17 (d, *J* = 12.5 Hz, 2 H, $H_{3,5\text{-aryl}}$), 7.81 (m, *J* = 6.3, 6.8, 4.5, 10.0, 7.0, 6.3, 3.3 Hz, 9 H, 3 x $H_{3,4,5\text{-phenyl}}$), 7.66 (d, *J* = 8.0 Hz, 2 H, $H_{2,6\text{-aryl}}$), 7.62 (d, *J* = 8.0 Hz, 2 H, 2 x C-$H_{aromatic}$), 7.47 (d, *J* = 8.8 Hz, 2 H, 2 x C-H_{vinyl}), 7.42 (t, *J* = 7.0, 8.0 Hz, 2 H, 2 x C-$H_{aromatic}$), 7.26 (t, *J* = 7.5, 7.5 Hz, 2 H, 2 x C-$H_{aromatic}$), 6.41 (d, *J* = 15 Hz, 2 H, 2 x C-H_{vinyl}), 4.22 (t, *J* = 7.5, 8.5 Hz, 2 H, 2 x CH_2), 2.89 (t, *J* = 5, 7.5 Hz,, 2 H, 2 x CH_2), 2.53 (t, *J* = 8.0, 15.0 Hz, 2 H, 2 x cyclic CH_2), 2.07 (t, *J* = 5.0, 7.0 Hz, 2 H, 2 x CH_2), 2.07 (t, *J* = 5.0, 7.0 Hz, 4 x H, 2 x CH_2), 1.85 (quin, *J* = 7.5, 8.0, 7.0, 8.0, Hz, 4 H, 2 x CH_2), 1.78 (quin, *J* = 8.0, 7.0, 8.0, 8.5 Hz, 2 H, 2 x CH_2), 1.63 (s, 12 H, 4 x CH_3). ^{13}C NMR

(DMSO-d_6, 500 MHz): δ (ppm) = 171.5 (**C_{17}**), 162.0 (**C_{12}**), 159.2 (**C_{18}**), 142.1 (**C_{21}**), 141.0 (**C_{15}**), 140.8 (**C_{22}**), 136.0 (**C_5**), 135.1 (**C_{19}**), 134.0 (**C_{23}**), 128.5 (**C_6**), 128.0 (**C_{10}**), 126.9 (**C_{24}**), 124.7 (**C_{11}**), 122.5 (**C_{25}**), 121.4 (**C_{15}**), 120.0 (**C_{26}**), 119.9 (**C_{20}**), 119.1 (**C_9**), 111.3 (**C_7**), 100.6 (**C_8**), 50.6 (**C_{13}**), 48.7 (**C_{14}**), 43.6 (**C_4**), 27.4 (**C_1**), 26.0 (**C_2**), 23.6 (**C_{16}**), 22.5 (**C_3**). HRMS (ESI): Calcd for $C_{82}H_{75}N_6O_7S_2$: *m/z* 1321.6473 ([M-Na^+]$^+$). Found: *m/z* 1322.5324 ([M-Na^+]$^+$).

5.5.2. Photophysical characterization

For all UV-Vis spectra, photoluminescence and nanosecond absorption spectroscopy shown, the instrumentation used is detailed in Chapter **3** (section **3.4.2**).

Femtosecond transient absorption spectroscopy

Fs-TA experiments were performed with a Spectra-Physics Solstice Titanium:Sapphire regenerative amplifier system. The 515 nm pump pulse was generated using an optical parametric amplifier (Spectra-Physics OPA 800C). Residual 800 nm light was focussed on a sapphire plate to produce white probe light which was detected with a charge-coupled device detector (Ocean Optics). The polarization of the pump beam was at the magic angle (54.7°) with respect to that of the probe (Berek Polarization Compensator (New Focus)). The excitation pulse was passed over an optical delay line (Physik Instrumente, M-531DD) that generated an experimental time window of up to 3.6 ns between the excitation and probe pulses with a maximal resolution of 0.6 fs/ step. The laser output was typically ~2 μJ $pulse^{-1}$ (130 fs FWHW) with a repetition rate of 1 kHz. The samples were placed in cells of 2 mm path length (Hellma) and stirred with a downward projected PTFE shaft using a direct drive spectro-stir (SPECTRO-CELL).

Data were analyzed using Glotaran software.[37]

5.6. Supplementary information

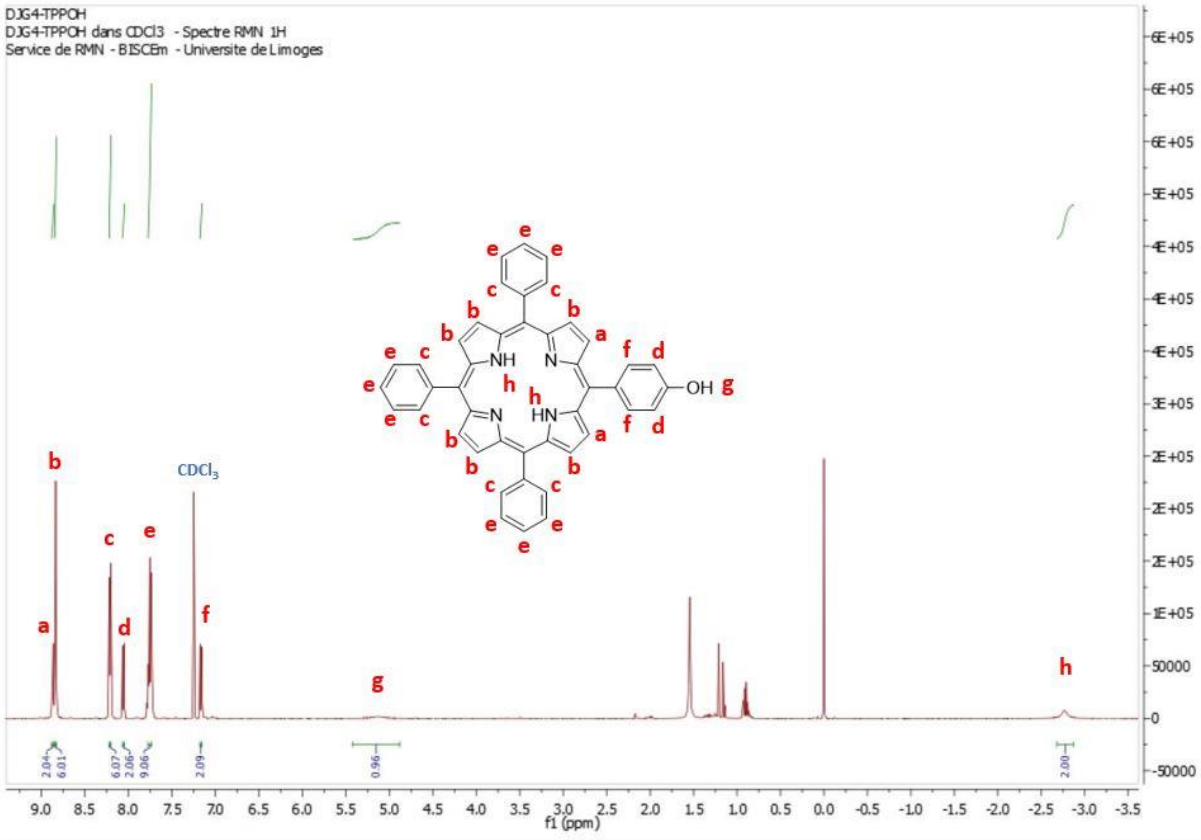

Figure S5.1. *Fully Integrated ^{1}H NMR spectrum at room temperature of 5-(4-hydroxyphenyl)-10,15,20-triphenylporphyrin (**TPPOH**), in $CDCl_3$, with the structure and labels for the protons in the structure.* ***Note:*** *peaks at from 1.5 to 0.8 ppm are due to the NMR tube and are unrelated to the sample.*

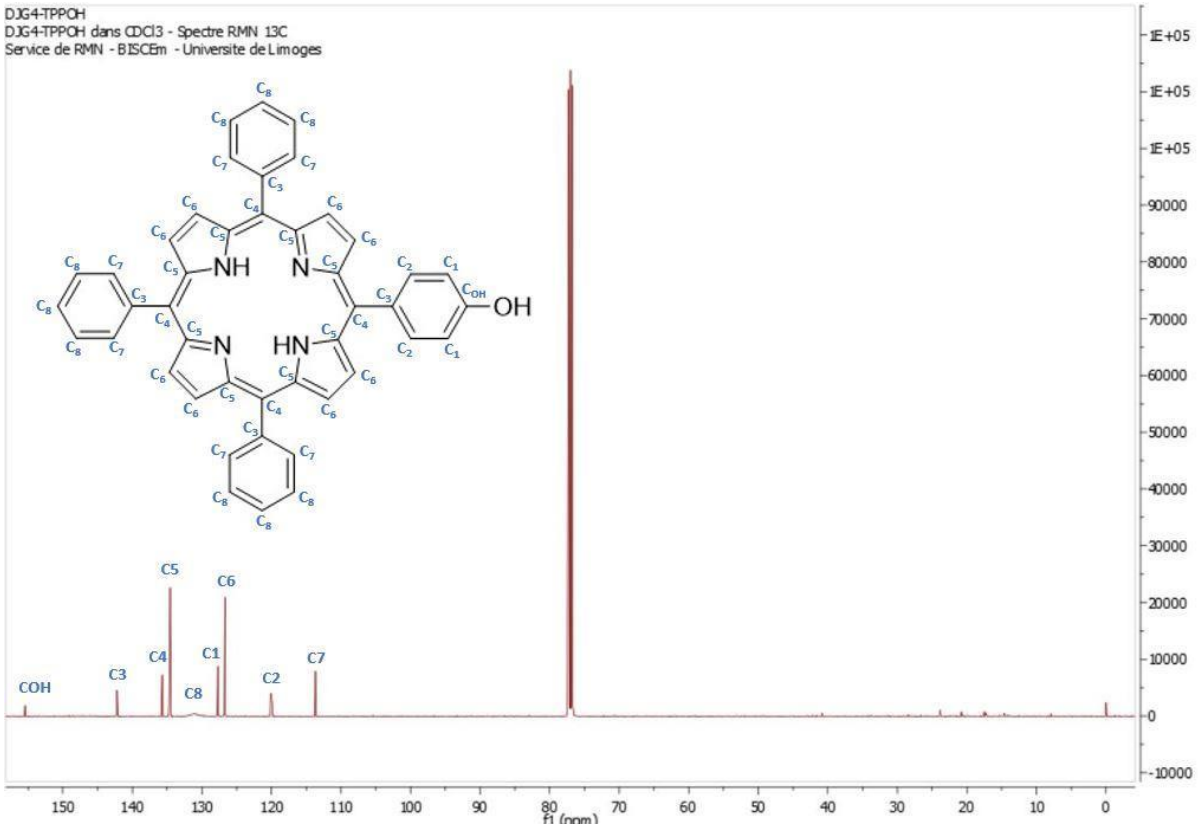

Figure S5.2. *^{13}C NMR spectrum at room temperature of 5-(4-hydroxyphenyl)-10,15,20-triphenylporphyrin (**TPPOH**), in $CDCl_3$, with the structure and labels for the carbons in the structure.*

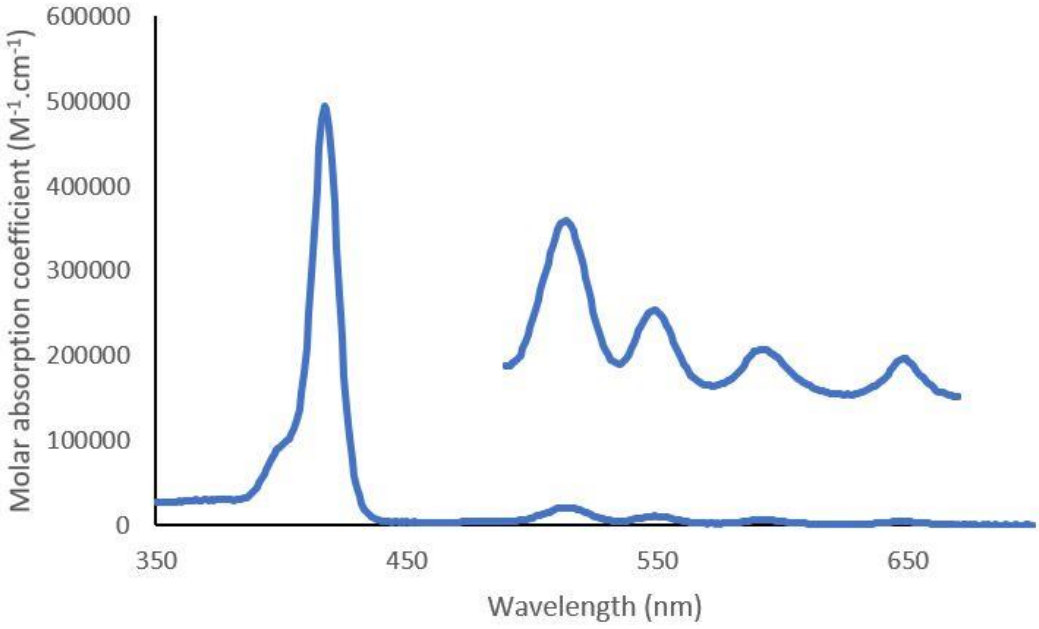

Figure S5.3. *UV-Vis spectrum at room temperature of 5-(4-hydroxyphenyl)-10,15,20-triphenylporphyrin (**TPPOH**) in tetrahydrofuran (THF) using a molar absorption scale.*

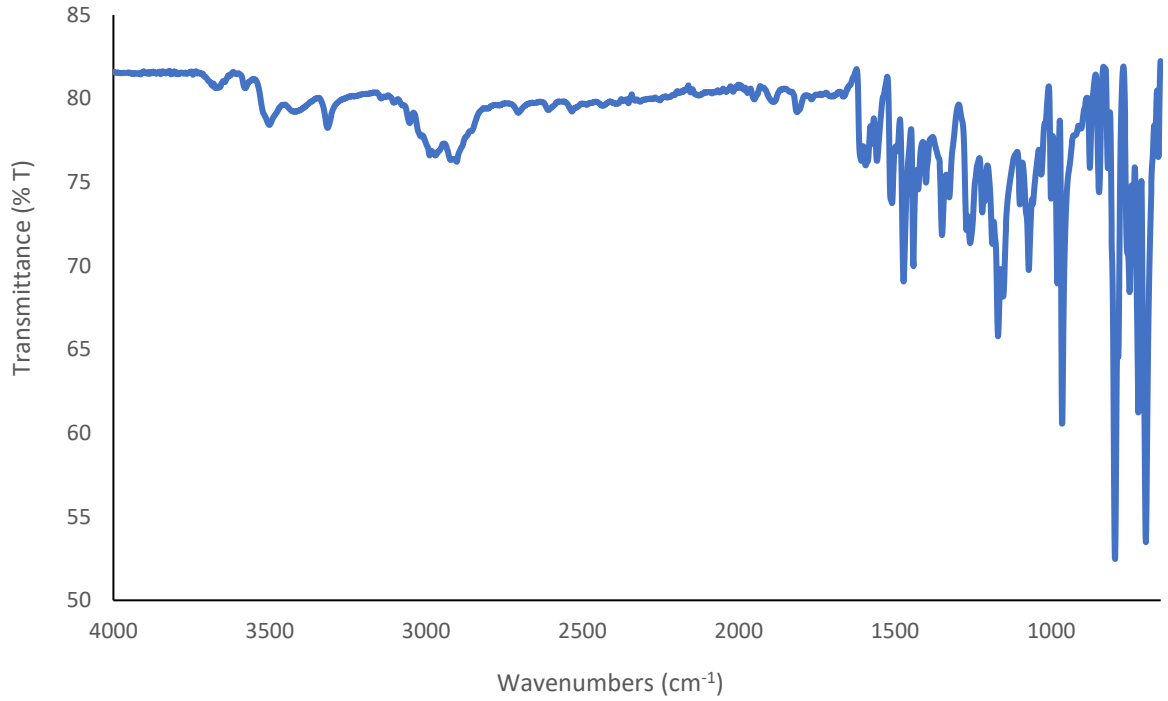

Figure S5.4. *IR spectrum at room temperature of 5-(4-hydroxyphenyl)-10,15,20-triphenylporphyrin (**TPPOH**).*

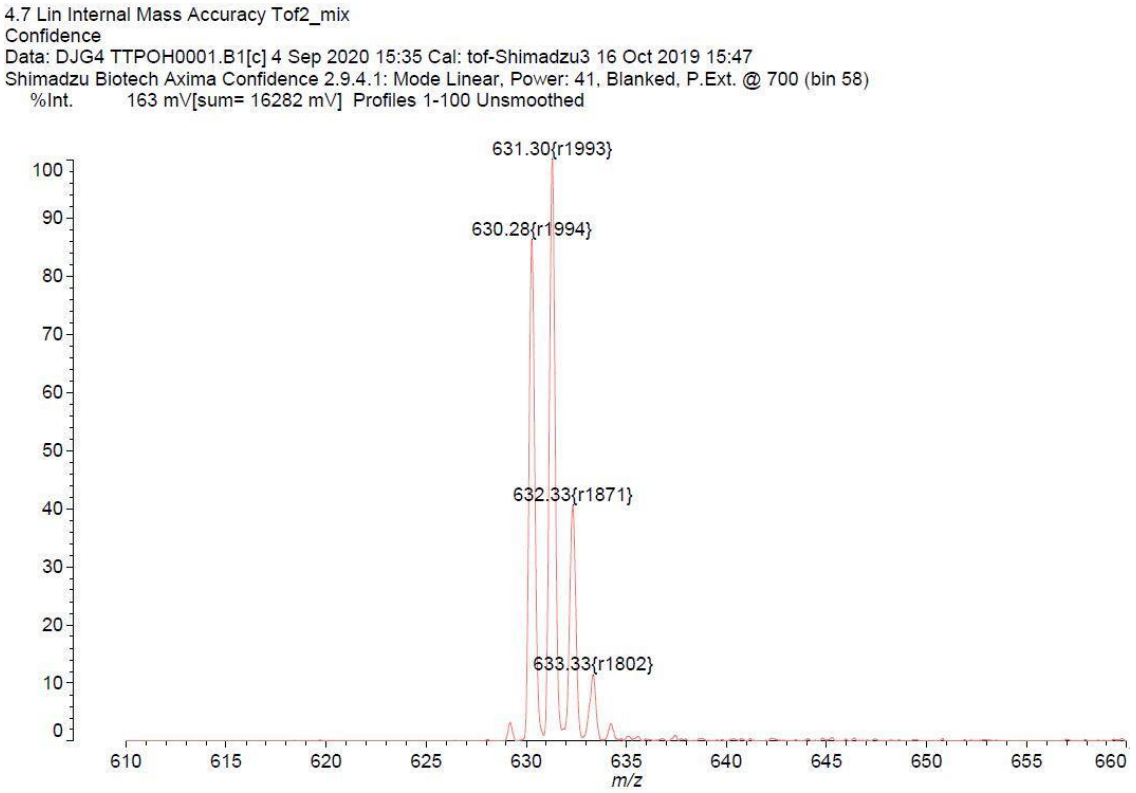

Figure S5.5. *Mass spectrum zoom at room temperature, displaying the isotope pattern of **TPPOH**, dissolved in chloroform ($CHCl_3$).*

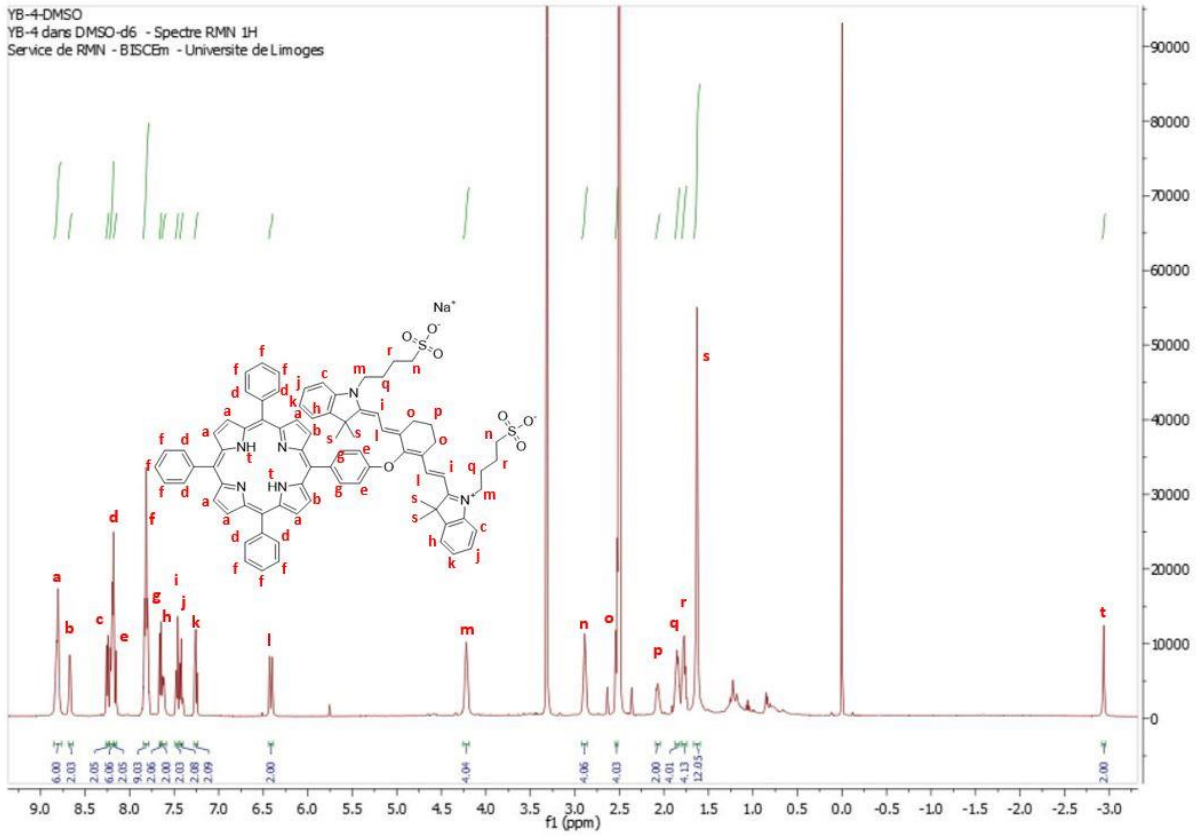

Figure S5.6. *Fully Integrated ^{1}H NMR spectrum at room temperature of* ***TOI****, in DMSO-d_6, with the structure and labels for the protons in the structure.*

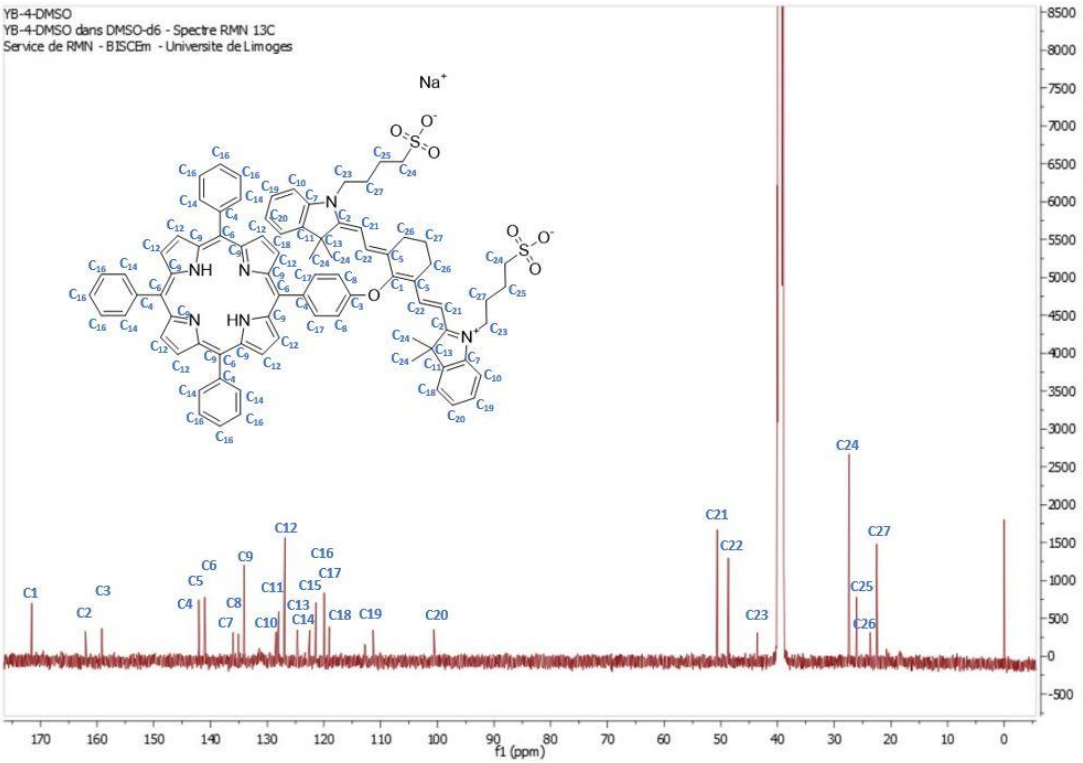

Figure S5.7. *^{13}C NMR spectrum at room temperature of **TOI**, in DMSO-d_6, with the structure and labels for the carbons in the structure.*

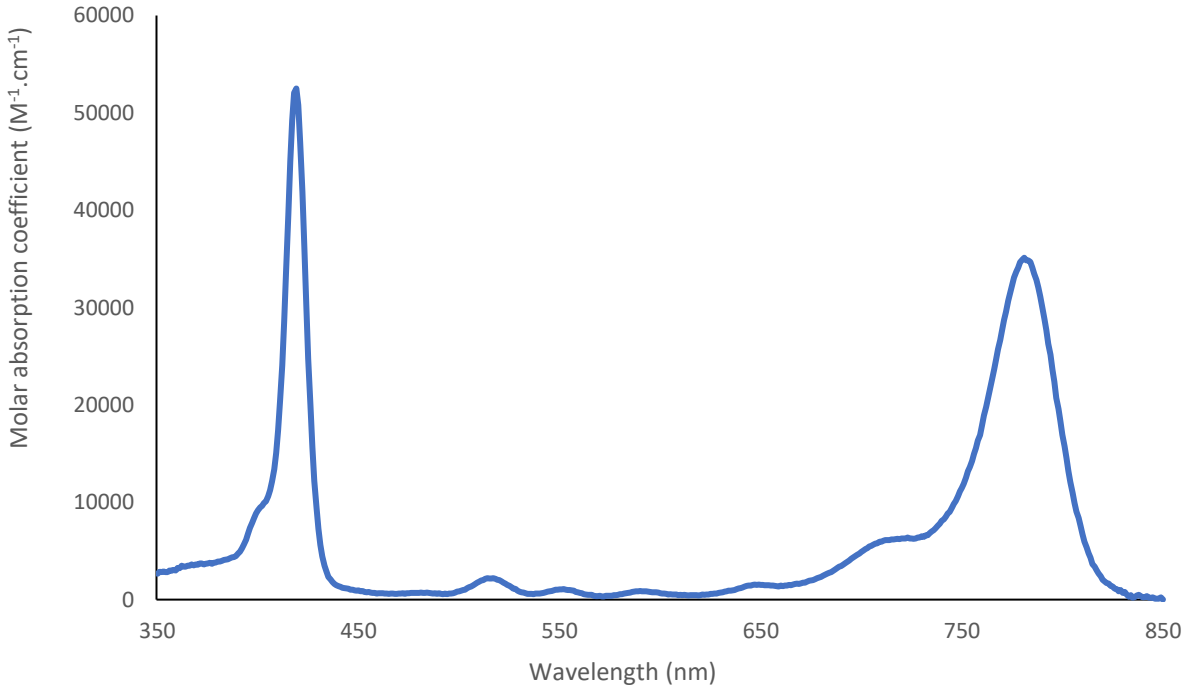

Figure S5.8.*UV-Vis spectrum at room temperature of **TOI** in $CHCl_3$ using a molar absorption scale.*

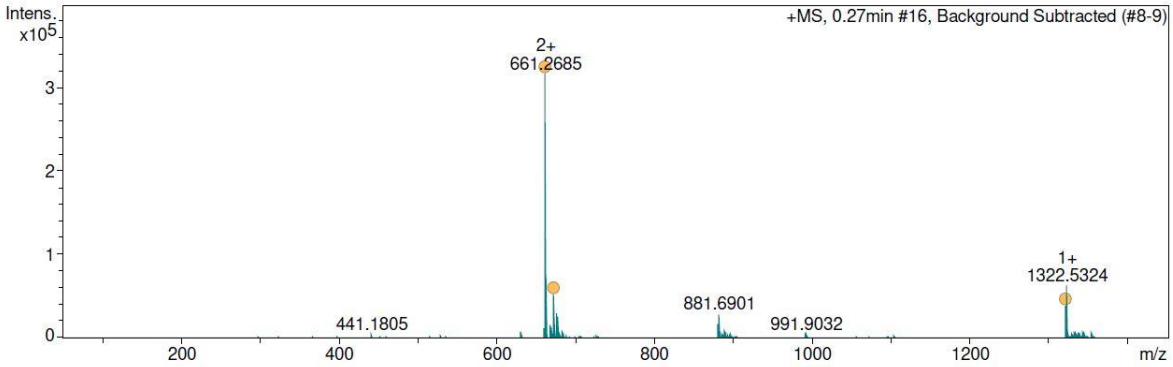

Figure S5.9. *Mass spectrum, obtained via electron spray ionization of* ***TOI*** *in methanol.*

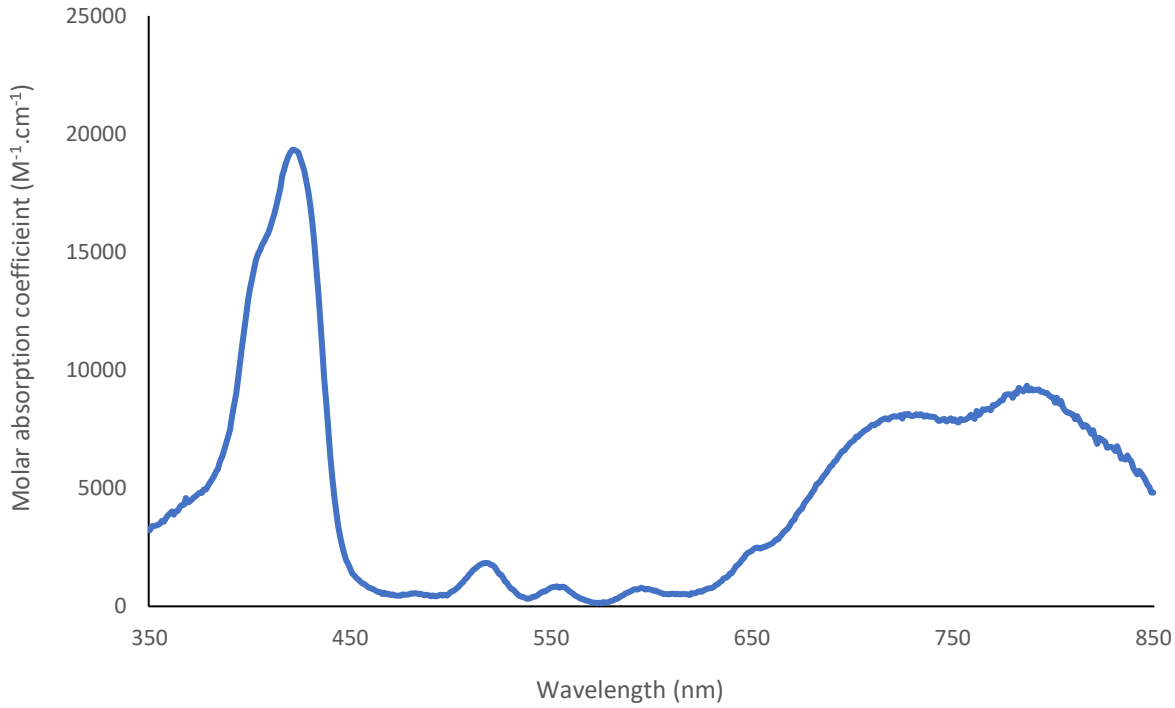

Figure S5.10.*UV-Vis spectrum at room temperature of* ***TOI*** *in PBS using a molar absorption scale.*

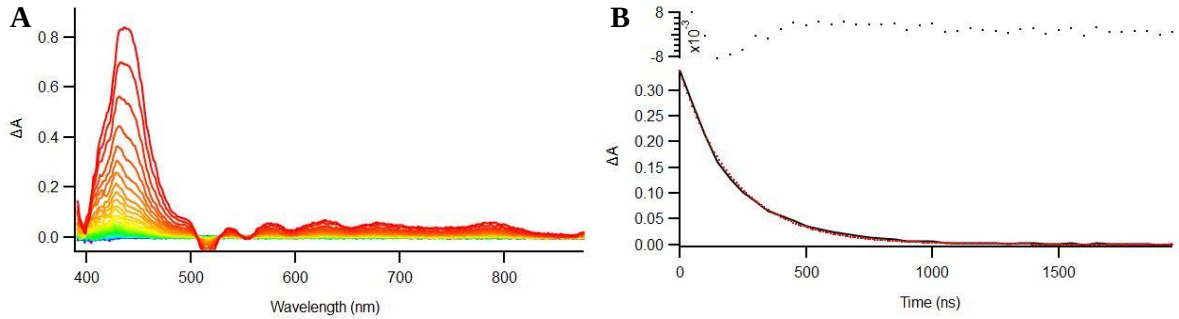

Figure S5.11. (A): *Ns-TA spectrum of* ***TPPOH*** *in THF;* ***(Right):*** *Decay spectrum of* ***TPPOH*** *in THF. Excitation wavelength is 548 nm. Incremental delay = 50 ns.* τ_T *= 312* $\pm$ *8 ns.*

5.7. References

[1] T. Tanaka and A. Osuka, Conjugated Porphyrin Arrays: Synthesis, Properties and Applications for Functional Materials, *Chem. Soc. Rev.*, 2015, **44**, 943–969. doi: 10.1039/C3CS60443H.

[2] M. O. Senge, N. N. Sergeeva and K. J. Hale, Classic Highlights in Porphyrin and Porphyrinoid Total Synthesis and Biosynthesis, *Chem. Soc. Rev.*, 2021, **50**, 4730–4789. doi: 10.1039/C7CS00719A.

[3] H. A. Shindy, Fundamentals in the Chemistry of Cyanine Dyes: A Review, *Dyes Pigm.*, 2017, **145**, 505–513. doi: 10.1016/j.dyepig.2017.06.029.

[4] A. R. Nödling, E. M. Mills, X. Li, D. Cardella, E. J. Sayers, S.- H. Wu, A. T. Jones, L. Y. P. Luk and Y.- H. Tsai, Cyanine Dye Mediated Mitochondrial Targeting Enhances the Anti-Cancer Activity of Small-Molecule Cargoes, *Chem. Commun.*, 2020, **56**, 4672–4675. doi: 10.1039/C9CC07931A.

[5] R. M. Abd El-Aal and M. Younis, Synthesis and Antimicrobial Activity of Certain Novel Monomethine Cyanine Dyes, *Dyes Pigm.*, 2004, **60**, 205–214. doi: 10.1016/S0143-7208(03)00131-1.

[6] F. Eissa, Preparation, Antibacterial Activity and Absorption Spectra of Pyrazolo-Oxadiazine Cyanine Dyes, *J. Chin. Chem. Soc.*, 2009, **56**, 843–849. doi: 10.1002/jccs.200900125.

[7] E. Delaey, F. van Laar, D. De Vos, A. Kamuhabwa, P. Jacobs and P. de Witte, A Comparative Study of the Photosensitizing Characteristics of Some Cyanine Dyes, *J. Photochem. Photobiol. B, Biol.*, 2000, **55**, 27–36. doi: 10.1016/S1011-1344(00)00021-X.

[8] Y. Li, Y. Zhou, X. Yue and Z. Dai, Cyanine Conjugates in Cancer Theranostics, *Bioact. Mater.*, 2021, **6**, 794–809. doi: 10.1016/j.bioactmat.2020.09.009.

[9] C. Shi, J. B. Wu and D. Pan, Review on Near-Infrared Heptamethine Cyanine Dyes as Theranostic Agents for Tumor Imaging, Targeting, and Photodynamic Therapy, *J. Biomed. Opt.*, 2016, **21**, 050901. doi: 10.1117/1.JBO.21.5.050901.

[10] L. Feng, W. Chen, X Ma, S. H. Liu and J. Yin, Near-Infrared Heptamethine Cyanines (Cy7): From Structure, Property to Application, *Org. Biomol. Chem.*, 2020, **18**, 9385–9397. doi: 10.1039/D0OB01962C.

[11] R. Giovannetti, The Use of Spectrophotometry UV-Vis for the Study of Porphyrins, 2012. doi: 10.5772/38797.

[12] H. -G. Jeong and M. -S. Choi, Design and Properties of Porphyrin-Based Singlet Oxygen Generator, *Isr. J. Chem.*, 2016, **56,** 110–118. doi: 10.1002/ijch.201500026.

[13] N. S. James, R. R. Cheruku, J. R. Missert, U. Sunar and R. K. Pandey, Measurement of Cyanine Dye Photobleaching in Photosensitizer Cyanine Dye Conjugates Could Help in Optimizing Light Dosimetry for Improved Photodynamic Therapy of Cancer, *Molecules*, 2018, **23**, 1842–1853. doi: 10.3390/molecules23081842.

[14] K. Ogawa, Y. Nagatsuka and Y. Kobuke, Synthesis and Photophysical Properties of Doubly Porphyrin-Substituted Cyanine Dye, *J. Porphyr. Phthalocyanines*, 2011, **15**, 678–685. doi: 10.1142/S1088424611003616.

[15] K. A. Zhdanova, A. V. Ezhov, N. A. Bragina and A. F. Mironov, Synthesis of New Binary Porphyrin–Cyanine Conjugates and Their Self-Aggregation in Organic-Aqueous Media, *Mendeleev Commun.*, 2018, **28**, 626–628. doi: 10.1016/j.mencom.2018.11.021.

[16] A. D. Adler, F. R. Longo, J. D. Finarelli, J. Goldmacher, J. Assour and L. Korsakoff, A simplified synthesis for meso-tetraphenylporphine, *J. Org. Chem.*, 1967, **32**, 476. doi: 10.1021/jo01288a053

[17] G. Yang, Y. Zhang, J. Zou, L. -P. Huang, M. D. Chordia, W. Yue, J. -J. Wu and D. -F. Pan, Synthesis and Biological Evaluation of Genistein-IR783 Conjugate: Cancer Cell Targeted Delivery in MCF-7 for Superior Anti-Cancer Therapy, *Molecules*, 2019, **24**, 4120–4136. doi: 10.3390/molecules24224120.

[18] B. Ventura, L. Flamigni, G. Marconi, F .Lodato and D. L. Officer, Extending the Porphyrin Core: Synthesis and Photophysical Characterization of Porphyrins with π-Conjugated β-Substituents, *New J. Chem.*, 2008, **32**, 166–178. doi: 10.1039/B707505G.

[19] M. W. Lee, D. L. Lee, W. N. Yen and C. Y. Yeh, Synthesis, Optical and Photovoltaic Properties of Porphyrin Dyes, *J. Macromol. Sci. A*, 2009, **46**, 730–737. doi: 10.1080/10601320902938558.

[20] M. P. A. Williams, M. Ethirajan, K. Ohkubo, P. Chen, P. Pera, J. Morgan, W. H. White, M. Shibata, S. Fukuzumi, K. M. Kadish and R. K. Pandey, Synthesis, Photophysical, Electrochemical, Tumor-

Imaging, and Phototherapeutic Properties of Purpurinimide-N-Substituted Cyanine Dyes Joined with Variable Lengths of Linkers, *Bioconj. Chem.*, 2011, **22**, 2283–2295. doi: 10.1021/bc200345p.
[21] N. J. Patel, Y. Chen, P. Joshi, P. Pera, H. Baumann, J. R. Missert, K. Ohkubo, S. Fukuzumi, R. R. Nani, M. J. Schnermann, P. Chen, J. Zhu, K. M. Kadish and R. K. Pandey, Effect of Metalation on Porphyrin-Based Bifunctional Agents in Tumor Imaging and Photodynamic Therapy, *Bioconjug. Chem.*, 2016, **27**, 667–680. doi: 10.1021/acs.bioconjchem.5b00656.
[22] J. L. Bricks, Y. L. Slominskii, I. D. Panas and A. P. Demchenko, Fluorescent J-Aggregates of Cyanine Dyes: Basic Research and Applications Review, *Methods Appl. Fluoresc.*, 2017, **6**, 012001. doi: 10.1088/2050-6120/aa8d0d.
[23] U. Subuddhi, S. Haldar, S Sankararaman and A. Mishra, Photophysical Behaviour of 1-(4-N,N-Dimethylaminophenylethynl)Pyrene (DMAPEPy) in Homogeneous Media, *Photochem. Photobiol. Sci*., 2006, **5**, 459–466. doi: 10.1039/b600009f.
[24] P. G. Seybold and M. Gouterman, Porphyrins. XIII: Fluorescence Spectra and Quantum Yields, *J. Mol. Spectrosc.*, 1969, **31**, 1–13. doi: 10.1016/0022-2852(69)90335-X.
[25] Y. Wang, Y. Gu, Z. Zuo and N. Huang, Choosing Optimal Wavelength for Photodynamic Therapy of Port Wine Stains by Mathematic Simulation, *J. Biomed. Opt.*, 2011, **16**, 098001. doi: 10.1117/1.3616127.
[26] K. P. Nielsen, A. Juzeniene, P. Juzenas, K. Stamnes, J. J. Stamnes and J. Moan, Choice of Optimal Wavelength for PDT: The Significance of Oxygen Depletion, *Photochem. Photobiol.*, 2005, **81**, 1190–1194. doi: 10.1562/2005-04-06-RA-478.
[27] S. K. Panigrahi and A. K. Mishra, Inner Filter Effect in Fluorescence Spectroscopy: As a Problem and as a Solution, *J. Photochem. Photobiol.*, 2019, **41**, 100318. doi: 10.1016/j.jphotochemrev.2019.100318.
[28] G. Brancato, G. Signore, P. Neyroz, D. Polli, G. Cerullo, G. Abbandonato, L. Nucara, V. Barone, F. Beltram and R. Bizzarri, Dual Fluorescence through Kasha's Rule Breaking: An Unconventional Photomechanism for Intracellular Probe Design, *J. Phys. Chem. B.*, 2015, **119**, 6144–6154. doi: 10.1021/acs.jpcb.5b01119.
[29] N. Hananya, O. Green, R. Blau, R. Satchi-Fainaro and D. Shabat, A Highly Efficient Chemiluminescence Probe for the Detection of Singlet Oxygen in Living Cells, *Angew. Chem. Int. Ed.*, 2017, **56**, 11793–11796. https://doi.org/10.1002/anie.201705803.
[30] N. S. James, Y. Chen, P. Joshi, T. Y. Ohulchanskyy, M. Ethirajan, M. Henary, L. Strekowsk and R. K Pandey, Evaluation of Polymethine Dyes as Potential Probes for Near Infrared Fluorescence Imaging of Tumors: Part – 1, *Theranostics*, 2013, **3**, 692–702. doi: 10.7150/thno.5922.
[31] L. M. Mazur, T. Roland, S. Leroy-Lhez, V. Sol, M. Samoc, I. D. W. Samuel and K. Matczyszyn, Efficient Singlet Oxygen Photogeneration by Zinc Porphyrin Dimers upon One- and Two-Photon Excitation, *J. Phys. Chem. B.*, 2019, **123**, 4271–4277. doi: 10.1021/acs.jpcb.8b12561.
[32] R. Schmidt, C. Tanielian, R. Dunsbach and C. Wolff, Phenalenone, a Universal Reference Compound for the Determination of Quantum Yields of Singlet Oxygen O2(1Δg) Sensitization, *J. Photochem. Photobiol. A*, 1994, **79**, 11–17. doi: 10.1016/1010-6030(93)03746-4.
[33] F. Wilkinson, W. P. Helman and A. B. Ross, Rate constants for the decay and reactions of the lowest electronically excited singlet state of molecular oxygen in solution. An expanded and revised compilation, *J. Phys. Chem. Ref. Data*, 1995, **24**, 663–677. doi: 10.1063/1.555965
[34] D. J. Gibbons, A. Farawar, P. Mazzella, S. Leroy-Lhez and R. M. Williams, Making Triplets from Photo-Generated Charges: Observations, Mechanisms and Theory, *Photochem. Photobiol. Sci.*, 2020, **19**, 136–158. doi: 10.1039/C9PP00399A.
[35] M. A. Filatov, S. Karuthedath, P. M. Polestshuk, S. Callaghan, K. J. Flanagan, M. Telitchko, T. Wiesner, F. Laquai and M. O. Senge, Control of Triplet State Generation in Heavy Atom-Free BODIPY–Anthracene Dyads by Media Polarity and Structural Factors, *Phys. Chem. Chem. Phys.*, 2018, **20**, 8016–8031. doi: 10.1039/C7CP08472B.
[36] M. T. Colvin, A. B. Ricks, A. M. Scott, D. T. Co and M. R. Wasielewski, Intersystem Crossing Involving Strongly Spin Exchange-Coupled Radical Ion Pairs in Donor–bridge–Acceptor Molecules, *J. Phys. Chem. A*, 2012, **116**, 1923–1930. doi: 10.1021/jp212546w
[37] J. J. Snellenburg, S. Laptenok, R. Seger, K. M. Mullen and I. H. M. Van Stokkum, Glotaran: A Java-Based Graphical User Interface for the R Package TIMP, *J. Stat. Softw.*, 2012, 49, 1–22. doi: 10.18637/jss.v049.i03.

Synthesis of photosensitizers for photomedicine

Abstract

This chapter gives an overview of the synthesis that was conducted during the PhD research, that is not described in the other chapters. This chapter shows the synthesis of starting materials for photosensitizers consisting of cyanine dyes and porphyrins for photomedicine. The synthesis and their impact are discussed with the aid of synthetic reaction schemes. Detailed experimental procedures and characterization are presented.

6.1. Introduction

The research described in this Thesis contains a strong synthetic component, as shown in chapters 3, 4 and 5. These chapters describe the synthesis of 5,10,15,20-tetra-(4-hexyloxyphenyl)porphyrin, lignin functionalized with porphyrines and with cyanine dyes a well as a porhyrin-cyanin dyad, respectively. This chapter describes additional synthesis that was performed.

The introduction is split into two parts: porphyrin-cyanine dye conjugates and porphyrins for thin films.

6.1.1. Porphyrin-cyanine dye conjugates

Indoles [1] (See chemical structure in figure **6.1**) are common starting materials for near-IR absorbing fluorophores – heptamethine cyanine dyes (see Figure **6.2** for one of these dyes – **MIH-148**).[2, 3] These dyes can absorb near-IR light and have applications in *in vivo* imaging[4] and DNA sequencing.[5] **MIH-148** is known for its selective accumulation in solid tumors, compared to healthy cells.[6, 7] It is non-toxic towards healthy cells, which is one of the reasons why it has been applied in *in vivo* human diagnostic optical imaging.[3, 7]

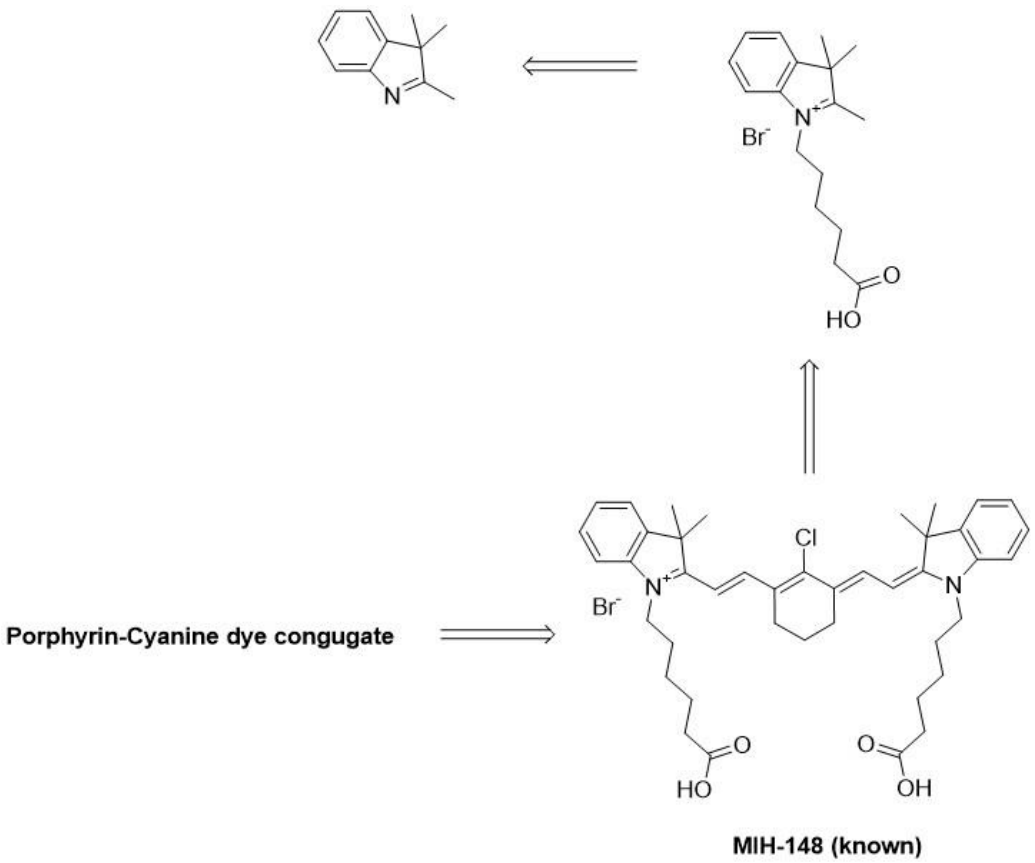

Figure 6.1. *Retrosynthetic pathway for the formation of cyanine dyes (eg. a known heptamethine cyanine dye,* ***MIH-148)*** *from indolenium salts and indoles.*

These cyanine dyes, like **MIH-148**, **IR-783** and **IR-783-SPA**, from chapter **4** and **5**, are the desired synthetic intermediates (see Figure **6.1** and **6.2**) to be combined to porphyrins. As a starting point, combining an A_3B porphyrin (Figure **6.3**) with the three cyanine dyes to form a porphyrin-cyanine dye (P-C) conjugate could create a new class of PSs for photomedicine.

It is well known that cyanine dyes have low singlet oxygen quantum yields[8] and that porphyrins have large singlet oxygen quantum yields.[9] Thus, coupling the cyanine to a porphyrin (see chapter **5** as an example) could theoretically increase the overall singlet oxygen production. Furthermore, they could ideally be photo-activated at low energy wavelengths within the therapeutic window (650–900 nm, as discussed in chapter **1**), and have the ability to target cancer cells.[6, 7] The proposed photophysical mechanism of singlet oxygen production in this new class of PSs could be *via* triplet formation by charge

recombination.[10] Exciting the cyanine dye with near-IR light could form the triplet state on the porphyrin *via* this triplet forming mechanism.

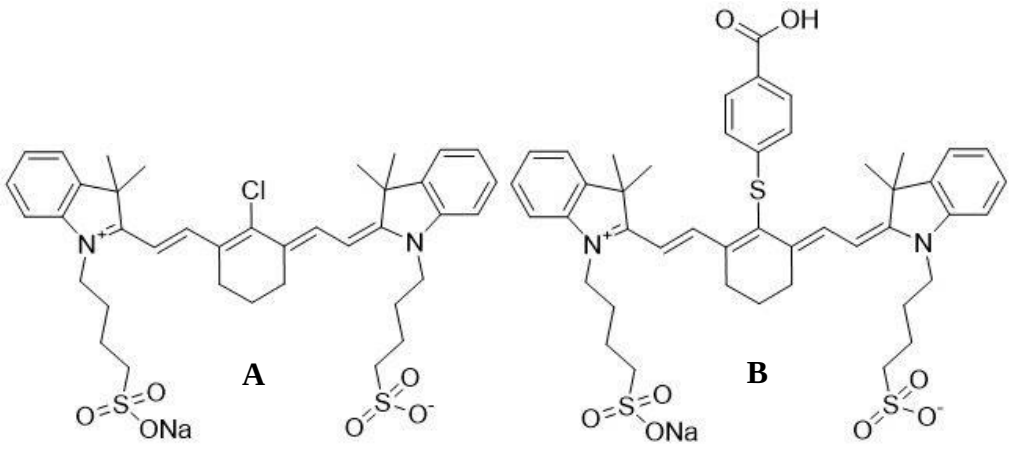

Figure 6.2. *Chemical structures of (**A**): IR-783 and (**B**): IR-783-SPA.*

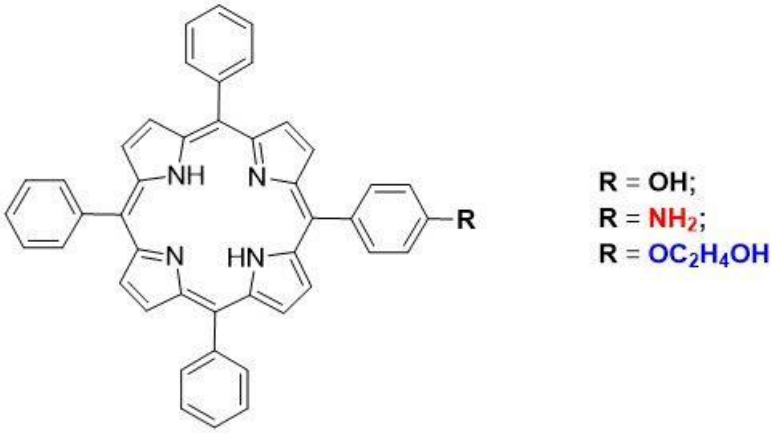

Figure 6.3. *Chemical structure of target A_3B porphyrins to be combined with cyanine dyes.*

The target porphyrin-cyanine conjugates are shown below in Scheme **6.1**. The nature of the cyanine dye and the linker between the two units are the factors to modify. Changes can also be made to the porphyrin to see what effect this would have on the photophysical properties.

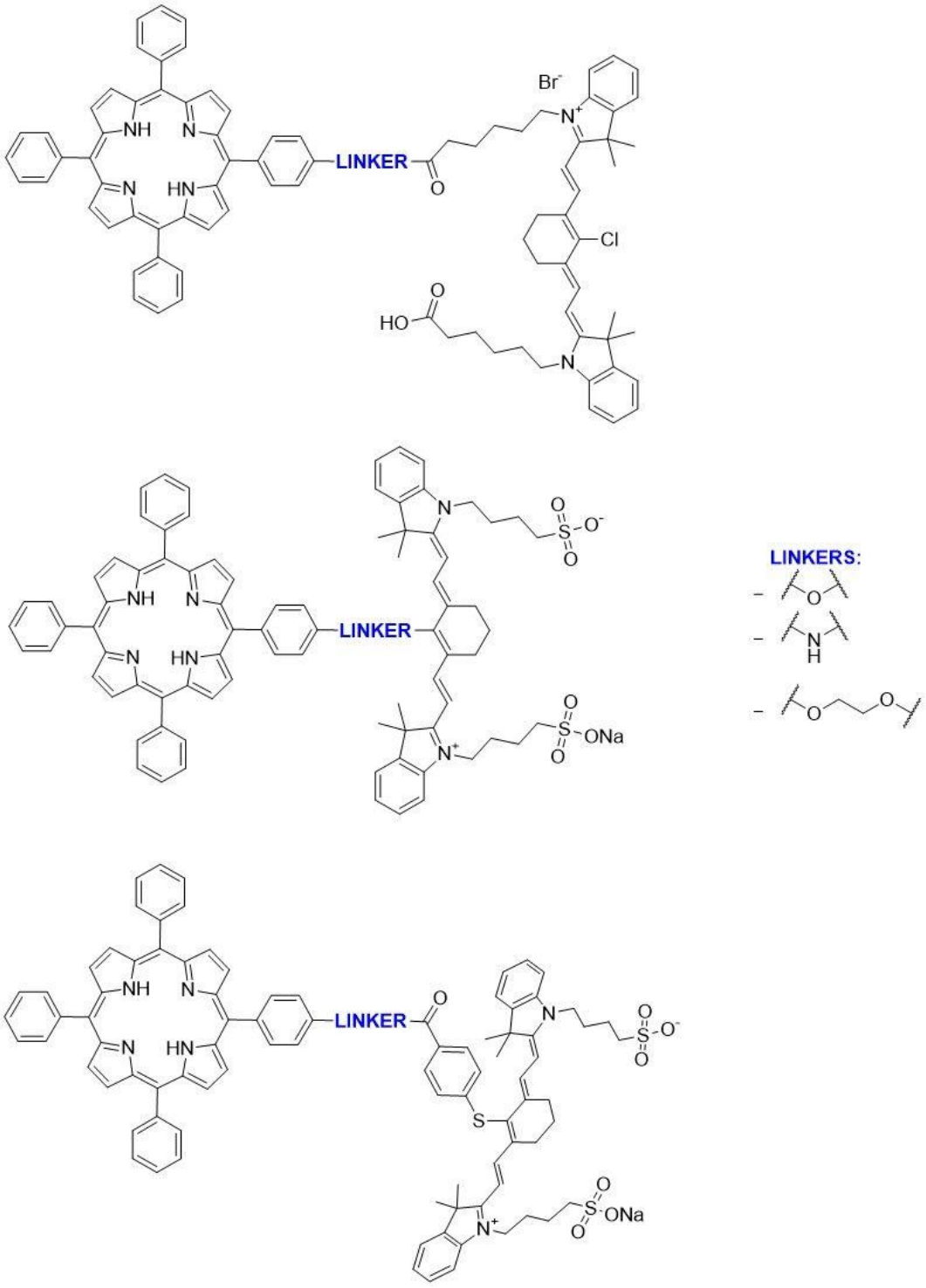

Scheme 6.1. *Target compounds of porphyrin-cyanine dye (P-C) conjugates with the linkers on the right.* ***Note:*** *The linkers consist of ester, ether, amine or amide bonds.*

6.1.2. Porphyrins in thin films

Like described in the **THOPP** chapter (Chapter **3**), free base tetra-alkyloxyphenylporphyrins can form homogenous thin films. Zn(II) derivatives of these porphyrins have also been shown to form ordered films that can even undergo electroluminescence.[19] These porphyrin thin films, like those containing **THOPP** and even metalated derivatives, can likely produce singlet oxygen and could potentially have applications in photodynamic therapy. Moreover, in order to avoid the drawbacks of inserting heavy atoms that can 'elevate dark toxicity, introduce poor photostability,' unnecessarily increase the cost of the PS, and increase the intersystem crossing to the ground state,[10, 11] a heavy atom-free approach was chosen. Therefore, the study of other free base tetra-alkoxyphenylporphyrins, and free base tetra-alkoxynaphthylporphyrins was initiated. The alkyl chain on the periphery of these porphyrin macrocycles can aid the functioning of the porphyrin as a PS in a thin film.[12, 19] The long alkyl chains aid in forming ordered thin films and minimize aggregation of the porphyrin macrocycles. Furthermore, while the tetra-alkoxyphenylporphyrins are known for their thin film formation, the naphthyl derivatives are unknown to the best of our knowledge. Thus, free base tetra-*p*-alkoxyphenyl- and tetra-*p*-alkoxynaphthyl-porphyrins are the desired molecules for film formation and subsequent use as 'heavy metal-atom free PSs' in a thin film (see Figure **6.4**).

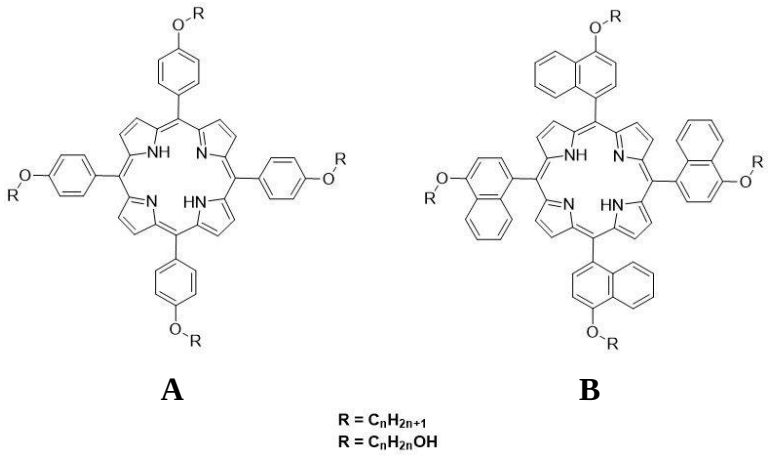

Figure 6.4. *Chemical structures of (**A**): 5,10,15,20-tetra-alkoxyphenylporphyrins (tetra-alkoxyphenylporphyrins) and (**B**): 5,10,15,20-tetra-alkoxynaphthylporphyrins (tetra-alkoxynaphthylporphyrins).*

The synthesis of the intermediates for derivatives similar to **THOPP** (Chapter **3**) and **TPPO-IR-783** (Chapter **5**) are discussed below.

6.2. Discussion

This synthetic discussion is split into two sections: **1)** Porphyrin-cyanine dye conjugates and **2)** tetra-alkoxy-arylporphyrins.

6.2.1. Porphyrin-cyanine dye conjugates

In order to synthesize the **MIH-148** cyanine dye, it's precursor 2,3,3-trimethylindolenium bromide was synthesized, as shown in figure **6.5**.[13]

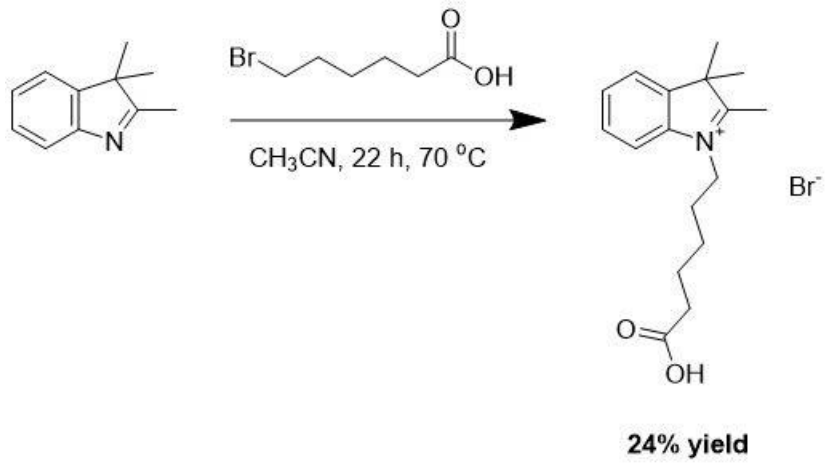

Figure 6.5. *Reaction scheme of 1-(5-carboxypentyl)-2,3,3-trimethylindolenium bromide.*[13]

The 2,3,3-trimethyl indole starting material for the reaction above (Figure **6.5**), was dissolved in acetonitrile (CH_3CN) and refluxed in the presence of 6-bromohexanoic acid. The product was formed *in-situ via* a substitution reaction (S_N2). Followed by removal of the solvent and precipitation of the product in diethyl ether, the quaternary salt product was obtained by filtration in a 24% yield (see section **6.4** for full experimental details of all compounds synthesized in this chapter and Figures **S6.1**–**6.4** for synthetic characterization spectra of this product). This yield is far lower than the 75% yield obtained in the literature and is likely due to the large increase in scale of the reaction (10-fold increase in quantity

of starting materials used).[13] Attempts to synthesize the **MIH-148** dye from this intermediate proved to be unsuccessful after purification *via* column chromatography and using a variety of different synthetic protocols.

The next group of compounds to be discussed is the A_3B porphyrins (see Figures **6.6** and **6.7**). The synthesis of 5-(4-hydroxyphenyl)-10,15,20-triphenylporphyrin (**TPPOH**) involved a porphyrin condensation reaction using modified Adler-Longo conditions (see chapter **5** for experimental spectra and synthetic protocol).[14] Once pure, this porphyrin was dissolved in DMF. The subsequent 'hydroxy-ethyl' spacer (see Figure **6.6**) was attached using a S_N2 reaction, using anhydrous potassium carbonate as the base and under dry conditions. This second step created a better nucleophile in the form of 5-(4-(2-hydroxyethoxy)phenyl)-10,15,20-triphenylporphyrin (**TPPOEtOH**; see Figures **S6.5**–**6.8** for synthetic characterization).

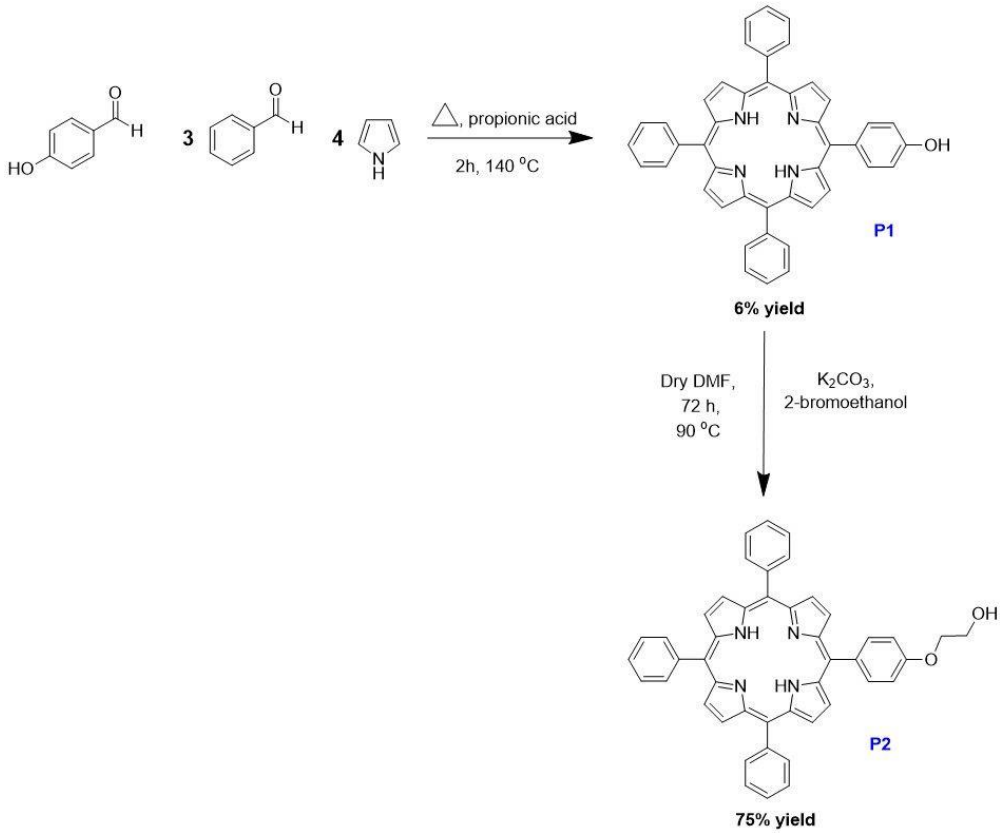

Figure 6.6. *Reaction scheme of 5-(4-hydroxyphenyl)-10,15,20-triphenylporphyrin (**TPPOH**) and 5-(4-(2-hydroxyethoxy)phenyl))-10,15,20-triphenylporphyrin (**TPPOEtOH**).*

The synthesis of **TPPNO$_2$** was conducted in a microwave-assisted iodine-catalyzed reaction reported by Zerrouki and co-workers (see Figure **6.7**).[15] Even though the yield obtained for the **TPPNO$_2$** is much lower (7% yield) than that obtained in the literature (22% yield), it was the highest yield obtained for these A_3B porphyrin reactions (see Figures **6.9**–**6.12** for experimental spectra). This reduction to the aniline containing porphyrin (**TPPNH$_2$**, Figure **6.7**) was conducted using stannous chloride in acidic conditions.[16] The obtained yield was 61% and the full characterization spectra for $TPPNH_2$ are in section **6.5** (Figures **S6.13**–**S6.17**).[17]

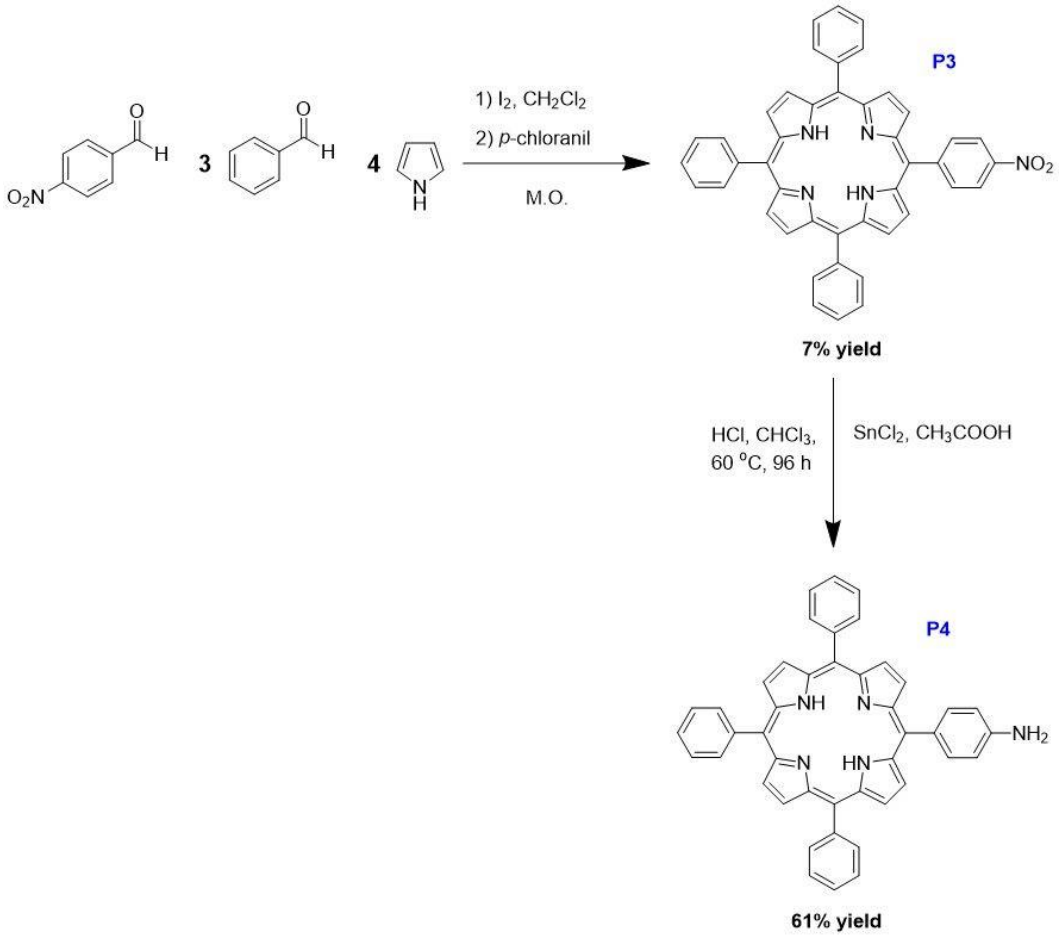

Figure 6.7. *Reaction scheme of 5-(4-nitrophenyl)-10,15,20-triphenylporphyrin (**TPPNO$_2$**) and subsequent reduction to 5-(4-aminophenyl)-10,15,20-triphenylporphyrin (**TPPNH$_2$**).*[15, 16, 17]

Reactions were then conducted to combine the porphyrins **TPPOH**, **TPPOEtOH**, and **TPPNH$_2$** to cyanine dyes: **MIH-148**, **IR-783** and **IR-783-SPA** (see Figure **6.2** for their

chemical structures). However, only **TPPOH** could be covalently attached to **IR-783** (Chapter **5**). The rest of the porphyrins could not be combined with these cyanine dyes even though different reaction conditions were used including S_N2 reactions (**TPPNH$_2$** or **TPPOEtOH** to combine with **IR-783**), amide condensation reactions (**TPPNH$_2$** to combine with **IR-783-SPA**) and esterification reactions (**IR-783-SPA** to combine with **TPPOEtOH** or **TPPOH**).

Future work include the synthesis of conjugates consisting of **IR-783** and **TPPOEtOH** or **TPPNH$_2$** using reaction conditions like in chapter **5**.[18] For the products containing the amide and ester linkers, these reaction conditions can be optimized. Once pure, they can be studied for their photophysical properties, as was done in chapter **5** for **TPPO-IR-783**. As previously mentioned, the ideal situation would be to excite a porphyrin-cyanine conjugate with near-IR light to have a large amount of singlet oxygen generation *via* the TCR mechanism from Chapter **2**.[10]

6.2.2. Tetra-alkoxy-arylporphyrins

In order to synthesize tetra-alkoxy-*meso*-arylporphyrins, aldehydes must be firstly altered, then the porphyrin can be synthesized using appropriate porphyrin condensation reactions. Alternatively, the porphyrin containing tetra-*meso*-4-hydroxyaryl groups can be first formed and then alkylated using S_N2 conditions (see Figure **6.8**).

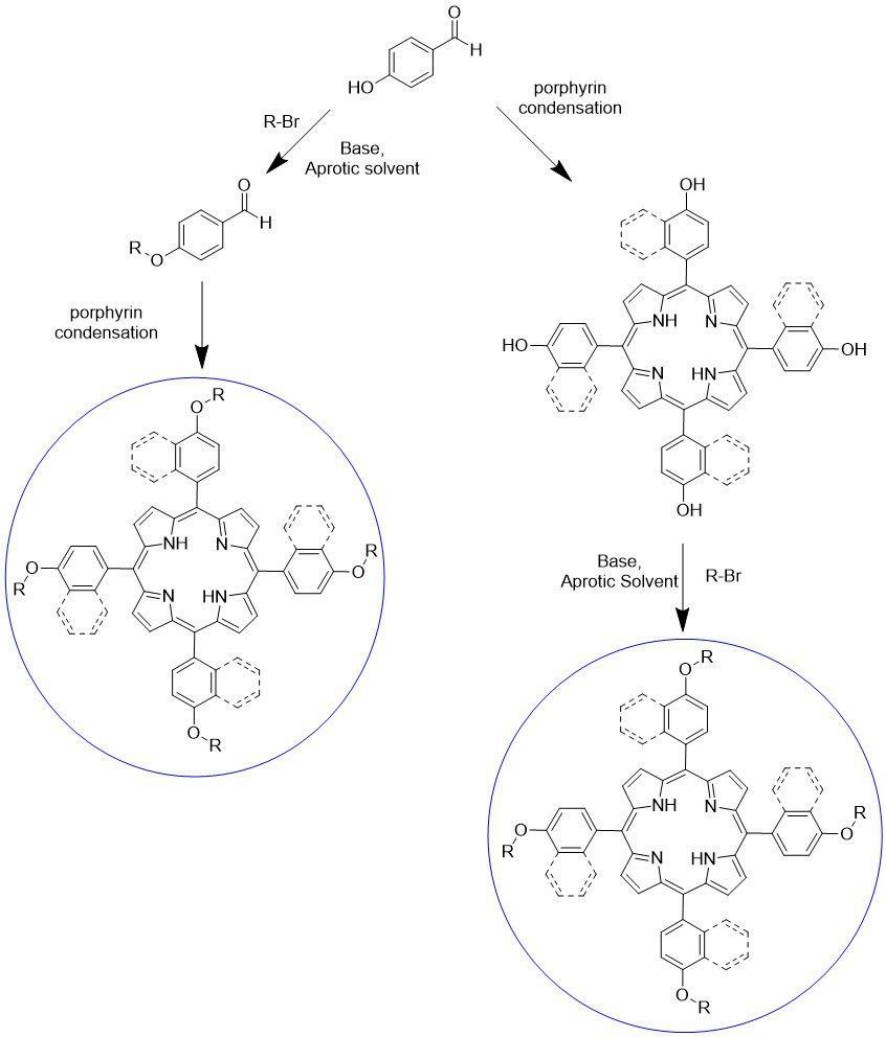

Figure 6.8. *Chemical reaction scheme of two methods to make tetra-alkoxyarylporphyrins. The first method includes modifying the aldehyde precursor, followed by porphyrin formation. The second consists of first forming the porphyrin, then chemical modification of the porphyrin periphery.*

The 5,10,15,20-tetra-4-propanxoyphenylporphyrin (**TPrOPP**), was synthesized *via* an S_N2 reaction in a 29% yield (see figure **6.9** for reaction scheme and see figure **S6.18** for proton NMR spectrum).[19]

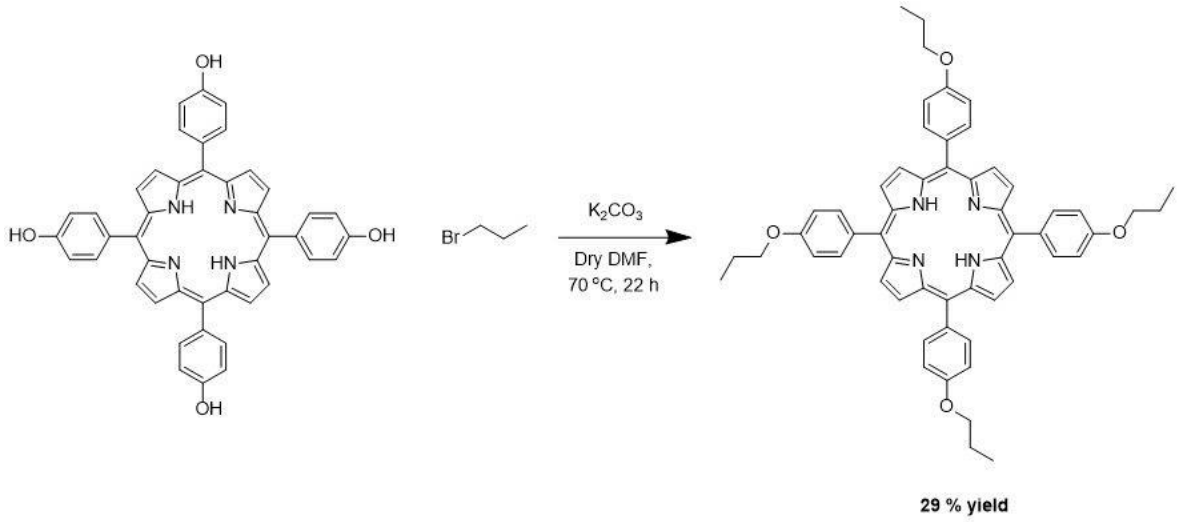

Figure 6.9. *Reaction scheme of 5,10,15,20-tetra-4-propanoxyphenylporphyrin.*[19]

In the reaction mixture, the 4 protons on the periphery of the *meso*-aryl groups, were all deprotonated using anhydrous potassium carbonate (**K_2CO_3**) in the aprotic solvent, **dry DMF**. Once this 'tetra anionic intermediate' was formed, the 3-bromopropane electrophile was added to the reaction and allowed to reflux at 70°C overnight. The bromine acted as the leaving group, allowing the desired product to form in a rather low yield (29%). This low yield is likely due to the rather short activation time (1 hour). In the future, an overnight activation would be sufficient, followed by refluxing for longer than 24 hours (after adding 3-bromopropane) to give a higher yielding product.

The starting materials for other tetra-alkoxyarylporphyrins were synthesized (see Figures **6.10** and **6.11** for general reaction schemes and see Figures **S6.19**–**S6.23** for NMR spectra).[19] These reactions were similar S_N2 reactions in aprotic solvents to that of figure **6.9**.

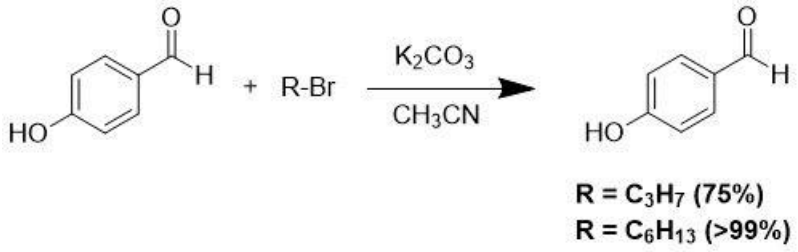

Figure 6.10. *Reaction scheme of 4-propanoxybenzaldehyde and 4-hexanoxybenzaldehyde.*[19]

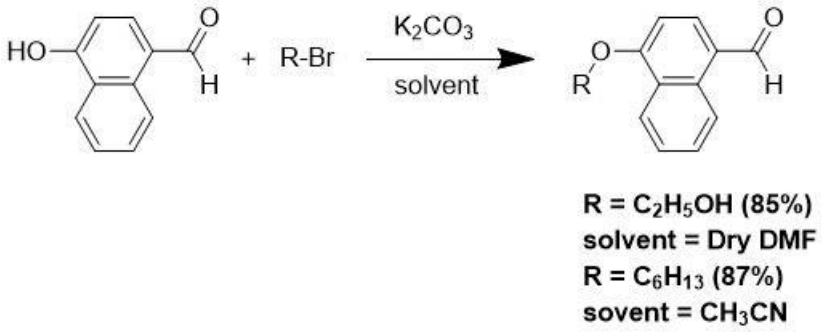

Figure 6.11. *Reaction scheme of 4-(2-hydroxyethoxy)naphthaldehyde and 4-hexanoxynaphthaldehyde.*[19]

The following porphyrin condensation reactions that led to their porphyrin formation were unsuccessful. In the future, other porphyrin forming conditions, like the Lindsey porphyrin condensation method could be employed to achieve the synthesis of these porphyrins.[20] There are no reports of *meso*-tetra-naphthoxy-porphyrins in the literature according to our knowledge. The presence of naphthyl groups on the periphery could improve the photophysical properties in solution and in thin films for their applications in PDT.

6.3. Conclusions

This chapter contains the synthesis of starting materials for novel photosensitizers. The first starting material for the cyanine dye **MIH-148** was synthesized in a low yield. However, the precursor was pure and synthetic methods for synthesizing **MIH-148** need to be optimized. Then, this dye amongst others (**IR-783** and **IR-783-SPA**), can be combined with porphyrins to be studied for their application in photodynamic therapy. The ideal goal would be to have irradiation of the cyanine dye, in a porphyrin-cyanine conjugate, using near IR light (700-800 nm) to produce singlet oxygen, with a high quantum yield. Other future synthesis would include the synthesis of tetra-alkoxy naphthylporphyrins with varying chain length to observe whether these structural changes improve their photophysical properties in solution and in thin films.

6.4. Synthetic experimental procedures

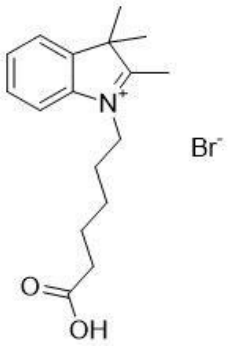

Synthesis of **1-(5-carboxypentyl)-2,3,3-trimethylindolenium bromide**:[13] 6-bromohexanoic acid (3.16 g, 16.20 mmol, 1.00 eq.) and 2,3,3-trimethyl-*3H*-indole (3.2 mL, 3.17 g, 19.91 mmol, 1.23 eq.) were dissolved in 35 mL acetonitrile in a 100 mL three-neck round bottom flask with a stirrer bar. This clear dark orange mixture was stirred under reflux conditions at 70°C for 22 hours. The solvent was removed to afford a dark red residue that was dissolved in 100 mL dichloromethane, layered with 300 mL diethyl ether and the product was allowed to precipitate in the fridge overnight. The purple/pink solid product was obtained *via* filtration using a fritz funnel. The product was washed several times using diethyl ether and dried until pure *via* TLC (9/1 dichloromethane/methanol) to obtain a brick red solid (**1.40 g**, **24% yield**). R_f = 0.1 (8/2 dichloromethane/methanol); ^{1}H NMR (DMSO-d_6, 500 MHz): δ (ppm) = 7.98 (t, *J* = 4.0, 5.0 Hz, 1 H, $H_{aromatic}$), 7.85 (t, *J* = 4.5, 4.0 Hz, 1 H, $H_{aromatic}$), 7.63 (t, *J* = 4.5, 4.5 Hz, 2 H, 2 x $H_{aromatic}$), 4.46 (t, *J* = 7.5, 8.5 Hz, 2 H, CH_2), 2.85 (s, 3 H, CH_3), 2.23 (t, *J* = 7.3, 7.3 Hz, 2 H, CH_2), 1.85 (quintet, *J* = 9.0, 6.8, 8.3, 8.0 Hz, 2 H, CH_2), 1.58 (q, *J* = 7.5, 7.0, 7.5, 4.0 Hz, 2 H, CH_2), 1.55 (s, 6 H, 2 x CH_3), 1.43 (q, *J* = 8.3, 7.3, 8.5, 7.0 Hz, 2 H, CH_2). ^{13}C NMR (DMSO-d_6, 500 MHz): δ (ppm) = 196.4 (**C**$_{COOH}$), 174.2 (**C**$_1$), 141.8 (**C**$_2$), 140.9 (**C**$_3$), 129.3 (**C**$_4$), 128.9 (**C**$_5$), 123.4 (**C**$_6$), 115.4 (**C**$_7$), 54.1 (**C**$_8$), 47.3 (**C**$_9$), 33.3 (**C**$_{10}$), 26.8 (**C**$_{11}$), 25.3 (**C**$_{12}$), 23.9 (**C**$_{13}$), 21.9 (**C**$_{14}$), 13.9 (**C**$_{15}$). UV-Vis ($CHCl_3$) λ_{max} (log ε) = 283 nm (3.76). IR (cm^{-1}) = 3676, 3306, 2981, 2953, 2704, 2112, 1743.

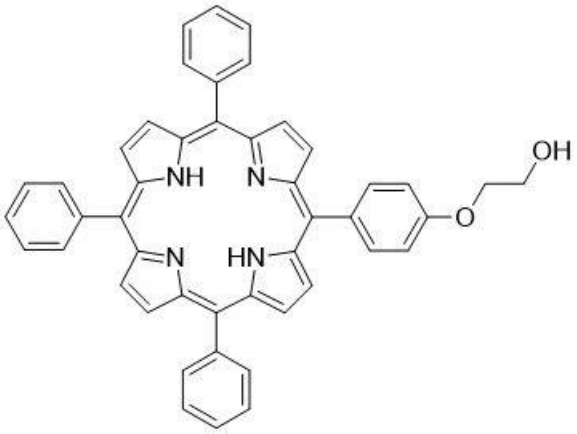

Synthesis of 5-(4-(2-hydroxyethoxy)phenyl)-10,15,20-triphenylporphyrin (TPPOEtOH): 5-(4-hydroxyphenyl)-10,15,20-triphenylporphyrin (160 mg, 0.253 mmol, 1.00 eq.) and K_2CO_3 (940 mg, 6.77 mmol, 26.76 eq.) were dissolved in 20 mL dry DMF

in a 100 mL three-neck round bottle flask with a stirrer bar. The solution was stirred under argon at 50°C for 3 hours. 2-bromoethanol (1.40 g, 0.80 mL, 11.29 mmol, 44.62 eq.) was then added and the reaction was allowed to stir at reflux (90°C) for 72 hours. The reaction mixture was then allowed to cool to room temperature. 250 mL of deionized water and 200 mL of dichloromethane were added, the mixture was decanted, the organic layer was washed with deionized water (60 and 90 mL). The organic layer was dried over $MgSO_4$. After filtration and evaporation, the residue was purified *via* column chromatography (stationary phase: silica gel, eluent: toluene with a gradient of acetone ranging from 0% to 6%) to give a purple crystalline solid (**119.8 mg, 75% yield**). R_f = 0.5 (85/15 toluene/acetone). ^{1}H NMR ($CDCl_3$, 500 MHz): δ (ppm) = 8.86 (d, *J* = 5.0 Hz, 2 H, 2 x $H_{\beta\text{-pyrrolic}}$), 8.83 (d, *J* = 2.5 Hz, 6 H, 6 x $H_{\beta\text{-pyrrolic}}$), 8.21 (d, *J* = 6.0 Hz, 6 H, 3 x $H_{2,6\text{-phenyl}}$), 8.11 (d, *J* = 9.0 Hz, 2 H, $H_{3,5\text{-aryl}}$), 7.78-7.71 (m, *J* = 7.5, 8.9, 8.3, 6.8 Hz, 9 H, 3 x $H_{3,4,5\text{-phenyl}}$), 7.27-7.23 (d, *J* = 14.5 Hz, 2 H, $H_{2,6\text{-aryl}}$), 4.32 (t, *J* = 4.0, 5.0 Hz, 2 H, O-CH_2C**H**$_2$OH), 4.11 (t, *J* = 3.4, 6.4 Hz, 2 H, O-C**H**$_2$$CH_2$OH) -2.76 (s, 2 H, 2 x N-H). ^{13}C NMR ($CDCl_3$, 500 MHz): δ (ppm) = 158.4 (**C**$_{OR}$), 142.2 (**C**$_3$), 135.6 (**C**$_4$), 134.5 (**C**$_5$), 131.1 (**C**$_8$), 127.7 (**C**$_1$), 126.7 (**C**$_6$), 120.1 (**C**$_2$), 112.8 (**C**$_7$), 69.4 (**C**$_8$), 61.6 (**C**$_9$). UV-Vis (THF) λ_{max} (log ε) = 418 (5.66), 515 (4.29), 550 (4.02), 592 (3.81) and 649 nm (3.71). IR (cm^{-1}) = 3575, 3319, 2920, 2854. HRMS (MALDI) [$C_{46}H_{34}N_4O_2$]: m/z calcd. 674.78; found 675.31.

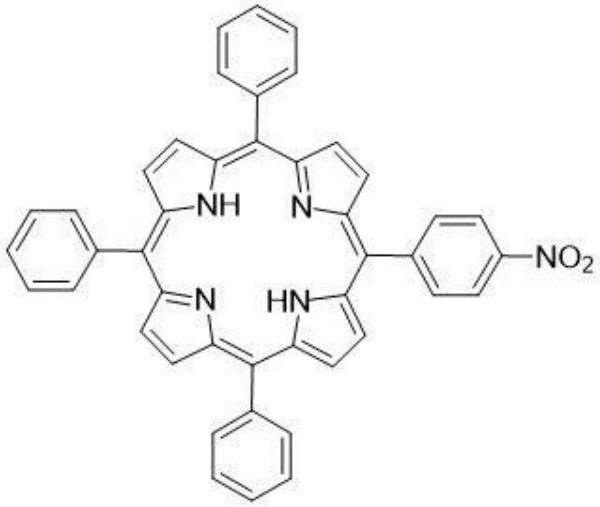

Synthesis of 5-(4-nitrophenyl)-10,15,20-triphenylporphyrin (TPPNO$_2$):[15] 4-nitrobenzaldehyde (370 mg, 2.45 mmol, 1.00 eq.) and benzaldehyde (760 mg, 790 ml, 7.44 mmol, 3.00 eq.) were dissolved in dichloromethane (100 mL) in a 250 mL two-neck round bottom flask with a stirrer bar under argon. Iodine (260 mg, 1.02 mmol, 0.42 eq.) and pyrrole (0.70 mL, 680 mg, 10.14 mmol, 4.14 eq.) were added *via* the side neck while stirring before putting into the microwave. The reaction was activated 4 times, for 2 minutes each (100 W, 30°C). After each activation, the reaction mixture was analyzed using TLC (7/3 chloroform/petroleum ether) to check the consumption of starting materials. *P*-chloranil (1.83 g, 7.18 mmol, 3.00 eq.) was then added to the reaction using a 1 minute activation followed by 10 minutes reaction time. The product was purified using column chromatography *via* an eluent gradient of 2/8 chloroform/petroleum ether to 5/5 chloroform/petroleum ether to obtain a pure purple product (**112 mg, 7% yield**). R_f = 0.65 (7/3 chloroform/petroleum ether). ^{1}H NMR ($CDCl_3$, 500 MHz): δ (ppm) = 8.89 (d, *J* = 4.5 Hz, 2 H, 2 x $H_{\beta\text{-pyrrolic}}$), 8.86 (d, *J* = 5.0 Hz, 4 H, 4 x $H_{\beta\text{-pyrrolic}}$), 8.73 (d, *J* = 5.0 Hz, 2 H, 2 x $H_{\beta\text{-pyrrolic}}$), 8.62 (d, *J* = 8.8 Hz, 2 H, $H_{2,6\text{-aryl}}$), 8.39 (d, *J* = 9.0 Hz, 2 H, $H_{3,5\text{-aryl}}$), 8.21 (d, *J*

= 7.0 Hz, 6 H, 3 x $H_{2,6\text{-phenyl}}$), 7.75 (m, *J* = 7.5, 6.3, 4.5, 7.5, 6.5 Hz, 9 H, 3 x $H_{3,4,5\text{-aryl}}$), -2.78 (s, 2 H, 2 x N-H). ^{13}C NMR ($CDCl_3$, 500 MHz): δ (ppm) = 168.7 (**C_{NO2}**), 149.2 (**C_{11}**), 147.7 (**C_5**), 141.9 (**C_2**), 140.0 (**C_3**), 135.1 (**C_8**), 134.5 (**C_9**), 131.5 (**C_6**), 127.9 (**C_{10}**), 126.8 (**C_4**), 121.8 (**C_7**), 121.1 (**C_{12}**), 120.7 (**C_{13}**), 116.6 (**C_1**). UV-vis (THF) λ_{max} (log ε) = 418 (5.78), 515 (4.47), 549 (4.11), 591 (3.92) and 647 nm (3.75). IR (cm^{-1}) = 3665, 3316, 2989, 2902.

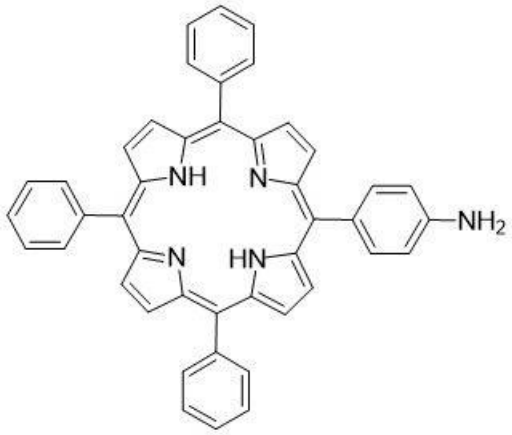

Synthesis of 5-(4-aminophenyl)-10,15,20-triphenylporphyrin (TPPNH$_2$):[16, 17] In a 250 mL two-neck round bottom flask, 5-(4-nitrophenyl)-10,15,20-triphenylporphyrin (70 mg, 0.11 mmol, 1.00 eq.) and $SnCl_2$ (210 mg, 1.11 mmol, 10.00 eq.) were dissolved in chloroform (40 mL). HCl (40 mL, 37% v/v) and acetic acid (40 mL) were then added and the reaction mixture was allowed to stir at reflux (60^{o}C) for 96 hours. The pH of the reaction was brought to 8 by adding 600 mL of 2 M NaOH. The product was extracted using 3 x 100 mL chloroform and the organic phase was washed with 2 x 100 mL deionized water. The organic phase was dried over $MgSO_4$ and the crude product was purified *via* column chromatography using an eluent gradient of 2/8 chloroform/petroleum ether to 100% chloroform to obtain a pure purple solid (**40.6 mg, 61% yield**). R_f = 0.3 (7/3 chloroform/petroleum ether). ^{1}H NMR ($CDCl_3$, 500 MHz): δ (ppm) = 8.93 (d, *J* = 5.0 Hz, 2 H, 2 x $H_{\beta\text{-pyrrolic}}$), 8.83 (br s, 6 H, 6 x $H_{\beta\text{-pyrrolic}}$), 8.21 (d, *J* = 8.0 Hz, 6 H, 3 x $H_{2,6\text{-phenyl}}$), 7.97 (d, *J* = 8.0 Hz, 2 H, $H_{2,\ 6\ aryl}$), 7.70-7.77 (m, *J* = 7.0, 8.5, 6.0 Hz, 9 H, 3 x $H_{3,4,5\text{-phenyl}}$), 6.99 (d, *J* = 8.8 Hz, 2 H, $H_{3,5\text{-aryl}}$), 3.92 (s, 2 H, *p*-N**H**$_2$), -2.73 (s, 2 H, 2 x N-H). ^{13}C NMR ($CDCl_3$, 500 MHz): δ (ppm) = 146.0 (**C_{NH2}**), 142.3 (**C_1**), 135.7 (**C_2**), 134.5 (**C_3**), 132.3 (**C_4**), 131.0 (**C_5**), 127.6 (**C_6**), 126.6 (**C_7**), 120.9 (**C_8**), 120.0 (**C_9**), 119.7 (**C_{10}**), 113.4 (**C_{11}**). UV-vis (THF) λ_{max} (log ε) = 419 (5.56), 517 (4.31), 555 (4.11), 595 (3.80) and 652 nm (3.80). IR (cm^{-1}) = 3671, 3316, 2972, 2924. HRMS (MALDI) *m/z* calcd. for $C_{44}H_{31}N_5$ (M+): 629.75; found 630.09.

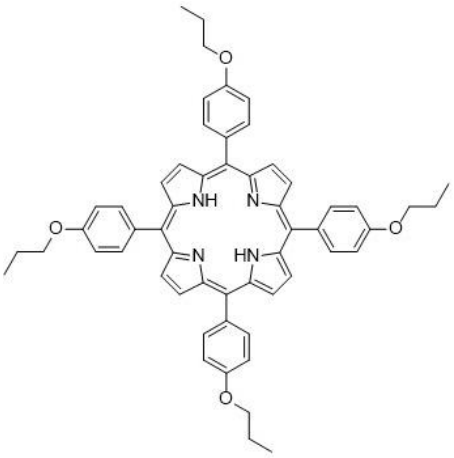

Synthesis of **5,10,15,20-tetra-4-propanoxyphenylporphyrin**:[19] 5,10,15,20-tetra-4-hydroxyphenylporphyrin (27.50 mg, 0.04 mmol, 1.00 eq.) and K_2CO_3 (0.20 g, 1.45 mmol, 33.57 eq.) were dissolved in 5 mL dry DMF in a 50 ml two-neck round bottom flask with a stirrer bar under argon. The reaction mixture was stirred at reflux for 1 hour at 60°C. **Bromopropane** (0.30 mL, 0.41 g, 3.29 mmol, 81.27 eq.) was added to the reaction mixture and it was allowed to stir under reflux and argon at 70°C for 21 hours. The reaction mixture was allowed to cool to room temperature and the solvent was removed *via* reduced pressure. The organic phase was extracted using 2 x 50 ml ethyl acetate and dried over $MgSO_4$. After filtration and removal of the solvent *in vacuo*, a purple crystalline solid product was obtained (**10 mg, 29% yield**). ^{1}H NMR ($CDCl_3$, 500 MHz): δ (ppm) = 8.86 (s, 8 H, 8 x $H_{\beta\text{-pyrrolic}}$), 8.10 (d, *J* = 8.8 Hz, 8 H, 4 x $H_{2,6\text{-aryl}}$), 7.26 (d, *J* = 13.3 Hz, 8 H, 4 x $H_{3,5\text{-aryl}}$), 4.21 (t, *J* = 6.5, 6.5 Hz, 8 H, 4 x O-C**H**$_2$CH$_2$CH$_3$), 2.01 (m, *J* = 7.5, 6.3, 8.0, 6.3, 7.5 Hz, 8 H, 4 x O-CH$_2$C**H**$_2$CH$_3$), 1.20 (t, *J* = 7.8, 7.8 Hz, 12 H, 4 x O-CH$_2$CH$_2$C**H**$_3$), -2.74 (s, 2 H, 2 x N-H).

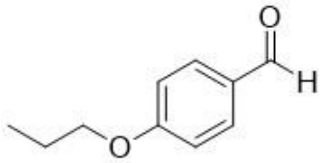

Synthesis of **4-propanoxybenzaldehyde**:[19] 4-hydroxybenzaldehyde (2.57 g, 21 mmol, 1.00 eq.) and K_2CO_3 (3.08g, 22.00 mmol, 1.05 eq.) were dissolved in 20 mL CH_3CN in a 100 mL three-neck round bottom flask with a stirrer bar under argon. The reaction mixture was stirred under reflux conditions at 60°C for 1 hour. Bromopropane (1.5 mL, 2.03 g, 22.00 mmol, 1.05 eq.) was added to the reaction mixture and it was refluxed at 80°C for 24 hours. The reaction mixture was allowed to cool to room temperature and the solvent was removed until dry. The organic phase was extracted with 2 x 50 ml ethyl acetate then dried over $MgSO_4$. A dark brown oil was obtained after removal of the solvent *in vacuo* (**2.55 g, 75% yield**). ^{1}H NMR ($CDCl_3$, 500 MHz): δ (ppm) = 9.87 (s, 1 H, C**H**O), 7.83 (d, *J* = 9.5 Hz, 2 H, $H_{2,6\text{-aryl}}$), 6.99 (d, *J* = 9.0 Hz, 2 H, $H_{3,5\text{-aryl}}$), 4.01 (t, *J* = 7.0, 6.8 Hz, 2 H, O-C**H**$_2$CH$_2$CH$_3$), 1.84 (m, *J* = 7.0, 7.5, 7.5, 7.3, 7.3 Hz, 2 H, O-CH$_2$C**H**$_2$CH$_3$), 1.05 (t, *J* = 7.5, 7.5 Hz, 3 H, O-CH$_2$CH$_2$C**H**$_3$).

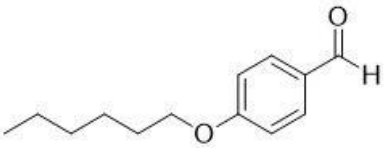

Synthesis of **4-hexanoxybenzaldehyde**:[19] 4-hydroxybenzaldehyde (1.25 g, 10.24 mmol, 1.32 eq.) and K_2CO_3 (1.07g, 7.74 mmol, 1.00 eq.) were dissolved in 20 mL acetonitrile in a 50 ml two-neck round bottom flask with a stirrer bar under argon. The reaction mixture was stirred at 60°C reflux for 1 hour. 6-bromohexane (1.40 mL, 1.94 g, 10.01 mmol, 1.29 eq.) was added to the reaction mixture and it was allowed to stir under reflux (70°C) for 24 hours. The reaction was allowed to cool to room temperature and the solvent was removed under reduced pressure. The organic phase was extracted with 2 x 50 ml ethyl acetate and dried over $MgSO_4$. Following filtration and removal of the solvent *in vacuo*, a light-yellow oil was obtained (**2.29 g**, **>99% yield**). ^{1}H NMR ($CDCl_3$, 500 MHz): δ (ppm) = 9.88 (s, 1 H, C**H**O), 7.82 (d, *J* = 8.5 Hz, 2 H, $H_{2,6\text{-aryl}}$), 6.99 (d, *J* = 8.5 Hz, 2 H, $H_{3,5\text{-aryl}}$), 4.04 (t, *J* = 7.5, 7.5 Hz, 2 H, O-C**H**$_2$$C_5H_{11}$), 1.81 (q, *J* = 7.0, 7.5, 7.5, 7.0 Hz, 2 H, O-CH_2C**H**$_2$$C_4H_9$), 1.47 (q, *J* = 7.3, 7.8, 7.8, 7.3 Hz, 2 H, O-C_2H_4C**H**$_2$$C_3H_7$) 1.35 (dq, *J* = 4.0, 4.0, 7.5, 3.5, 3.5 Hz, 4 H, O-$C_3H_7C_2$**H**$_4$$CH_3$), 0.91 (t, *J* = 7.0, 7.0 Hz, 3 H, O-$C5H_{10}$C**H**$_3$).

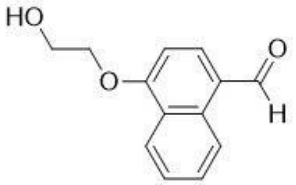

Synthesis of **4-(2-hydroxyethanoxy)naphthaldehyde**:[19] 4-hydroxynaphthaldehyde (0.20 g, 1.16 mmol, 1.00 eq.) and K_2CO_3 (1.60 g, 11.58 mmol, 10.00 eq.) were dissolved in 20 mL dry DMF in a 50 ml two-neck round bottom flask with stirrer bar under argon. This reaction mixture was stirred at 60°C reflux for 1 hour. 2-bromoethanol (0.82 mL, 1.44 g, 11.57 mmol, 10.00 eq.) was added to the reaction mixture and it was allowed to stir under reflux at 70°C for 21 hours under argon. The solvent was removed using reduced pressure and the organic phase was extracted by 2 x 50 ml ethyl acetate and dried over $MgSO_4$. An orange crystalline solid was obtained after filtration and drying under vacuum (**0.23 g**, **92% yield**). ^{1}H NMR ($CDCl_3$, 500 MHz): δ (ppm) = 10.21 (s, 1 H, 1 x C**H**O), 9.30 (d, *J* = 8.5 Hz, 1 H, $H_{9\text{-aryl}}$), 8.35 (d, *J* = 8.3 Hz, 1 H, $H_{6\text{-aryl}}$), 7.91 (d, *J* = 8.0 Hz, 1 H, $H_{2\text{-aryl}}$), 7.71 (t, *J* = 8.0, 8.0 Hz, 1 H, $H_{8\text{-aryl}}$), 7.58 (t, *J* = 7.8, 7.8 Hz, 1 H, $H_{7\text{-aryl}}$), 6.94 (d, *J* = 8.0 Hz, 1 H, $H_{3\text{-aryl}}$), 4.51 (s, 1 H, O**H**), 4.38 (t, *J* = 4.5, 4.5 Hz, 2 H, Ar-OC**H**$_2$-), 4.17 (t, *J* = 3.8, 3.8 Hz, 2 H, HOC**H**$_2$-).

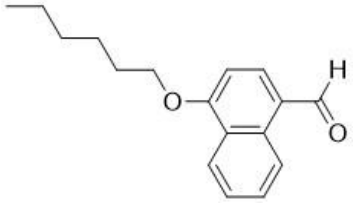

Synthesis of **4-hexanoxynaphthaldehyde**:[19] 4-hydroxynaphthaldehyde (0.17 g, 1.00 mmol, 1.00 eq.) and K_2CO_3 (1.38 g, 33.43 mmol, 33.43 eq.) were dissolved in 40 mL

acetonitrile in a 100 ml three-neck round bottom flask with stirrer bar under argon. This reaction mixture was stirred at 60°C reflux for 1 hour. 6-bromohexane (1.50 mL, 1.77 g, 10.72 mmol, 10.72 eq.) was added to the reaction mixture and it was allowed to stir under reflux at 70°C for 21 hours under argon. The solvent was removed *in vacuo* and the product was extracted by 2 x 50 ml ethyl acetate and dried over $MgSO_4$. A dark orange crystalline solid was obtained after evaporation of solvent (**0.22 g**, **87% yield**). ^{1}H NMR ($CDCl_3$, 500 MHz): δ (ppm) = ^{1}H NMR ($CDCl_3$, 500 MHz): δ (ppm) = 10.10 (s, 1 H, 1 x C**H**O), 9.30 (d, *J* = 3.8 Hz, 1 H, $H_{9\text{-aryl}}$), 8.35 (d, *J* = 9.0 Hz, 1 H, $H_{6\text{-aryl}}$), 7.89 (d, *J* = 8.0 Hz, 1 H, $H_{2\text{-aryl}}$), 7.69 (t, *J* = 8.0, 8.0 Hz, 1 H, $H_{8\text{-aryl}}$), 7.56 (t, *J* = 7.8, 7.8 Hz, 1 H, $H_{7\text{-aryl}}$), 6.89 (d, *J* = 8.0 Hz, 1 H, $H_{3\text{-aryl}}$), 4.23 (t, *J* = 7.0, 7.0 Hz, 2 H, Ar-OC**H**$_2$-), 1.96 (q, *J* = 6.0, 7.3, 7.3, 6.0 Hz, 2 H, Ar-OCH_2C**H**$_2C_4H_9$), 1.58 (q, *J* = 6.5, 7.0, 7.0, 6.5 Hz, 2 H, Ar-OC_2H_4C**H**$_2C_3H_7$), 1.39 (m, *J* = 8.3, 6.3, 4.0, 4.4, 3.5, 8.5, 5.0, 8.5, 3.0 Hz, 4 H, Ar-OC_3H_6C**H**$_2C$**H**$_2CH_3$), 0.93 (t, *J* =8.5, 3.0 Hz, 3 H, Ar-$OC_5H_{10}C$**H**$_3$). ^{13}C NMR ($CDCl_3$, 500 MHz): δ (ppm) = 192.2 (**C**$_{\text{CHO}}$), 160.4 (**C**$_{\text{4-aryl}}$), 139.7 (**C**$_{\text{2-aryl}}$), 132.0 (**C**$_{\text{10-aryl}}$), 129.5 (**C**$_{\text{8-aryl}}$), 125.7 (**C**$_{\text{7-aryl}}$), 124.9 (**C**$_{\text{5-aryl}}$), 124.8 (**C**$_{\text{1-aryl}}$), 122.5 (**C**$_{\text{9-aryl}}$), 120.0 (**C**$_{\text{6-aryl}}$), 103.5 (**C**$_{\text{3-aryl}}$), 68.8 (**C**$_{11}$), 31.6 (**C**$_{12}$), 29.0 (**C**$_{13}$), 25.9 (**C**$_{14}$), 22.6 (**C**$_{15}$), 14.0 (**C**$_{12}$).

6.5. Experimental Spectra

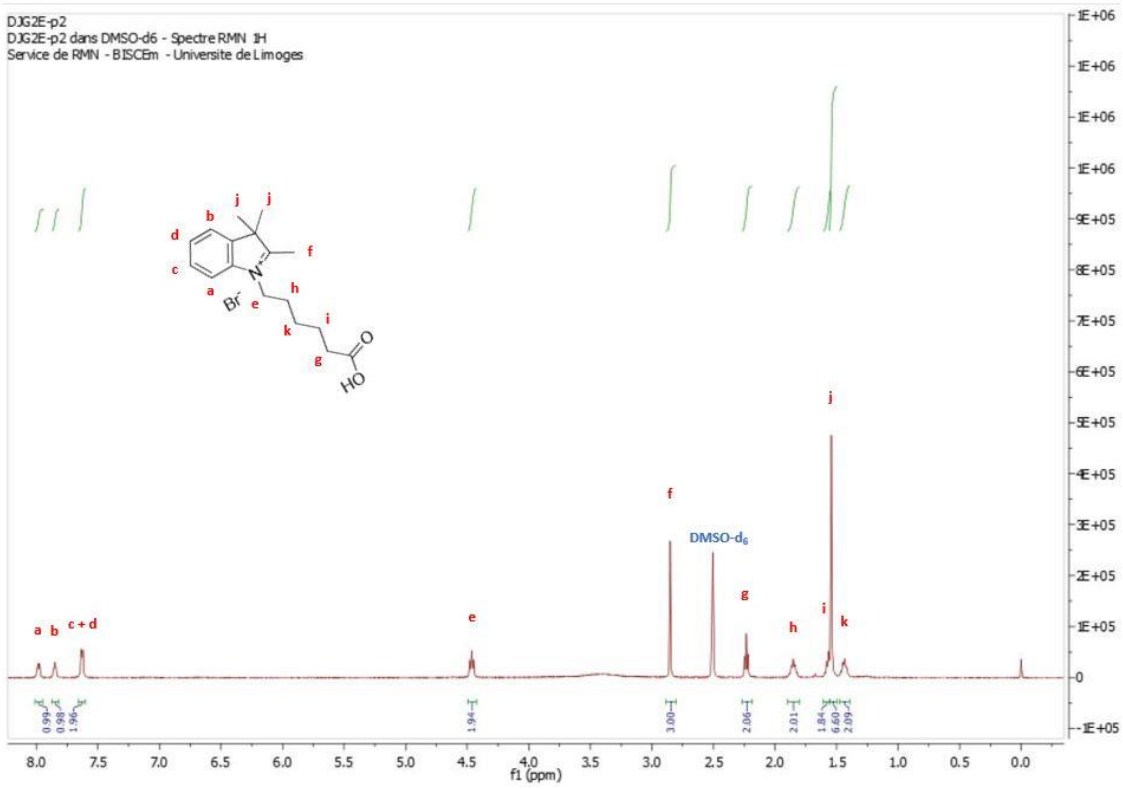

Figure S6.1. *Fully Integrated ^{1}H NMR spectrum at room temperature of 1-(5-carboxypentyl)-2,3,3-trimethylindolenium bromide explained, in DMSO-d_6, with the structure and labels for the protons in the structure.*

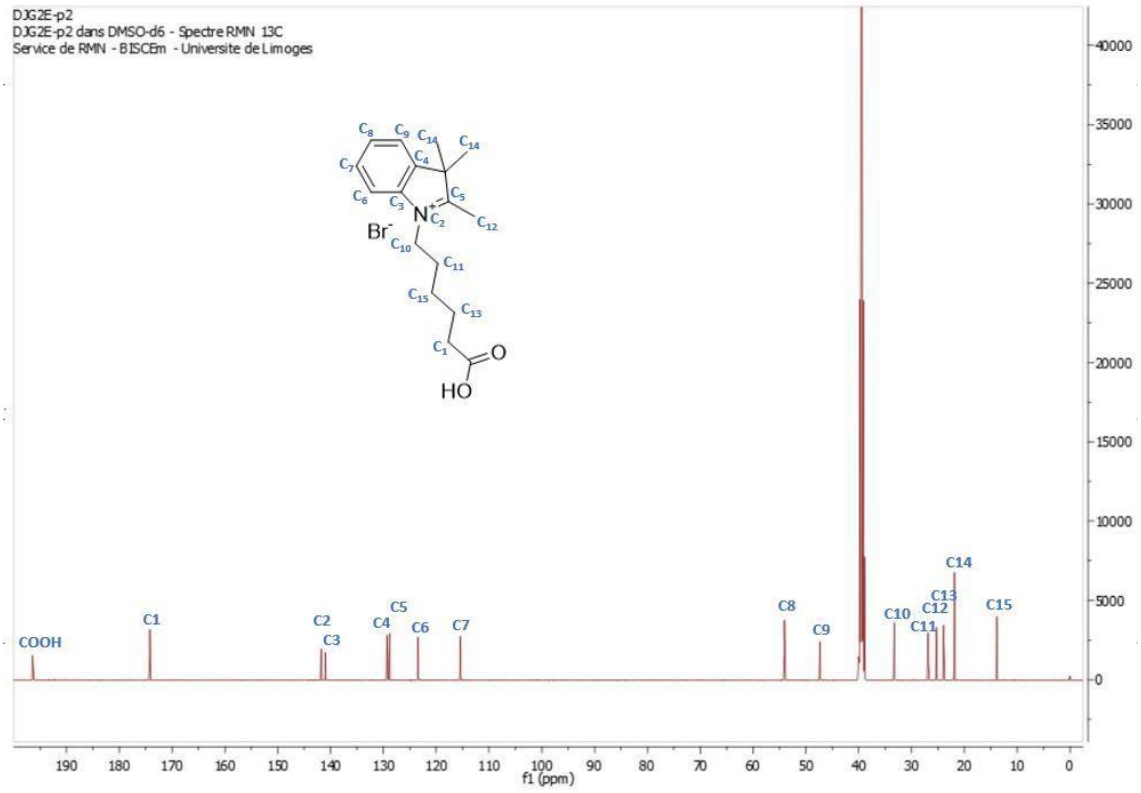

Figure S6.2. *^{13}C NMR spectrum at room temperature of 1-(5-carboxypentyl)-2,3,3-trimethylindolenium bromide explained, in DMSO-d_6, with the structure and labels for the carbons in the structure.*

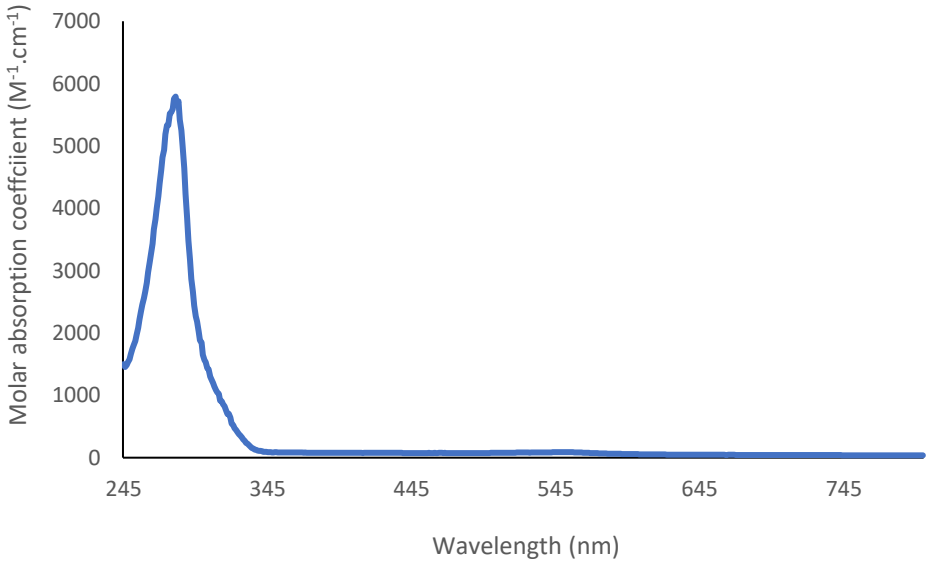

Figure S6.3. *UV-Vis spectrum at room temperature of 1-(5-carboxypentyl)-2,3,3-trimethylindolenium bromide in methanol, using a molar absorption coefficient scale.*

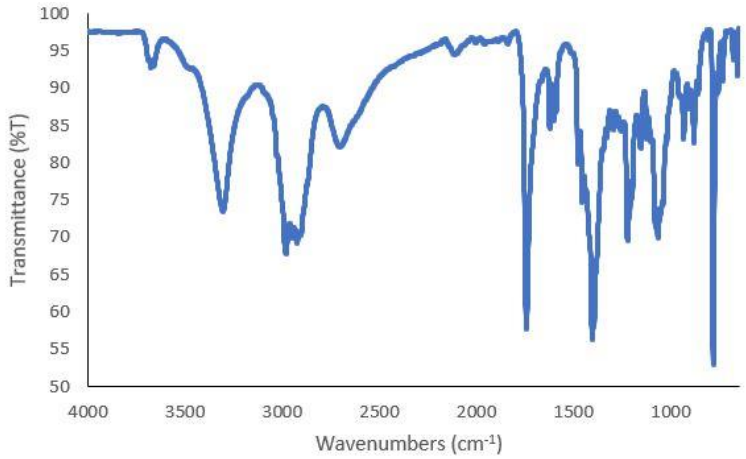

Figure S6.4. *IR spectrum at room temperature of 1-(5-carboxypentyl)-2,3,3-trimethylindolenium bromide.*

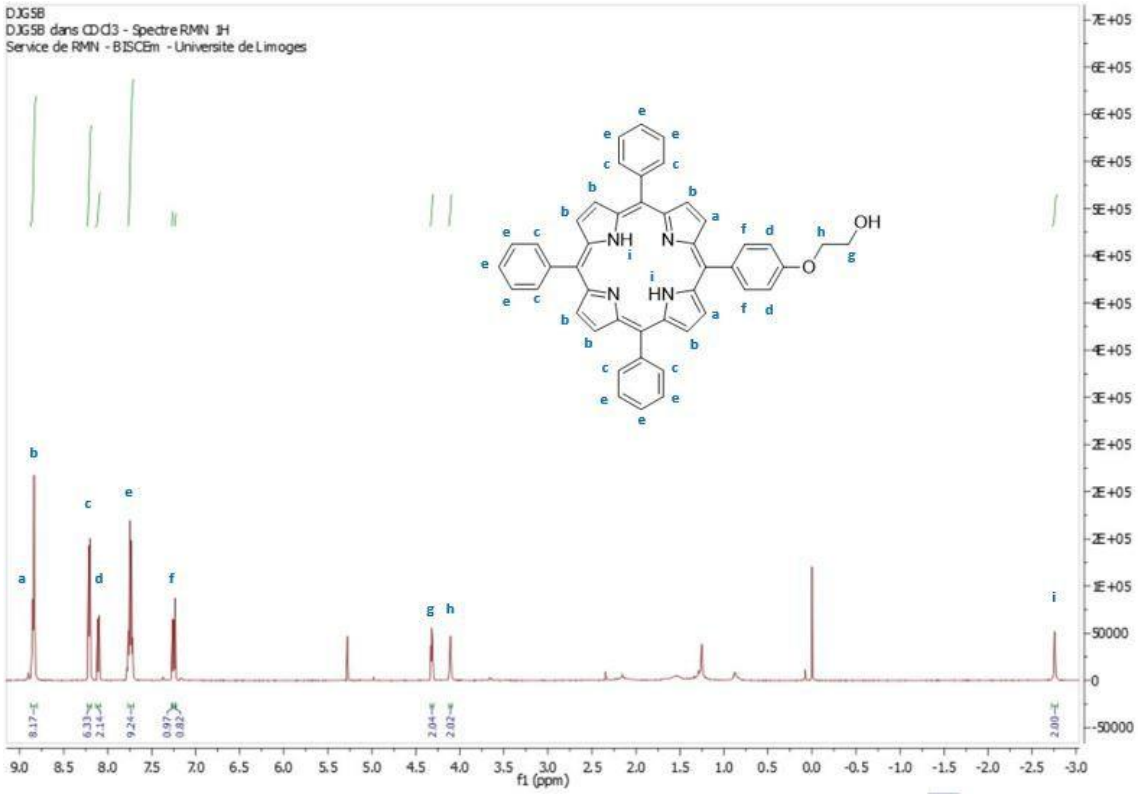

Figure S6.5. *Fully Integrated ^{1}H NMR spectrum of 5-(4-hydroxyethoxyphenyl)-10,15,20-triphenylporphyrin (**TPPOEtOH**), in $CDCl_3$, with the structure and labels for the protons in the structure.*

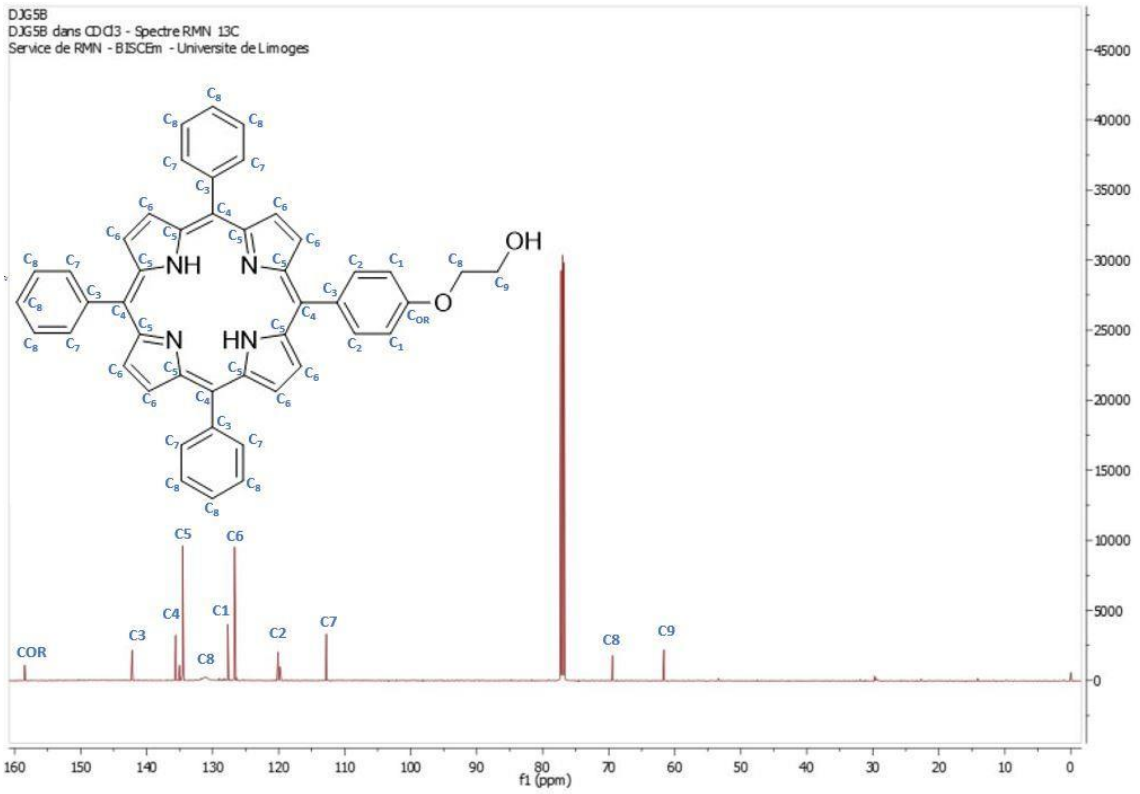

Figure S6.6. *^{13}C NMR spectrum at room temperature of 5-(4-hydroxyethoxyphenyl)-10,15,20-triphenylporphyrin explained (**TPPOEtOH**), in $CDCl_3$, with the structure and labels for the carbons in the structure.*

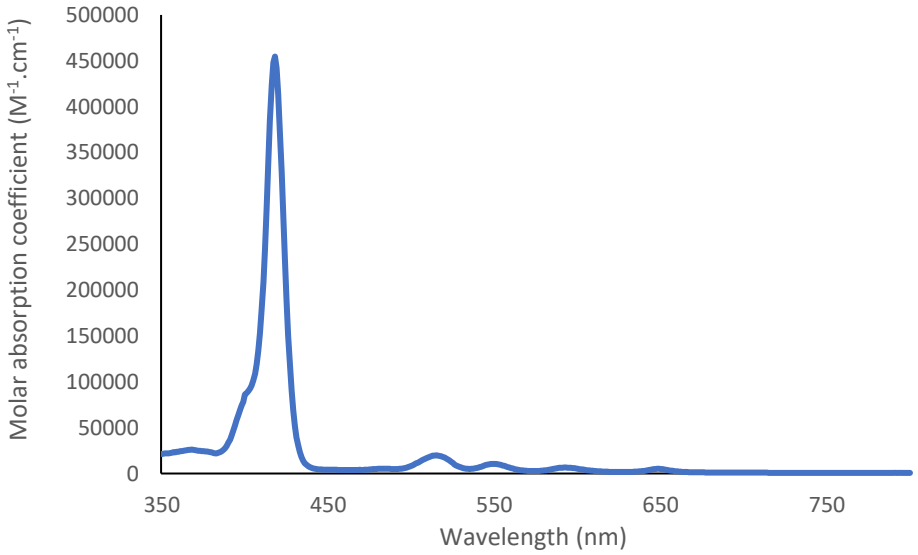

Figure S6.7. *UV-Vis spectrum at room temperature of 5-(4-(2-hydroxyethoxy)phenyl)-10,15,20-triphenylporphyrin (**TPPOEtOH**) in tetrahydrofuran (THF), using a molar absorption coefficient scale.*

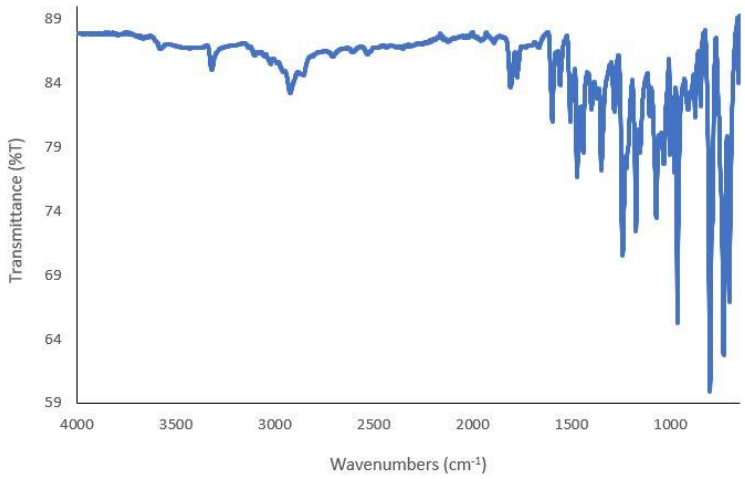

Figure S6.8. *IR spectrum at room temperature of 5-(4-hydroxyethoxyphenyl)-10,15,20-triphenylporphyrin (**TPPOEtOH**).*

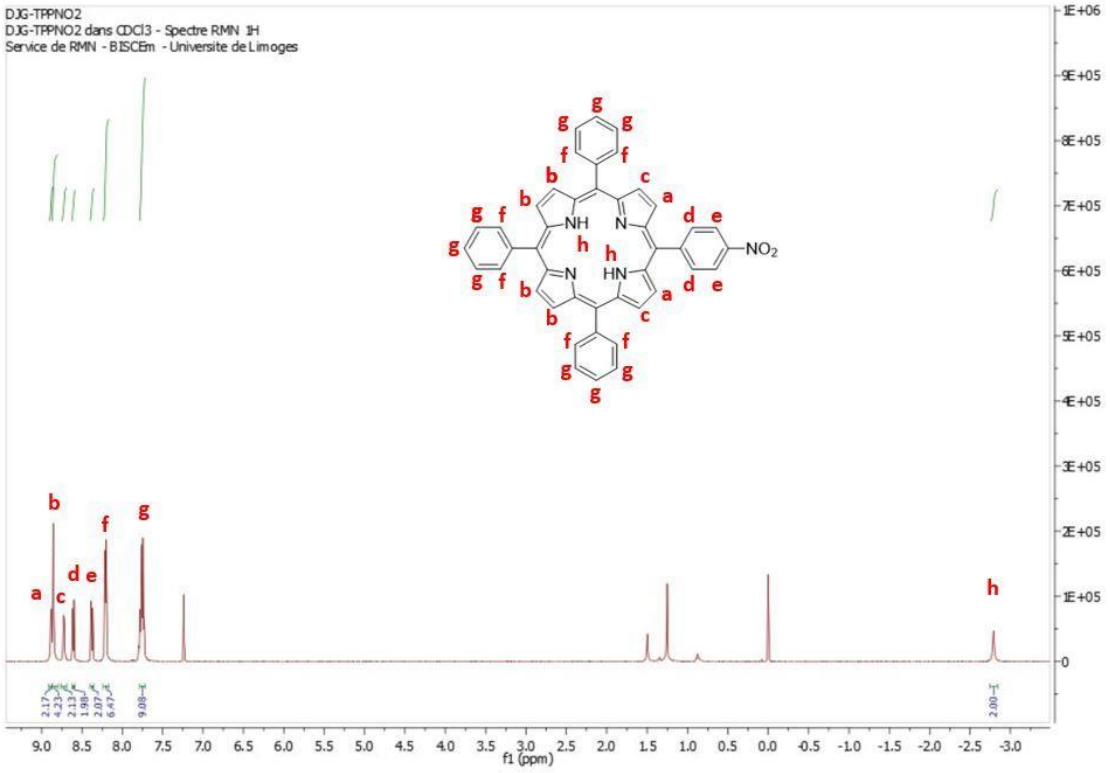

Figure S6.9. *Fully Integrated ^{1}H NMR spectrum of 5-(4-nitrophenyl)-10,15,20-triphenylporphyrin explained (**$TPPNO_2$**), in $CDCl_3$, with the structure and labels for the protons in the structure.*

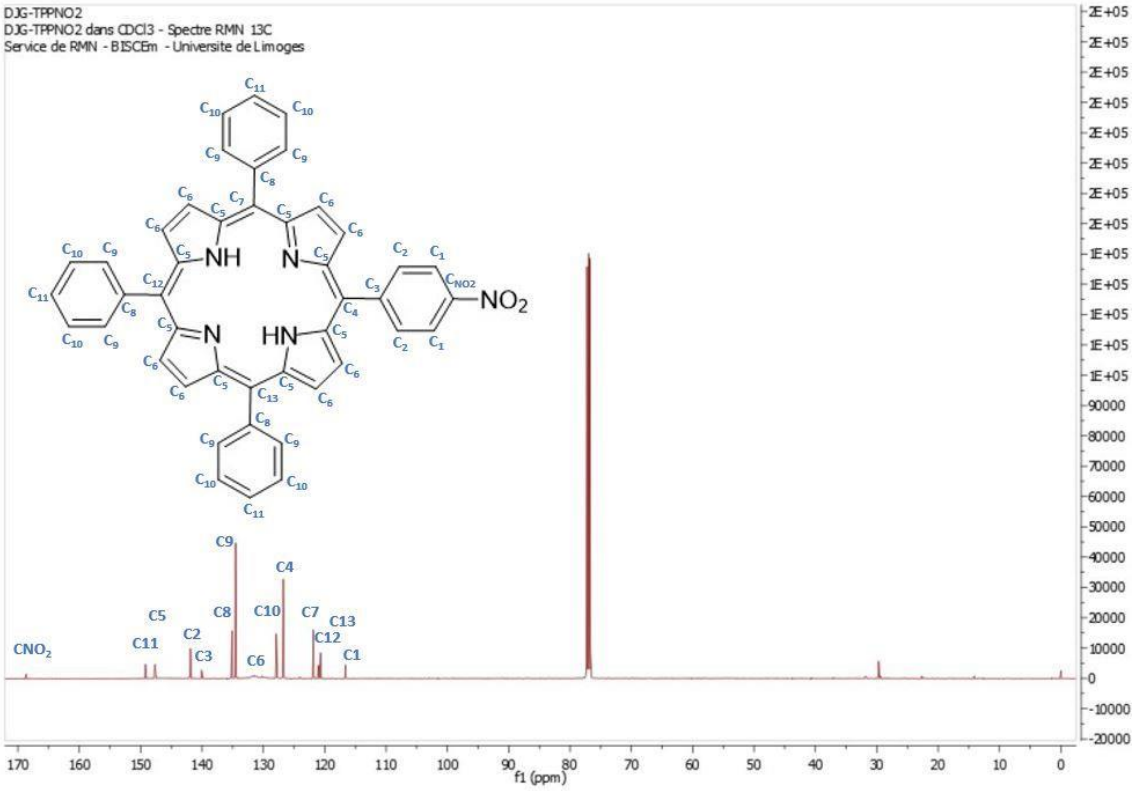

Figure S6.10. *^{13}C NMR spectrum at room temperature of 5-(4-nitrophenyl)-10,15,20-triphenylporphyrin explained (**TPPNO₂**), in $CDCl_3$, with the structure and labels for the carbons on the structure.*

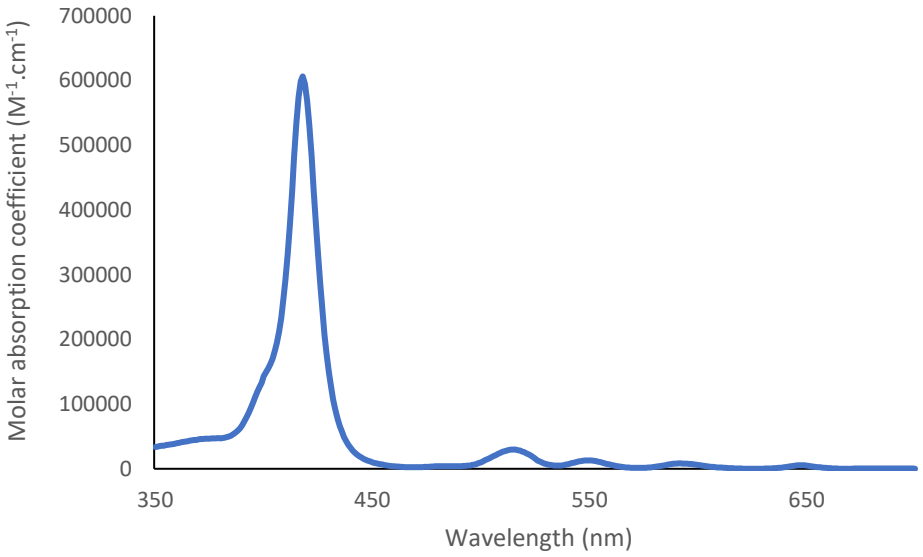

Figure S6.11. *UV-Vis spectrum at room temperature of 5-(4-nitrophenyl)-10,15,20-triphenylporphyrin (**TPPNO₂**) in THF, using a molar absorption coefficient scale.*

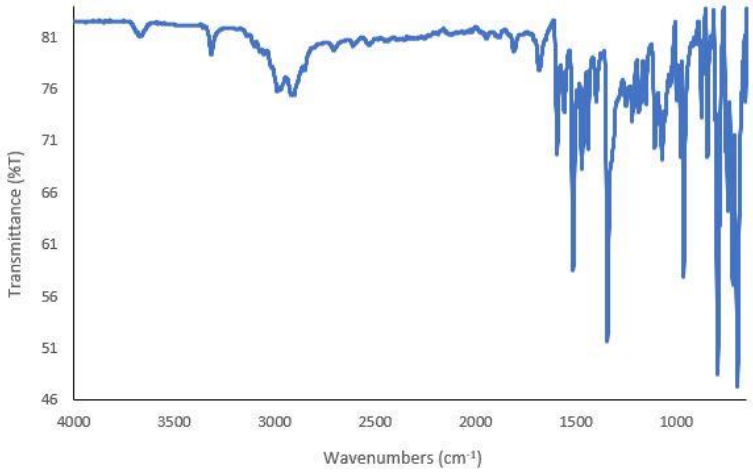

Figure S6.12. *IR spectrum at room temperature of 5-(4-nitrophenyl)-10,15,20-triphenylporphyrin (**TPPNO$_2$**).*

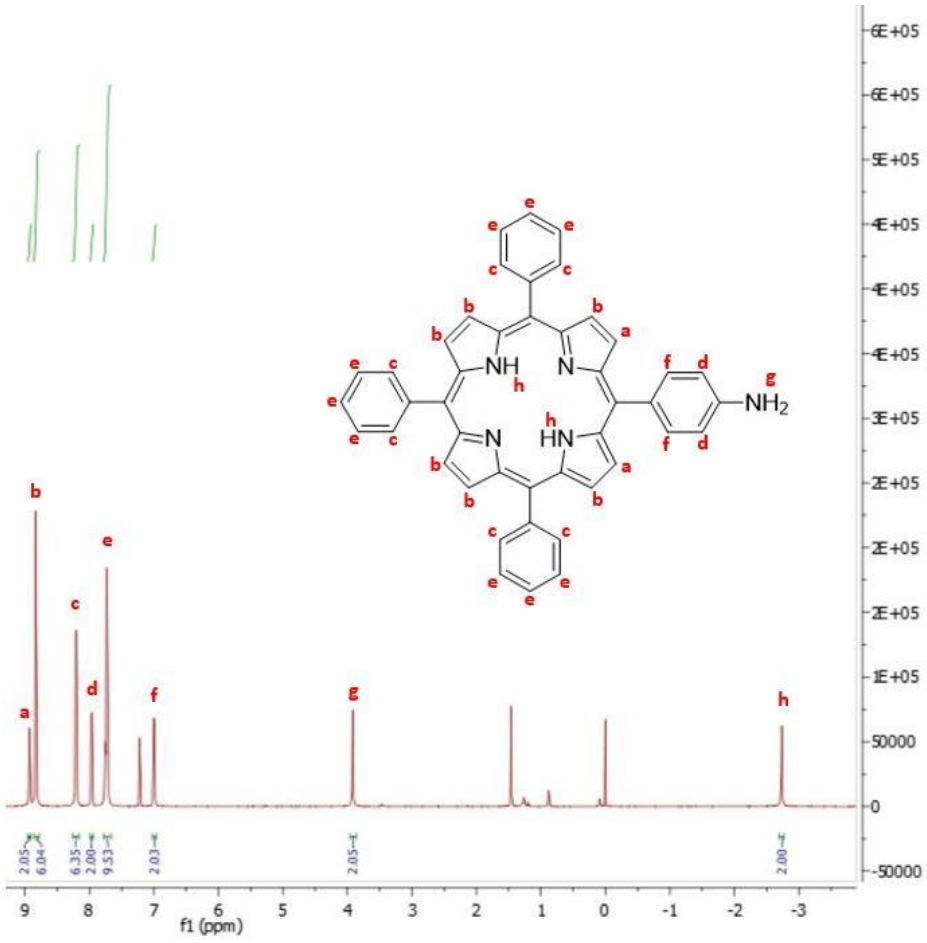

Figure S6.13. *Fully Integrated ^{1}H NMR spectrum of 5-(4-aminophenyl)-10,15,20-triphenylporphyrin explained (**TPPNH$_2$**), in $CDCl_3$, with the structure and labels for the protons in the structure.*

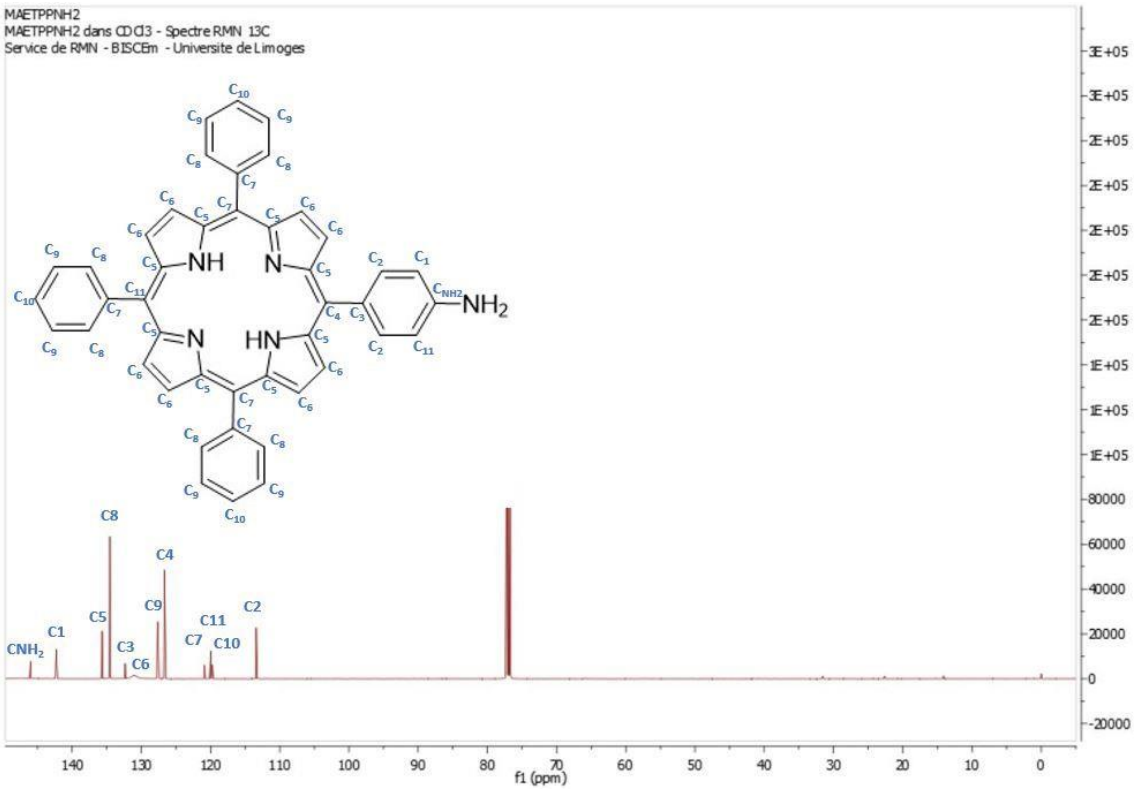

Figure S6.14. *^{13}C NMR spectrum at room temperature of 5-(4-aminophenyl)-10,15,20-triphenylporphyrin explained (**TPPNH$_2$**), in $CDCl_3$, with the structure and the labels for the carbons in the structure.*

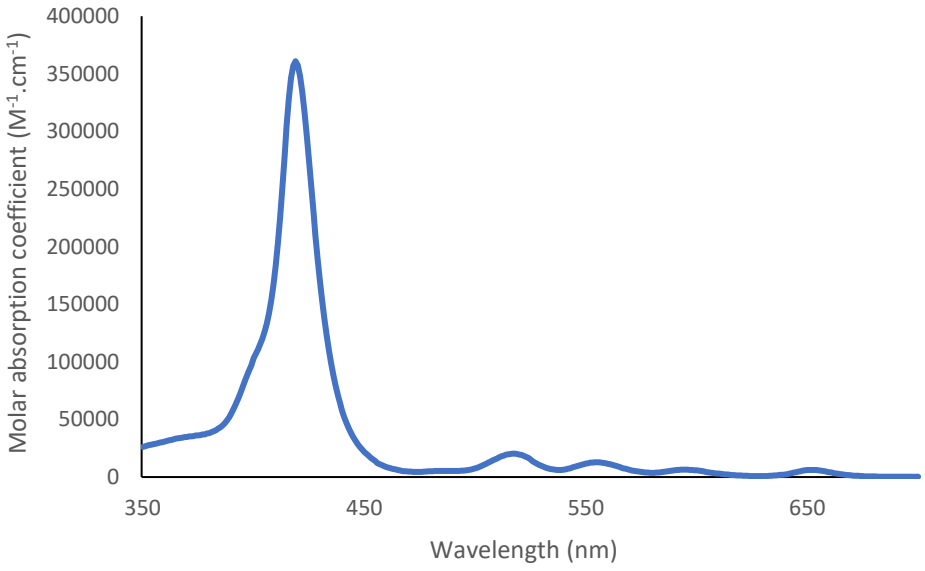

Figure S6.15. *UV-Vis spectrum at room temperature of 5-(4-aminophenyl)-10,15,20-triphenylporphyrin (**TPPNH$_2$**) in THF, using a molar absorption coefficient scale.*

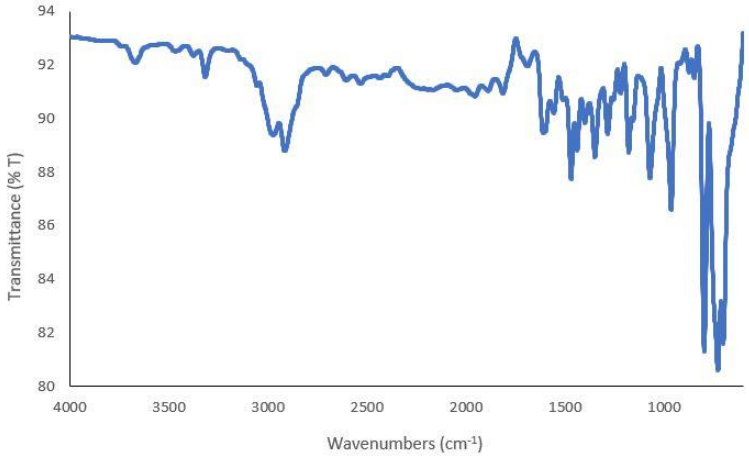

Figure S6.16. *IR spectrum at room temperature of 5-(4-aminophenyl)-10,15,20-triphenylporphyrin (**TPPNH$_2$**).*

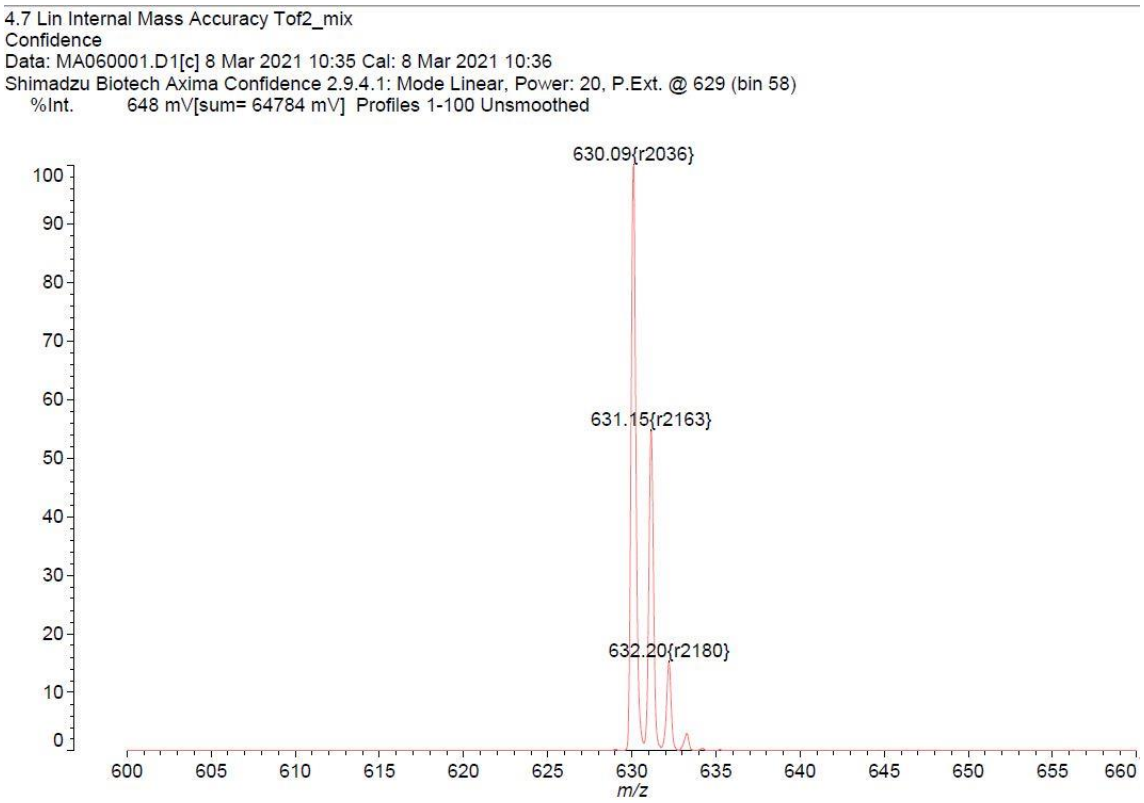

Figure S6.17. *Maldi mass spectrum at room temperature of 5-(4-aminophenyl)-10,15,20-triphenylporphyrin (**TPPNH$_2$**) in $CHCl_3$.*

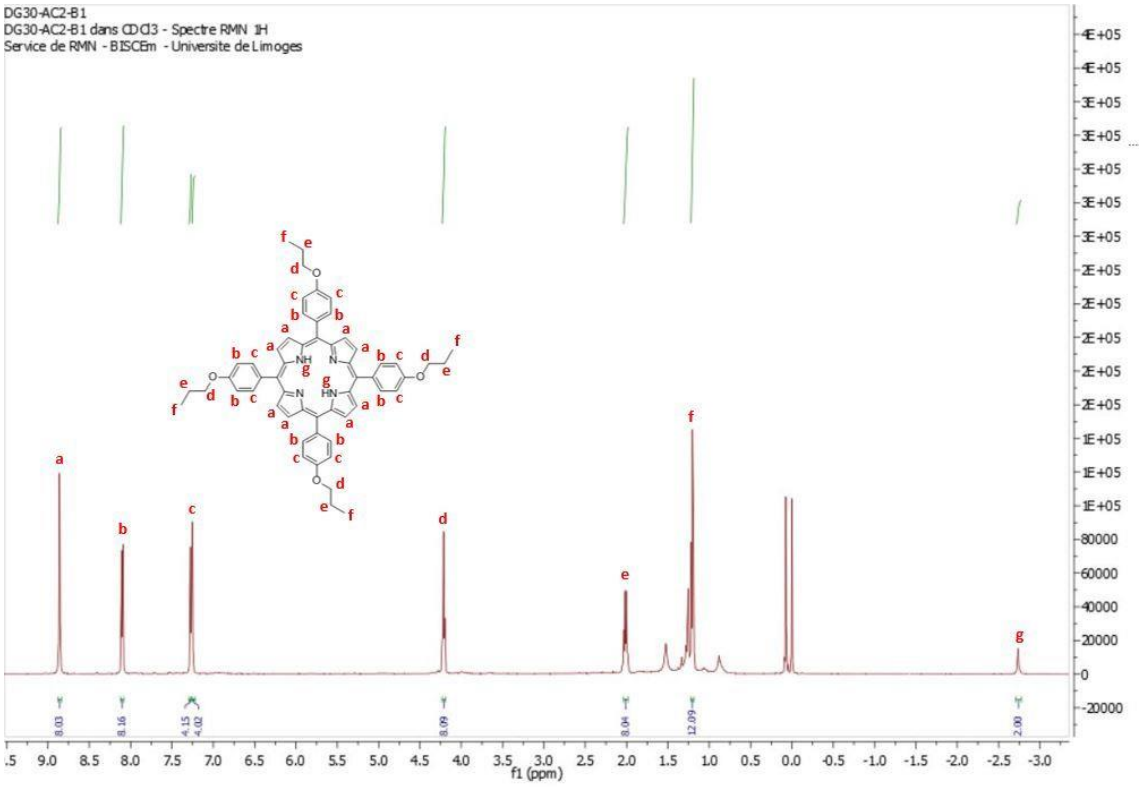

Figure S6.18. *Fully Integrated ^{1}H NMR spectrum at room temperature of 5,10,15,20-tetra-(4-propanoxyphenyl)porphyrin explained, in $CDCl_3$, with the structure and labels for the protons in the structure.*

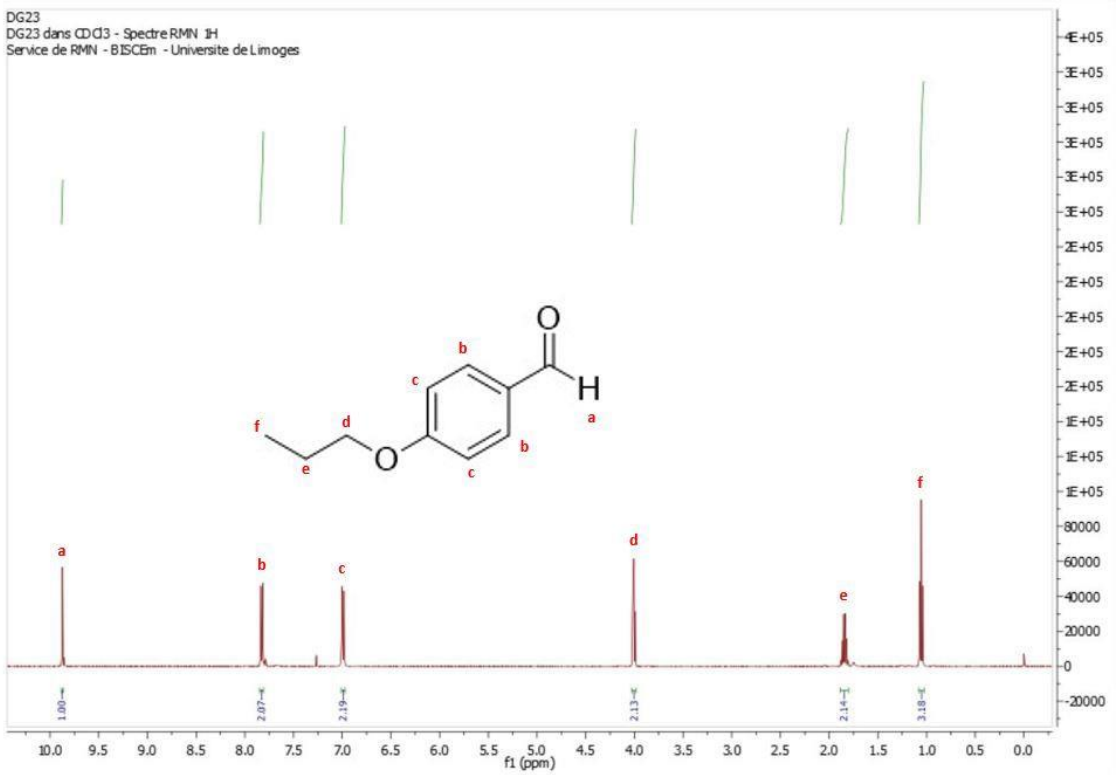

Figure S6.19. *Fully Integrated ^{1}H NMR spectrum at room temperature of 4-propanoxybenzaldehyde explained, in $CDCl_3$, with the structure and labels for the protons in the structure.*

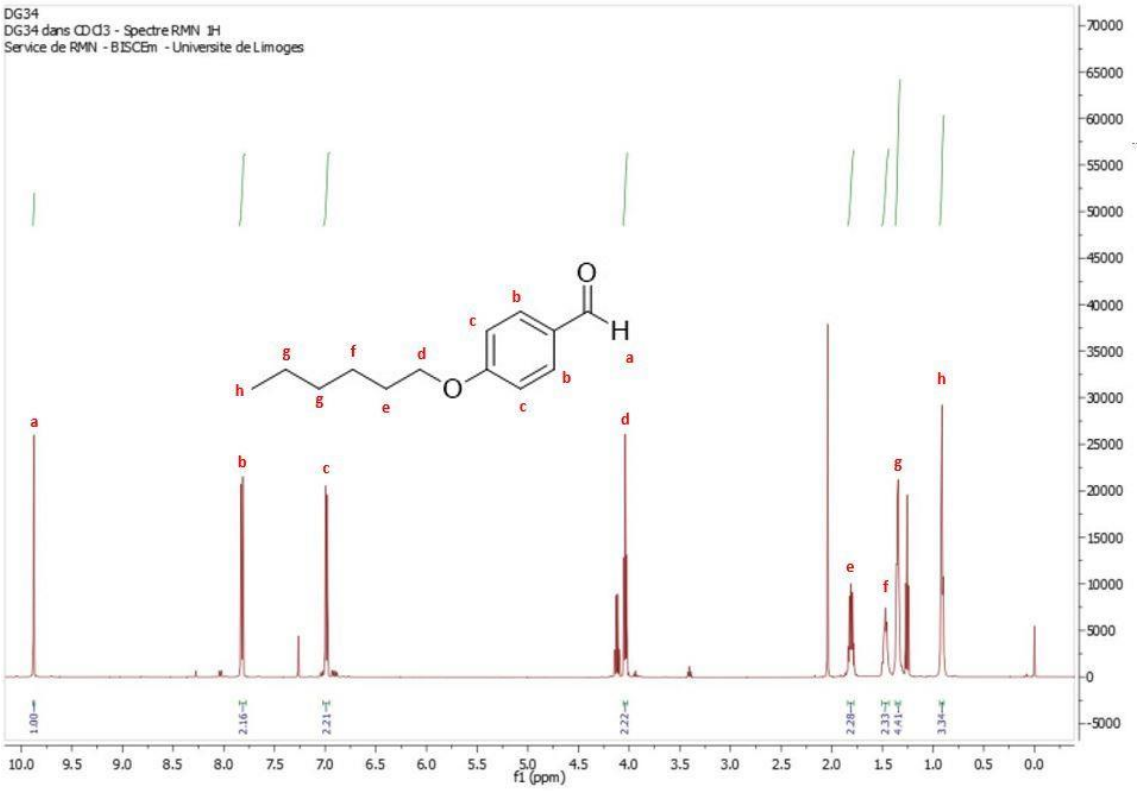

Figure S6.20. *Fully Integrated ^{1}H NMR spectrum at room temperature of 4-hexanoxybenzaldehyde explained, in $CDCl_3$, with the structure and labels for the protons in the structure.*

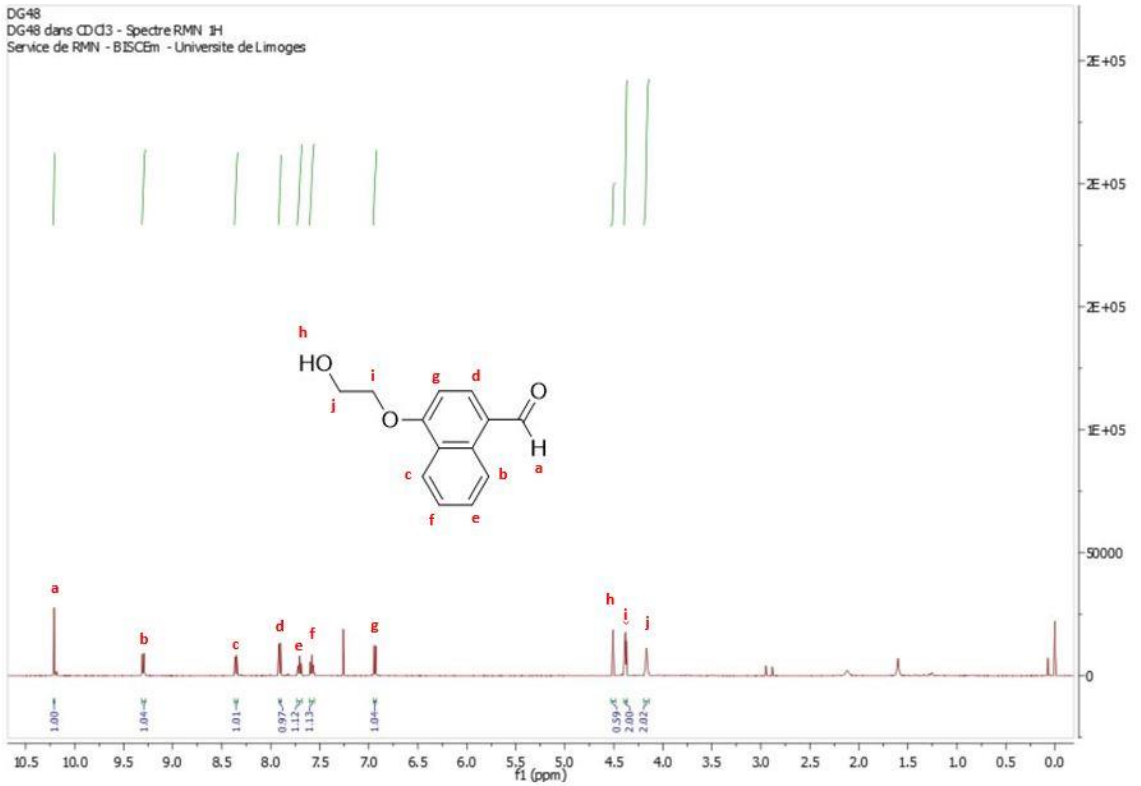

Figure S6.21. *Fully Integrated ^{1}H NMR spectrum at room temperature of 4-(2-hydroxy)ethoxy-naphthaldehyde explained, in $CDCl_3$, with the structure and labels for the protons in the structure.*

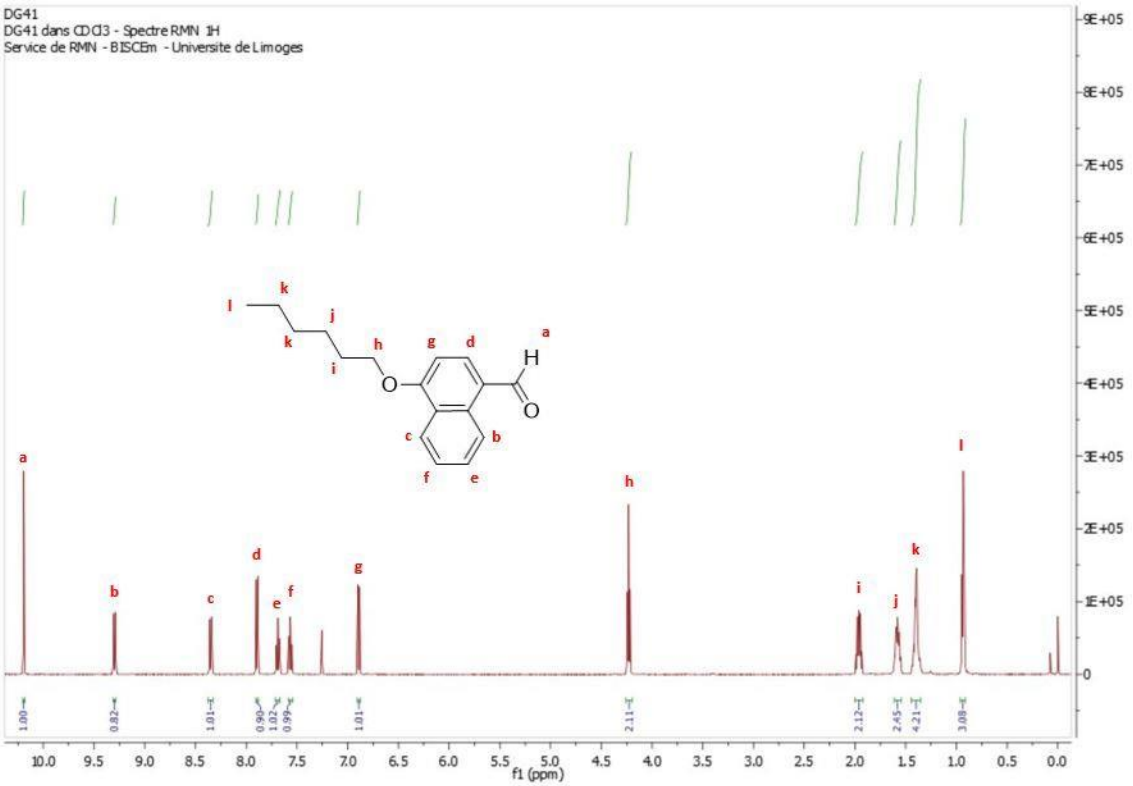

Figure S6.22. *Fully Integrated ^{1}H NMR spectrum at room temperature of 4-hexanoxy-naphthaldehyde explained, in $CDCl_3$, with the structure and labels for the protons in the structure.*

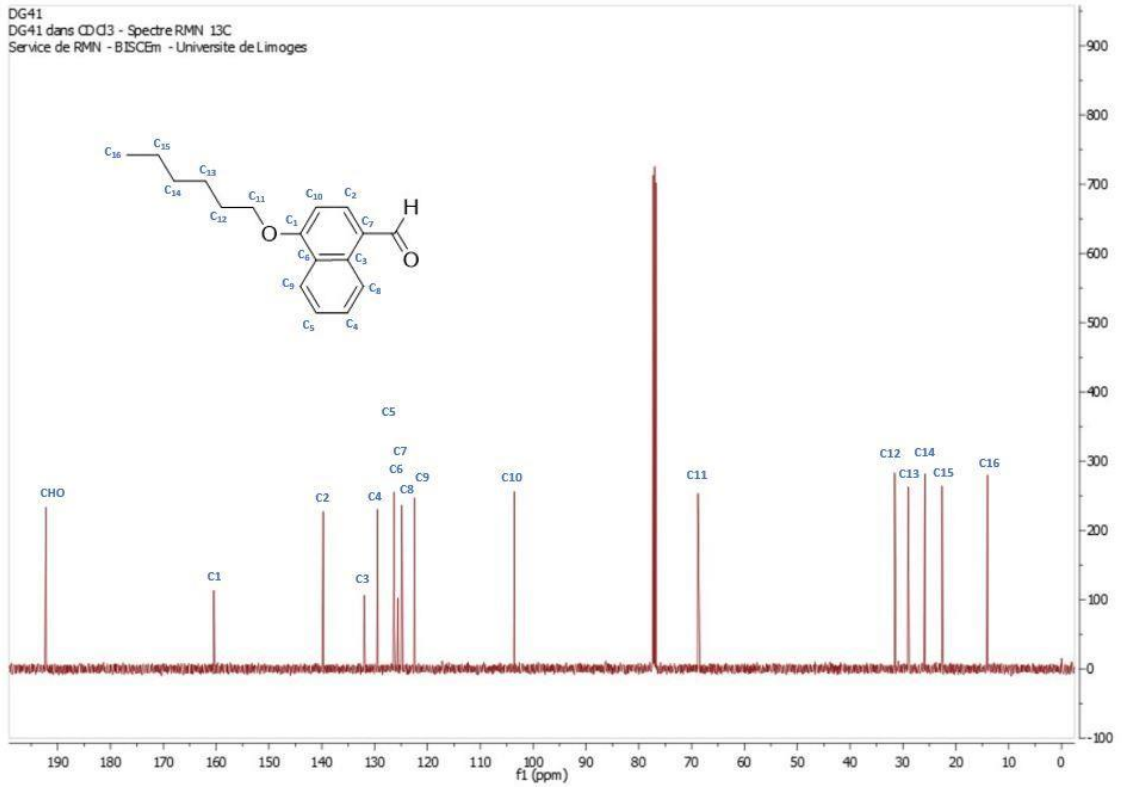

Figure S6.23. *^{13}C NMR spectrum at room temperature of 4-hexanoxy-naphthaldehyde explained, in $CDCl_3$, with the structure and labels for the carbons in the structure.*

6.6. References

[1] A. -K. Holm, M. Rini, E. T. J. Nibbering and H. Fidder, Femtosecond UV/Mid-IR Study of Photochromism of the Spiropyran 1′,3′-Dihydro-1′,3′,3′-Trimethyl-6-Nitrospiro[2H-1-Benzopyran-2,2′-(2H)-Indole] in Solution, *Chem. Phys. Lett.*, 2003, **376**, 214–219. doi: 10.1016/S0009-2614(03)00949-7.

[2] Y. Gu, X. Fei, Y. Liu, Y. Wang and X. Yang, Trimethine Cyanine Dyes with an Indole Nucleus: Synthesis and Spectral Properties Studies, *J. Lumin.*, 2013, **134**, 184–190. doi: 10.1016/j.jlumin.2012.08.050.

[3] Y. -S. Cho, M. -H. Do, H. D. Thanh, C. Moon, K. Kim, S. -H. Cho, H. Kim, H. -H. Ha and C. Jung, A Heptamethine Cyanine Dye Serves as a Potential Marker for Myeloid-Derived Suppressor Cells, *Am. J. Cancer Res.*, 2021, **11**, 2853–2866.

[4] S. A. Hilderbrand, K. A. Kelly, R. Weissleder and C. -H. Tung, Monofunctional Near-Infrared Fluorochromes for Imaging Applications, *Bioconjug. Chem.*, 2005, **16**, 1275–1281. doi: 10.1021/bc0501799.

[5] N. Kretschy and M. M. Somoza, Comparison of the Sequence-Dependent Fluorescence of the Cyanine Dyes Cy3, Cy5, DyLight DY547 and DyLight DY647 on Single-Stranded DNA, *PLoS One*, 2014, **9**, e85605. doi: 10.1371/journal.pone.0085605.

[6] J. Yuan, X. Yi, F. Yan, F. Wang, W. Qin, G. Wu, X. Yang, C. Shao and L. W. K. Chung, Near-Infrared Fluorescence Imaging of Prostate Cancer Using Heptamethine Carbocyanine Dyes, *Mol. Med. Rep*., 2015, **11**, 821–828. doi: 10.3892/mmr.2014.2815.

[7] X. Yang, C. Shao, R. Wang, C. -Y. Chu, P. Hu, V. Master, A. O. Osunkoya, H. L. Kim, H. E. Zhau and L. W. K. Chung, Optical Imaging of Kidney Cancer with Novel Near Infrared Heptamethine Carbocyanine Fluorescent Dyes, *J. Urol*., 2013, **189**, 702–710. doi: 10.1016/j.juro.2012.09.056

[8] N. S. James, Y. Chen, P. Joshi, T. Y. Ohulchanskyy, M. Ethirajan, M. Henary, L. Strekowsk and R. K. Pandey, Evaluation of Polymethine Dyes as Potential Probes for near Infrared Fluorescence Imaging of Tumors: Part – 1, *Theranostics*, 2013, **3**, 692–702. doi: 10.7150/thno.5922.

[9] H. -G. Jeong and M. -S. Choi, Design and Properties of Porphyrin-Based Singlet Oxygen Generator, *Isr. J. Chem.*, 2016, **56**, 110–118. doi: 10.1002/ijch.201500026.

[10] D. J. Gibbons, A. Farawar, P. Mazzella, S. Leroy-Lhez and R. M. Williams, Making Triplets from Photo-Generated Charges: Observations, Mechanisms and Theory, *Photochem. Photobiol. Sci.*, 2020, **19**, 136–158. doi: 10.1039/C9PP00399A.

[11] V. -N. Nguyen, Y. Yan, J. Zhao and J. Yoon, Heavy-Atom-Free Photosensitizers: From Molecular Design to Applications in the Photodynamic Therapy of Cancer, *Acc. Chem. Res.*, 2021, **54**, 207–220. doi: 10.1021/acs.accounts.0c00606.

[12] A. Ghosh, T. Selvamani, D. A. Jose, A. Das, I. Mukhopadhyay, Generation of Nanostructures by the Aggregation of Porphyrin Derivatives with Long Alkane Chain in Mix-Solvent, *J. Nanomater*., 2007, **8**, 47234. doi: 10.1155/2007/47234

[13] L. Wang, J. Jin, X. Chen, H. -H. Fan, B. K. F. Li, K. -W. Cheah, N. Ding, S. Ju, W. -T. Wong and C. Li, A cyanine based fluorophore emitting both single photon near-infrared fluorescence and two-photon deep red fluorescence in aqueous solution, *Org. Biomol. Chem.*, 2012, **10**, 5366–5370. doi: 10.1039/C2OB25619C.

[14] A. D. Adler, F. R. Longo, J. D. Finarelli, J. Goldmacher, J. Assour and L. Korsakoff, A Simplified Synthesis for Meso-Tetraphenylporphine, *J. Org. Chem.*, 1967, **32**, 476–476. doi: 10.1021/jo01288a053.

[15] B. Boëns, P. -A. Faugeras, J. Vergnaud, R. Lucas, K. Teste and R. Zerrouki, Iodine-Catalyzed One-Pot Synthesis of Unsymmetrical Meso-Substituted Porphyrins, *Tetrahedron*, 2010, **66**, 1994–1996. doi: 10.1016/j.tet.2010.01.055.

[16] C. Ringot, Élaboration de nouveaux matériaux cellulosiques photobactéricides, Université de Limoges, 2010.

[17] Jean Kerim Nzambe Ta Keki, Elaboration de matériaux bioactifs à partir de fibres lignocellulosiques, Université de Limoges, 2015.
[18] G. Yang, Y. Zhang, J. Zou, L. -P. Huang, M. D. Chordia, W. Yue, J. -J. Wu and D. -F. Pan, Synthesis and Biological Evaluation of Genistein-IR783 Conjugate: Cancer Cell Targeted Delivery in MCF-7 for Superior Anti-Cancer Therapy, *Molecules*, 2019, **24**, 4120–4136. doi: 10.3390/molecules24224120.
[19] A. Charisiadis, A. Bagaki, E. Fresta, K. T. Weber, G. Charalambidis, C. Stangel, A. G. Hatzidimitriou, P. A. Angaridis, A. G. Coutsolelos and R. D. Costa, Peripheral Substitution of Tetraphenyl Porphyrins: Fine-Tuning Self-Assembly for Enhanced Electroluminescence, *ChemPlusChem*., 2018, **83**, 254–265. doi: 10.1002/cplu.201700416.
[20] J. S. Lindsey, The Synthesis of Meso-Substituted Porphyrins, In *Metalloporphyrins Catalyzed Oxidations*, edited by F. Montanari and L. Casella, 49–86. Catalysis by Metal Complexes. Dordrecht: Springer Netherlands, 1994. doi: 10.1007/978-94-017-2247-6_2.

Phenalenone-Triazolium Salt Derivatives for Antimicrobial Photodynamic Therapy[‡]

Abstract

The increasing number of hospital-acquired infections demand the development of innovative antimicrobial treatments. Antimicrobial photodynamic therapy (APDT) is a versatile technique which relies on the production of reactive oxygen species (ROS) generated by light-irradiated photosensitizers (PS) in the presence of oxygen (O_2). 1*H*-Phenalen-1-one (phenalenone) is a very efficient photosensitizer known for its high singlet oxygen quantum yield and its antimicrobial potential in APDT when covalently bound to quaternary ammonium groups. Triazolium salts are stable aromatic quaternary ammonium salts that recently appeared as interesting moieties endowed with antimicrobial activity. As expected, most of the compounds within this chapter retained the initial singlet oxygen quantum yield, close to unity. The Minimum Inhibitory Concentrations (MIC) of 14 new phenalenone-triazolium salt derivatives and 2 known phenalenone-triazolium salt derivatives were determined against 6 bacterial strains (Gram-negatives and Gram-positives species). Most of these PSs showed significant photoinactivation activities, the strongest effects being observed against Gram-positive strains with as low as submicromolar MIC values. Herein, this chapter will be mainly focused on the photophysical studies conducted, namely: on the UV-vis absorption spectra and the photoluminescence (PL) spectra conducted (fluorescence and singlet oxygen emission).

[‡]The content of this chapter is adapted from: Jérémy Godard, Dáire Gibbons, Stéphanie Leroy-Lhez, René M. Williams, Nicolas Villandier, Tan-Sothéa Ouk, Frédérique Brégier and Vincent Sol, *Development of Phenalenone-Triazolium Salt Derivatives for aPDT: Synthesis and Antibacterial Screening*, Antibiotics, 2021, 10, 626–638, doi: 10.3390/antibiotics10060626.

7.1. Introduction

The rapid global spread of multidrug-resistant bacteria is a growing health concern. Hospital-acquired infections occur worldwide, with 7–10% of the total hospitalized patients acquiring these infections with a particular incidence of surgical-site infections.[1] *Staphylococcus* spp., *Escherichia coli*, *Pseudomonas aeruginosa*, *Klebsiella pneumoniae*, *Enterobacter* spp., *Enterococcus* spp., and *Acinetobacter* spp. are the most commonly isolated bacteria, that cause lung, urinary tract, and bloodstream infections.[2, 3] Furthermore, even previously "benign" strains, such as *Bacillus cereus*, have reportedly become more dangerous.[4] In order to counter the propagation of these pathogenic bacteria, alternative treatments have been developed which allow to bypass the use of antibiotics: immunotherapy,[5] phage therapy,[6] and antimicrobial photodynamic therapy (APDT).[7, 8]

APDT involves the use of photosensitizers (PSs), which, upon excitation with light of a certain wavelength and in the presence of dioxygen ($^3O_2$), give rise to organic free radicals and reactive oxygen species (ROS) or to singlet oxygen, according to type I or type II PDT mechanisms, respectively. These two mechanisms lead to the photodynamic inactivation (PDI) of bacteria and, for the most potent photosensitizers, bacterial cell death.[9] In addition, no bacterial resistance against these ROS has been observed, constituting a huge advantage compared to the use of antibiotics. PSs display strong photo bactericidal activities when covalently bound to specific permeabilizing agents, positively charged or bacteria-targeting moieties, e.g., pyridylporphyrin bound to polymyxins[10, 11] or phenalenone-bound pyridinium, also known as **SAPYR** (Figure **7.1**). The latter is of particular interest, due to its easy synthesis, high singlet oxygen quantum yield, stability toward Hoffman elimination as compared with non-aromatic quaternary ammonium salts, and its strong phototoxic activity against a wide range of bacterial species.[12, 13, 14] However, this compound presents a major drawback as it is difficult to add substituents which could further increase its photodynamic activity.

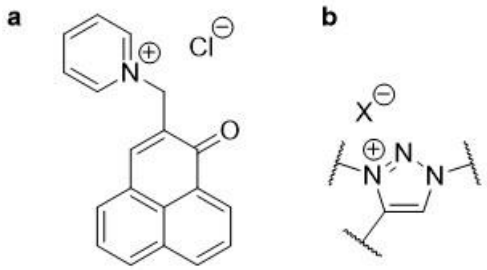

Figure 7.1. *Structure of (**a**) SAPYR and (**b**) 1,3,4-trisubstituted-1,2,3-triazolium salt.*

Recently, triazolium salts (Figure **7.1**), another class of aromatic quaternary ammonium salts, were evaluated as very promising antimicrobial agents, effective against Gram-positive and Gram-negative bacteria, as well as several yeast species.[15] Triazolium salts are easy to synthesize and, in addition, it is possible to graft three different functional groups in a regioselective manner. Moreover, to the best of our knowledge, these cationic triazolium rings have never been coupled with a photosensitizer for antimicrobial applications. In order to design new photosensitizers for photo-antimicrobial applications,[16, 17] the photophysical studies of phenalenone derivatives bearing 1,3,4-trisubstituted-1,2,3-triazolium salts were performed. The synthetic details and characterization is present in the original article.[18] The photophysical properties of these new photosensitizers were evaluated and compared to their photoinactivation properties against six bacterial strains.

7.2. Photophysical Results and Discussion

The chemical structures of all phenalenone (PN) derivatives are given in Scheme **7.1**.[18] These compounds were subject to a photophysical investigation for their application in APDT. This included conducting UV-Vis spectroscopy and calculating their molar absorption coefficients (at 370 nm). Furthermore, the photoluminescence spectra (fluorescence emission and singlet oxygen emission) in water were measured and from these, their fluorescence quantum yields (Φ_f) and singlet oxygen quantum yields (Φ_Δ) were calculated in water.

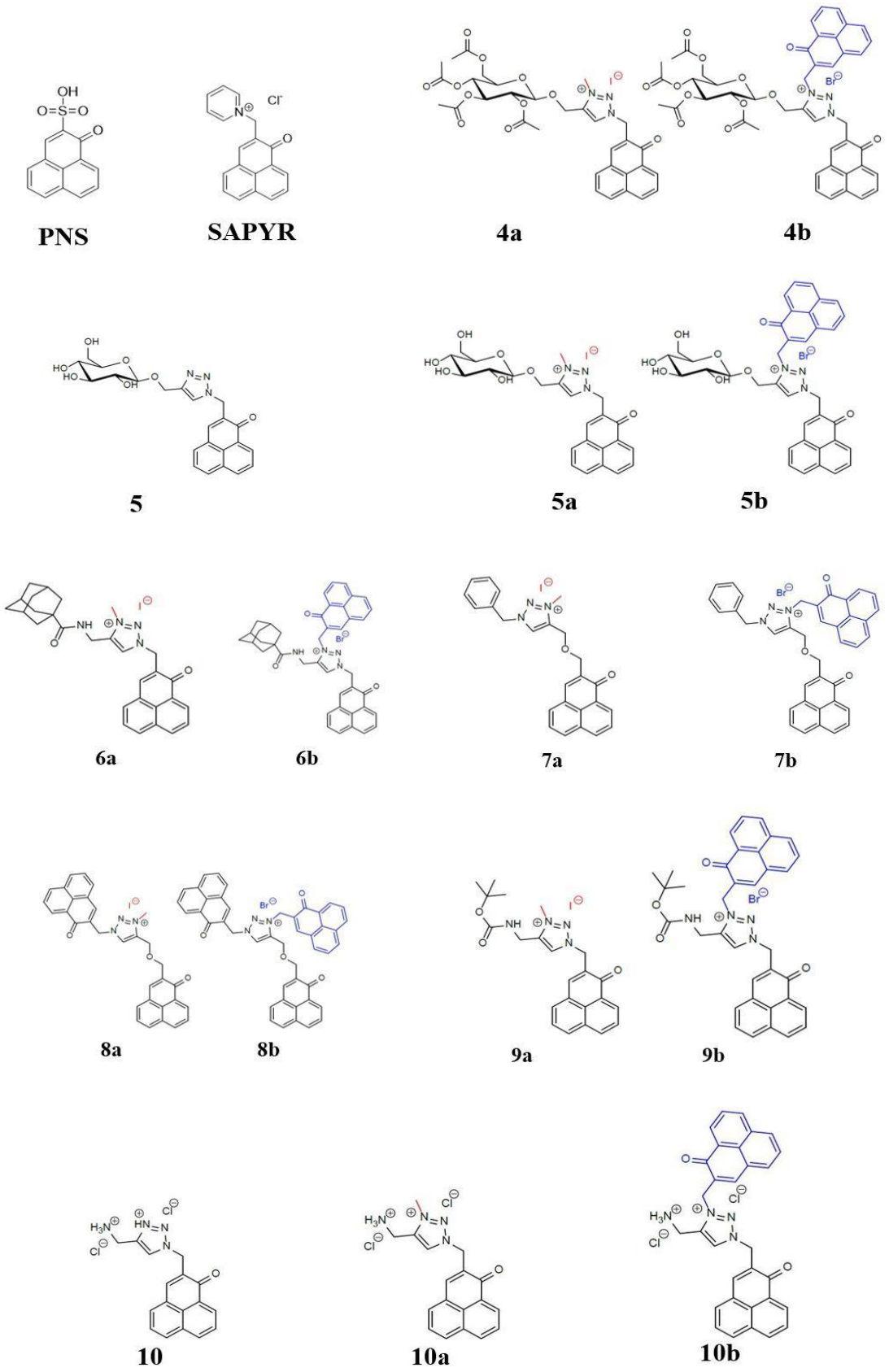

Scheme 7.1. *Chemical structures of all of the PN derivatives synthesized with* ***PNS*** *and* ***SAPYR*** *references (top left).*

These PN derivatives were dissolved in water (HPLC grade) and their UV-vis spectra were recorded (Figure **7.2**). Their molar absorption coefficients (ε) at 370 nm were calculated and the results are shown in Table **7.1**.

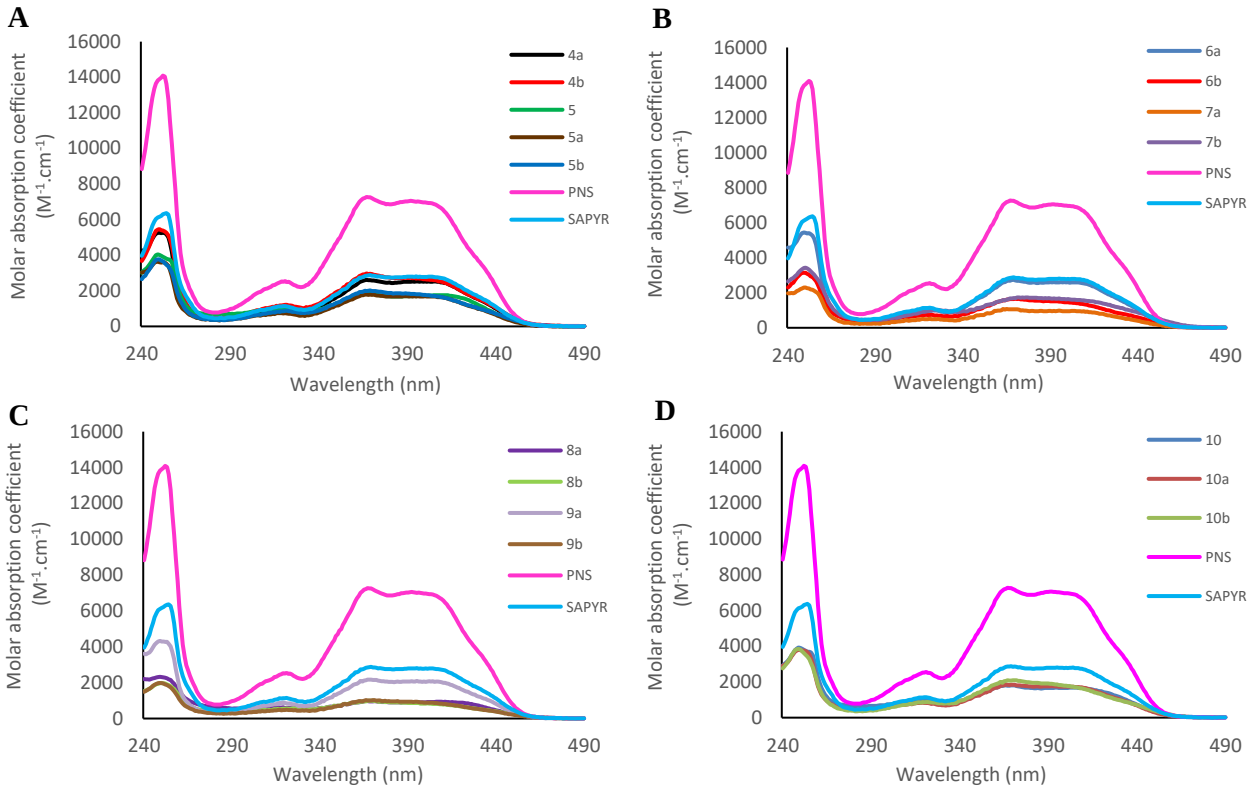

Figure 7.2. *UV-Vis spectra of PN derivatives in water with the molar absorption coefficient scale.* ***(A):*** *PN derivatives* ***4a–5b*** *versus* ***PNS*** *and* ***SAPYR*** *in water;* ***(B):*** *PN derivatives* ***6a–7b*** *versus* ***PNS*** *and* ***SAPYR*** *in water;* ***(C):*** *PN derivatives* ***8a–9b*** *versus* ***PNS*** *and* ***SAPYR*** *in water;* ***(D):*** *PN derivatives* ***10a–10b*** *versus* ***PNS*** *and* ***SAPYR*** *in water.*

While there are no obvious trends in the ε values, sodium (1-oxo-1H-Phenalen-2-yl)sulfonate (**PNS**) has the highest molar absorption coefficient. This value is over twice as large as **4b**, which has the second highest ε in this series. A possible reason for this is the fact that **PNS** is the structure with a heteroatom on the PN system. Furthermore, there is a CH_2 spacer between every aromatic moiety (PN, triazole, sugar, amide, etc) in the other PN derivatives. Another possible reason is the fact that the sulfonate has a high charge density which could also play a role in its higher ε compared to the rest of the PN structures. The likely aggregation that is seen to affect the singlet oxygen quantum yields (Φ_Δ) could also play a role in decreasing the molar absorption coefficients of the other PN derivatives, with respect to **PNS**. The PN derivative, **4b**, is closely followed by structures 2-((4-pyridinyl)methyl)-1H-phenalen-1-one chloride (**SAPYR**) and **6a**. The

lowest values are observed in **8a** and **8b**, which suggests that the covalent attachment of two PN moieties reduces its ability to absorb light, possibly due to aggregation. However, there are examples where the molar absorption coefficient was increased upon adding more PN moieties. This latter effect is seen in the structures: **4a** to **4b**, **7a** to **7b**, **8a** to **8b** and **10** to **10b**.

Table 7.1. *Molar absorption coefficient (ε) at 370 nm, fluorescence quantum yield (**Φ_f**), and singlet oxygen quantum yield (**Φ_Δ**) of the tested PN-derivatives in water.*

PS	ε_{370} ($M^{-1}.cm^{-1}$)	Φ_f [a]	Φ_Δ [b]
PNS	7201	<0.01	0.97
SAPYR	2843	0.02	0.83
4a	2573	0.02	0.80
4b	2940	0.01	>0.98
5	1825	0.02	0.87
5a	1769	0.02	0.97
5b	1986	<0.01	0.31
6a	2708	<0.01	0.70
6b	1655	<0.01	N/A [c]
7a	1050	<0.01	>0.99
7b	1690	<0.01	N/A [c]
8a	964	<0.01	>0.99
8b	987	<0.01	N/A [c]
9a	2156	0.02	0.93
9b	1026	0.01	0.23
10	1796	0.02	0.91
10a	1837	0.02	0.87
10b	2083	0.02	N/A [c]

*[a] **Φ_f** = fluorescence quantum yield was calculated in water using 5,10,15,20-tetraphenylporphyrin (**TPP**) in toluene as a reference (**Φ_f** = 0.11);[19] [b] **Φ_Δ** = singlet oxygen quantum yield was calculated using **PNS** in water as a reference (**Φ_Δ** = 0.97).[20] The molar absorption coefficient (ε) was measured at 370 nm and the excitation wavelength used for both fluorescence emission and singlet oxygen emission was 370 nm; [c] N/A = not available due to lack of clear signal.*

Using 5,10,15,20-tetraphenylporphyrin (**TPP**) in toluene as a reference (**Φ_f** = 0.11),[19] the fluorescence quantum yields of the PN derivatives were calculated using water as a solvent, using the equation **7.1**. (see section **7.4** for experimental details). The graphs are shown below (Figure **7.3**) and even though **SAPYR** has the highest fluorescence, it is still only a low 2% fluorescence.

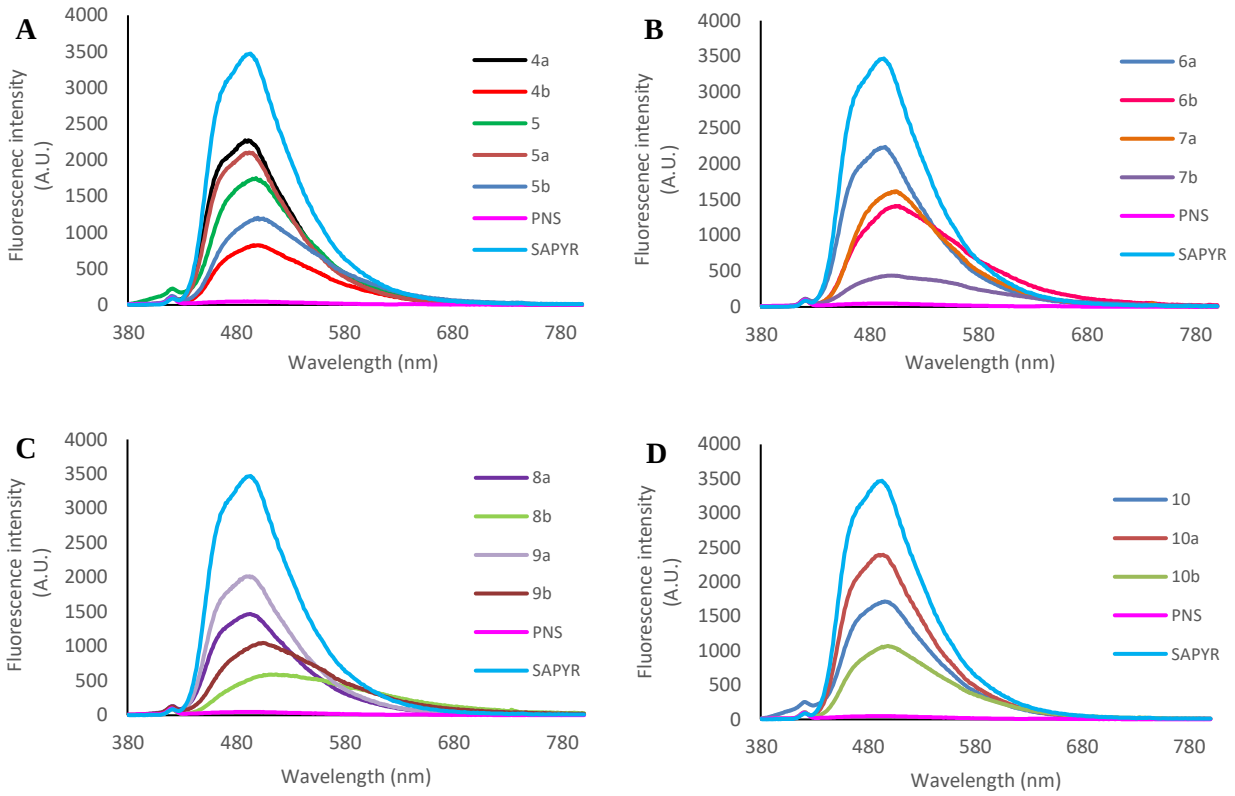

Figure 7.3. *Fluorescence spectra of the PN derivatives in water.* ***(A)****:* ***4a****–****5b*** *vs* ***PNS*** *and* ***SAPYR****;* ***(B)****:* ***6a****–****7b*** *vs* ***PNS*** *and* ***SAPYR****;* ***(C)****:* ***8a****–****9b*** *vs* ***PNS*** *and* ***SAPYR*** *and* ***(D)****:* ***10****–****10b*** *vs* ***PNS*** *and* ***SAPYR****. The excitation wavelength was 370 nm and the reference was* ***TPP*** *in toluene (*Φ_f *= 0.11).*[19]

Using the sulfonated PN derivative (**PNS**, structure in Scheme **7.1**) as a reference, the singlet oxygen quantum yields of the PN derivatives were calculated (see section **7.4** for experimental details). The structures **7a** and **8a** possess the highest Φ_Δ values. Also, notably high singlet oxygen production is associated with all samples except **5b**, **6b**, **7b**, **8b**, **9b** and **10b**. While it appears that the structures with one PN unit in the structure signifies a high Φ_Δ**,** there are exceptions in the form of **4b** and **8a**, whereby the presence of 2 PN moieties yields a large Φ_Δ. The reason for the low singlet oxygen emission observed in the majority of the structures with more than one PN moiety, is likely due to the aggregation occurring in solution.

For the high Φ_Δ values in **4b** and **8a**, similar structures within the PN derivatives (Scheme **7.1**) were compared. Comparing **8a** to **7a**, the only difference is that **7a** contains a benzyl moiety, whereas **8a** contains a PN group. The iodide counterion is also present in **7a** and likely plays a role in the very high Φ_Δ due to the heavy atom effect.[21] Thus, the presence of the iodide counterion and the lack of self-aggregation in this structure could be the reason for the high Φ_Δ observed in **8a**. In the case of **4b**, it has a much larger singlet oxygen generation compared to **5b**. These structures are the same except for the fact that the sugar moiety is acetylated on the periphery. This extra electron

density can prevent self-aggregation in the molecule and increase the overall Φ_{Δ}.

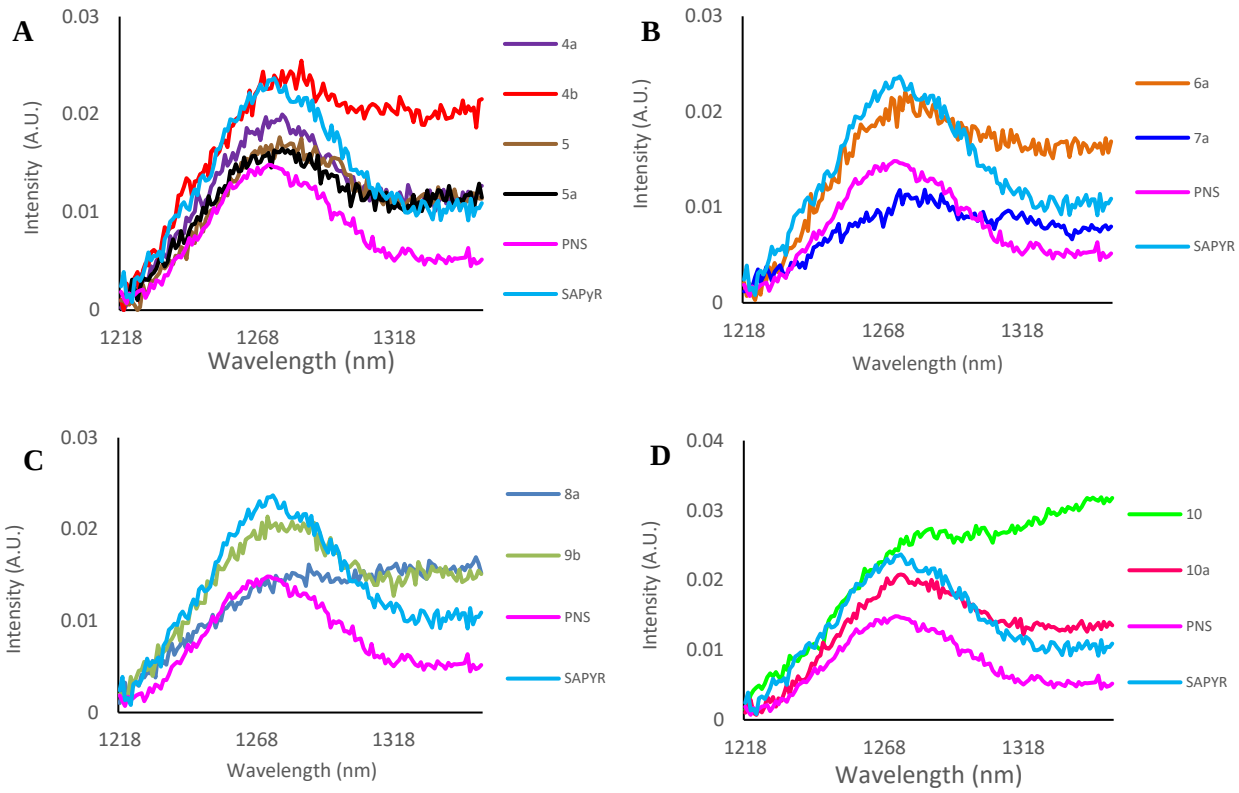

Figure 7.4. *Singlet oxygen emission spectra in water.* ***(A)****:* ***4a****–****5a*** *vs PNS and SAPYR;* ***(B)****:* ***6a*** *and* ***7a*** *vs PNS and SAPYR;* ***(C)****:* ***8a*** *and* ***9b*** *vs PNS and SAPYR and* ***(D)****:* ***10*** *and* ***10a*** *vs PNS and SAPYR. The excitation wavelength was 370 nm and the reference was PNS in water (0.97).*[19]

Overall, the short lifetime of singlet oxygen in water made it difficult to obtain clear emission bands at 1270 nm. Very similar compounds were shown to have very strong singlet oxygen emission signal in chloroform.[23] The lifetime of singlet oxygen in this halogenated solvent is much longer and gives very clear emission. Thus, further measurements in solvents with longer singlet oxygen lifetimes (like chloroform) are required to obtain more Φ_{Δ} data of these PN derivatives.

7.3. *In vitro* bacterial studies

This work was carried out in collaboration with researchers from the Université of Limoges. They conducted the synthesis, the determination of the log P and the *in vitro* bacterial studies. Full details of the synthesis and biological experiments can be found in the original article.[18] The bacterial studies were included in this chapter to correlate them with the obtained photophysical properties.

Before determining the efficacy of these PN derivatives as PSs against bacteria *in vitro*, the octanol/water partition coefficient (log P) was estimated using MarvinSketch Software v. 21.2 (Table **7**.**2**).[18]

Table 7.2. *Partition coefficients (log P) of the PN derivatives, including SAPYR, calculated at pH = 7.3.*

PS	Log P
4a	-2.0
4b	+0.4
5	-0.7
5a	-3.7
5b *	-1.3
6a	+0.7
6b	+3.1
7a	+0.7
7b	+3.2
8a	+1.4
8b	+3.8
9a	-0.4
9b	+2.0
10	+0.6
10a	-1.8
10b	+0.7
SAPYR	-0.5 (Literature = -1.3) [13]

** Compound obtained with a purity of 70%, mixed with 30% of compound **5**.*

Following the determination of their log P, the minimum inhibitory concentration (MIC) of the 16 PN derivatives and SAPYR was determined against Gram-positive (*Staphylococcus aureus*, *Staphylococcus epidermidis*, *Bacillus cereus*) and Gram-negative (*Escherichia coli*, *Pseudomonas aeruginosa*) bacteria (Table **7**.**3**). All compounds were tested at different concentrations ranging from 0.39 to 200 µM in triplicate in 96-well plates. For the most active compounds, concentrations down to 0.05 µM were tested. Subsequently, the 96-well plates were irradiated with LED visible light (4.83 $mW.cm^{-2}$) for a total fluence of 25 $J.cm^{-2}$. Controls consisting of 96-well plates were prepared in the same conditions but kept in the dark.

***Table 7.3**. Minimum Inhibitory Concentration determination of 16 PN derivatives, including SAPYR, against 6 bacterial strains (E.c. 1: Escherichia coli CIP54.8T, E.c. 2: Escherichia coli CIP53.126, P.a.: Pseudomonas aeruginosa CIP76.110, S.a.: Staphylococcus aureus CIP76.25, S.e.: Staphylococcus epidermidis CIP109.562 and B.c.: Bacillus cereus CH,) under dark (D) and light (L) conditions.*

PS	Minimum Inhibitory Concentration (µM)											
	E.c. 1		*E.c. 2*		*P.a.*		*S.a.*		*S.e.*		*B.c.*	
	D	**L**	**D**	**L**	**D**	**L**	**D**	**L**	**D**	**L**	**D**	**L**
4a	>200	100	>200	100	>200	200	>200	100	>200	200	>200	200
4b	>200	>200	>200	100	200	200	100	12.5	100	12.5	100	50
5	>200	>200	>200	>200	>200	>200	>200	100	>200	>200	>200	>200
5a	>200	>200	>200	>200	>200	>200	>200	>200	>200	200	>200	>200
5b *	>200	>200	>200	>200	>200	200	>200	200	>200	200	>200	200
6a	>200	50	>200	25	>200	200	50	6.25	200	12.5	>200	100
6b	*ND*	*ND*	*ND*	*ND*	*ND*	*ND*	25	3.12	6.25	0.78	25	6.25
7a	>200	200	>200	100	>200	>200	50	6.25	25	6.25	100	50
7b	>200	>200	>200	>200	>200	>200	6.25	0.78	6.25	0.78	12.5	3.12
8a	>200	100	>200	50	>200	100	25	0.78	12.5	1.56	25	12.5
8b	>200	200	>200	100	>200	200	50	0.39	12.5	0.78	50	6.25
9a	>200	100	>200	50	>200	>200	>200	25	>200	12.5	>200	200
9b	>200	>200	>200	>200	25	25	6.25	1.56	12.5	1.56	6.25	6.25
10	>200	100	>200	50	>200	12.5	>200	50	>200	100	>200	>200
10a	>200	>200	>200	>200	>200	200	>200	200	>200	100	>200	>200
10b	>200	>200	>200	>200	>200	>200	100	50	>200	12.5	>200	>200
SAPYR	>200	200	>200	>200	>200	50	>200	50	200	25	>200	50

** Compound obtained with a purity of 70%, mixed with 30% of compound **5**. ND: No data, compounds not soluble at the concentrations.*

Due to its low solubility in water, no result could be obtained with **6b** at concentrations higher than 50 µM. However, the bacterial strains that were tested with **6b** showed very impressive MIC values despite the very low singlet oxygen emission in water. This further suggests that there is toxicity induced by the presence of **6b** that is not related to a photodynamic action. All the tested compounds displayed an increased toxicity in the presence of light, and some of them were also active in the dark.

Hydrophilic compounds (containing glucose or amine moieties) showed low effects against all the tested bacterial strains, as compared with more hydrophobic derivatives. This was rather surprising as these compounds have a high singlet oxygen production. No significant difference

was observed between neutral **5** and its triazolium salt derivatives, **5a** and **5b**, suggesting that hydrophobicity is a critical factor for a better efficacy of these salts. This was confirmed by the increase in cytotoxicity brought by acetylation of the hydroxyl groups of **5** (**4a** and **4b**), or by the addition of hydrophobic substituents, such as adamantane (**6a** and **6b**) or benzyl (**7a** and **7b**).

"Phenalenomethylated" compounds bearing an additional hydrophobic moiety (**6b**, **7b**, **8b**, and **9b**) proved to be the most active derivatives against Gram-positive strains under light as well as dark conditions. This result is likely explained by the higher hydrophobicity of the phenalenone moiety compared with the methyl group. Furthermore, these 4 compounds have a value $\boldsymbol{\Phi_\Delta}$ of 0.23 or 0. This is further evidence that compounds bearing the highest singlet oxygen production do not necessarily have the highest bactericidal capacity.

The best results were obtained at sub micromolar concentrations with **6b**, **7b**, or **8b**. Low MIC values were also obtained in dark conditions, in particular with **6b**, **7b**, and **9b**. The activity against Gram-negative is completely different as these strains are much less sensitive to APDT than Gram-positive strains, mainly due to the presence of an outer layer of lipopolysaccharides lowering the degree of permeability to hydrophobic compounds.[22] No significant activity was detected in the dark against Gram-negative strains, except for **9b** against *P. aeruginosa*, with an MIC value of 25 µM. Under light irradiation, compounds with a methylated triazole moiety seem to be more active than "phenalenomethylated" derivatives, which could be explained by the larger size of the latter as well as by their higher hydrophobicity. Compounds **6a** and **10** presented the strongest activity against *E. coli*, and half of the compounds had equal to better activity than SAPYR. Surprisingly, **10** also exhibited an important photodynamic effect against *P. aeruginosa*, while its triazolium derivatives **10a** and **10b** showed very low or no activity.

In terms of correlating the photophysical characteristics and the antibacterial efficiency of these new PN derivatives against 6 bacterial strains (containing both Gram-positive and Gram-negative strains), it appears that a high singlet oxygen production does not ensure a high antibacterial efficiency. There are other factors to consider when constructing the ideal PN photosensitizer for APDT. One must consider including water-soluble and hydrophobic moieties within their design. Moreover, it is beneficial, but not necessary, to include an extra "phenalenomethyl" substituent to further increase the APDT efficiency even though the singlet oxygen production is largely decreased.

In summary, compared with SAPYR, these 14 new phenalenone derivatives bearing the triazolium group have shown medium to good water solubility. The hydrophobic triazolium salt derivatives tested in these specific conditions seem to exhibit a better inhibitory activity against all the tested bacterial strains except *P. aeruginosa*. Furthermore, there photophysical parameters were

determined; how strongly light is absorbed, and the fluorescence and singlet oxygen quantum yields. The next step will be to evaluate whether these new phenalenone derivatives are able to show photo bactericidal activity when exposed to low fluence rates of light. More precisely, plans are being put in place to check these compounds for their activity against bacterial biofilms, which represent the real clinical challenge for APDT. In terms of photophysical experiments, the singlet oxygen production in organic solvents that involve longer singlet oxygen lifetimes should be considered to obtain a more data on the singlet oxygen quantum yields.

7.4. Experimental section

General methods. *2-(bromomethyl)-1*H-*phenalen-1-one* (***1***), *2-(azidomethyl)-1*H-*phenalen-1-one* (***2***), *2-((prop-2-yn-1-yloxy)methyl)-1*H-*phenalen-1-one* (***3***), *(2R,3R,4S,5R,6R)-2-(acetoxymethyl)-6- ((1-((1-oxo-1*H-*phenalen-2-yl)methyl)-1*H-*1,2,3-triazol-4-yl)methoxy)tetrahydro-2*H-*pyran-3,4,5- triyl triacetate* (***4***), *2-((4-((((2R,3R,4S,5S,6R)-3,4,5-trihydroxy-6-(hydroxymethyl)tetrahydro-2*H- *pyran-2-yl)oxy)methyl)-1H-1,2,3-triazol-1-yl)methyl)-1*H-*phenalen-1-one* (***5***), *(3r,5r,7r)-N-((1-((1-oxo-1*H-*phenalen-2-yl)methyl)-1*H-*1,2,3-triazol-4-yl)methyl)adamantane-1-carboxamide* (***6***), *tert-butyl ((1-((1-oxo-1*H-*phenalen-2-yl)methyl)-1*H-*1,2,3-triazol-4-yl)methyl)carbamate* (***9***), *and (1-oxo-1*H-*phenalen-2-yl)methanaminium chloride* (***10***) were synthesized as described earlier.[23] SAPYR was synthesized following the protocol described by Späth et al.[13] All other reagents and solvents were purchased from Alfa Aesar, TCI, Carlo Erba, Fisher Chemical, VWR, or Sigma Aldrich and were used as received. Column chromatography was conducted with a silica gel 60 (0.015–0.040 mm) which was purchased from Merck.

Photophysical characterization: The photophysical characterization was conducted in as water as a solvent (HPLC grade, supplier = Merck). Both UV-Vis absorption spectra and fluorescence emission spectra were recorded at room temperature (21˚C). UV-Vis absorption and photoluminescence spectra were measured in quartz cuvettes (1 cm path-length, Hellma). The UV-Vis absorption spectra were recorded on a Shimadzu UV2700 spectrophotometer and fluorescence emission spectra were recorded on a SPEX Fluorolog 3 fluorometer. In this fluorometer, double grating monochromators are used in the excitation and emission channels. A Xenon arc lamp (450 W, Osram) is the excitation light source, and a Peltier cooled photomultiplier tube (R636-10, Hamamatsu) is the detector for the fluorescence. For the singlet oxygen emission at 1275 nm, a highly sensitive liquid nitrogen-cooled InGaAs detector (Electro-Optical Systems DSS series cryogenic receiver, 2 mm InGaAs photodiode) was coupled to a Spex Fluorolog 3

spectrofluorometer. The fluorescence signal from the fluorophores in solution is collected in a right-angle geometry, and the fluorescence spectra are corrected for fluctuations of the excitation source flux and for the wavelength dependence of the detection sensitivity. The absorbance for photoluminescence spectra was 0.1 and the excitation wavelength used was 370 nm.

Both fluorescence and singlet oxygen quantum yields were determined using the SPEX fluorolog 3 fluorometer relative to a standard of known quantum yield. The quantum yields were calculated using the equation **7.1** below:[19]

$$\Phi_x = \Phi_r \left[\frac{A_r(\lambda_r)}{A_x(\lambda_x)}\right]\left[\frac{I(\lambda_r)}{I(\lambda_x)}\right]\left[\frac{n_x^2}{n_r^2}\right]\left[\frac{D_x}{D_r}\right] \qquad (\mathbf{7.1})$$

where Φ_x = the desired quantum yield (fluorescence or singlet oxygen) of an unknown sample; Φ_r = the quantum yield of an reference sample according to literature; $A_r(\lambda_r)$ = absorbance of a reference sample at the 370 nm; $A_x(\lambda_x)$ = absorbance of an unknown sample at 370 nm; $I(\lambda_r)$ = relative intensity of the exciting light of a known reference sample at wavelength λ; $I(\lambda_x)$ = relative intensity of the exciting light of an unknown sample at wavelength λ; n_x = refractive index of the solvent in which an unknown sample is dissolved; n_r = refractive index of the solvent in which a reference sample is dissolved; D_x = integrated area under the corrected emission spectrum of an unknown sample; D_r = integrated area under the corrected emission spectrum of a known reference sample. These integrations were measured in the Origin program and the skewed baselined was corrected to integrate the total area under the curve.[24] Refractive indices of the solvent, n_x and n_r, must be equal for the singlet oxygen determination (ie. in the same solvent). The data were analyzed using the Origin program and Microsoft excel.[24]

Microbiological Assays

Bacterial strains and conditions of culture. Two Gram-positive (*Staphylococcus aureus* CIP76.25 and *Staphylococcus epidermidis* CIP109.562) and three Gram-negative (*Pseudomonas aeruginosa* CIP76110; *Escherichia coli* CIP53.126 and *Escherichia coli* CIP54.8T) bacterial strains were obtained from the Collection Institut Pasteur (CIP, Institut Pasteur Paris, France). *Bacillus cereus* CH was obtained from Anyang Yuanshou Biopharmaceutical (China). These strains were cultured in liquid Tryptic Soy Broth (pancreatic casein extract 17 $g.L^{-1}$, soy flour papaic digest 3

$g.L^{-1}$, dextrose 2.5 $g.L^{-1}$, NaCl 5 $g.L^{-1}$, and K_2HPO_4 2.5 $g.L^{-1}$) and incubated overnight at 37ºC under aerobic conditions.

Minimum Inhibitory Concentration (MIC) assays. Inoculum were prepared following a standard microdilution assay procedure using tryptic soy broth (TSB) and performed in triplicate. All the compounds were dissolved in a water/ethanol 99:1 mixture to obtain stock solutions at a concentration of 1 mM and kept at 4˚C. Then, fresh solutions of each compound at 400 µM in TSB were prepared. A total of 200 µL of these solutions were added in 96-well plates, and a 1:1 serial dilution was performed from 400 µM to 1.56 µM. A total of 100 µL of a bacterial suspension at 2 x 10^6 CFU mL^{-1} was added to each well, which resulted in a range of concentrations from 200 to 0.78 µM. Subsequently, the 96-well plates were irradiated with white LED visible light (wavelength approximately 390–700 nm, 4.83 $mW.cm^{-2}$) for a total fluence of 25 $J.cm^{-2}$. Controls consisting of 96-well plates were prepared in the same conditions but kept in the dark. After irradiation, the 96-well plates were incubated overnight at 37˚C under aerobic conditions. The lowest concentration of each compound that prevented bacterial growth was considered the minimum inhibitory concentration (MIC) of each compound. All compounds displaying activity at the minimum 0.78 µM concentration of the original assay were tested again with 25 µM as the initial concentration instead of 200 µM and using the same procedure previously described. A total of three independent experiments were performed with each strain.

Supplementary Materials: The supplementary information from the original article is available online at https://www.mdpi.com/article/10 .3390/antibiotics10060626/s1.

7.5. References

[1] B. Allegranzi, S. B. Nejad, C. Combescure, W. Graafmans, H. Attar, L. Donaldson and D. Pittet, Burden of Endemic Health-Care- Associated Infection in Developing Countries: Systematic Review and Meta-Analysis, *Lancet.*, 2011, **377**, 228–241. doi: 10.1016/S0140-6736(10)61458-4.
[2] P. Agaba, J. Tumukunde, J. V. B. Tindimwebwa and A. Kwizera, Nosocomial Bacterial Infections and Their Antimicrobial Susceptibility Patterns among Patients in Ugandan Intensive Care Units: A Cross Sectional Study, *BMC Res. Notes*, 2017, **10**, 349–360. doi: 10.1186/s13104-017-2695-5.
[3] G. G. Zhanel, M. DeCorby, N. Laing, B. Weshnoweski, R. Vashisht, F. Tailor, K. A. Nichol, A. Wierzbowski, P. J. Baudry, J. A. Karlowsky, P. Lagacé-Wiens, A. Walkty, M. McCracken, M. R. Mulvey and J. Johnson, Canadian Antimicrobial Resistance Alliance (CARA) and D. J. Hoban, Antimicrobial-Resistant Pathogens in Intensive Care Units in Canada: Results of the Canadian National Intensive Care Unit (CAN-ICU) Study, 2005–2006, *Antimicrob. Agents Chemother.*, 2008, **52**, 1430–1437. doi: 10.1128/AAC.01538-07.
[4] B. Glasset, S. Herbin, S. A. Granier, L. Cavalié, E. Lafeuille, C. Guérin, R. Ruimy, F. Casagrande-Magne, M. Levast, N. Chautemps, J. -W. Decousser, L. Belotti, I. Pelloux, J. Robert, A. Brisabois and N. Ramarao, Bacillus Cereus, a Serious Cause of Nosocomial Infections: Epidemiologic and Genetic Survey, *PLoS ONE*, 2018, **13**, e0194346. doi: 10.1371/journal.pone.0194346
[5] D. Roux, G. B. Pier and D. Skurnik, Magic Bullets for the 21st Century: The Reemergence of Immunotherapy for Multi- and Pan-Resistant Microbes, *J. Antimicrob. Chemother.*, 2012, **67**, 2785–2787. doi: 10.1093/jac/dks335
[6] D. M. Lin, B. Koskella and H. C. Lin, Phage Therapy: An Alternative to Antibiotics in the Age of Multi-Drug Resistance, *World J. Gastrointest. Pharmacol. Ther.*, 2017, **8**, 162–173. doi: 10.4292/wjgpt.v8.i3.162
[7] L. Huang, T. Dai and M. R. Hamblin, Antimicrobial Photodynamic Inactivation and Photodynamic Therapy for Infections, In *Photodynamic Therapy*; C. J. Gomer, Ed.; Methods in Molecular Biology; Humana Press: Totowa, NJ, USA, 2010, **635**, 155–173. ISBN 978-1-60761-696-2.
[8] M. Wainwright, T. Maisch, S. Nonell, K. Plaetzer, A. Almeida, G. P. Tegos and M. R. Hamblin, Photoantimicrobials—Are We Afraid of the Light?, *Lancet. Infect. Dis.*, 2017, **17**, e49–e55. doi: 10.1016/S1473-3099(16)30268-7
[9] H. Mahmoudi, A. Bahador, M. Pourhajibagher and M. Y. Alikhani, Antimicrobial Photodynamic Therapy: An Effective Alternative Approach to Control Bacterial Infections, *J. Lasers Med. Sci.*, 2018, **9**, 154–160. doi: 10.15171/jlms.2018.29
[10] F. Le Guern, V. Sol, C. Ouk, P. Arnoux, C. Frochot and T. -S. Ouk, Enhanced Photobactericidal and Targeting Properties of a Cationic Porphyrin Following the Attachment of Polymyxin B, *Bioconj. Chem.*, 2017, **28**, 2493–2506. doi: 10.1021/acs.bioconjchem.7b00516
[11] Y. Nitzan, M. Gutterman, Z. Malik and B. Ehrenberg, Inactivation of gram-negative bacteria by photosensitized porphyrins, *Photochem. Photobiol.*, 1992, **55**, 89–96. doi: 10.1111/j.1751-1097.1992.tb04213.x
[12] F. Cieplik, A. Späth, J. Regensburger, A. Gollmer, L. Tabenski, K. -A. Hiller, W. Bäumler, T. Maisch and G. Schmalz, Photodynamic Biofilm Inactivation by SAPYR—An Exclusive Singlet Oxygen Photosensitizer, *Free Radic. Biol. Med.*, 2013, **65**, 477–487. doi: 10.1016/j.freeradbiomed.2013.07.031
[13] A. Späth, C. Leibl, F. Cieplik, K. Lehner, J. Regensburger, K. -A. Hiller, W. Bäumler, G. Schmalz and T. Maisch, Improving Photodynamic Inactivation of Bacteria in Dentistry: Highly Effective and Fast Killing of Oral Key Pathogens with Novel Tooth-Colored Type-II Photosensitizers, *J. Med. Chem.*, 2014, **57**, 5157–5168. doi: 10.1021/jm4019492
[14] I. Tabenski, F. Cieplik, L. Tabenski, J. Regensburger, K. -A. Hiller, W. Buchalla, T. Maisch and A. Späth, The Impact of Cationic Substituents in Phenalen-1-One Photosensitizers on Antimicrobial Photodynamic Efficacy, *Photochem. Photobiol. Sci.*, 2016, **15**, 57–68. doi: 10.1039/C5PP00262A
[15] J. T. Fletcher, J. M. Sobczyk, S. C. Gwazdacz and A. J. Blanck, Antimicrobial 1,3,4-Trisubstituted-1,2,3-Triazolium Salts, *Bioorganic Med. Chem. Lett.*, 2018, **28**, 3320–3323. doi: 10.1016/j.bmcl.2018.09.011
[16] A. Jiblaoui, S. Leroy-Lhez, T. -S. Ouk, K. Grenier and V. Sol, Novel Polycarboxylate Porphyrins: Synthesis, Characterization, Photophysical Properties and Preliminary Antimicrobial Study against Gram-Positive Bacteria, *Bioorganic Med. Chem. Lett.*, 2015, **25**, 355–362. doi: 10.1016/j.bmcl.2014.11.033
[17] F. Le Guern, T. -S. Ouk, C. Ouk, R. Vanderesse, Y. Champavier, E. Pinault and V. Sol, Lysine

Analogue of Polymyxin B as a Significant Opportunity for Photodynamic Antimicrobial Chemotherapy, *ACS Med. Chem. Lett.*, 2018, **9**, 11–16. doi: 10.1021/acsmedchemlett.7b00360
[18] J. Godard, D. Gibbons, S. Leroy-Lhez, R. M. Williams, N. Villandier, T. -S. Ouk, F. Brégier and V. Sol, Development of Phenalenone-Triazolium Salt Derivatives for APDT: Synthesis and Antibacterial Screening, *Antibiotics*, 2021, **10**, 626–638. doi: 10.3390/antibiotics10060626.
[19] P. G. Seybold and M. Gouterman, Porphyrins. XIII: Fluorescence Spectra and Quantum Yields, *J. Mol. Spec.*, 1969, **31**, 1–13. doi: 10.1016/0022-2852(69)90335-X.
[20] S. Nonell, M. González and F. R. Trull, 1H-Phenalen-1-One-2-Sulfonic Acid: An Extremely Efficient Singlet Molecular Oxygen Sensitizer for Aqueous Media, *Afinidad*, 1993, **448**, 445–450.
[21] E. Pomarico, P. Pospíšil, M. E. F. Bouduban, J. Vestfrid, Z. Gross, S. Záliš, M. Chergui and A. Vlček, Photophysical Heavy-Atom Effect in Iodinated Metallocorroles: Spin–Orbit Coupling and Density of States, *J. Phys. Chem. A.*, 2018, **122**, 7256–7766. doi: 10.1021/acs.jpca.8b05311.
[22] F. F. Sperandio, Y. -Y. Huang and M. R. Hamblin, Antimicrobial Photodynamic Therapy to Kill Gram-Negative Bacteria, *Recent Pat. Anti-Infect Drug Discov.*, 2013, **8**, 108–120. doi: 10.2174/1574891x113089990012
[23] J. Godard, F. Brégier, P. Arnoux, B. Myrzakhmetov, Y. Champavier, C. Frochot and V. Sol, New Phenalenone Derivatives: Synthesis and Evaluation of Their Singlet Oxygen Quantum Yield, *ACS Omega*, 2020, **5**, 28264–28272. doi: 10.1021/acsomega.0c04172
[24] Origin, Version 2018b; OriginLab Corporation: Northampton, MA, USA, 2018.

List of publications

Publications covered in this thesis:

Chapter **2:** D. J. Gibbons, A. Farawar, P. Mazzella, S. Leroy-Lhez and R. M. Williams, Making triplets from photo-generated charges: observations, mechanisms and theory, *Photochem. Photobiol. Sci*., 2020, **19**, 136–158. doi: 10.1039/c9pp00399a.

Chapter **7:** J. Godard, D. Gibbons, S. Leroy-Lhez, R. M. Williams, N. Villandier, T. -S. Ouk, F. Brégier and V. Sol, Development of Phenalenone-Triazolium Salt Derivatives for aPDT: Synthesis and Antibacterial Screening, *Antibiotics*, 2021, **10**, 626–638. doi: 10.3390/antibiotics10060626.

Other publications:

K. J. Flanagan, M. Paradiz Dominguez, Z. Melissari, H. -G. Eckhardt, R. M. Williams, D. Gibbons, C. Prior, G. M. Locke, A. Meindl, A. A. Ryan and M. O. Senge, Structural Effects of Meso-Halogenation on Porphyrins, *Beilstein J. Org. Chem.* 2021, **17**, 1149–1170. doi: 10.3762/bjoc.17.88.

K. Norvaiša, J. E. O'Brien, D. J. Gibbons and M. O. Senge. Elucidating Atropisomerism in Nonplanar Porphyrins with Tunable Supramolecular Complexes, *Chemistry*, 2020, **27**, 331–339. doi: 10.1002/chem.202003414.

K. Norvaiša, K. J. Flanagan, D. Gibbons and M. O. Senge. Conformational Re-engineering of Porphyrins as Receptors with Switchable N–H···X-Type Binding Modes, *Angew. Chem. Int. Ed*., 2019, **58**, 16553–16557. doi: 10.1002/anie.201907929.

J. M. O'Brien, E. Sitte, K. J. Flanagan, H. Kühner, L. J. Hallen, D. Gibbons and M. O. Senge, Functionalization of Deutero- and Protoporphyrin IX Dimethyl Esters via Palladium-Catalyzed Coupling Reactions, *J. Org. Chem*., 2019, **84**, 6158−6173. doi: 10.1021/acs.joc.9b00350

D. Gibbons, K. J. Flanagan, L. Pounot and M. O. Senge, Structure and conformation of photosynthetic pigments and related compounds. 15. Conformational analysis of chlorophyll derivatives – implications for hydroporphyrins in vivo, *Photochem. Photobiol. Sci*., 2019, **18**, 1479–1494. doi: 10.1039/c8pp00500a.

D. Gibbons, G. Emandi and M. O. Senge, Crystal structure and synthesis of 3-(1H-pyrrol-2-yl)-1-(thiophen-2-yl)propanone, *Acta Cryst*., 2018, **E74**, 1463–1466. doi: 10.1107/S2056989018012331.

Summary

Triplet state access in multi-component heavy atom free photo-sensitizers in photomedicine

Photodynamic therapy (PDT) has been a known clinical treatment for cancer for at least 30 years. More recently, PDT has been shown to be efficient against killing microbial cells (Antimicrobial Photodynamic Therapy or APDT). The scientific community has since aimed to improve the therapeutic efficacy of PDT. This thesis describes a comprehensive study into recent advances made towards improving the drug candidates (photosensitizers) for this therapy. More specifically, novel photosensitizers (PSs) have been synthesized, modified and studied with time-resolved and steady-state spectroscopy techniques, to determine their potential.

This thesis commences with an introduction to photodynamic therapy. It describes how the therapy functions, in principle, and discusses its advantages and limitations. Furthermore, the photochemistry and mechanisms to reach the triplet state are introduced. The triplet state plays an essential role in PDT. Finally, the structural design for an ideal PS is discussed in detail to provide the readers with all the properties that are needed for the optimal design. This "synthetic toolbox" was conducted to equip the future PDT community with the tools needed to create the next generation of PSs for PDT.

Chapter 2 describes the mechanism of an exotic triplet forming mechanism called triplet formation by charge recombination. It involves the combination of a donor and acceptor molecule to form a dyad. Upon excitation of the dyad, there is photoinduced electron transfer from the donor to the acceptor to form the singlet charge transfer state (^{1}CT). From here, spin–orbit charge transfer intersystem crossing (SOCT-ISC) can occur to form the triplet state. Proton hyperfine interactions occur to form the triplet charge transfer state (^{3}CT), followed by charge recombination to the triplet state. The SOCT-ISC pathway has been found in fullerene-containing thin-film blends as well as in BODIPY-based dyads in solution. This mechanism as well as the more conventional one (described in the introduction) were investigated in the following chapters.

The third chapter describes the potential of a *meso* tetra-(hexyloxyphenyl)porphyrin for photomedicine (PDT and APDT). The details of the synthesis are described, followed by the photophysical studies of the porphyrin in solution and in a thin-film (solid state). The photophysical studies exhibited that the

Summary

triplet state of this porphyrin can be accessed in solution and in a thin film. The singlet oxygen generation was detected by a sensitive singlet oxygen probe in water.

In the fourth chapter, the natural polymer kraft lignin is attached to porphyrin and cyanine fluorophores to afford four novel lignin conjugates. The synthesis of these lignin conjugates is described followed by the investigation of their potential in photomedicine. It was shown that these new systems have efficient activity as novel PSs. These lignin systems were able to produce singlet oxygen, despite the lignin carrier encapsulating the system.

Chapter 5 contains the synthesis and photochemistry of a novel porphyrin-near-IR cyanine dye conjugate. Dissolving this conjugate in THF and exciting the molecule using near-IR and visible light, allowed for singlet oxygen to be produced. The production of singlet oxygen was only observed in THF and thus indicates that triplet formation *via* charge recombination occurs. Exciting the cyanine moiety gives the fluorescence signature of the cyanine dye. However, upon irradiation of the porphyrin subunit, fluorescence of both the cyanine and porphyrin moieties were observed and triplet formation was confirmed using nanosecond transient absorption spectroscopy. The triplet lifetime was even longer than that of the porphyrin starting material in the same THF solvent. Thus, it indicates that this conjugate undergoes triplet formation *via* charge recombination when the porphyrin moiety is promoted to the singlet excited state using near-IR light.

The penultimate chapter (chapter 6) includes the synthetic methods used to create porphyrin and cyanine dyes. These can be combined to synthesize more porphyrin-near-IR cyanine dye conjugates that may have improved properties.

The last chapter encompasses the photophysical characterization of 16 novel phenalenone PSs. The photophysical properties were compared to their efficacy against gram-positive and gram-negative bacteria. These derivatives of the natural PS, phenalenone, were dissolved in water and their capacity to absorb light, their fluorescence and singlet oxygen generation was measured. The derivatives bearing the triazolium group exhibited medium to good water solubility.

Overall, this thesis has provided novel molecules that are activated *via* near-IR light which is in the ideal therapeutic region. It is clear that the novel PSs synthesized and studied, exemplify a new generation of PSs, especially the porphyrin-near-IR cyanine dye conjugates.

Samenvatting

Toegang tot de triplet toestand in zware-atoom-vrije multi-component fotosensibilisatoren in de geneeskundige lichttherapie

Fotodynamische therapie (PDT) is al minstens 30 jaar een bekende klinische behandeling voor kanker. Meer recentelijk is aangetoond dat PDT effectief is voor de vernietiging van microbiële cellen (antimicrobiële fotodynamische therapie of APDT). Sindsdien zoekt de wetenschappelijke gemeenschap naar nieuwe manieren om de therapeutische werkzaamheid van PDT te verbeteren. Dit proefschrift beschrijft een diepgaande studie van recente ontwikkelingen naar het verbeteren van kandidaat-geneesmiddelen (fotosensibilisatoren) voor deze therapie. In het bijzonder zijn nieuwe fotosensibilisatoren (= photosensitizers, PS) gesynthetiseerd, gemodificeerd en bestudeerd met tijds-opgeloste en steady-state spectroscopietechnieken om hun potentieel te bepalen.

Dit proefschrift begint met een inleiding in de fotodynamische therapie. Het beschrijft hoe de therapie in principe werkt en bespreekt de voordelen en beperkingen. Daarnaast worden de fotochemie en de mechanismen voor het bereiken van de triplettoestand geïntroduceerd. De triplettoestand speelt een essentiële rol bij PDT. Ten slotte wordt het structurele ontwerp van een ideale PS in detail besproken om de lezers inzicht in de eigenschappen te bieden die nodig zijn voor het optimale ontwerp. Deze "synthetische toolkit" is gemaakt om de toekomstige PDT-gemeenschap uit te rusten met de tools die nodig zijn om de volgende generatie PS voor PDT te creëren.

Hoofdstuk 2 beschrijft een exotisch mechanisme voor tripletvorming, genaamd tripletvorming door ladingsrecombinatie. Het omvat het combineren van een donor- en acceptormolecuul om een dyade te vormen. Bij excitatie van de dyade is er een foto-geïnduceerde elektronenoverdracht van de donor naar de acceptor om de singlet-ladingsoverdrachtstoestand (^{1}CT) te vormen. Van daaruit kan spin-baan koppeling gekoppeld met ladings-overdacht (SOCT-ISC) plaatsvinden waarmee de triplettoestand wordt gevormd. Hyperfijne proton interacties kunnen optreden waarmee de triplet-ladingsoverdrachtstoestand (^{3}CT) gevormd kan worden (uit de ^{1}CT), gevolgd door ladingsrecombinatie naar de triplet-toestand. De SOCT-ISC-route werd gevonden in dunne-filmmengsels die fullerenen bevatten en in op BODIPY gebaseerde dyades, in oplossing. Dit mechanisme en het meer conventionele mechanisme (beschreven in de inleiding) worden in de volgende hoofdstukken bestudeerd.

Het derde hoofdstuk beschrijft het potentieel van een meso tetra-(hexyloxyfenyl)porfyrine voor geneeskundige lichttherapie (PDT en APDT). De details

van de synthese worden beschreven, gevolgd door foto-fysische studies van deze porfyrine in oplossing en in dunne film (vaste toestand). Fotofysische studies hebben aangetoond dat de triplettoestand van dit porfyrine toegankelijk is in oplossing en in dunne film. De vorming van singlet-zuurstof werd gedetecteerd door een gevoelige moleculaire singlet-zuurstofsonde in water.

In het vierde hoofdstuk wordt het natuurlijke polymeer, lignine, gehecht aan porfyrine en cyanine om vier nieuwe lignine-systemen te geven. De synthese van deze lignine-systemen wordt beschreven, gevolgd door de studie van hun potentieel in de fotodynamische therapie. Van deze nieuwe systemen is aangetoond dat ze een effectieve activiteit hebben als nieuwe PS's. Deze lignine-systemen waren in staat om singletzuurstof te produceren, terwijl de ligninedrager het systeem omkapselde.

Hoofdstuk 5 bevat de synthese en fotochemie van een nieuw porfyrine-cyanine kleurstof systeem. Door dit molecuul op te lossen in THF en het molecuul te exciteren met nabij-infrarood en zichtbaar licht, werd singlet-zuurstof geproduceerd. Singlet-zuurstofproductie werd alleen waargenomen in THF en geeft hiermee aan dat tripletvorming door ladingsrecombinatie plaatsvindt. Excitatie van het cyanine deel geeft de fluorescentie-signatuur van de cyanine kleurstof. Na bestraling van de porfyrine sub-eenheid werd echter fluorescentie van de cyanine- en porfyrine delen waargenomen en tripletvorming werd bevestigd door tijdsopgeloste absorptiespectroscopie op de tijdschaal van nanoseconden. De duur van de triplet-toestand was zelfs langer dan die van het porfyrine-uitgangsmateriaal in hetzelfde oplosmiddel, THF. Daarom geeft dit aan dat dit systeem tripletvorming ondergaat via ladingsrecombinatie wanneer de porfyrinegroep wordt bevorderd tot de geëxciteerde singlettoestand met behulp van nabij-infraroodlicht.

Het voorlaatste hoofdstuk (hoofdstuk 6) bevat de synthetische methoden die worden gebruikt om porfyrine- en cyanine kleurstoffen te maken. Deze kunnen worden gecombineerd om meerdere NIR-cyanine kleurstof - porfyrine verbindingen te synthetiseren, die mogelijk verbeterde eigenschappen hebben.

Het laatste hoofdstuk omvat de fotofysische karakterisering van 16 nieuwe phenalenone PS. De fotofysische eigenschappen werden vergeleken met hun effectiviteit tegen grampositieve en gramnegatieve bacteriën. Deze natuurlijke PS-derivaten, phenalenonen, werden opgelost in water en hun vermogen om licht te absorberen, de fluorescentie en singlet-zuurstofvorming werd gemeten. Derivaten die

Samenvatting

de triazolium-groep dragen vertoonden een gemiddelde tot goede oplosbaarheid in water.

Dit proefschrift heeft nieuwe moleculen opgeleverd die worden geactiveerd met nabij-infrarood licht, hetgeen in het ideale therapeutische gebied valt. Het is duidelijk dat de nieuwe fotosensibilisatoren die zijn gesynthetiseerd en bestudeerd, een nieuwe generatie verbindingen illustreert, in het bijzonder de porfyrine-nabije IR-cyanine-systemen.

Resumé

Formations des états triplet de photosensibilisateurs sans atomes lourds pour des applications en photomédecine

La thérapie photodynamique (PDT) est un traitement clinique du cancer connu depuis 30 ans. La communauté scientifique a depuis cherché des nouvelles voies pour améliorer son efficacité thérapeutique. Cette thèse décrit une étude approfondie des avancées récentes réalisées dans l'amélioration des candidats-médicaments (photosensibilisateurs) pour cette thérapie. Le chapitre 2 décrit un mécanisme nouveau, appelé formation de triplet par recombinaison de charges. Ce mécanisme a le potentiel d'ouvrir la voie à une nouvelle génération de photosensibilisateurs. De plus, une tétra (hexyloxy) phénylporphyrine a été synthétisée et formulée sous la forme d'un film mince capable de générer de l''oxygène singulet sous irradiation. Des photosensibilisateurs (PS) contenant de la lignine kraft ont été synthétisés, modifiés et étudiés avec des techniques de spectroscopie résolue en temps et en régime permanent, afin de déterminer leur potentiel en photomédecine. De même, une nouvelle dyade associant cyanine et porphyrine a été synthétisée et étudiée. Les observations faites tendent à prouver la formation de triplet par recombinaison de charges. De plus, les méthodes synthétiques utilisées pour créer de nouveaux colorants de porphyrine et de cyanine sont discutées ainsi que la caractérisation photophysique de 16 nouveaux PS dérivés de la phénalénone. Ces propriétés photophysiques ont été comparées à leur efficacité contre des bactéries à Gram positif et Gram négatif. Dans l'ensemble, cette thèse a fourni de nouveaux photosensibilisateurs et il est clair que certains d'entre eux, en particulier la nouvelle dyade associant cyanine et porphyrine, pourraient ouvrir la voie à une nouvelle génération de PS.

Sommario

Accesso a stati di tripletto in fotosintetizzatori senza atomi pesanti ed applicazioni in fotomedicina

La terapia fotodinamica conosciuta anche come PDT (acronimo inglese di photodynamic therapy) è un trattamento clinico utilizzato per curare il cancro, o piu' in generale affezioni e di disturbi cutanei da almeno 30 anni. Più recentemente, l'utilizzo di tale terapia è stato esteso alla lotta contro i microorganismi. Si parla dunque in questo caso di terapia fotodinamica antimicrobica o APDT (acronimo inglese di antimicrobial photodynamic therapy).

La PDT e l'APDT si avvalgono di sostanze particolari, chiamate fotosensibilizzatori (PS) che, per espletare la propria funzione, devono essere attivate da una fonte luminosa. Cio' fa si che si instauri una reazione fotodinamica, il cui risultato finale e' la formazione di specie reattive dell'ossigeno, ROS (acronimo inglese Reactive oxygen species), in grado di distruggere cellule maligne.

Questa tesi inizia con un'introduzione riguardante il funzionamento generico della terapia fotodinamica, ed i suoi vantaggi e limitazione. I meccanismi fotochimici ed processi che permettono il raggiungimento dello stato di tripletto, elemento essenziale nella PDT sono introdotti. Nella parte finale del capitolo vengono descritte dettagliatamente le caratteristiche che dovrebbe aver un PS ideale, cosi da fornire al lettore gli elementi essenziali, necessari alla creazione di futuri PS.

Nel secondo capitolo è descritto un raro meccanismo di formazione di tripletto chiamato formazione di tripletto tramite ricombinazione di carica. Questo meccanismo prevede la combinazione di una molecola donatrice ed una accettatrice che inducono la formazione di una diade. Quando questa diade viene eccitata, vi è un trasferimento di elettroni dal donatore all'accettore che porta alla formazione di uno stato di trasferimento di carica di singoletto (^{1}CT).

Da qui, la formazione di uno stato di tripletto puo' avvenire tramite il trasferimento di carica inter-sistema via spin-orbita (SOCT-ISC). Le interazioni protoniche iperfini concorrono alla formazione di uno stato di trasferimento di carica di tripletto (3CT), seguito poi da processi di ricombinazione di carica verso lo stato di tripletto. Il SOCT-ISC e' osservabile in miscele di film sottili contenenti fullereni e in soluzioni contenenti diadi basate su BODIPY. Questo meccanismo e quello più convenzionale (descritto nell'introduzione) sono stati studiati nei capitoli successivi.

Sommario

Il terzo capitolo descrive il potenziale di una meso tetra- (esilossifenil) porfirina per la fotomedicina (PDT e APDT). Dopo aver descritto i dettagli del processo di sintesi, i risultati delle investigazioni fotofisiche della porfirina, sia in soluzione, che come film sottile (stato solido) sono presentati.

Tali studi dimostrano che lo stato di tripletto di questa porfirina è ottenibile in entrambe le configurazioni. La generazione di ossigeno singoletto è stata rilevata in acqua, utilizzando una sonda sensibile alla presenza di ossigeno singoletto.

Il quarto capitolo è dedicato alla lignina polimerica naturale, ottenuta tramite processo Kraft, che, in seguito alla funzionalizzazione con i fluorofori della porfirina e della cianina, da luogo a quattro nuovi coniugati della lignina. In questo capitolo sia la sintesi di questi coniugati della lignina che lo studio del loro potenziale in fotomedicina sono presentati. Risultati molto incoraggianti sono riportati alla fine di questo capitolo.

Nel quinto capitolo viene descritta la sintesi e la fotochimica di un nuovo coniugato porfirina-cianina eccitatabile nella regione del vicino infrarosso (porphyrin-near-IR cyanine dye conjugate). Sciogliendo questo coniugato in THF ed eccitando la molecola contemporaneamente con luce nel vicino infrarosso e nello spettro visibile è possibile produrre ossigeno singoletto. La produzione di ossigeno singoletto è stata osservata solamente in THF, il che indica la formazione di stato di tripletto avviene unicamente tramite ricombinazione di carica. L'eccitazione della parte cianininica del coniugato porta all’emissione di fluorescenza soltanto da parte di quest’ultima. Al contrario, quando e’ la porfirina ad essere eccitata, entrambe le componenti del coniugato fluorescono(cianina e porfirina) e la formazione di stati di tripletto è confermata tramite misure spettroscopia di assorbimento risolta in tempo alla scale del nanosecondo.

Sorprendentemente, la durata dello stato di tripletto risulta essere più lunga persino di quella osservata nel composto porfirinico di partenza disciolto nel medesimo solvente (THF). Pertanto, in tale coniugato, la formazione di stati di tripletto avviene tramite ricombinazione di carica nel momento in cui la componente porfirinica viene promossa allo stato di singoletto tramite luce nel vicino infrarosso,

Il penultimo capitolo (Capitolo 6) include i metodi sintetici utilizzati per creare coloranti porfirinici e cianinati. Questi ultimi possono essere combinati per formare nuovi coloranti coniugati cianina-porfirina (capace di assorbire nel vicino infrarosso), che potrebbero avere proprietà migliori.

Sommario

Il capitolo finale descrive la caratterizzazione fotofisica di 16 nuovi PS a base di fenalenone. Le loro proprietà fotofisiche sono state confrontate con la loro efficacia contro i batteri gram-positivi e gram-negativi. Questi derivati del PS naturale, fenalenone, sono stati disciolti in acqua e successivamente la loro capacità di assorbire la luce, la loro fluorescenza e la loro capacità di generare ossigeno singoletto sono state misurate. I derivati contenti triazolo hanno mostrato una solubilità in acqua da media a buona.

Nel complesso, grazie a questo lavoro di tesi sono state sintetizzati e caratterizzati dei nuovi PS eccitabili nel vicino infrarosso, che risulta essere la regione dello spettro della luce più interessante da un punto di vista terapeutico.

Acknowledgements

As I sit here, inside from the cold, trying to keep safe from the scary omicron (latest Covid-19 strain) or some other transformer like Megatron or Optimus Prime, I reflect on the moments and people that helped me reach this point. I want to thank every single one of the people that helped me finish my PhD, from the people that didn't even realise they were helping me, to those that actively went out of their way to help me.

Firstly, I can't help but thank Prof. Dr. Mathias O. Senge for helping me finish my MSc. Thank you for responding to a mail on the 18th of August 2017 enquiring about MSc opportunities in your lab. You took a chance on me to work on the NSD program that led to my second first author publication (after an ACTA C publication). It is thanks to you that I was able to get an impressive number of publications from my one-year masters (6 at the moment, but who knows if more could come 😉), to be able to make friends for life, to be able to go to international conferences and workshops, and to also be able to put me in the direction of my PhD. Without Prof. Senge, this thesis would not exist and I cannot thank him enough for my introduction to porphyrins and the applications that they can have.

From my master's and into my PhD, I would like to thank Dr. Stéphanie Leroy-Lhez and Dr. René M. Williams for selecting me for the project: Optimization of the excitation mode of photosensitizer *via* nanoplatforms. I would also like to thank Dr. Nicolas Villandier for his expertise and guidance on the lignin project, and for the whole thesis. I would also like to acknowledge the hard work of Aurore Berthier for organising the selection school for the Marie-Sklodowska Curie Innovative Training Network – POLYTHEA, for responding to all of the tedious mails over the three years, for solving all of our problems and for making everything so much easier for us throughout the entire PhD. One thing that I will not thank you for is that hand-written cover letter for our PhD applications. Je l'ai écrite trois fois! But, you have more than made up for that at this stage and thank you for all of your hard work!

To Dr. Stéphanie Leroy-Lhez, first of all, I would like to thank you for making POLYTHEA a reality, without your determination and perseverance, POLYTHEA would simply not exist and I would not be sitting here writing this. On a more personal note, I would like to thank you for picking up a young Irish PhD student, with very broken French, from Limoges airport on a sunny Saturday afternoon and bringing him to his accommodation, to also bringing him to the doctor when he was sick with gastro (still have no idea what it is and seems to only be a French thing according to my sources), and finally, for all of your help, guidance and feedback throughout this Irish student's PhD.

Acknowledgements

I want to thank Dr. Williams for his help in teaching me all about the photo-sciences. Before this PhD, I had a very basic understanding of the subject and through his patience, his enthusiasm, and his critical feedback to make me the best researcher I can be, I feel like I can say that I have a more profound knowledge of the subject. Thank you René for the great discussions, the time that you invested into our zoom calls during the numerous lockdowns, moments of freedom, the jokes, good humour and your unwavering support.

Throughout this PhD, I have had the pleasure of collaborating with some terrific scientists that have led to publications. I would like to thank everyone for their hard work. Many thanks to the works of Aram Farawar and Paul Mazzella that helped publish the TCR review (chapter 2). Furthermore, chapter 3 would not have been possible without my secondment in Porphychem in Dijon, France. The supervision of Alexandre Boh, Dr. Benoit Habermeyer, and the rest of the Porphychem staff, proved pivotal for the recent submission of this chapter into the journal of porphyrins and phthalocyanines.

I would like to thank Yann Berbiguier for coupling the cyanine to the porphyrin in chapter 5 of this thesis. For the collaboration in chapter 7, from what started as a discussion after dinner, became a reality when Jérémy Godard messaged me one random Tuesday asking whether I was serious about doing some photophysical measurements on his phenalenone compounds that he synthesized. From there, a publication was made for the journal of Antibiotics and I would like to thank Jérémy, Tan-Sothéa Ouk, Frédérique Brégier and Vincent Sol for their essential work related to this paper.

Throughout the PhD, the day-to-day life would have been a lot more difficult without the people around me. This is where the PEIRENE group, the POLYTHEA students and the Molecular Photonics group came into play! Throughout the selection school, winter and summer schools lockdowns, the zoom calls, the group meetings, and the WhatsApp banter, the PhD was much more fun with all of you. In the PEIRENE group, I want to thank Prof. Vincent Sol for allowing me to work in his lab and the lab members for making the workplace a much more enjoyable place to run a million columns: Veronica, Jérémy, Abdelchakour, Soukaina, Zineb, Nidia (and of course Wenses), Emma, João, Bhavya, Corinna, Prof. Chaleix, Dr. Villaindier, Dr. Brégier, Sylvie, Aurore, Dorthée, and of course, my boss Dr. Stéphanie Leroy-Lhez. Merci beaucoup à tous!

In the Molecular photonics group, I want to thank Prof. Wybren Jan Buma and Prof. Fred Brouwer for allowing me to work in their very impressive laboratories. I want to also

Acknowledgements

thank the hardworking technicians Wim, Michiel and Hans for their banter, help setting up my experiments, for answering random questions about how things work in the Netherlands, the chemical orders and for being able to fix the million things that went wrong. Furthermore, I would like to thank Prof. Zhang, Prof. Woutersen and Dr. Petrignani for their challenging questions during group meetings that led me to critically review my research and improve it. For moral and the chats, I would like to thank Paola, Joen (for giving me your office), Federico (for correcting my italian resumé…FINALLY! and for showing me where to find the cheapest beers in Amsterdam), Giulia (your Kerry accent was very impressive), Kefan, Orr, Chao (you should know this and UNBELIEVABLE JEFF), Hernan (THERE HE IS! Coffee? Thanks for the good times my man and for being always up for a beer), Yanni (thank you for showing me how to set up the laser in the SPEX), Zoi (thanks for the great laughs!), Max (thanks for always responding to my millions questions, help with data processing and always smiling), Jiayun (so smart), Ivan (my Russian chap that was always so serious and then immediately started laughing whenever I said something, it is thanks to you that I think I will become a comedian), Begum, Robert (Bordeaux wine?) and Jun Yuan. I would also like to thank Molphot alumni Roberto (for giving me your desk and for the help with the thesis printing, sorry, I did not learn LaTeX…), Maarten, Janani (thanks for the nice welcome back card to Amsterdam 😊) and last but not least, John (I know you weren't in the group, but just had to throw you in here bcoz you are such a ledge).

Many thanks to Professor Patrick Trouillas for the really nice cover!

To my friends outside the PhD, thank you for your continued friendship through this emotional rollercoaster. I am glad that when we meet up, even after a long without seeing each other, it is like nothing has changed.

Qua, voglio ringraziare Gabriella, Claudia e Mariano per il loro amore e supporto. Mi avete mostrato la luce nei momenti più bui di questo dottorato. Grazie mille per tutto!

To my family, thank you for everything that you have ever given to me. Through your sacrifices and love, I was able to get here today and I will never be ever to repay you for this. Thanks to the stun hun, Niamh, for the great laughs even though we were afar, even when you didn't mean to, I was always able to laugh.

Infin, Un grazie speciale alla mia fidanzata per tutto l'amore che mi ha dato e che mi da ogni giorno. Sono tanto fortunato ad averti. Ti amo chicken dipperino mio.